STUDY OF METALLOPHTHALOCYANINES ATTACHED ONTO PRE-MODIFIED GOLD SURFACES

A thesis submitted in fulfillment of the requirements for the degree of

MASTER OF SCIENCE

of

RHODES UNIVERSITY

by

PHILANI NKOSINATHI MASHAZI

January 2007

DEDICATION

To my dad (Insp. S. A. Mashazi) and my mom (Mrs. D. M. Mashazi), for their unconditional love, support and also standing by me even at odd times. "May God bless you and live longer to reap the fruits you have sown".

ACKNOWLEDGEMENTS

Firstly, I would like to thank God Almighty through His Son Jesus Christ our Lord and Savior for the great things He has done for me and whom all things are possible. For His faithfulness never comes to an end!!!!

I would like to express my sincere gratitude to my supervisor and co-supervisors: Prof. Tebello Nyokong, Dr. Kenneth I. Ozoemena and Dr. Philippe Westbroek for their great support, sharing their knowledge and guidance during my degree programme. I thank you all a million times and I remain eternally grateful to your assistance, Thank you!!!

I also wish to thank my family: mom, dad and everybody (too numerous to mention by names), for the support and encouragement throughout my academic years at Rhodes University. Ndaweni (mom) your prayers saw me through and I am grateful to be your son. Dad your wishes have stayed with me, I hope I have not disappointed you in anyway. My friends (too numerous to mention by names), I thank you guys for making Grahamstown and Ghent enjoyable. To the Chemistry Department staff (technical and academic) and post-graduate students, especially S22, thank you guys for the discussions we shared and for providing such a conducive environment and making Grahamstown a home away from home. I also wish to acknowledge all the helpful discussions, constructive criticism and concerns raised by referees of published work of this thesis, Thank you!!!

Finally, I will remain eternally grateful to Project AuTEK (Mintek and Gold-Fields) for the M.Sc. Scholarship and the National Research Foundation (NRF) for financial assistance. I also would like to thank Ghent University (Belgium) for the support and a rewarding experience through bilateral research project funded by NRF (SA) and UGent-BOF (Belgium).

ABSTRACT

Tetra-carboxy acid chloride phthalocyanine complexes of cobalt, iron and manganese were synthesized and characterized using spectroscopic and electrochemical techniques. These complexes were fabricated as thin films on gold electrode following a covalent immobilization and self-assembling methods. Surface electrochemical and spectroscopic characterization showed that these complexes are surface-confined species. The characterization using spectroscopic and electrochemical methods confirmed the formation of thiol and MPc SAMs on gold electrode. The electrocatalytic behaviour of the SAM modified gold electrodes was studied for the detection of L-cysteine and hydrogen peroxide. The limits of detection (LoD) for L-cysteine were of the orders of 10^{-7} mol.L^{-1} for all the MPc complexes studied and the LoD for hydrogen peroxide at cobalt phthalocyanine modified gold electrode was of the orders of 10^{-7} mol.L^{-1} for both electrocatalytic oxidation and reduction. The modification process for gold electrodes was reproducible and showed good stability, if stored in pH 4 phosphate buffer solutions and can be used over a long period of time.

The cobalt phthalocyanine modified gold electrode was also investigated for the fabrication of glucose oxidase (GOx)-based biosensor and as an electron mediator between the enzyme and gold electrode. The behaviour of the enzyme modified gold electrode towards the detection of glucose was studied and the results gave a limit of detection of the orders of 10^{-6} mol.L^{-1} with low binding constant (4.8 mM) of enzyme (GOx) to substrate (glucose) referred to as Michaelis-Menten constant. The practical applications, i.e. the real sample analysis and interference studies, for the enzyme modified gold electrodes were investigated. These studies showed that the enzyme electrode is valuable and can be used for glucose detection.

TABLE OF CONTENTS

LIST OF ABBREVIATIONS

AC	Alternating current
Ag|AgCl	Silver-silver chloride reference electrode
Au	Gold working electrode
CE	Counter electrode
CFE	Carbon film electrode
CNT	Carbon nanotube
$Co(bpy)_3$	Cobalt tris-bipyridine
CoOBTPc	Cobalt (II) octa-bytylthio phthalocyanine
CoOHETPc	Cobalt (II) octa-hydroxyethylthio phthalocyanine
CoTAPc	Cobalt tetra-amino phthalocyanine
CoTCAClPc	Cobalt (II) tetra-carboxy acid chloride phthalocyanine
CoTCAPc	Cobalt (II) tetra-carboxylic acid phthalocyanine
CPM	Carbon paste matrix
CV	Cyclic voltammetry
CV	Cyclic voltammogram
DC	Direct current
DMF	Dimethylformamide
DT	1,6-hexanedithiol
EDC	N-ethyl-N(3-dimethylaminopropyl) carbodiimide
EIS	Electrochemical impedance spectroscopy
ESCA	Electron spectroscopy for chemical analysis
FCA	Ferrocene monolayer acid
FeOBTPc	Iron (II) octa-bytylthio phthalocyanine
FeOHETPc	Iron (II) octa-hydroxyethylthio phthalocyanine
FeTCAClPc	Iron (II) tetra-carboxy acid chloride phthalocyanine
FeTCAPc	Iron (II) tetra-carboxylic acid phthalocyanine
FTIR	Fourier transform infrared
GCE	Glassy carbon electrode
GE	Graphite electrode

GEM	Graphite emulsion matrix
GOx	Glucose oxidase enzyme
HOMO	Highest occupied molecular orbital
IR	Infrared spectroscopy
LMCT	Ligand-to-metal charge transfer
LoD	Limit of detection
LUMO	Lowest unoccupied molecular orbital
M	Metal
ME	2-mercaptoethanol
MLCT	Metal-to-ligand charge transfer
MnTCAClPc	Manganese (III) tetra-carboxy acid chloride phthalocyanine
MnTCAPc	Manganese (III)-tetra carboxylic acid phthalocyanine
MP	Metalloporphyrin
MPA	Mercaptopropionic acid
MPc	Metallophthalocyanine
MPc SAM	Metallophthalocyanine self-assembled monolayer
MTCAClPc	Metal tetra-carboxy acid chloride phthalocyanine
MTCAPc	Metal tetra-carboxylic acid phthalocyanine
MV	Methyl viologen
Naf	Nafion membrane
Nano-CoPc	Nanoscaled unsubstituted cobalt phthalocyanine
nAu	Gold nanoparticle
NHS	N-hydroxy succinimide
nPt	Platinum nanoparticle
$(OEt)_8CoPc$	Octa-ethoxy cobalt phthalocyanine
OTE	Optically transparent electrode
$Os(byp)_2pic$	Osmium-2-2'-bipyridine picolinic acid
OsPVI	Osmium poly(4-vinylimidazole)
OsPVP	Osmium poly(4-vinyl)pyridine
OTTLE	Optically transparent thin layer electrode
PB	Prussian blue

PBS	Phosphate buffer saline
PGE	Poly graphite electrode
Poly-BQ	Poly-benzoquinone
Poly-MPD	Poly (m-phenyldiamine)
Poly-OAP	Poly (o-aminophenol)
Poly-PPD	Poly(p-phenyldiamine)
PySSPy	Bis-(4-pyridyl) disulphide
QCM	Quartz crystal microbalance
QCM-D	Quartz crystal microbalance with Dissipation
RE	Reference electrode
RSH	Thiol derivatives or cysteine
RSSR	Cystine
$Ru(byp)_2pic$	Ruthenium-2-2'-bipyridine picolinic acid
SAM	Self-assembled monolayer
SCE	Standard calomel electrode
SPCE	Screen-printed carbon electrode
SWV	Square wave voltammetry
TEAP	Tetraethylammonium perchlorate
TMA	Trimellitic anhydride
UPD	Under-potential deposition
UV-vis	Ultraviolet visible spectroscopy
WE	Working electrode
XPS	X-ray photoelectron spectroscopy

LIST OF SYMBOLS

A	Geometric or real surface area
Anal	Analyte
C	Concentration
C_{dl}	double-layer capacitance
$C_{glucose}$	Concentration of glucose
C_{MS}	Mass sensitivity constant
D	Diffusion coefficient
E	Potential
$E_{1/2}$	Half-wave potential
E_B	Binding energy
E_K	Kinetic energy
E_{pa}	Anodic peak potential
E_{pc}	Cathodic peak potential
E_W	Work function
F	Faraday's constant
f	Frequency
f_o	Resonance frequency
h	Plank's constant
Hz	Hertz
I	Current
I(t)	Sinusoidal current
i_{max}	Maximum current
I_o	Maximum current amplitude
I_p	Peak current
I_{pa}	Anodic peak current
I_{pc}	Cathodic peak current
I_{SS}	Steady-state current
j	Complex number
K	Kelvin

K_{amp}	Amperometric selective coefficient
K_m^{app}	Michaelis-Menten constant
Med	Mediators
ox	Oxidized species
Q	Charge
R	Universal gas constant
R_{CT}	Charge transfer resistance
R_E	Electrolyte or solution resistance
red	Reduced species
υ	Scan rate
V	Volt
V	Volume
V(t)	Sinusoidal potential
Vo	Maximum potential amplitude
Z	Impedance (or complex resistance)
Z'	Real component of impedance
Z''	Imaginary component of impedance
Zw	Warburg impedance
α	Transfer coefficient
ΔE_p	Anodic to cathodic peak potential separation
Δf	Change in frequency
$\Delta I_{glucose}$	Current of glucose
$\Delta I_{mixture}$	Current of the mixture (Glucose and interferent)
Δm	Change in mass
ε	Extinction coefficient
λ_{max}	Maximum wavelength
ω	Radial frequency
Γ_{SAM}	Surface coverage or concentration
Θ	Phase angle
π (π^*)	Pi bonding (anti-pi bonding)

LIST OF FIGURES

LIST OF SCHEMES

LIST OF TABLES

CHAPTER ONE:

INTRODUCTION

Metallophthalocyanines (MPcs) are planar, 18 π-electron systems with highly conjugated structure, as shown in Figure 1.1. MPc complexes are well known commercially as blue-green pigments [1,2] with the colour arising from their intense absorption band observed in the visible region of the spectrum called the Q band. MPcs have been found useful in many technological applications such as photovoltaic cells [3], fuel cells [4], semi-conductor devices [5,6], electronic and chemical sensors [7,8], catalysis [9-12] and recently in medical applications as photosensitizers for photodynamic therapy [13-15]. MPcs, if fabricated as thin films or monolayers on metal surfaces have attracted more attention in research. Several techniques have been used for MPc thin film and monolayer formation; such as Langmuir-Blodgetts [16-21], spin coating [20,21] and self-assembly [20-25]. The latter method (self-assembly) is a more favourable technique, due to its simplicity, ease of formation of a monolayer and controllable surface chemistry.

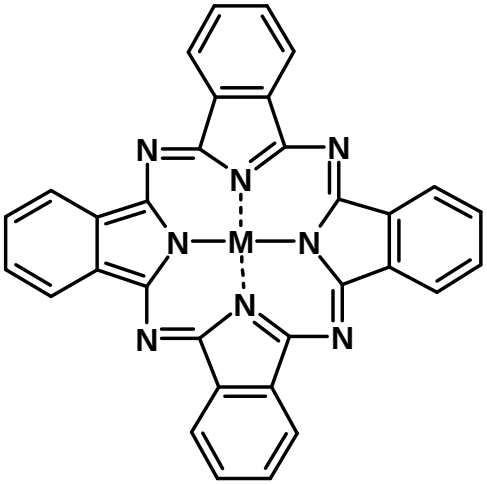

Figure 1.1: Chemical structure of metallophthalocyanine (MPc). M represents the metal ion at the centre of the macro-cycle.

1.1 General overview of self-assembled monolayers (SAMs)

Self-assembled monolayers (SAMs) are formed by spontaneous adsorption of chemical molecules (such as thiols or sulphur containing molecules) onto a metal surface (such as gold) forming an ultra thin film or monolayer [26-30]. SAMs are an incredible means of fabricating stable, easily controllable ultra-thin solid films (monolayer) onto gold surface. The ease of monolayer formation makes the SAM method desirable compared to other methods such as Langmuir-Blodgetts and spin coating which require specialized equipments and take several steps to form [27]. The stability of monolayer formation on gold surface, as will be used in this work, is due to a strong gold-sulfur (Au-S) covalent bond formation [27].

SAMs gained their popularity 20 years ago when Nuzzo and Allara [31] reported the self-assembled monolayer formation using alkanethiol (Figure 1.2). More groups joined the work on SAMs in the 1980s [32-37]. Due to the affinity of sulfur to gold, different functional groups can be incorporated on the exposed terminal group of the SAM [26,27,30,38] and this functionalization improves the properties of SAM such as sensitivity and the selectivity [27]. Functionalized SAMs are used to fabricate very interesting devices that can be used as electrochemical and chemical sensors [5,26,39], non-linear optics [5] and biosensors [40-44]. The unlimited applications of SAMs on gold surface play an increasingly important role which might surpass bulk gold in many technological aspects. The other advantage offered by the self-assembly over other methods is that orientation of the molecules forming the SAM may be controlled [45].

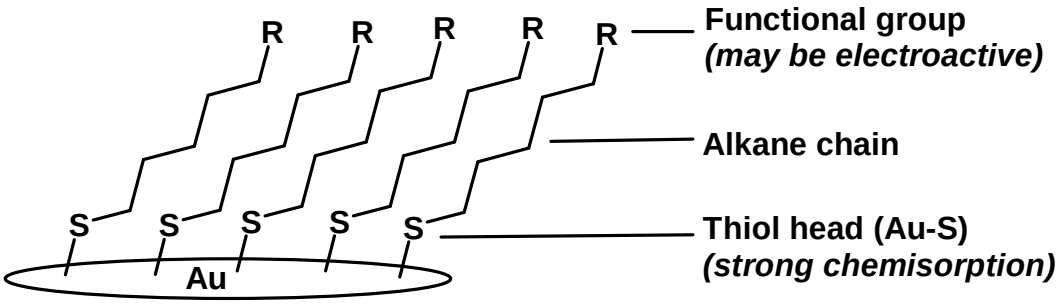

Figure 1.2: Schematic representation of the thiolates on gold (SAM).

The monolayer formation in this work will be on gold surface since thiols chemisorb as thiolates on gold surface. The choice of gold is due to the fact that gold is an inert material, i.e. does not form stable oxide under ambient conditions [42,46]. The affinity of sulfur to gold can be explained using the Hard-Soft Acid Base (HSAB) theory by Pearson [47,48]. The generalized qualitative HSAB principle states that 'hard acids prefer to coordinate with hard bases and soft acids prefer to coordinate with soft bases'. According to Pearson's [47,48] Lewis acid classification, Au is the soft acid and thiol derivatives (RSH) are soft bases, therefore a strong covalent bond (Au-SR) occurs between Au and RSH.

The properties of SAMs described above have attracted further research interest in many fields where metallophthalocyanines (MPc) and metalloporphyrins (MP) are being applied. This work focuses mainly on the MPc self-assembled monolayers (MPc SAMs) on gold surface. The fabrication of metallophthalocyanine complexes as SAMs on gold surface have been shown to yield important devices such as electrochemical and chemical sensors [5,6] which have potential applications in electrocatalysis and electroanalysis.

1.1.1 Metallophthalocyanine self-assembled monolayers (MPc SAMs)

The immobilization of metallophthalocyanine complexes onto gold electrodes have been extensively studied by various research laboratories [20,23-25,39,49-60]. In general, the immobilization of MPc complexes on gold electrodes requires the synthesis of MPc containing sulfur substituents on the peripheral position of the ring or on the central metal. This is then followed by direct immobilization of these sulfur-containing phthalocyanines (via sulfur moieties) onto the gold surface. Cook and colleagues [20,25,39,50,51] investigated the use of one-legged thiol substituted phthalocyanine for the formation of MPc SAMs. This approach had one limitation in that the MPc ring was tilted in an unpredictable angle on gold surfaces. The subsequent work by Lieberman's research group [22,53] and in our research group [55-58] addressed the drawback of Cook's approach by forcing an MPc ring to lie flat on gold surface. This was achieved by octa-subtitution of MPc complexes with thiol groups or by forming an axial ligand on the central metal ion within the MPc ring system, resulting in MPcs lying horizontal or flat to the surface of gold electrode forming an umbrella or an octopus-like orientation [22-24,53-60]. The disadvantage of the direct immobilization of thiol substituted MPc complexes is the difficulty that can be experienced when synthesizing sulfur or thiol substituted phthalocyanines. The synthesis of sulfur containing phthalocyanine is costly, tedious, time consuming and involves the use of toxic and expensive chemical reagents. Therefore an alternative method of immobilizing MPc molecules on gold surface that can avoid the synthesis of thiol MPc complexes is desirable.

1.1.2 Aim of this work

The aim of this work is to find an alternative and novel method of immobilizing metallophthalocyanine molecules onto gold surface that will avoid the synthesis of the thiol or sulfur containing phthalocyanine.

Gold surface will be used for monolayer formation since thiols chemisorbs as thiolates on gold surface. Gold surface has been chosen due to the fact that it is an inert material, i.e. does not form stable oxides at ambient conditions. MPc self-assembled monolayers will be studied as thin films on gold surfaces.

Metal tetra-carboxy acid chloride phthalocyanine (MTCAClPc) complexes which are easier to synthesize compared to thiol MPc will be employed. MTCAClPc will be immobilized onto pre-modified gold electrode surfaces. This will be followed by covalent immobilization of an enzyme (such as glucose oxidase) onto an acid modified phthalocyanine which is attached onto pre-modified gold electrode thus affording the enzyme layer surface.

1.2 Methods of characterization of SAMs

There are several known [28,30] methods for the characterization of modified electrodes such as gold electrodes modified with thiol self-assembled monolayers. These methods can be categorized [28,30] into two: (i) electrochemical methods and these include cyclic voltammetry (CV) and electrochemical impedance spectroscopy (EIS), (ii) non-electrochemical methods such as quartz crystal microbalance (QCM), X-ray photoelectron spectroscopy (XPS) and Raman spectroscopy. These methods differ from each other by sensitivity and the information obtained. However good agreement between the information obtained using different methods is crucial as it will prove the formation monolayer and gives convincing evidence of the surface modification. The principles, advantages offered and the data obtained by each of these methods will be discussed in this section. The importance and usefulness of using these methods for the characterization of SAM modified electrodes will be highlighted in studying surface chemistry, thus confirming surface modification. In general, electrochemical methods have been extensively used due to their simplicity and low cost. They also provide useful information regarding the integrity of the electroactive SAMs adsorbed onto gold surface [28-30]. On the other hand, non-electrochemical methods are very useful as they provide spectroscopic evidence and the composition of the organic film chemisorbed onto gold surface [28,30].

1.2.1 Cyclic voltammetry

Cyclic voltammetry (CV) has been extensively used for the characterization of SAMs of simple thiols and/or MPc SAMs on gold electrodes. CV is a well established electrochemical method for studying surface chemistry since it gives insight into electroactive species on the gold surface [28,29]. CV has also gained its popularity due to its simplicity and rapid location of

redox properties of electroactive species [28-30]. SAMs are known to exhibit a blocking behaviour towards a number of Faradaic processes and this phenomenon can be exploited easily using CV. Furthermore, SAMs have shown the blocking behaviour by inhibiting the metal deposition on gold surface and blocking of redox couples [28-30]. This blocking behaviour of SAMs has been shown to be dependent on the terminal functional groups of SAMs [38]. The SAM's functional groups behave differently in solutions containing redox probes such as ferricyanine solution where the electron transfer and the blocking behaviour of the SAMs can be investigated. The ferricyanine is a highly reversible system and this reversibility can either be inhibited or enhanced upon modifying the gold electrode with the SAM [33]. SAM characterization using CV can also be done in ferric ammonium sulfate $\{FeNH_4(SO_4)_2\}$ solution [33] that exhibits a redox couple at bare gold electrode which is then blocked after gold electrode modification with SAM. $FeNH_4(SO_4)_2$ is a slow electron transfer system [33] compared to ferricyanine and it involves redox couple due to $[Fe(H_2O)_6]^{3+}/[Fe(H_2O)_6]^{2+}$.

The inhibition of the metal deposition is done using the under-potential deposition (UDP) method which is a known method for studying inhibition of bulk deposition of a foreign metal such as copper (Cu) from copper sulphate ($CuSO_4$) solution onto gold surface [28,30]. The UDP method involves the ad-atom metallic layer formation of copper onto gold surface by reduction and this metallic layer is stripped from gold surface on the return scan. This copper metallic layer exhibits two very distinct reversible peaks at $E_{1/2} \sim 100$ mV (vs SCE) [28] which disappear upon modifying gold electrode, as the access to the gold surface is blocked.

CV experiments can also be used to estimate the surface coverage of the SAMs on gold surface, i.e. quantifying the amount of the immobilized organic film on gold surface. After the surface concentration estimation, the orientation of the organic film on gold electrode can also be

estimated. Several methods are used to calculate surface coverage of thin films or SAMs on gold electrodes. These methods include the oxidative or reductive desorption method [28-30]. Thiol SAMs are known to quantitatively desorb either oxidatively (equation 1.1) or reductively (equation 1.2) from gold surface in alkaline media (0.2 M KOH):

$$Au\text{-}SR + 4OH^- \longrightarrow Au + RSO_2^- + 2H_2O + 3e^- \quad (1.1)$$

$$Au\text{-}SR + e^- \longrightarrow Au + RS^- \quad (1.2)$$

The electrochemical desorption of thiol from gold results in either oxidative or reductive peak. The charge (Q) under this desorption peak is used to calculate the surface coverage (Γ_{SAM} / mol.cm^{-2}) of the SAM using the theoretical relationship in accordance to equation 1.3 [28-30,61-63]:

$$\Gamma_{SAM} = \frac{Q}{nFA} \quad (1.3)$$

where n represent the number of electrons involved in the desorption of thiol, F is the Faraday constant (C mol^{-1}) and A is the geometric surface area of the gold electrode.

Surface coverage may also be estimated using the metal (M^{III}/M^{II}) redox couple from the MPc SAM chemisorbed onto gold surface in a suitable electrolyte solution [28-30]. The surface coverage (Γ_{SAM} / mol.cm^{-2}) can then be calculated using equation 1.3 or the relationship shown in equation 1.4:

$$i_p = \frac{n^2F^2A\Gamma_{SAM}}{4RT}\upsilon \quad (1.4)$$

where i_p is the peak current (amps), n is the number of electrons, A is the area of the electrode (cm^2), υ is the scan rate (V/s) and the other symbols have their usual meanings. However, this method is only applicable if the SAM is electroactive and exhibits a reversible redox peak independent of scan rate.

Advantages of CV as a SAM characterization method are purely based on its popularity, simplicity and it can give very important information about the SAMs such as, (i) integrity of SAM, (ii) capacitive properties of SAM, (iii) surface coverage and (iv) estimate the orientation of the monolayer formed on gold surface. The information obtained by CV is important as it gives the evidence of the modification of gold surface and confirms the presence of the monolayer on gold electrode.

1.2.2 Electrochemical impedance spectroscopy (EIS)

Electrochemical impedance spectroscopy (EIS) is a powerful method used to study electrochemical properties of systems and their interfaces with conductive electrodes [64-67]. EIS can be used in various applications, and this work focuses on its ability to characterize thin film formation.

1.2.2.1 Basics of impedance spectroscopy

Impedance theory is a branch of alternating current (AC) theory [65,67] that illustrates the response of a circuit to an alternating current or voltage as a function of frequency. Impedance is a complex resistance which results when an AC voltage is applied to the material. Impedance measurements are done over suitable frequency ranges and the results can be related to the physical and chemical properties of the material [64-67]. In DC (direct current) theory,

Ohm`s law defines resistance (R) in terms of the ratio between voltage (V) and current (I), relationship as shown in equation 1.5:

$$R = \frac{V}{I} \qquad (1.5)$$

Impedance (or complex resistance) is measured by applying a sinusoidal potential, V(t), of small amplitude to an electrochemical cell and measuring the resulting sinusoidal current, I(t), through the cell [64,65,67]. The applied sinusoidal potential and the resulting sinusoidal current are represented as a function of time. Since the impedance is used as an analogue to resistance the relationship in equation 1.6 holds:

$$Z = \frac{V(t)}{I(t)} \qquad (1.6)$$

where V(t) is the sinusoidal applied voltage at time t, $V(t) = V_0 \sin \omega t$, where V_0 is the maximum potential amplitude, ω is the radial frequency (in $rad.s^{-1}$) which can be related to frequency f (Hz) as $\omega = 2\pi f$. The current response I(t) is sinusoidal at the same frequency as the applied sinusoidal potential but shift in phase, $I(t) = I_0 \sin (\omega t + \Theta)$, where I_0 is the maximum current amplitude and Θ is the phase shift by which the voltage lags the current [64,65,67] as shown in Figure 1.3(a). The impedance is a vector quantity with a magnitude and direction. The magnitude of impedance is Z (V/I) and the direction represented as a phase angle (Θ) as shown in Figure 1.3(b). The complex notation of impedance is shown in equation 1.7:

$$Z = Z' + jZ'' = Z_{real} + j\,Z_{imaginary} \qquad (1.7)$$

Where Z' and Z" are the real and imaginary parts of the impedance, respectively and j is a complex number.

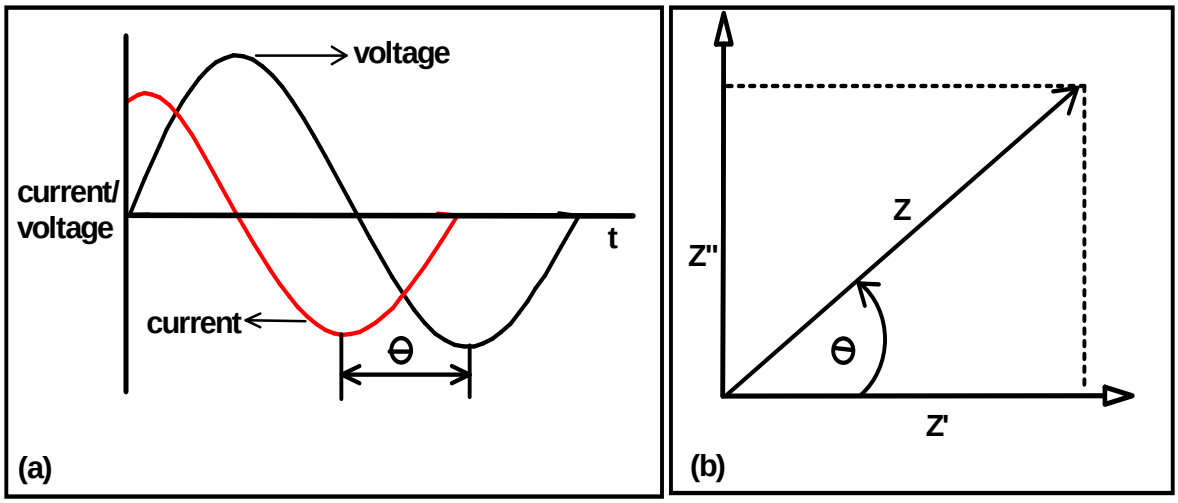

Figure 1.3: (a) Applied sinusoidal voltage and resulting sinusoidal current response and (b) vector representation of real (Z') and imaginary (Z") part of impedance (Z) [64,65].

1.2.2.2 Applications and data representation of EIS

Electrical equivalent circuits are used for the analysis of the impedance data, and within the circuit, simple electrical elements such as resistance (R) and capacitance (C) are connected to model the electrochemical process [64-67]. The resistance in the equivalent circuit represents the electrical conductivity of the electrolyte and the capacitance (double-layer capacitance) caused by the charge which is in excess at the of electrode-electrolyte interface. The most widely used equivalent circuit for the analysis of the impedance data is the Randles equivalent circuit [64-67] shown in Figure 1.4. The Randles equivalent circuit shows the solution or electrolyte resistance (R_E) connected in series to the parallel combination of charge transfer resistance (R_{CT}) and the

double-layer capacitance (C_{dl}). In other systems the reaction rate might be controlled by transport phenomenon and this effect needs to be taken into consideration, the measured impedance can be explained by the component that depends on the conditions of transport or diffusion of electroactive species [64,67]. This component is called Warburg impedance (Zw) and is connected in series with the charge transfer resistance.

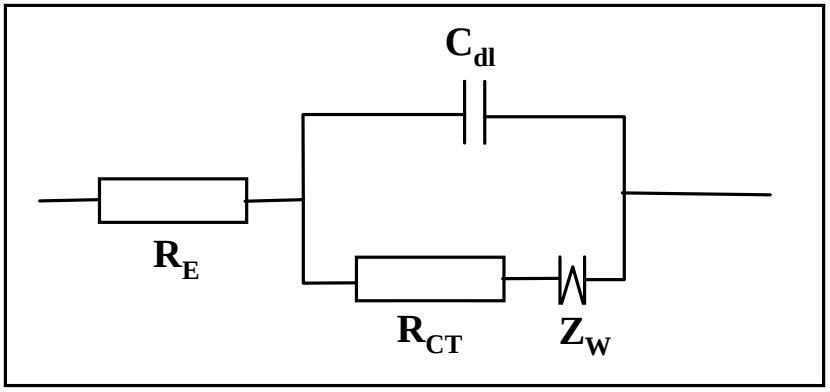

Figure 1.4: Randles circuit for the electrochemical system with diffusion-limited behaviour.

Impedance data can be graphically represented in two ways using Nyquist and Bode plot [64,67]. The most widely used impedance data representation is the Nyquist plot or sometimes referred to as complex plane. Nyquist plot is the plot of the imaginary part (Z") versus the real part (Z') of the impedance, Figure 1.5. The plot of imaginary part vs the real part gives the point in the Nyquist plot which is the absolute value for the impedance measured at that frequency.

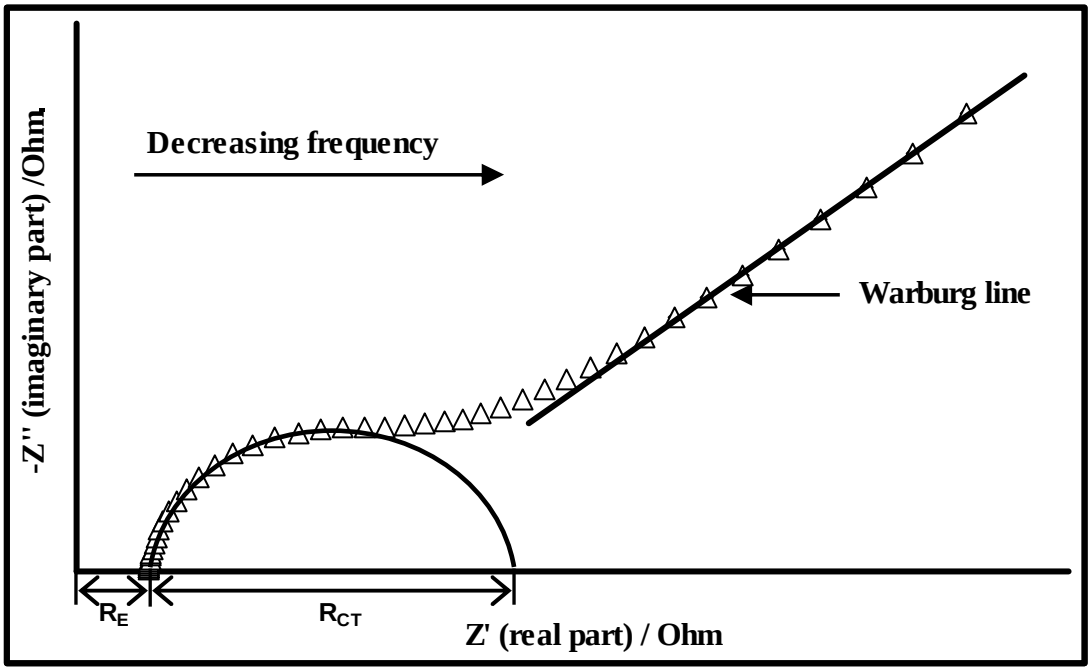

Figure 1.5: Nyquist plot for the electrochemical system with diffusion-limited behaviour, R_E (electrolyte or solution resistance) and R_{CT} (charge-transfer resistance).

Even though the Nyquist plot has been widely used for the graphic representation of impedance measurement, there is no indication of the frequency where the impedance was measured. Therefore, the use of different data representation of the impedance measurement which gives information about frequency where the impedance was measured is desirable. Bode plot is another form of impedance data representation which gives the frequency information at the measured impedance [64,67]. Bode data representation is the plot of the phase angle (Θ) and the logarithm of impedance magnitude (log Z) versus the logarithm of the frequency (log f) as shown in Figure 1.6. Sometimes using Bode data representation one can plot the log Z' and log Z" versus log f, and compare to Nyquist plot if both types of Bode plot are included all the information can be obtained for impedance measurements.

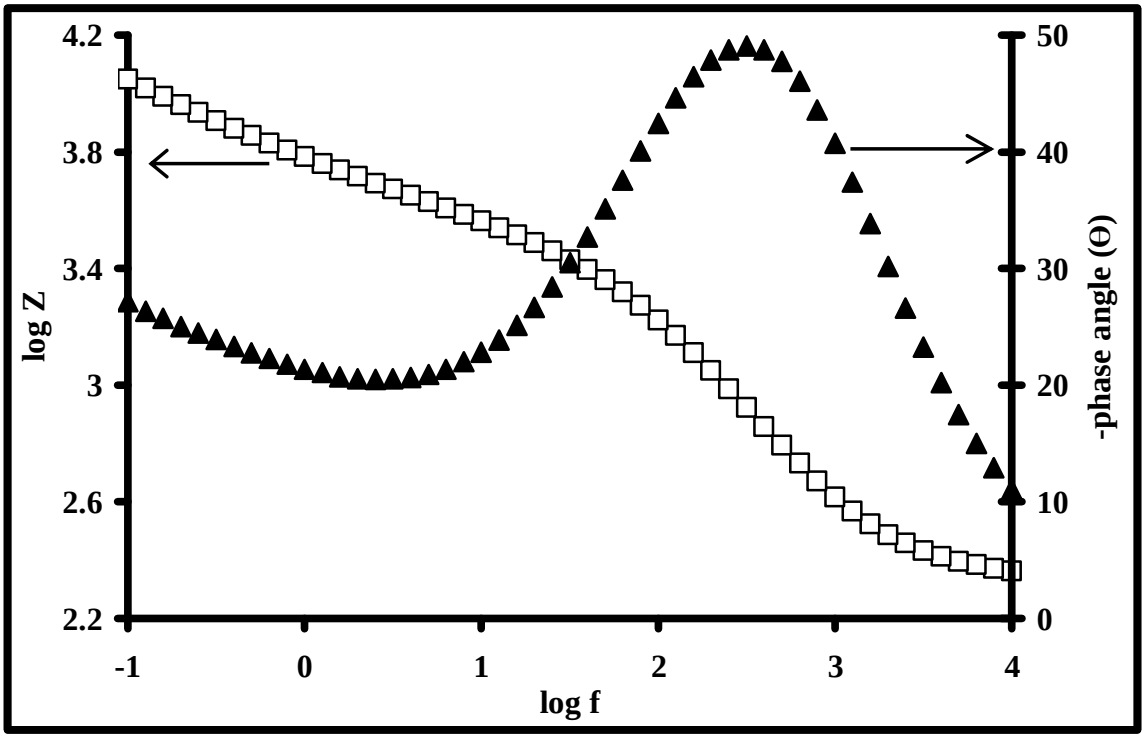

Figure 1.6: Bode plot for the Randles equivalent circuit with diffusion-limited behaviour.

Electrochemical impedance spectroscopy offers many advantages over other techniques and these include (i) the use of low-amplitude sinusoidal voltage (about 5 mV) which makes the system remain at equilibrium or at steady state, (ii) rapid acquisition and quantification of data such as ohmic resistance, double layer capacitance, conductivity of the film, as well as charge or electron transfer at the electrode-film interface and within the film in a single experiment, (iii) accurate, repeatable measurements can be acquired, (iv) high adaptability of this technique to different applications and (v) the characterizing interfacial properties in the absence of a redox reaction.

1.2.3 Quartz crystal microbalance (QCM)

The quartz crystal microbalance (QCM) is an ultra-sensitive weighing device that utilizes the mechanical resonance of the piezoelectric single crystalline quartz, discovered by Pierre and Jacques Curie in 1880 [68]. The quartz crystals (gold-coated surface in this work) are used as weighing devices (AT-cut crystals) and ensure high temperature stability and pure shear motion when subjected to an electric field. The mechanical resonance is a phenomenon [69] by which the crystal is subjected to the external field to induce a mechanical strain in a crystal making it oscillate. As illustrated in Figure 1.7, the thin crystal is sand-witched between a pair of circular metal electrodes [70].

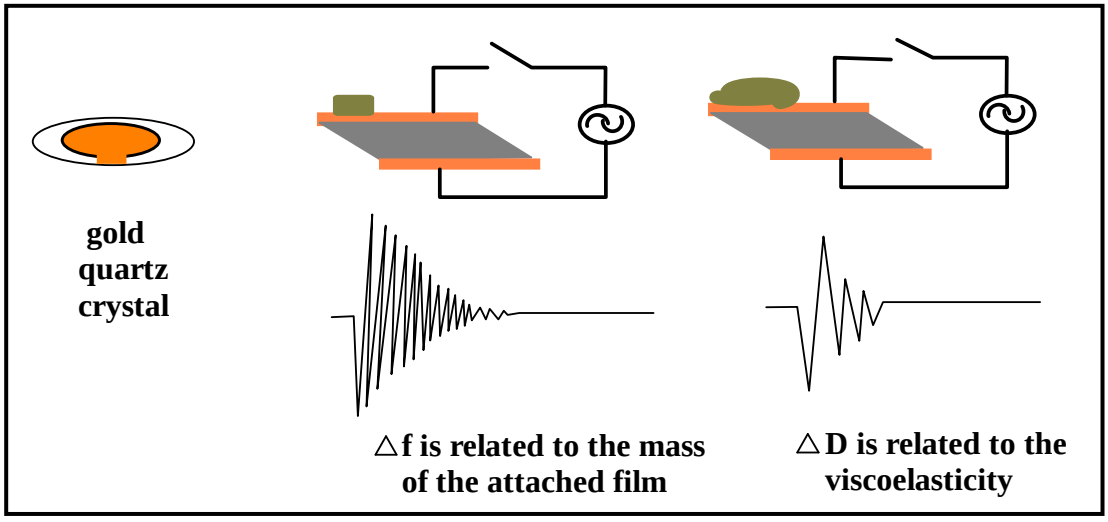

Figure 1.7: Schematic illustration of the QCM-D principle. The change in frequency (Δf) of the oscillating crystal is related to the total oscillating mass, while the energy dissipation (ΔD) is related to the visco-elastic properties of the oscillating mass.

When the AC voltage is applied, the frequency of the applied voltage corresponds to the resonance frequency (f_o) of the crystal. This resonance occurs when the thickness of the disc is an odd integer number of half-wavelength causing the oscillation to have its antinodes at each

electrode interface. The resonance frequency of the crystal is directly proportional to the total mass on the crystal provided that a mass that is added (Δm) on the surface results in the change of frequency (Δf). The relationship in equation 1.8 discovered by Sauerbrey in 1959 is used to relate the change in frequency to the amount of mass adsorbed [71].

$$\Delta m = -\frac{C_{MS}\Delta f}{n} \qquad (1.8)$$

where C_{MS} is the mass sensitivity constant (17.7 ng Hz $^{-1}$ cm^{-2} at an oscillation frequency of 5 MHz or overtone n = 1) and n is the overtone number (1, 3, 5, 7, 9…). However for equation 1.8 to be valid the following conditions should be met: (i) total mass of the adsorbed film should be small compared to the weight of the crystal, and (ii) the adsorbed film should be rigid and evenly distributed over the active area of the crystal. Then the change in the total mass of the crystal (Δm) induced upon adsorption is proportional to a change in frequency (Δf) according to Sauerbrey equation above. QCM has for a long time been used to monitor film deposition in gas and vacuum applications; recently QCM has been employed in liquid or solutions [66]. The use of QCM in liquid phase has resulted in an increase in number of applications for QCM in the field of biotechnology [72-78]. However, from the use of solutions on surface, it was realized that the adsorbed film does not obey the assumption underlying the Sauerbrey relationship. This is due to the presence of the water molecules (if water is used) trapped between the adsorbed film and the non-rigid character of the adsorbed film resulting in the friction and dampening of the crystals oscillation [72]. The technical solution was to adapt the equipment so that it can provide further information not only about the changes in resonance frequency but also changes in energy dissipation, ΔD, of the oscillating crystal. Therefore, other than its original use as a weighing device, the QCM then incorporates the energy dissipation capability which further measures the visco-elastic properties of the adsorbed layers, the equipment used is QCM-D.

The advantage of the using QCM is its ability to provide real-time characterization of the surface reactions, mass and structural changes on the metal surface. For SAM characterization QCM-D technique can be used to monitor the formation and the characterization of SAMs on gold surface and give the amount (i.e. the mass of the adsorbed film), the thickness and the viscoelastic properties of the immobilized molecules.

1.2.4 X-ray photoelectron spectroscopy (XPS)

X-ray photoemission spectroscopy (XPS) sometimes referred to as an electron spectroscopy for chemical analysis (ESCA) is an electron spectroscopic method for the determination of elemental and chemical composition of the materials or organic film on metal surface [28,79,80]. XPS is a well-established tool for the characterization of the molecular structure of organic films. The presence of the desired elements in the film can be confirmed using the XPS spectra and evaluation of atomic compositions [79-81]. XPS is based on the photoelectron effect [79,80] and this effect is illustrated in Figure 1.8, where the surface is irradiated with the photons (x-ray photons). The x-ray photons interact with the core-level electrons leading to the emission of photoelectron. After the ejection of photoelectron the atom re-organizes itself by dropping an electron from higher energy level to a vacant core hole followed by the ejection of an Auger electron from the higher level.

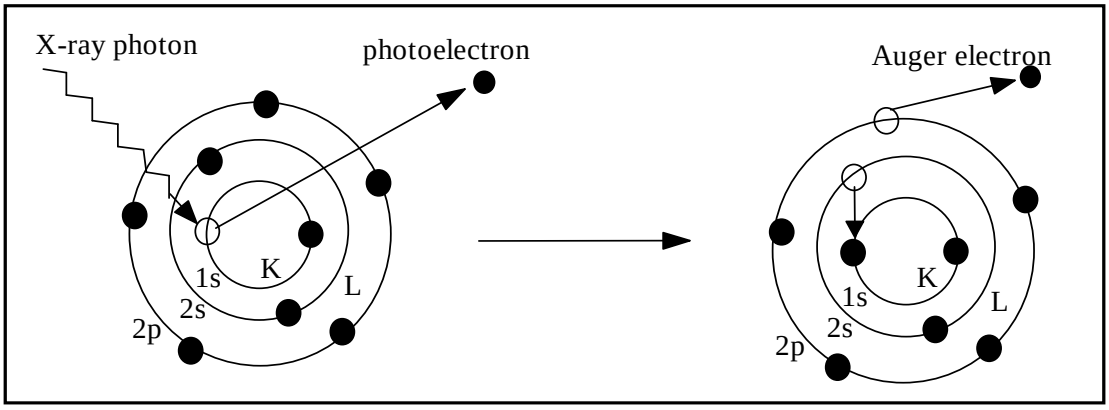

Figure 1.8: Representation of the processes that takes place in XPS and ejection of the Auger electron.

The kinetic energy (E_K) of ejected photoelectrons is the difference between the energy of the x-ray radiation ($h\nu$) and the electron binding energy (E_B). Since the kinetic energies of the excited photoelectrons is measured using the instrument, the work function (E_W) of the spectrometer is taken into consideration. Therefore the binding energy of an emitted electron is given by equation 1.9 [79,80]:

$$E_B = h\nu - E_K - E_W \qquad (1.9)$$

The binding energy (E_B) of the emitted electron is characteristic of the atom from which it has been ejected and it also depends on the chemical environment of the atom. The plot of electron intensity as a function of binding energy is a photoelectron XPS spectrum, Figure 1.9 gives the set characteristic lines at specific electron binding energies representing atoms.

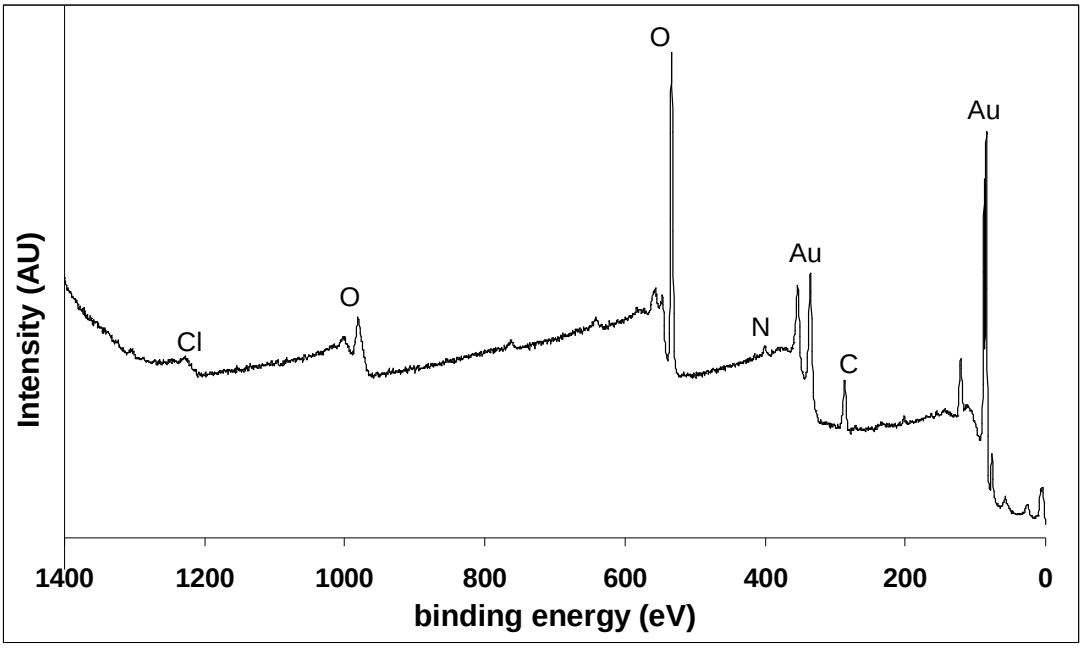

Figure 1.9: XPS survey spectrum shows the atoms/elements present in the phthalocyanine modified gold electrode.

XPS as a surface analytical technique has been widely used for characterization of organic and thin film modified metal surfaces, such as gold [28,30]. In this work XPS will be used to investigate the elemental composition of thiol and phthalocyanine modified gold surfaces. In comparison to other surface analytical techniques, XPS offers several advantages' such as its sensitivity as it gives "fingerprint" information about the atoms, i.e. the elements binding energies and their chemical environment. However, the use of this technique in combination with other surface techniques is desirable in order to further confirm the surface modification.

1.2.5 Raman Spectroscopy

Raman spectroscopy is an analytical technique which operates in a same manner as other spectroscopic techniques as it also involves the interaction of molecules with light (or energy). However, in contrast to other spectroscopic techniques, Raman spectroscopy is concerned with the scattering of radiation by the sample rather than the absorption process [82,83]. Similar to infrared spectroscopy, Raman spectroscopy is a useful technique in chemical industry as it provides structural information about the molecules based on the vibrational energy bands. This technique is based on the Raman effect which is the result of inelastic light scattering [82,83]. This effect occurs when the light collides with the molecule and the energy is transferred between the light and the molecule. The energy from the light excites the molecule from the ground state to a virtual state. This virtual state of the molecule is just a distortion of the electron distribution of a covalent bond (polarizability of the bond) which will determine the intensity and the frequency of the Raman shift [82,83]. The virtual state is not the stationary energy state of the molecule; therefore the molecule immediately relaxes back to the original ground state by emitting a photon. This process can be described using energy diagram shown in Figure 1.10, which shows that after the release or emission of the photon, the molecule relaxes to vibrational ground energy state following three-photon processes [82,83]: (i) Rayleigh, (ii) Stokes Raman and (iii) anti-Stokes Raman scattering. Rayleigh scattering takes place when there is no energy transfer, i.e. if the molecules returns to the vibrational ground state and the emitted photons have the same energy and wavelength as the initial photons. Stokes Raman scattering occurs when the molecule returns to a higher vibrational level, meaning the emitted photon has less energy and longer wavelength than the initial photon. Lastly the anti-Stokes Raman scattering takes place

when the molecule returns to a lower vibrational energy and shorter wavelength than the initial photon.

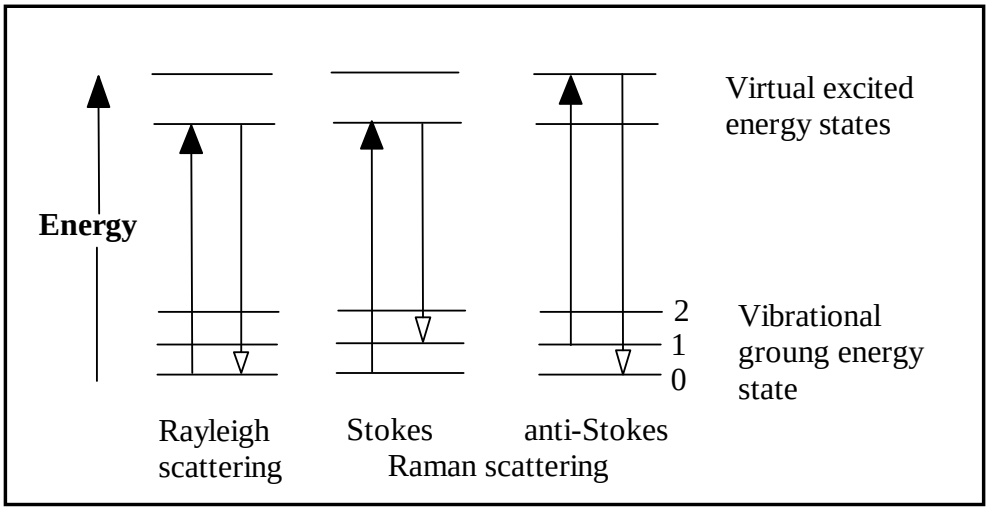

Figure 1.10: Energy level diagram showing Rayleigh, Stokes and anti-Stokes Raman scattering.

For analytical purposes Stokes Raman lines are mainly used as they exhibit larger intensities than the anti-Stokes [82,83]. Raman data from the sample are usually displayed as a plot of Raman scattering intensity against wave number (cm^{-1}) and this is called a Raman spectrum shown in Figure 1.11.

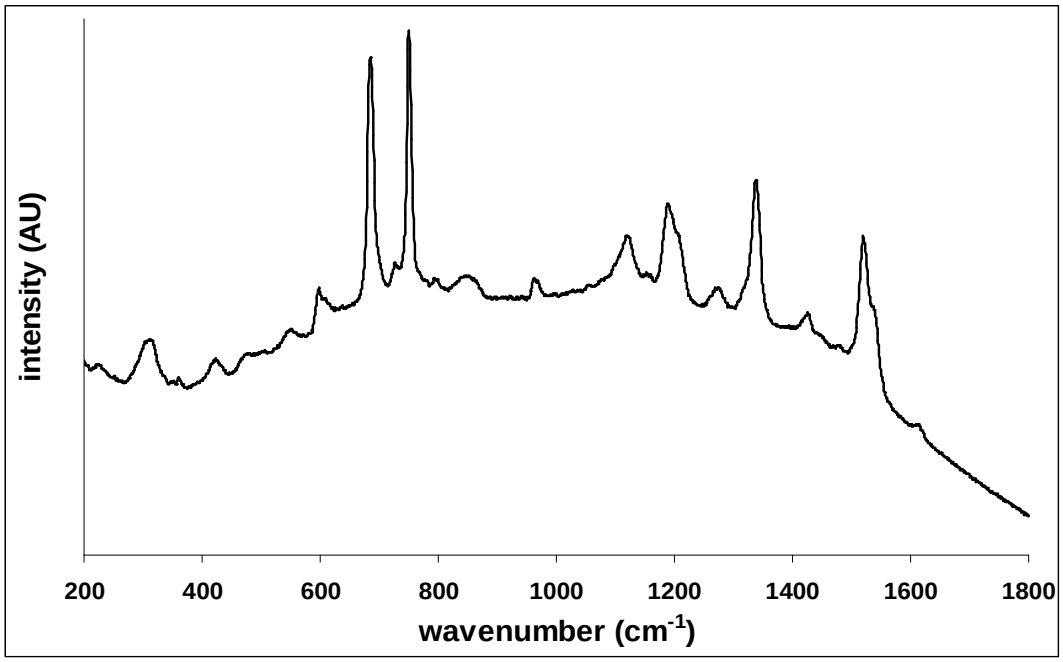

Figure 1.11: Raman spectrum of gold electrode modified with manganese phthalocyanine self-assembled monolayer.

In this work, Raman spectroscopy as a surface analytical technique has been used to confirm gold surface modification with SAMs of thiol and phthalocyanine complexes. This method has been useful in this study especially as it has been used in conjunction with other surface characterization techniques to study the structural information about the immobilized molecules on gold surface.

1.2.6 Aims

In this work detail surface characterization of SAM modified gold electrodes has been studied using different techniques such as (i) Cyclic voltammetry (CV), (ii) Electrochemical impedance spectroscopy (EIS), (iii) Quartz crystal microbalance (QCM), (iv) X-ray photoelectron spectroscopy (XPS) and (v) Raman spectroscopy.

The information obtained using each method has been analyzed and the agreement in the obtained information using different techniques is of importance as this will confirm and give evidence of surface modification. The amount of the monolayer on gold surface including its structural and elemental information has been investigated.

1.3 General Properties of MPc

Metallophthalocyanines exhibit unique properties which enable them to be used as semiconductors, photoconductors, electro-conductors as well as in non-linear optics [5,84]. Furthermore, MPc complexes exhibit interesting redox properties arising from the ring and if the central metal is electroactive, further redox properties arising from the central metal ion can be observed. MPc complexes are also known to be chemically and thermally stable and these properties have allowed them to be used in fuel cells, as photovoltaic materials and in molecular electronics [3,4,85,86]. Applications of MPc complexes are hindered by their low solubility in organic and aqueous solutions. However, this drawback can be improved by introducing substituents either in the ring system or as axial ligands on the central metal ion. The ring substituents can be attached in one of the two positions of the MPc ring as shown in Figure 1.12(a), i.e. β-position or α-position. The substituents at β-position are at positions 2, 3, 9, 10, 16, 17, 23 or 24 referred to as peripheral positions whereas the substituents at α-position are at positions 1, 4, 8, 11, 15, 18, 22 or 25 referred to as non-peripheral positions. In comparison to metalloporphyrins (MPs) complexes which are known to occur naturally, Figure 1.12(b), MPcs are more stable. The structures of MPc and MP complexes in Figure 1.12 exhibit some similarities except that the porphyrin ring system is made up of pyrrole units instead of isoindole units found in metallophthalocyanine ring system. The pyrrole units in porphyrins are linked via carbon atoms whereas the isoindole units in phthalocyanines are linked by an aza-bridge, i.e. nitrogen atoms. The MPc structure in Figure 1.12(a) shows the numbering system and positions where ring substituents can be attached.

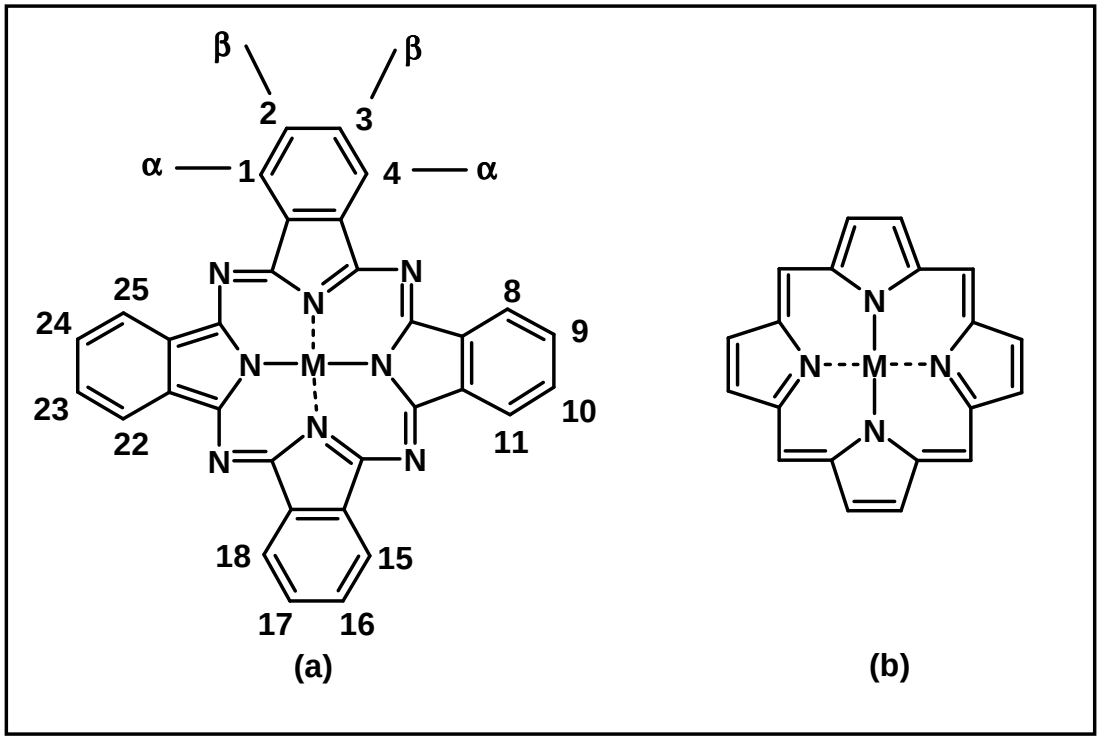

Figure 1.12: Molecular structure of (a) metallophthalocyanine showing α- and β-positions including numbering and (b) metalloporphyrin.

1.3.1 Synthesis of MPc

There are several methods reported for the synthesis of metallophthalocyanine complexes, the common method [87,88] is shown in Scheme 1.1. Inexpensive starting materials such as phthalic anhydride (**1**), 1,3-diiminoisoindoline (**2**), phthalimide (**3**), phthalic acid (**4**) and phthalonitrile (**5**) are utilized. This method involves heating the mixture of one of the starting materials in the presence of other reagents such as metal salt, urea, solvent and the catalyst to yield the MPc complex. The solvent used should have a high boiling point as the formation of MPc is accomplished at high temperatures, e.g. 195 – 200 ˚C when trichlorobenzene is used as a solvent [88]. This method is also known to give excellent yields (>70%) with minor imine impurities [88].

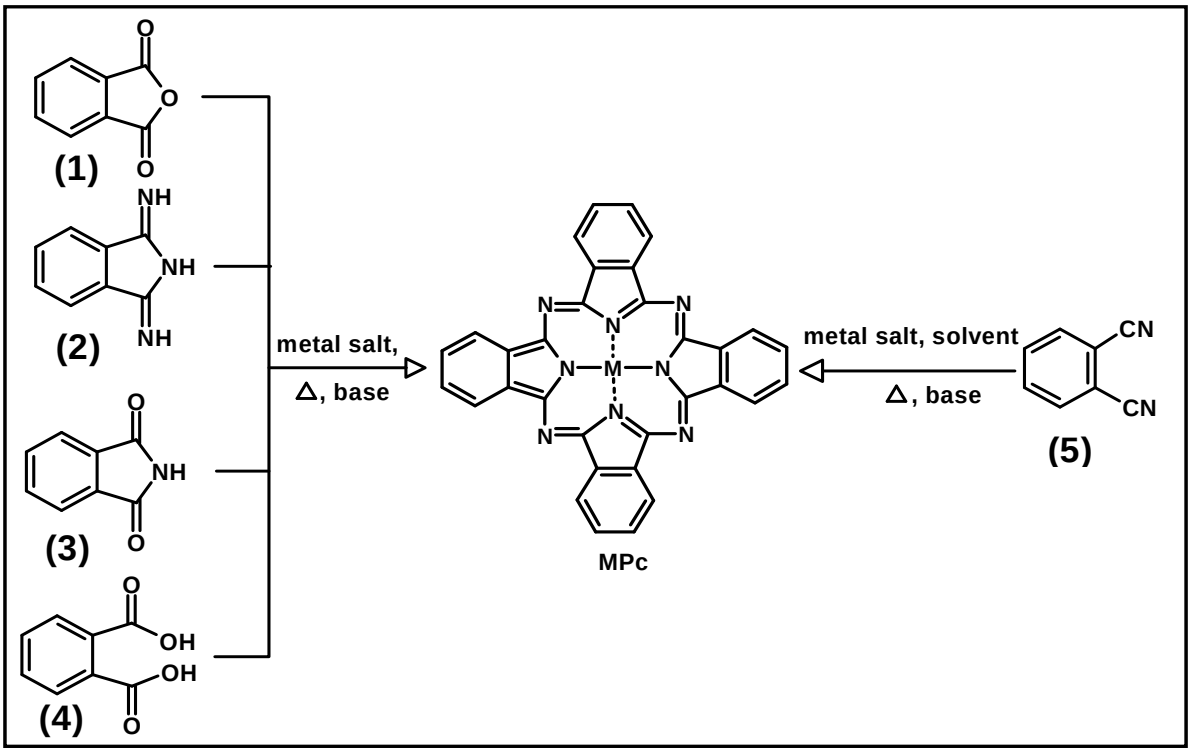

Scheme 1.1: General synthesis route for MPc complexes.

Substituted MPc complexes have been widely used; the substituents on the MPc enhance solubility and are useful in tailoring the use of MPc for various applications. The synthesis of the substituted MPc in Scheme 1.2 is achieved by cyclotetramerization of substituted phthalonitrile. 4,5-Disubstituted phthalonitrile (**6**) is used for the synthesis of a peripherally substituted octa(2,3,9,10,16,17,23,24)metallo-phthalocyanine (**7**) [89-91], Scheme 1.2(a). Mono substituted phthalonitrile (**8**) and substituted phthalic anhydride (**9**) at position 4 or 5, Scheme 1.2(b) are used for the synthesis of constitutional isomers with different geometries of tetra- 3,10,17,24- (C_{4h}); 3,10,16,24- (C_s); 3,9,16,24- (C_{2v}); 3,9,17,23- (D_{2h}) substituted MPc (**10**) [92-94,96,97].

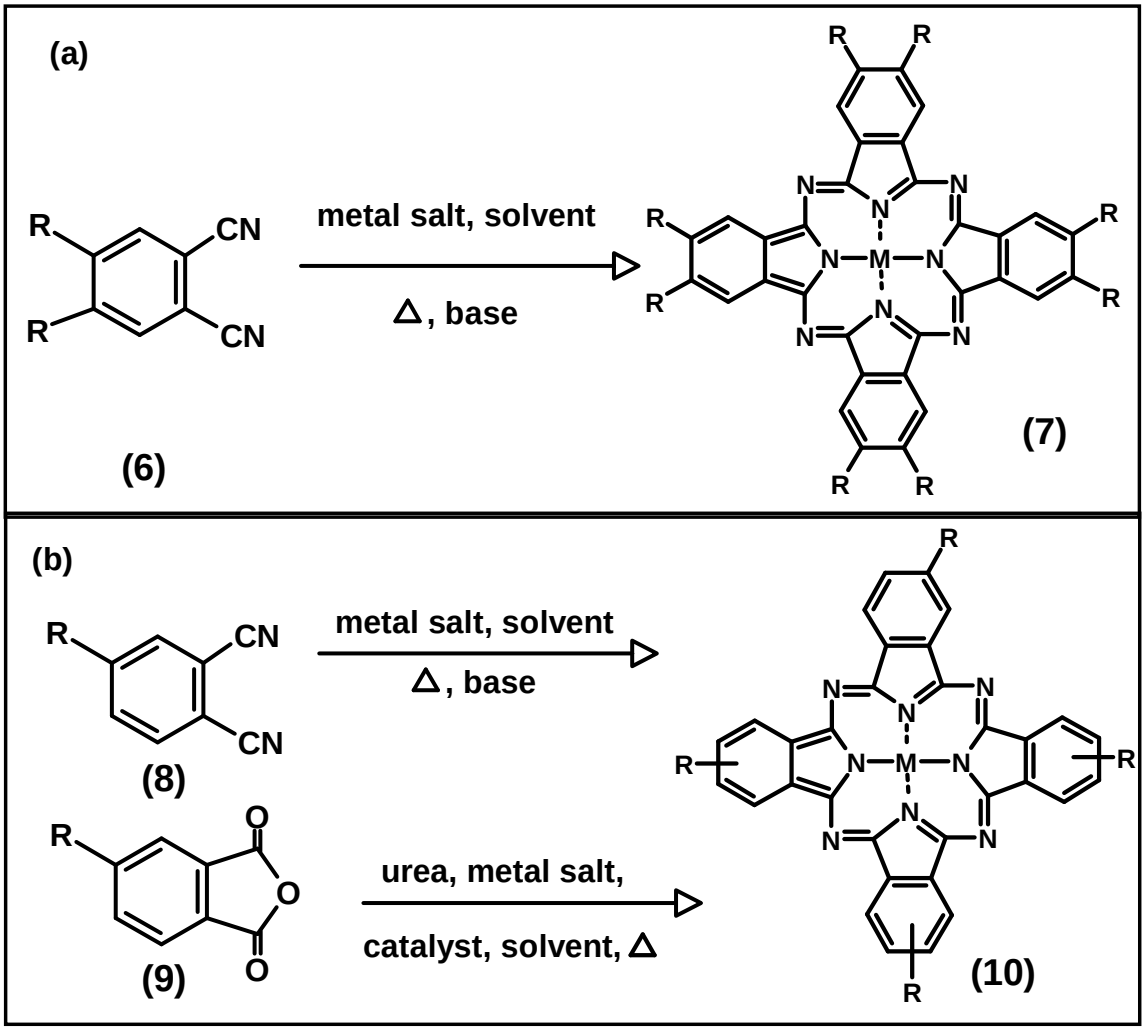

Scheme 1.2: Synthesis route for substituted metallophthalocyanine [87-94]. (a) octa substitution, (b) tetra substitution. R = substituents.

1.3.2 Electronic Absorption Spectrum of MPc

Ultraviolet-visible (UV-vis) absorption spectrum for metallophthalocyanine can be clearly identified from that of metalloporphyrins (Figure 1.13) by its characteristic and distinct intense Q band. The MPc absorption spectrum in Figure 1.13(a) shows two bands referred to as Soret (or B) band at the blue region (300 – 500 nm) of the UV-vis spectrum and the intense band known as Q band at the red region (600 – 800 nm) [95,96]. In comparison, metalloporphyrin

absorption spectrum shown in Figure 1.13(b) exhibits an intense B (or Soret) band in the blue region and a small Q band in the red region of the visible spectrum. These absorption bands (B and Q) of both phthalocyanine and porphyrins arises from the π-π* transitions of the ring.

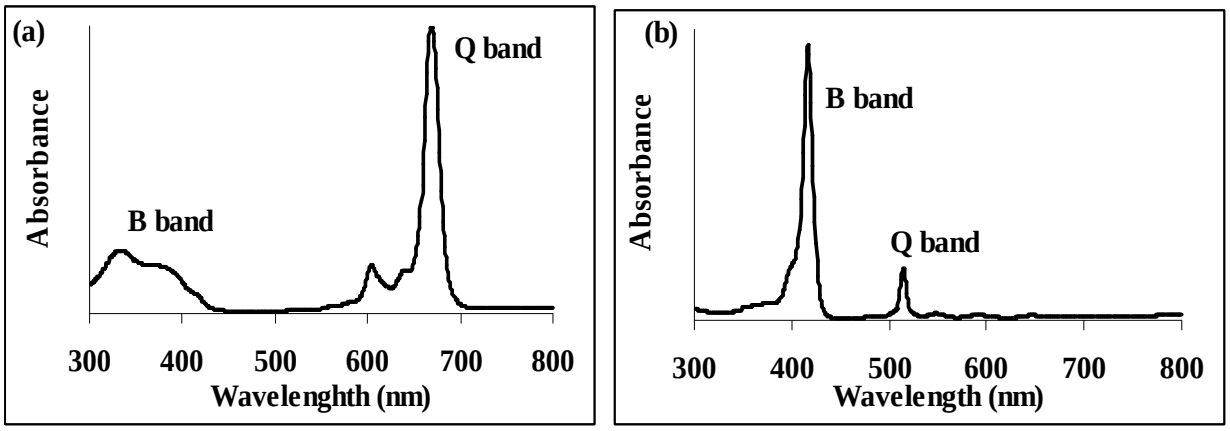

Figure 1.13: Typical absorption spectra of, (a) phthalocyanine and (b) porphyrin complexes.

The differences between the metallophthalocyanines and metalloporphyrins can also be understood in terms of their energy level diagrams referred to as Gouterman's four-orbital model [97]. This model can also be used to understand the origins of these π-π* transitions which gives rise to B and Q absorption bands. The Q band for MPc complexes occur from the electron transition from the a_{1u} orbital to the e_g orbital and the B band results from the a_{2u} or b_{2u} orbital to the e_g orbital, Figure 1.14. Whereas the Q band for MP complexes are from the a_{2u} orbitals to the e_g orbital and the B band from the a_{1u} to the e_g orbitals, Figure 1.14.

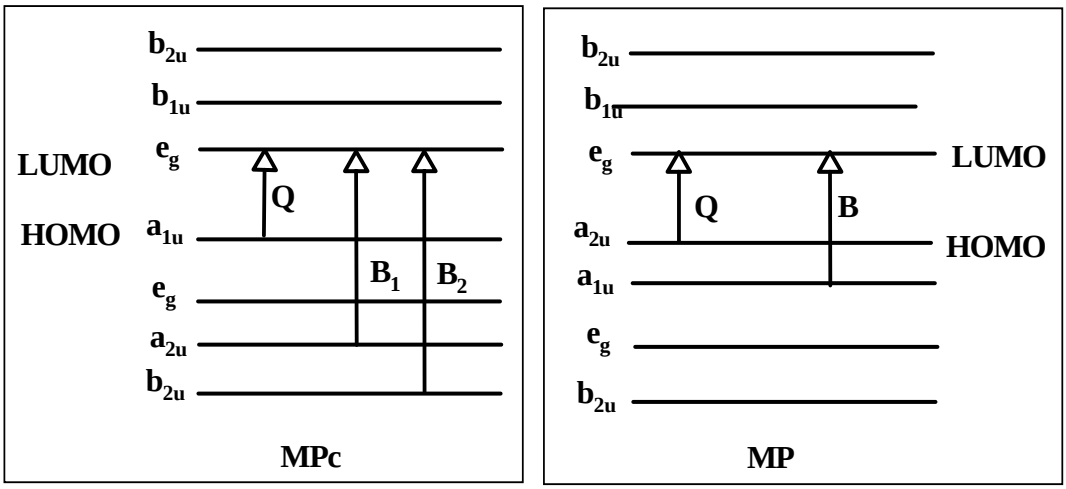

Figure 1.14: Gouterman's four model showing electron transitions and the origin of Q and B bands for MPc and MP. LUMO = Lowest unoccupied molecular orbital and HOMO = highest occupied molecular orbital.

The differences in UV-vis spectra of MPc and MP complexes are due to the fact that for MPc the a_{1u} lies above a_{2u} whereas for porphyrins a_{2u} lie above a_{1u} and are close together as shown in Figure 1.14, resulting in extensive configuration interaction as a consequence the MP spectrum shows the Q and B bands close together [95,98].

1.4 Fundamentals of electrochemistry

1.4.1 Electrochemical cell

Electrochemistry is the study of chemistry reactions that takes place at the interface of an electronic conductor and ionic conductor to produce electric power, e.g. in galvanic cells, or electrochemistry can also be defined as the use of electricity to affect the chemical reactions or processes, called electrolytic process [29]. The production of electric power is a result of the movement of electrons or ions from the solution to the metallic/semiconductor electrodes (oxidation process) and vice versa (reduction process). The movement of electrons in an electrochemical cell is controlled by mass transport processes and the mechanisms involved in the mass transport processes are migration, convection and diffusion [29,65,66]. During the electrochemical measurement, controlled conditions which allow the participation of one mechanism (diffusion) are chosen for the transportation of an electroactive species. Diffusion mechanism is preferred to migration and convection because the mass transport process in this mechanism is driven by chemical gradient [29]. The chemical gradient monitors and restores the homogeneity of the solution every time the concentration of the molecules or ions (charge not considered) is uneven in the solution. Migration which is the movement of the ions under the influence of an electric field and can be removed by adding large excess of supporting electrolyte (e.g. NaCl) which dissociates to produce inert ions [29]. Convection is the movement of the whole solution and is not a factor in mass transport process for as long as the solution is quiescent and the electrode is stationary [29]. Convection can be driven by stirring or flow of the solution, or by the movement of the electrode.

The electrochemical cell, typically three-electrode, is the most commonly used for electrochemical experiments. Three-electrode electrochemical cell (Figure 1.15) consists of: (i) the working electrode (WE), (ii) the reference electrode (RE) and (iii) counter electrode (CE).

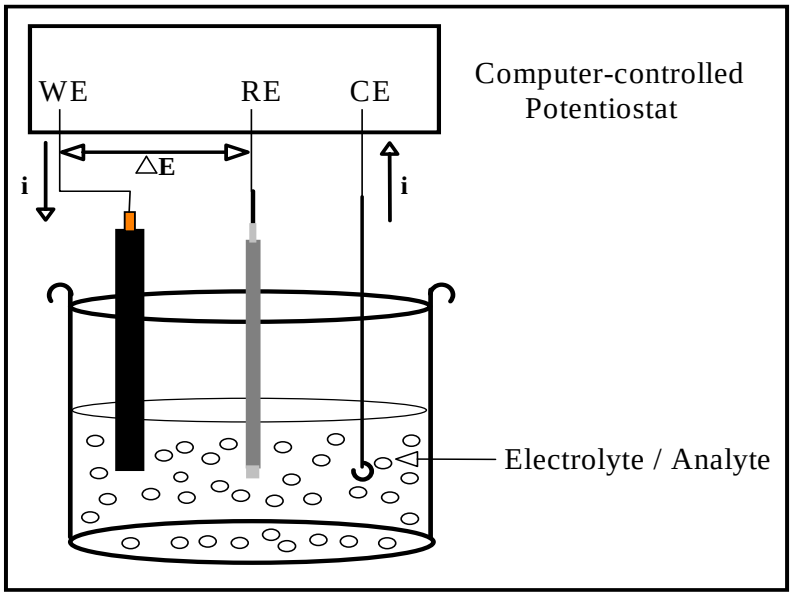

Figure 1.15: A diagrammatic representation of a conventional three-electrode electrochemical cell: WE (working electrode), RE (reference electrode) and CE (counter electrode).

The working electrode (WE) is where the electrochemical reaction of interest takes place and it provides high signal-to-noise characteristic and reproducible response. The selection of the WE depends on the redox behaviour of the target analyte and the background current over the potential region investigated [26,65]. The reference electrode (RE) has a characteristic of constant potential which is taken as a reference or standard potential against other electrodes in the cell. Reference electrodes with large surface area are used in order to maintain the low current densities and thus minimizing polarization of these electrodes [29]. The counter electrode (CE) is included to complete the electrochemical circuit and in modern potentiostat instruments it is used to eliminate polarization of the reference electrode [29,65,66]. CE serves as a source or

sink for electrons so that the current can be passed from the external circuit through the cell. The potential different (ΔE) in a potentiostat is maintained between the WE and RE, and the current (i) which is needed for affecting changes occur at the WE [29,66,99].

There are several reference electrodes used in electrochemical experiments, for example silver | silver chloride (Ag|AgCl) being the most common. This consists of a silver wire anodized with silver chloride in a glass tube. The wire is in contact with the saturated solution of KCl or NaCl [100]. At the tip of the tube, a semi-permeable salt bridge protects the electrode from the bulk solution. The commonly used counter electrodes are platinum wire and graphite rod, and these materials are chosen due to the fact that they are inert conducting materials. The working electrodes are commonly mercury, carbon and 'inert' metals such as platinum and gold.

The choice of the solvent together with the supporting electrolytes needs to be considered for an electrochemical experiment. The choice of the solvent is based upon the solubility of the analyte and its properties such as electrical conductivity, electrochemical and chemical inertness [29]. Therefore in an electrochemical experiment, the solvent should not react with the analyte or its products and should not undergo electrochemical reaction (i.e. should not readily be oxidized or reduced) in the potential range of interest. Also purity of solvents for electrochemistry is of practical importance. Solvents most commonly used include water, dimethylformamide (DMF), dimethylsulfoxide (DMSO), acetonitrile (ACN), dichloromethane (DCM) and methanol (MeOH). Supporting electrolytes in an electrochemical experiment play a very important role as they (i) eliminate the electromigration effect, (ii) decrease solution resistance and (iii) maintain constant ionic strength. In aqueous solution, the most commonly used supporting electrolytes are alkali chorides, nitrates, sulfates, perchlorates and phosphates (for pH buffer solution and pH control). Tetraalkylammonium salts, e.g. tetrabutylammonium

perchlorate (TBAP), tetrabutylammonium tetrafluoroborate ($TBABF_4$) and tetraethylammonium perchlorate (TEAP) are the electrolytes used in organic media. Supporting electrolytes are added in excess and should not undergo electrochemical reaction at the potential range of interest. The solutions are deaerated using inert gases before the electrochemical experiment to avoid the interference of oxygen which can dissolve in water, and the oxygen free atmosphere is maintained throughout the experiment.

1.4.2 Cyclic voltammetry

Cyclic voltammetry is the most widely used electrochemical technique for studying the nature of electrochemical reactions in detail [29,66]. During the cyclic voltammetry experiment the potential is scanned from the starting potential (E_i) to the final potential (E_f) and back to E_i and the resulting current is measured. During the electrochemical measurement the solution is kept stationary. The data obtained is represented as a current-potential plot known as a cyclic voltammogram shown in Figure 1.16.

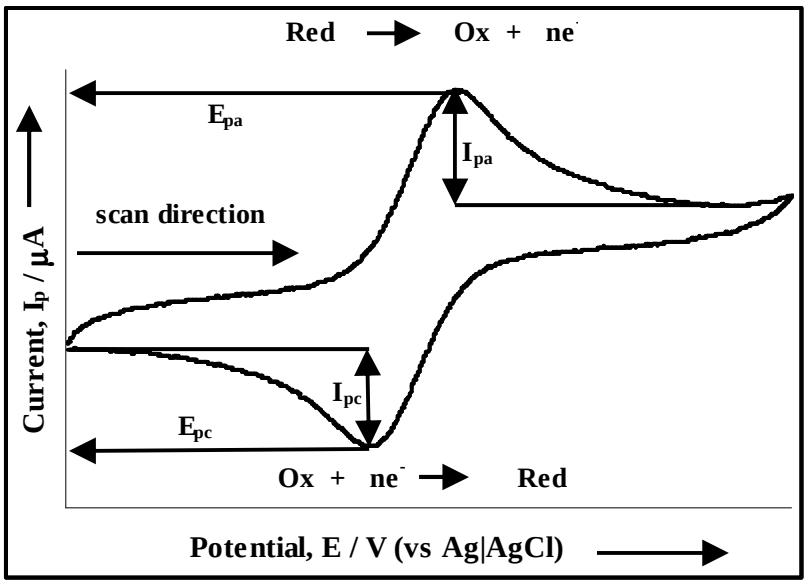

Figure 1.16: A typical cyclic voltammogram for a reversible process.

In Figure 1.16, the forward scan represents the oxidation of reductant (Red) to it oxidized (Ox) species, which on the backward scan is reduced. The electrochemical change in species from the reductant (Red) to the oxidized species (Ox) results in the loss of electrons and this process is observed in cyclic voltammogram as a peak, referred to as an anodic peak. The reverse scan, the oxidized species (Ox) undergo reduction to its reduced (Red) species resulting in the gain of electrons and a peak is observed in the cyclic voltammogram, referred to as cathodic peak. The information obtained from the cyclic voltammogram includes the anodic (E_{pa}) and cathodic (E_{pc}) peak potentials and the anodic (I_{pa}) and cathodic (I_{pc}) peak currents. Cyclic voltammetric processes may be reversible, irreversible or quasi-reversible [66].

(i) *Reversible process*: occurs when an electroactive species in solution is oxidized (or reduced) in a forward scan and reduced (or oxidized) in the backward scan. This type of system is in equilibrium throughout the potential scan, i.e. the Nernst conditions hold where the electron transfer is rapid enough to assume that the concentrations of Red and Ox are in equilibrium as shown in equation 1.10:

$$Ox + ne^- \rightleftharpoons Red \qquad (1.10)$$

Under these conditions, following parameters characterize the reversibility of the reversible process:

- The separation between the anodic and the cathodic peak potentials ($\Delta E_p = E_{pa} - E_{pc}$) is independent of scan rate and at 25˚C is equal to 0.059/n (V).
- The average of the two peak potentials gives the half-wave potential ($E_{1/2}$) equation 1.11:

$$E_{1/2} = \frac{E_{pa} + E_{pc}}{2} \qquad (1.11)$$

- The ratio of the anodic to cathodic peak current (I_{pa} / I_{pc}) is equal to 1 for a totally reversible process for all scan rates.
- The plot of peak current (I_p) vs square root scan rate ($v^{1/2}$) increases linearly indicative of a diffusion controlled process.

(ii) *Irreversible process* is the process where the reaction goes one-way, the most common is when only a single oxidation or reduction peak with a weak or no reverse peak [66] is observed. Irreversible processes are a result of slow electron transfer or chemical reactions at the surface of the working electrode. A large peak potential separation (>200 mV) also indicates an irreversible reaction, if there is a return peak.

(iii) *Quasi-reversible process* exhibits behaviour which lies between the reversible and irreversible processes. Differences between these three cyclic voltammetric processes are shown in Table 1.1.

Table 1.1: A summary of parameters for the diagnosis of reversible, irreversible and quasi-reversible cyclic voltammetric processes.

Parameter	**Reversible**	**Quasi-reversible**	**Irreversible**
E_p	Independent of υ	Shift with υ	Shift cathodically by 0.03/αn V for a 10-fold increase in υ
$E_{pa} - E_{pc}$	~ 0.059/n V at 25˚C	May approach 60/n mV at low υ but increases as υ increases	No return peak or >200 mV
I_{pa} / I_{pc}	Equals 1 and independent of υ	Equals 1 only if α = 0.5	Usually no current on the reverse scan
Ip / $v^{1/2}$	Constant	Constant	Constant

Note: α = transfer coefficient, υ = scan rate (Vs^{-1}), V = Volts.

1.4.3 Square wave voltammetry

Square wave voltammetry (SWV) is an electrochemical technique which relies on excitation function that combines the features of a large amplitude square wave modulation with a simple staircase waveform [29,66] as in Figure 1.17. During the each square wave cycle, the current is sampled twice, once at the end of the forward pulse (i_f) and once at the end of the reverse pulse (i_r). The differences in current (i_f - i_r) is displayed as a function of potential which results in a peak-shaped voltammograms shown in Figure 1.18. The advantages of measuring the difference in current results in (a) an increase in the discrimination against the charging current, since any residual charging current is subtracted and (b) the shape of the current response is symmetrical about the half-wave potentials ($E_{1/2}$) of the oxidation and reduction of the electroactive species at the electrode surface [29,101]. Further advantages of the square wave voltammetry are optimum peak separation, excellent sensitivity and very low detection limits.

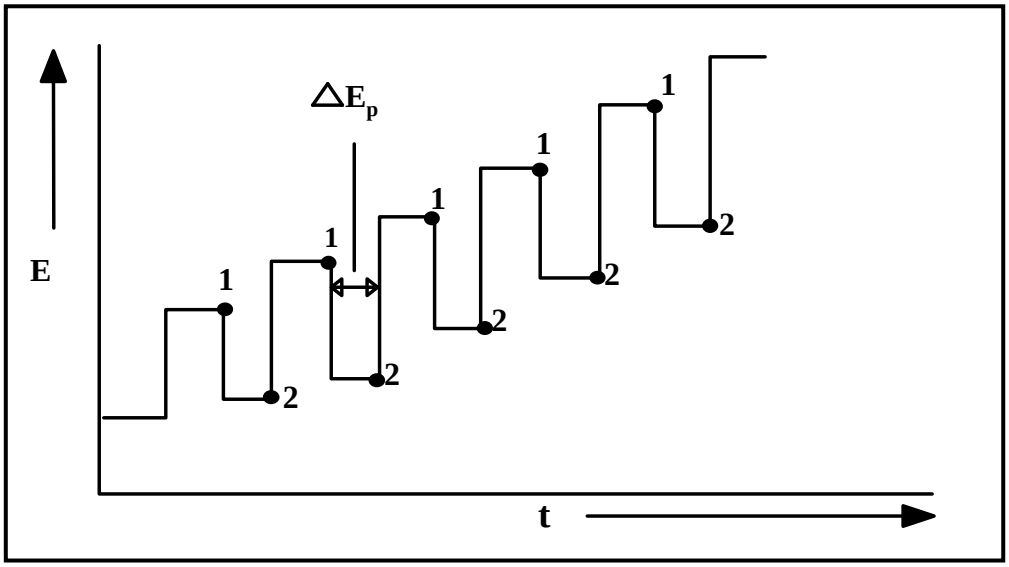

Figure 1.17: A typical excitation function for square wave voltammetry.

Figure 1.18 shows the square wave voltammograms, plot of differences in measured current ($i_f - i_r$) as a function of base staircase potential. The observed peak-shaped potentials are

symmetrical about the half-wave potentials of the oxidation and reduction of the electroactive species at an electrode surface. The peak current is proportional to the concentration of the electroactive species in solution.

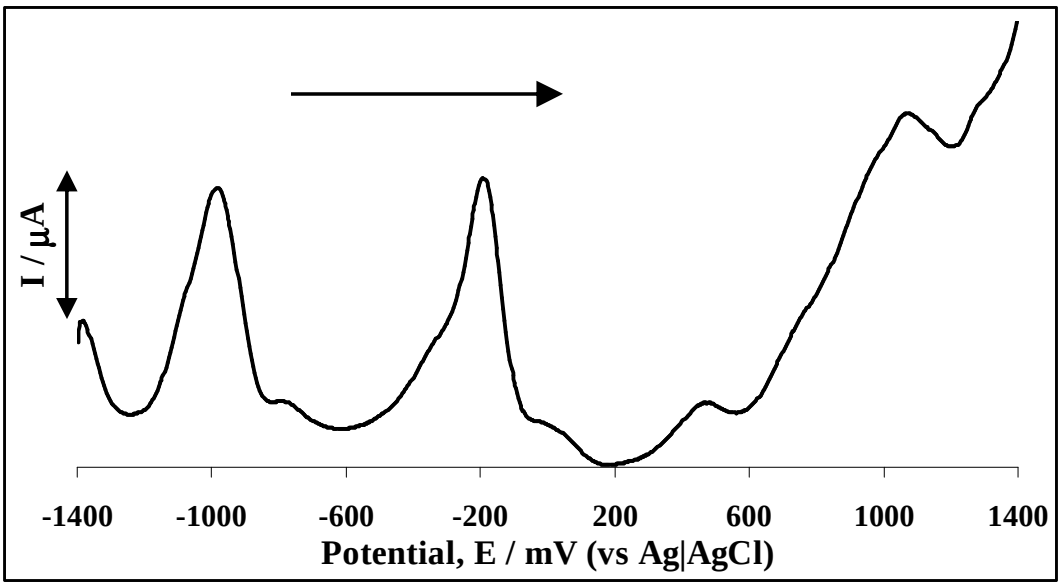

Figure 1.18: A typical square wave voltammogram.

1.4.4 Spectroelectrochemistry

Spectroelectrochemistry is the technique that combines electrochemical measurements while monitoring spectral changes. This phenomenon was made possible from the development of optically transparent electrodes (OTEs) which allows monitoring of spectral changes as a result of electrochemical perturbations [74,88,102]. The thin layer electrochemical cell that incorporates these electrodes (OTEs) is called optically transparent thin layer electrode (OTTLE) cell. This technique is useful in studying the reaction mechanism and characterization of products resulting from the oxidation or reduction of the redox active species in the OTTLE cell [103]. UV-vis spectrum is used to monitor these products (or electro-generated species) in the

OTTLE cell. Spectroelectrochemical characterization of MPc complexes is based on either oxidation or reduction mechanisms which results in the Q band shift or decrease in intensity [104,105]. If the spectral changes result in the decrease in Q band intensity, the ring-based process is taking place and if the Q band wavelength shifts without decrease in intensity a metal-based redox process is implied. Spectroelectrochemical technique can also be used to monitor the number of electrons transferred, during the redox process using the Faraday's Law [29], given by the equation 1.12:

$$n = Q/FVC \qquad (1.12)$$

where n is the number of electrons, Q is the amount of charge passed (Coulombs), F is Faraday's constant, V is the volume of the OTTLE cell and C is the concentration of the solution in the OTTLE cell.

1.5 Electrochemistry of MPc

1.5.1 Electrochemical properties of MPc

Electrochemistry of MPc complexes occurs at the Pc ring or at the central metal ion, provided the metal ion is electroactive and its orbitals lie between the HOMO and LUMO energy gap of the Pc ring [95,106]. The most commonly used electroactive metal ions for MPcs are Co, Fe and Mn. The potentials at which these redox reactions occur can be influenced by the nature of the substituents on the Pc ring, oxidation state of the central metal ion and if present the axial ligand and the solvent used [96].

MPc exists as dianion (MPc^{-2}) in their neutral form [107]. The oxidation process which is the successive removal of two electrons from the HOMO (a_{1u}) of the neutral MPc^{-2} results in the formation of the MPc^{-1} and MPc^{0} species. Reduction process is the successive addition of four

electrons to the LUMO (e_g) of an MPc^{-2} results in the formation of MPc^{-3}, MPc^{-4}, MPc^{-5} and MPc^{-6} species [107,108]. The removal or addition of electrons from or to the ring is characterized by decrease in Q band intensity, formation of weak bands in the red and the visible region (700 – 850 nm) and increase in intensity at 500 nm region. The changes observed in the spectra during oxidation or reduction of a neutral MPc^{-2} complex can be represented by the energy level diagrams shown in Figure 1.19.

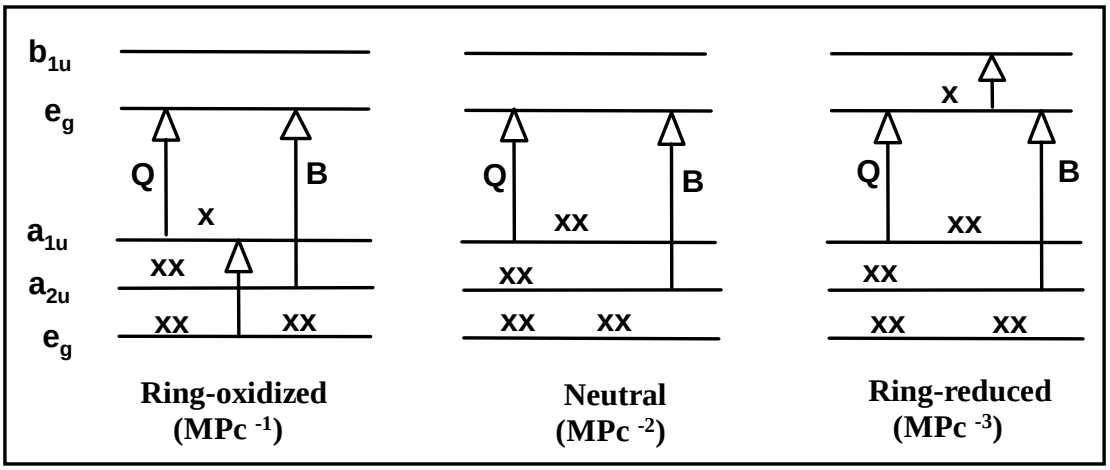

Figure 1.19: Energy level diagrams of neutral, one-electron ring reduced and one-electron ring oxidized MPc complexes. 'x' represents an electron.

This work presents electrochemical characterization of MPc complexes using cyclic voltammetry, square wave voltammetry and spectroelectrochemistry which assists in identifying and assigning redox reaction.

1.5.2 Electrocatalytic properties of MPc

MPcs have established themselves as excellent electrocatalysts, especially MPcs that contain transition metals such as Co, Fe and Mn [9,55-60,108-112]. By definition the term "electrocatalyst" is a metal-rich catalyst used to promote the efficiency of a half-reaction of an

electrochemical reaction. This promotion of electrochemical reaction can be accomplished in one of the three ways: (i) lowering of applied potentials to accessible values, (ii) increase in peak current densities and (iii) increase in slope and improved peak shapes. For example, the detection of cysteine at conventional or unmodified electrode (gold) takes place at high anodic potentials; hence the introduction of an electrocatalyst (MPc) onto gold surface which reduces the potential at which these analytes can be detected [23,24,55]. MPc complexes have π donor-acceptor functionality which increases their catalytic activities making them excellent electrocatalysts. The catalytic activity of MPc complexes is mediated by redox process centered at the central metal or at the ring system [108-112]. The electrocatalytic activity of MPc has been related to redox potentials of the central metal [111,113]. A general mechanism of the metal oxidation-mediated catalytic oxidation of species or analytes (Anal) to its oxidized products [12,111,113-115] is given by equations 1.13 – 1.14:

$$M^{II}Pc^{-2} \longrightarrow M^{III}Pc^{-2} + e^{-} \qquad (1.13)$$

$$M^{III}Pc^{-2} + Anal \longrightarrow M^{II}Pc^{-2} + Products \qquad (1.14)$$

In general, SAM modified gold electrodes have been extensively used for analytical prospects, such as heterogeneous electron transfer [116]. Most analytical applications that have been explored are based on the use of SAMs for the fabrication of biosensors [41-44] and chemical sensors [50-52]. MPc SAM modified electrodes, especially MPc complexes which contain Co, Fe and Mn as central metals, have been investigated as electrocatalysts for the detection and analysis of environmental, biomedical and industrial important molecules [55,57-60,117-123]. This work has investigated the covalent attachment of MPc complexes in Figure 1.20 onto preformed SAM on gold electrode (described for the first time in this work and details will be presented in the results and discussion). The potential applications of MPc SAM

modified gold electrodes have been investigated as electrochemical sensors for the detection and analysis of L-cysteine, hydrogen peroxide and the fabrication of glucose oxidase based biosensor for the detection of glucose.

1.5.3 Aims

(i) Synthesis and characterization (using electrochemistry and spectroscopic techniques) of the transition metal tetra-carboxylic acid chloride phthalocyanine complexes with Co, Fe and Mn as central metal (Figure 1.20).

(ii) Investigate the electrochemical properties of these MPc SAM modified complexes as potential electrocatalysts for molecules of environmental, biomedical and industrial importance.

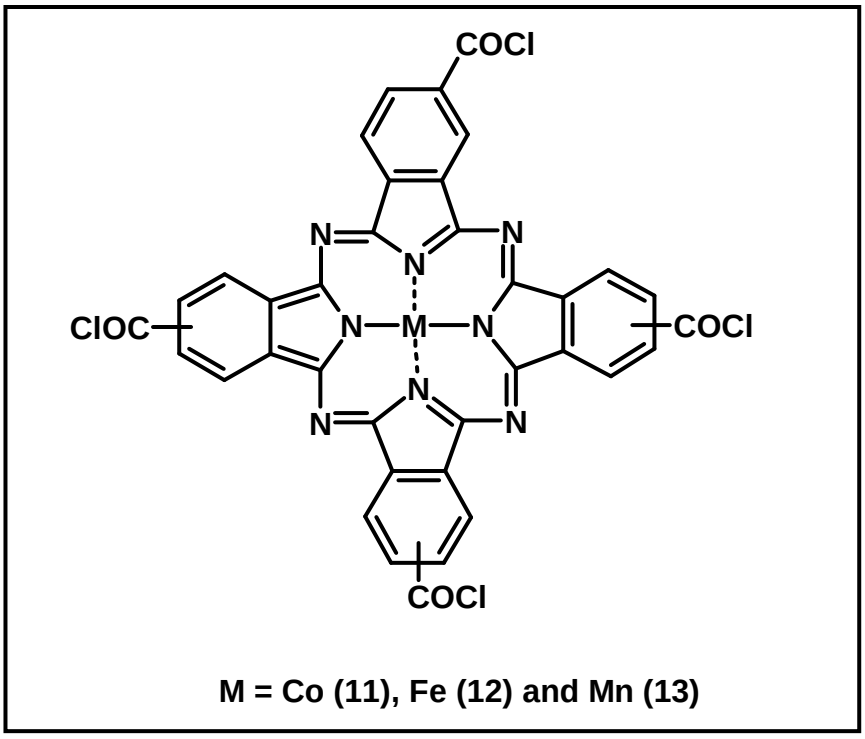

Figure 1.20: Structure of tetra carboxylic acid chloride substituted metallophthalocyanine (MTCAClPc) complexes studied in this thesis.

1.6 Overview of properties of L-cysteine, hydrogen peroxide and glucose

1.6.1 L-Cysteine

Cysteine {(R)-2-amino-3-mercaptoproprionic acid} is a thiol (sulfur-containing) α-amino which is commonly found in natural proteins. Cysteine plays an important role in biological systems as it acts as a key extra-cellular reducing agent, it also acts as a crucial substrate for protein synthesis and a rate-limiting precursor for glutathione and taurine synthesis [124]. Cysteine is of paramount importance to chemists, biochemists and healthcare practitioners as is available in body fluids at controlled concentrations. High amounts of cysteine have been implicated in pathological conditions, such as Alzheimer's and Parkinson's diseases [125,126] and also epileptic seizures [127]. Low levels of cysteine in body fluids may be linked to increased risks of cervical dysplasia [128]. Furthermore cysteine has been used industrially for light oil-sweetening purposes [129]. Detection and monitoring the levels of cysteine in patients during early clinical diagnosis is important as it will provide the clinician with data from which effectiveness or response of the patient to subsequent treatments is of importance.

Electrooxidation of cysteine at bare electrodes occur at high anodic potentials [130] and this is due to slow electron transfer thus limiting the use of these electrodes for analysis of cysteine. The use of MPc SAM modified gold electrodes have been shown to lower oxidation potential and substantially improve electrocatalytic activity of the bare gold electrode towards the detection of cysteine [55,57,58,60] by improving the rate of electron transfer. MPc SAM gold electrodes were found to be better [55,57,58,60] electrocatalysts, compared to the cobalt phthalocyanine on glassy carbon electrode (GCE) [113], Table 1.2. The current work aims at testing the new easier method to construct electrodes for the detection of cysteine and compare their effectiveness with the reported complexes.

Table 1.2: Comparative peak potentials and limit of detection (LoD) for cysteine electrooxidation using selected MPc complexes.

MPc	Electrode Material	E_P / V (vs Ag|AgCl)	LoD (x 10^{-7}M)	Ref.
CoPc	C-Cement	0.67	1.0	[122]
CoOBTPc	SAM-Au	0.42	3.1	[55]
CoOHETPc	SAM-Au	0.50	5.2	[24]
FeOBTPc	SAM-Au	0.33	3.0	[23]
FeOHETPc	SAM-Au	0.38	5.2	[24]
CoPc	SAM-Au	0.20	-----	[60]
FePc	SAM-Au	0.18	-----	[60]
MnPc	SAM-Au	0.20	-----	[60]

Abbreviations: CoOBTPc (cobalt octabutylthiophthalocyanine), CoOHETPc (cobalt octahydroxyethylthiophthalocyanine), FeOBTPc (iron octabutylthiophthalocyanine), FeOHETPc (iron octahydroxyethylthiophthalocyanine).

1.6.2 Hydrogen peroxide (H_2O_2) and glucose

Hydrogen peroxide (H_2O_2) monitoring and detection is of importance in biomedical, environmental and industrial samples [125,131-135]. In clinical and biomedical field, H_2O_2 is studied as it is a by-product of many enzyme-based reactions [136,137] and the analysis of H_2O_2 is mostly studied in neutral or physiological conditions. Environmental and industrial methods for the detection of H_2O_2 have been done in alkaline media. Several methods have been used for the determination of H_2O_2 and these methods include spectrometry [138], chromatography [120,139], chemilumiscence [140,141], titrimetry [142], electrochemistry [135,137,143-152] and spectroscopy [153]. Electrochemically based methods are preferred to others due to their simplicity, low detection limits, fast response time and relatively low costs. Similar to cysteine detection, H_2O_2 determination at bare electrodes occurs at high anodic potentials and bulk gold electrode is a poor electrode for the detection of H_2O_2. Therefore modified electrodes with electrocatalysts are useful in lowering the potentials for the detection of H_2O_2, as shown in Table 1.3, to easily accessible values.

Table 1.3: Comparative peak potential (both oxidation and reduction), limit of detection (LoD) or hydrogen peroxide electrooxidation and electroreduction using different modified electrodes.

Modifier	Electrode Material	E_p / V (vs Ag|AgCl)		Medium	LoD / M	Ref.
		Oxidation	Reduction			
HRP	Au-HRP	———	-0.050	pH 6.0	———	[143]
	Au-HRP				1.0×10^{-8}	[144]
	Au-HRP				1.0×10^{-9}	[145]
HRP	GEB-HRP	———	-0.30	pH 7.0	———	[146]
	GEB-Pt-HRP		-0.40			
Cmt-nMnO_2	CPE- Cmt-nMnO_2	0.30	———	pH 7.4	2.0×10^{-6}	[147]
MPc	SPCE-CoPc	0.63	-0.35	pH 9.2	———	[148]
	SPCE-FePc	0.16	———			
	SPCE-MnPc	0.46	0.35			
CoTRP	GCE-poly-CoTRP	0.30	———	0.5 M NaOH	2.0×10^{-7}	[149]
Cu	Cu	———	-0.25	pH 6.7	1.2×10^{-7}	[150]
$CoPc(CoTPP)_4$	GCE-$CoPc(CoTPP)_4$	0.45	———	pH 7.0	8.0×10^{-6}	[151]
		0.55		pH 10	2.0×10^{-6}	
HRP	ITO-APTMS-cAu-HRP	———	-0.25	pH 7.0	8.0×10^{-6}	[152]
HRP	Au-CNE-cAu-HRP	———	-0.30	pH 7.0	5.8×10^{-7}	[154]
MCNOTPP	GCE-FeCNOTPP(Cl)	0.65	-0.65	pH 7.4	5.0×10^{-4}	[155]
	GCE-CoCNOTPP	———	———	———	———	
Fe	Au-MPS-Fe	0.40	0.10	pH 7.0	6.4×10^{-6}	[156]

Abbreviations: HRP (horseradish peroxidase), GEB (graphite-epoxy biocomposite), Cmt-nMnO_2 (cryptomelane-type nanostructured manganese oxide), CPE (carbon paste electrode), SPCE (screen-printed carbon electrode), CoTRP (m-{5,10,15,20-tetra[4-pyridyl]porphyrinato cobalt tetrakis-{chloro-bis-[2,2'-bipyridine}ruthenium (II)}), $CoPc(CoTPP)_4$ (cobalt phthalocyanine tetra{5-phenoxy-10,15,20-triphenylporphyrin}), ITO (indium tin oxide conductive glass support), APTMS ({3-aminopropyl}trimethoxysilane), cAu (colloidal gold), CNE (cysteamine), MCNOTPP (metal {Fe,Co}5-[4-(3,4-dicyanophenoxy) phenyl],10,15,20-triphenylporphyrin), MPS ({3-mercaptopropyl}-trimethoxysilane).

Glucose detection and analysis is of importance in many biomedical applications and in medical practices due to its usefulness in diagnosis of diabetes [157]. Glucose detection and monitoring is mostly done at glucose oxidase (GOx) enzyme based biosensor. Enzyme electrodes (particularly glucose oxidase based) are very important as they are selective and highly specific towards the analyte of interest (glucose). Glucose oxidase enzyme based biosensors have been extensively studied due to their high stability and practicality.

The mechanism of action of glucose oxidase (GOx) based enzyme biosensor is based on monitoring either the consumption of oxygen or the production of hydrogen peroxide with the latter being more convenient. However as stated before, the amperometric determination of hydrogen peroxide occurs at high anodic potential and this has lead to the introduction of mediators [117-123,158-173] which reduce the potential to more favorable potentials. Mediators are used to facilitate electron transfer between the redox centre of the enzyme and the electrode surface, the mechanism is shown in Scheme 1.3.

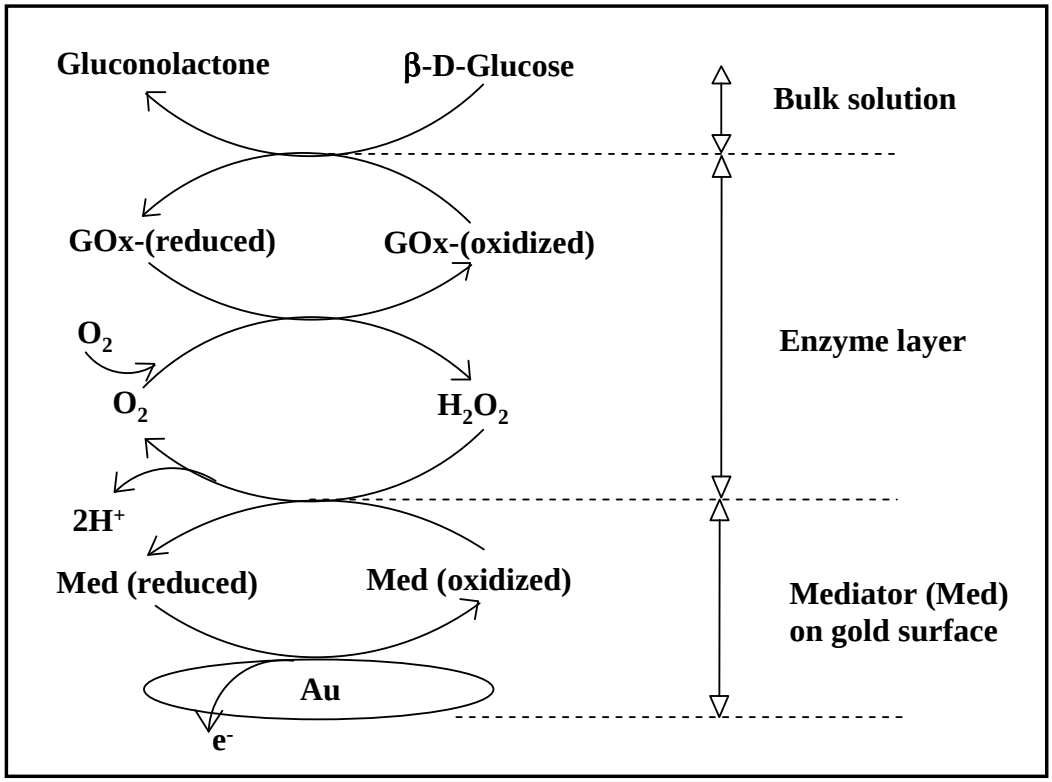

Scheme 1.3: Schematic representation of enzyme reaction with an electron-mediator (Med).

From the Scheme 1.3, the enzyme (due to its specificity) oxidizes β-D-glucose leading to the generation of electroactive H_2O_2, which diffuses to the mediator (Med) layer on gold electrode and get oxidized. MPcs, particularly cobalt phthalocyanines have been found to be biocompatible with glucose oxidase enzyme [117-122] and have been used as mediators in glucose detection. Table 1.4 shows the comparative kinetic data for glucose oxidase based biosensor with different mediators including different cobalt phthalocyanine derivatives. In this work, glucose oxidase enzyme has been covalently immobilized onto MPc SAM modified gold electrode and this enhances the stability of the immobilized enzyme onto gold electrode. The enzyme modified gold electrode has been used to study the detection and analysis of glucose.

Table 1.4: Comparative kinetic data, linear concentration range (LCR), limit of detection (LoD), Michaelis-Menten constant (K_m^{app}), response time, sensitivity and maximum current (i_{max}), for the different electrode modifiers as mediators at electrodes surfaces for glucose oxidase (GOx)-based enzyme sensors.

Modifier	**Method**	**LCR / mM**	**LoD**	K_m^{app} **/mM**	**Response time (s)**	**Sensitivity**	i_{max}	**Ref.**
CoPc	GEM-CoPc-GOx	0 – 5	———	———	10	———	———	[117]
$(OEt)_8CoPc$	CPM-$(OEt)_8$CoPc-GOx	≤ 4	3 μM	———	< 5	———	———	[118]
	CPM-CoPc-GOx	≤ 4	3 μM		< 5			
CoPc	SPCE-CoPc-GOx	19.4	———	———	57	———	———	[119]
CoTAPc	GCE-CoTAPc-GOx-Naf	0.001 – 5	0.5 μM	———	———	———	———	[120]
Nano-CoPc	PGE-nano-CoPc-GOx	0.02 – 18	5 μM	12.4 mM	5	7.7 mA mM^{-1} cm^{-2}	———	[121]
CoPc	SPCE-CoPc-GOx	0.2 – 5	0.2 mM	———	———	1.12 μA mM^{-1}	———	[122]
$CoPc(CoTPP)_4$	GCE-$CoPc(CoTPP)_4$-GOx	≤ 11	10 μM	14.91 mM	5	24.20 nA mM^{-1}	0.428 μA	[123]
OsPVP	Au-MPS-OsPVP-GOx	0.1 – 10	50 μM	8.5 mM	10	———	———	[158]
FCA	Au-PySSPy-FCA-GOx	1 – 20	———	20 mM	20	———	———	[161]
Poly-PPD	Pt-poly-PPD-GOx	0.5 – 3.0	———	3.94 mM	2	———	607.5 μA cm^{-2}	[162]
Poly-BQ	Au-MPA-poly-BQ-GOx	0 – 23	———	———	———	0.41 mA cm^{-2} mM^{-1}	15 mA cm^{-2}	[163]
Os-complex	SPCE-Os-complex-GOx	0.1 – 10	0.03 mM	———	———	———	———	[164]

Au	CPE-Au-GOx	0.04 – 0.28	0.01 mM	———	———	8.4 mA mM^{-1}	———	[165]
OsPVI	Au-OsPVI-GOx	0 – 30	0.03 mM	16.55 mM	< 5	0.34 μA mM^{-1}	0.203 mA cm^{-2}	[157]
POAP	Pt-PB-POAP-GOx	≤ 5	0.01 mM	14.4 mM	< 5	44 mA M^{-1} cm^{-2}	0.72 mA cm^{-2}	[156]
	Pt-POAP-GOx	≤ 5	0.02 mM	22.8 mM	< 5	47 mA M^{-1} cm^{-2}	0.14 mA cm^{-2}	
CNT	GE-CNT-Pt-GOx-Naf	0.1 – 13.5	———	10.11 mM	5	91 mA M^{-1} cm^{-2}	1.176 μA cm^{-2}	[166]
PMPD	Pt-PMPD-GOx	0.5 – 10	———	15.33 mM	3	———	231.4 mA cm^{-2}	[167]
MV	CFE-MV-GOx	≤ 1.2	20 μM	4.6 mM	30	2.36 μA/mM	———	[159]
	CFE-MV-GOx-Naf	≤ 1.67	32 μM	3.16 mM	———	———	———	
Cu	Au-Cu-POAP-GOx	≤ 6	0.01 mM	17.8 mM	5	12.6 mA M^{-1} cm^{-2}	0.45 mA cm^{-2}	[168]
	Au-PAOP-GOx	≤ 10	0.02 mM	22.8 mM	5	4.7 mA M^{-1} cm^{-2}	0.15 mA cm^{-2}	
$M(byp)_2pic$ M = Ru, Os	GCE-$Ru(byp)_2pic$-GOx-Naf	≤ 2	———	5.7mM	———	51 nA mM^{-1}	0.29 μA	[155]
	GCE-$Os(byp)_2pic$-GOx-Naf	≤ 10	———	16.11 mM	———	18 nA mM^{-1}	0.298 μA	
$Co(byp)_3^{3+}$	Au-MPS-nAu-GOx-$Co(byp)_3^{3+}$	———	0.1 nM	———	———	———	———	[160]
Nano-Au	Au-DT-nAu-CNE-GOx	0.02 – 5.7	8.2 μM	4.3 mM	8	8.8 mA mM^{-1} cm^{-2}	———	[169]
CNT	Au-POAP-GOx	≤ 10	0.02 mM	22.8 mM	3	4.7 mA M^{-1} cm^{-2}	0.15 mA cm^{-2}	[170]
	Au-POAP-CNT-GOx	≤ 5	0.01 mM	18.8 mM	3	11.4 mA M^{-1} cm^{-2}	0.24 mA cm^{-2}	

1.7 Summary of thesis aims

Overall aims of this thesis are as follows:

(i) Gold surface will be used for monolayer formation since thiols chemisorbs as thiolates on gold surface. Gold surface has been chosen due to the fact that it is an inert material, i.e. does not form stable oxides at ambient conditions.

(ii) MPc self-assembled monolayers will be studied as thin films on gold surfaces

(iii) Synthesis and characterization of metal tetra carboxylic acid chloride phthalocyanine [MTCAClPc (**11-13**)] (Figure 1.20).

(iv) To covalent immobilize metallophthalocyanine as SAMs on gold electrode and characterize them using different techniques such as (i) cyclic voltammetry, (ii) electrochemical impedance spectroscopy, (iii) Raman spectroscopy, (iv) X-ray photoelectron spectroscopy and (v) quartz crystal microbalance.

(v) To investigate the electrocatalytic properties of MPc SAM modified electrodes for the detection of L-cysteine, H_2O_2 and fabrication of glucose oxidase modified MPc SAM modified gold electrode for the detection of glucose.

CHAPTER TWO:

EXPERIMENTAL

2.1 Materials

Glucose oxidase (GOx, EC 1.1.3.4, from *Aspergillus niger*, Type VII), N-ethyl-N(3-dimethylaminopropyl) carbodiimide hydrochloride (EDC), N-hydroxy succinimide (NHS), 2-mercaptoethanol (2-ME), thionyl chloride, dimethylformamide (DMF), urea, trimellitic anhydride (TMA), ferricyanide ($K_3Fe(CN)_6$), ferrocyaninde ($K_4Fe(CN)_6$), sulfuric acid, sodium chloride, potassium chloride, nitrobenzene, 30% and 35% hydrogen peroxide and glucose for laboratory use were purchased from Sigma Aldrich. Absolute ethanol (EtOH), potassium hydroxide pellets, potassium dihydrogen phosphate (KH_2PO_4), sodium hydrogen phosphate (Na_2HPO_4), ammonium molybdate, manganese (II) chloride and cobalt (II) chloride were purchased from SAARCHEM and used as received. Iron (II) chloride tetrahydrate and L-cysteine were purchased from Merck. Clinical glucose powder (Alpha®, South Africa) was bought from a local pharmacy shop. All other reagents were of analytical grade. DMF was stored over alumina, distilled and stored dry over molecular sieves before use.

All aqueous solutions were prepared using doubly distilled water or ultra pure water obtained from a Milli-Q Water System (Millipore Corp., Bedford, MA, USA). Buffer tablets purchased from SAARCHEM were used to prepare the buffer solutions of pH 4.0 and pH 7.0. Tetraethylammonium perchlorate (TEAP), employed as an electrolyte in electrochemical characterization of MPc complexes, was recrystallized from ethanol before use. Electroanalysis of L-cysteine was performed in freshly prepared buffer (pH 4.0) solution, whereas the electroanalysis of H_2O_2 and glucose were performed in freshly prepared phosphate buffer saline solution (PBS) pH 7.0 or pH 7.4. Phosphate-buffered solution (0.01 M, pH 7.4) was prepared

following the reported method [174] using appropriate amounts of Na_2HPO_4, KH_2PO_4 and chloride salts, dissolved in ultra-pure (Milli-Q) water.

2.2 Equipment

Spectroelectrochemical data were recorded using an optically transparent thin-layer electrochemical (OTTLE) cell, connected to a BioAnalytical System (BAS) CV 27 voltammograph. Cyclic and square wave voltammetry were performed on either BioAnalytical System (BAS) B/W 100 Electrochemical Workstation, PARSTAT 2273 potentiostat from AMETEK (controlled by the Powersuite software, run on a DELL Pentium computer) or AUTOLAB PGSTAT potentiostat/galvanostat (connected to a computer and controlled by GPES software). The work was done in different laboratories (South Africa and Belgium), hence different potentiostats. A conventional three-electrode system was used, with the working electrode either a bare or modified gold (0.8 mm radius) or glassy carbon electrode (3.00 mm diameter). The platinum wire was used as a counter electrode. The reference electrode was either the silver-silver chloride (Ag|AgCl) pseudo-reference or silver-silver chloride in 3.0 $mol.L^{-1}$ solution of sodium chloride (Ag|AgCl, 3.0 $mol.L^{-1}$ NaCl). Ag|AgCl pseudo-reference electrode is related to Ag|AgCl (3.0 $mol.L^{-1}$ NaCl) by 0.015 V. UV-vis spectra were recorded on a Varian 500 UV-vis/NIR spectrophotometer. Infrared (IR) spectra (KBr pellets) were recorded on a Perkin-Elmer spectrum 2000 Fourier Transform Infrared (FTIR) spectrophotometer. A WTW pH meter was used for pH measurements.

Electrochemical impedance spectroscopy (EIS) experiments were performed on an AUTOLAB PGSTAT30 potentiostat/galvanostat, controlled by FRA software which was used

for the acquisition and analysis of the impedance data. EIS experiments were recorded in the frequency range between 10 kHz to 100 mHz at a formal potential of 150 mV ($E_{1/2}$ of $Fe(CN)_6^{3-/4-}$ redox couple on bare gold electrode) and with an amplitude 5 mV rms sinusoidal modulation.

X-ray photoelectron spectroscopy (XPS) measurements were performed with a Perkin-Elmer Phi ESCA 5500 system equipped with a monochromated 450 W Al Kα source. The base pressure of the ESCA system was below 1 x 10^{-7} Pa. XPS experiments were recorded with 220 W power source and an angular acceptance angle of $\pm 7^{o}$. The analyzer axis made an angle of 45^{o} with the specimen surface. The elemental analysis and metal core levels were recorded with a step of 0.125 eV and pass energy of 117.4 eV. XPS data analysis was performed with the XPS Peak 4.1 program while a Shirley function was used to subtract the background. XPS measurements were performed on modified gold surfaces.

Raman experimental measurements were performed on a Renishaw system-1000 spectrometer (Renishaw, Wotton Under Edge, UK). Electrodes for Raman measurements were mounted on the microscope table and the laser light (780 nm, 5 mW at the sample) was focused directly on the electrode surface by using an Olympus 50 x objective, obtaining a spot size of approximately 2 μm diameter. The black scattered radiation was collected by the same objective lens and the Rayleigh line was suppressed by a notch filter. The light was dispersed over a 1200 lines/mm diffraction grating and was collected on Peltier cooled charged couple device (CCD) detector. Raman spectra were recorded in the Stokes branch of the spectrum, within the range 200-1800 cm^{-1}. The Raman spectra were performed for modified gold surfaces and powder samples.

Quartz crystal microbalance experiments were recorded using the Quartz Crystal Microbalance with Dissipation (QCM-D) equipment purchased from Q-Sense (Sweden). Crystals used were AT-cut quartz crystals, QSX-301, surfaced with gold. These were mounted in titanium QCM-D flow chambers, which were in turn housed in a Q-Sense E4 QCM-D sensor system. All of the above were sourced directly from Q-Sense®, Sweden. Flow was regulated by an Ismatec® peristaltic pump. The sensor surfaces and all QCM-D measurements were performed at room temperature (20 ^{o}C).

2.3 Synthesis

The synthesis of the metallo-tetra carboxylic acid chloride phthalocyanine {MTCAClPc (**11-13**), Figure 1.20} was achieved following the reported method by Shirai and colleagues [87]. This method first involves the synthesis of the metallo-carboxylic acid phthalocyanine derivative (MTCAPc), followed by the conversion of the carboxylic acid groups to acid chloride groups as shown in Scheme 3.1.

2.3.1 Synthesis of metallo-tetra carboxylic acid phthalocyanine (MTCAPc) [87]

The mixture of trimellitic anhydride (**14**, 10g, 0.05 mol), urea (30g, 0.5 mol), ammonium molybdate (1g, 0.8 mmol) and the required metal salt (0.06 mol): {i.e. cobalt (II) chloride for cobalt tetra carboxylic acid phthalocyanine (CoTCAPc, **15**), iron (II) chloride tetrahydrate for iron tetra carboxylic acid phthalocyanine (FeTCAPc, **16**) and manganese (II) chloride for manganese tetra carboxylic acid phthalocyanine (MnTCAPc, **17**)} were finely ground and added to nitrobenzene (150 ml). The mixture was refluxed for 3 hours at 458 K. A dark-blue solid resulted which was filtered off and washed with methanol under Soxhlet extraction overnight

until the smell of nitrobenzene could no longer be detected. Potassium hydroxide (10%, enough to dissolve the resulting solid) was added to the solid mixture and refluxed for 5 hours, allowed to cool to room temperature and the insoluble impurities separated by centrifugation. The resulting fluid was acidified with concentrated hydrochloric acid to precipitate the carboxylic acid phthalocyanines (**15-17**), which was filtered, washed three times with water and dried in oven at 373K.

CoTCAPc (**15**): Yield (37%), IR (KBr, cm^{-1}): 3439 (OH), 3239, 3180, 3077, 1701 (C=O), 1649, 1639, 1605, 1531, 1483, 1402, 1325, 1159, 1098, 864, 739, 665. UV-vis (DMF) {λ_{max} (nm)}: 672, 603, 337.

FeTCAPc (**16**): Yield (33%), IR (KBr, cm^{-1}): 3422 (OH), 3146, 1710 (C=O), 1660, 1554, 1406, 1314, 1289, 1237, 1152, 1123, 1070, 901, 774, 735, 661, 604, 481. UV-vis (DMF) {λ_{max} (nm)}:674, 611, 438, 328.

MnTCAPc (**17**): Yield (42%), IR (KBr, cm^{-1}): 3450 (OH), 3239, 3173, 3078, 1701 (C=O), 1653, 1635, 1605, 1531, 1484, 1399, 1159, 1093, 854, 741, 668. UV-vis (DMF) {λ_{max} (nm)}:726, 503.

2.3.2 Synthesis of metallo-tetra carboxylic acid chloride phthalocyanine (MTCAClPc)

The synthesis of the metallo-tetra carboxy acid chloride phthalocyanine complexes (**11-13**) was achieved from their metallo-tetra carboxylic acid phthalocyanine (MTCAPc) derivatives (**15-17**). The metallo-carboxylic acid phthalocyanine derivative (1.3 mmol) was refluxed for 10 hours with thionyl chloride (10 ml, 0.01 mol) in the presence of a few drops of pyridine in 10 ml dry benzene. The liquid was removed from the solid green product by centrifugation upon which

it was washed with dry benzene. The solid product was then dried at 70 ^{o}C in vacuo to yield the metallo-tetra carboxy acid chloride phthalocyanine (MTCAClPc) complexes (**11-13**).

CoTCAClPc (**11**): Yield (52%). IR (KBr, cm^{-1}): 3213, 3154, 3102, 1752 (C=O), 1655, 1634, 1603, 1526, 1479, 1327, 1188, 1095, 1050 (C-Cl), 888, 749, 677. UV-vis (DMF) {λ_{max} (nm), log ε)}: 678 (4.55), 608 (1.10), 342 (1.37).

FeTCAClPc (**12**): Yield (55%). IR (KBr, cm^{-1}): 3223, 3167, 3104, 3074, 1755 (C=O), 1655, 1633, 1606, 1533, 1484, 1329, 1198, 1167, 1093, 1027 (C-Cl), 873, 736, 668. UV-vis (DMF) {λ_{max} (nm), log ε)}: 676 (5.37), 607 (4.87), 443 (4.80), 335 (5.28).

MnTCAClPc (**13**): Yield (57%). IR (KBr, cm^{-1}): 3102, 1773 (C=O), 1719, 1657, 1635, 1525, 1484, 1406, 1258, 1160, 1071, 905 (C-Cl), 733, 667. UV-vis (DMF) {λ_{max} (nm), log ε)}: 713 (4.94), 685 (4.58), 648 (4.18), 495 (3.18), 349 (4.84).

2.4 Electrochemical characterization MTCAClPc (11-13)

Cyclic voltammogram and square wave voltammogram for the characterization of MnTCAClPc (**11-13**) complex was recorded using BioAnalytical System (BAS) B/W 100 Electrochemical Workstation. A conventional three-electrode setup was used, whereby a glassy carbon electrode (GCE) (3.00 mm diameter) was used as a working electrode, platinum wire counter electrode and silver-silver chloride (Ag|AgCl) pseudo-reference electrode. Tetraethyl-ammonium perchlorate (TEAP) was used as a supporting electrolyte. The GCE was polished with alumina on a Beuhler-felt pad followed by washing thoroughly with deionized water and rinsed with dry DMF before transferring into an electrochemical cell. All electrochemical experiments were performed under nitrogen atmosphere at ambient temperature in a freshly distilled dry DMF solution containing TEAP (0.10 $mol.L^{-1}$). Spectroelectrochemical experiments used for the characterization of MnTCAClPc (**13**) were performed using an OTTLE cell connected to a BAS CV 27 voltammograph. Spectral changes arising during electrolysis were monitored using Varian 500 UV-vis-NIR spectrophotometer.

2.5 Electrode modification

Surface modification and electrochemical characterization was followed by either a Bio-Analytical System (BAS) 100 B/W Electrochemical Workstation, PARSTAT 2273 potentiostat from AMETEK (controlled by Powersuite software running on a DELL Pentium computer) or AUTOLAB PGSTAT potentiostat/galvanostat (controlled by GPES and FRA software running on a computer). A conventional three-electrode system consisting of a bare or modified gold (r = 0.8 mm, BAS) electrode used as a working electrode. An Ag|AgCl pseudo-reference or Ag|AgCl

(3.0 mol.L^{-1} NaCl) used as a reference electrode and platinum wire used as a counter electrode. The gold electrode was modified using self-assembly method leading to the formation of SAMs.

2.5.1 Fabrication of MPc SAMs on gold electrode

The modification requires the use of a clean gold surface which can be achieved by following the established procedures [28,30,45,175]. Briefly, the gold electrode was first polished using an aqueous slurries of alumina (<10 μm) on a SiC-emery paper (type 2400 grit), and then to a mirror finish on a Buehler felt pad. The electrode was then placed in ethanol and subjected to ultrasonic vibration to remove residual alumina particles that might be trapped at the surface. After this mechanical treatment, the gold electrode was chemically treated by etching for about two minutes in a "Piranha" solution {3:1 (v/v) 30% hydrogen peroxide (H_2O_2) and concentrated sulphuric acid (H_2SO_4)} and then rinsed with copious amounts of doubly distilled water or ultra-pure Milli-Q water followed by ethanol. The chemical treatment with "Piranha" solution serves to remove the organic contaminants on gold electrode surface. The cleanliness of bare gold electrode surface was finally established by placing the electrode in 0.5 mol.L^{-1} H_2SO_4 and scanning the potential between -0.5 and 1.0 V (versus Ag|AgCl pseudo-reference or Ag|AgCl in 3.0 mol.L^{-1} NaCl) at a scan rate of 50 mV.s^{-1} until reproducible scans were obtained.

Following this pre-treatment, the gold electrode was modified following the method shown in Scheme 4.1. The gold electrode is pre-modified with a simple thiol (2-mercaptoethanol) which exposes the hydroxyl group at the surface of the SAM (Au-ME SAM). This is followed by the attachment of metal tetra-carboxylic acid chloride phthalocyanine

(MTCAClPc) complexes (M= Co, Fe and Mn). Detailed modification procedure of gold electrode in Chapter 4, Section 4.2.1.

2.5.2 Fabrication of glucose oxidase (GOx) enzyme modified gold electrode

The immobilization of the enzyme electrode was achieved from the acid activated cobalt phthalocyanine SAM (Au-ME-CoTCAPc SAM) as shown in Scheme 4.3. Briefly, the acid groups from the cobalt tetra-carboxy acid phthalocyanine modified gold electrode (Au-ME-CoTCAPc SAM) were first activated using coupling agents (EDC and NHS) such that they are susceptible to attack by an amino groups from the enzyme [41-44,176]. In this work the immobilization protocol of GOx enzyme shown in Scheme 4.3 was followed. The Au-ME-CoTCAPc SAM electrode was rinsed with pH 7.4 PBS solution and immediately immersed in the solution containing 2 mM EDC and 5 mM NHS [41-44,176] for 3 hours. This step (*activation*) as shown in Scheme 4.3 (step 1), converts the exposed carboxylic acid groups into reactive intermediates which are susceptible to attack by amino groups. The EDC/NHS activated Au-ME-CoTCAPc SAM electrode was then briefly rinsed in pH 7.4 PBS solution and immediately immersed in the pH 7.4 PBS solution containing 150 $mg.ml^{-1}$ of GOx (*enzyme immobilization*) for 3 hours at $4^{o}C$ (as shown in Scheme 4.3, step 2) to afford covalent attachment of the enzyme onto Au-ME-CoTCAPc SAM (represented as Au-ME-CoTCAPc-GOx SAM). QCM-D measurements for the immobilization of GOx enzyme was achieved using Au-coated sensor crystals (Q-Sense AB) which was cleaned following the reported method by Limson et al [177]. Briefly, all crystals used were cleaned by exposure to ozone-producing ultraviolet light (UV-O) for 5 minutes. Following UV-O treatment, the crystals were immersed in a solution of NH_3: H_2O_2: H_2O in a ratio of 1: 1: 5, heated at 75 ^{o}C for 5 minutes. The crystals

were then rinsed thoroughly with water, dried under nitrogen gas and then exposed to UV-O for a further 5 minutes prior to use. QCM-D analysis took place under the following parameters: 20 ºC temperature and a flow rate of 25 µl / minute. The poor compatibility of the QCM-D flow chamber components with organic solvent made it difficult to assess layer-by-layer immobilization of the organic-phase components, i.e. 2-mercaptoethanol and CoTCAClPc. Then the enzyme layer was the only layer monitored using QCM-D and this was due to the fact that the enzyme immobilization was achieved in aqueous buffer solution.

RESULTS AND DISCUSSION :

Part of the research work presented in chapters three, four and five have been published and are not referenced further in this thesis:

1. **Self-assembled monolayers (SAMs) of cobalt tetracarboxylic acid chloride phthalocyanine covalently attached onto a preformed mercaptoethanol SAM: A Novel Method**,
   P. N. Mashazi, K. I. Ozoemena, D. M. Maree, T. Nyokong, *Electrochimica Acta*, 2006 (**51**) 3489 - 3494.

2. **Tetracarboxylic acid cobalt phthalocyanine SAM on gold: Potential applications as amperometric sensor for H_2O_2 and fabrication of glucose biosensor**,
   P. N. Mashazi, K. I. Ozoemena, T. Nyokong, *Electrochimica Acta*, 2006 (**52**) 177 – 186.

3. **Surface electrochemistry and electrochemical behaviour of tetra carboxy substituted iron, cobalt and manganese phthalocyanine monolayers on gold electrode**,
   P. N. Mashazi, P. Westbroek, K. I. Ozoemena, T. Nyokong, *Electrochimica Acta*, 2006 (*submitted*).

4. **Critical assessment of the quartz-crystal microbalance as an analytical tool for biosensor development and fundamental studies: metallophthalocyanine-glucose oxidase biocomposite sensors,**
   R. Fogel, P. N. Mashazi, T. Nyokong, J. Limson, *Biosens. Bioelectron.*, 2006 (*submitted*).

CHAPTER THREE:

CHARACTERISATION

3.1 Synthesis and characterization of MTCAClPc (11-13) complexes

The metal tetra-carboxy acid chloride phthalocyanine (MTCAClPc) complexes {where M = Co (**11**), Fe (**12**) and Mn (**13**)} were synthesized following the reported method by Shirai and colleagues [87], Scheme 3.1.

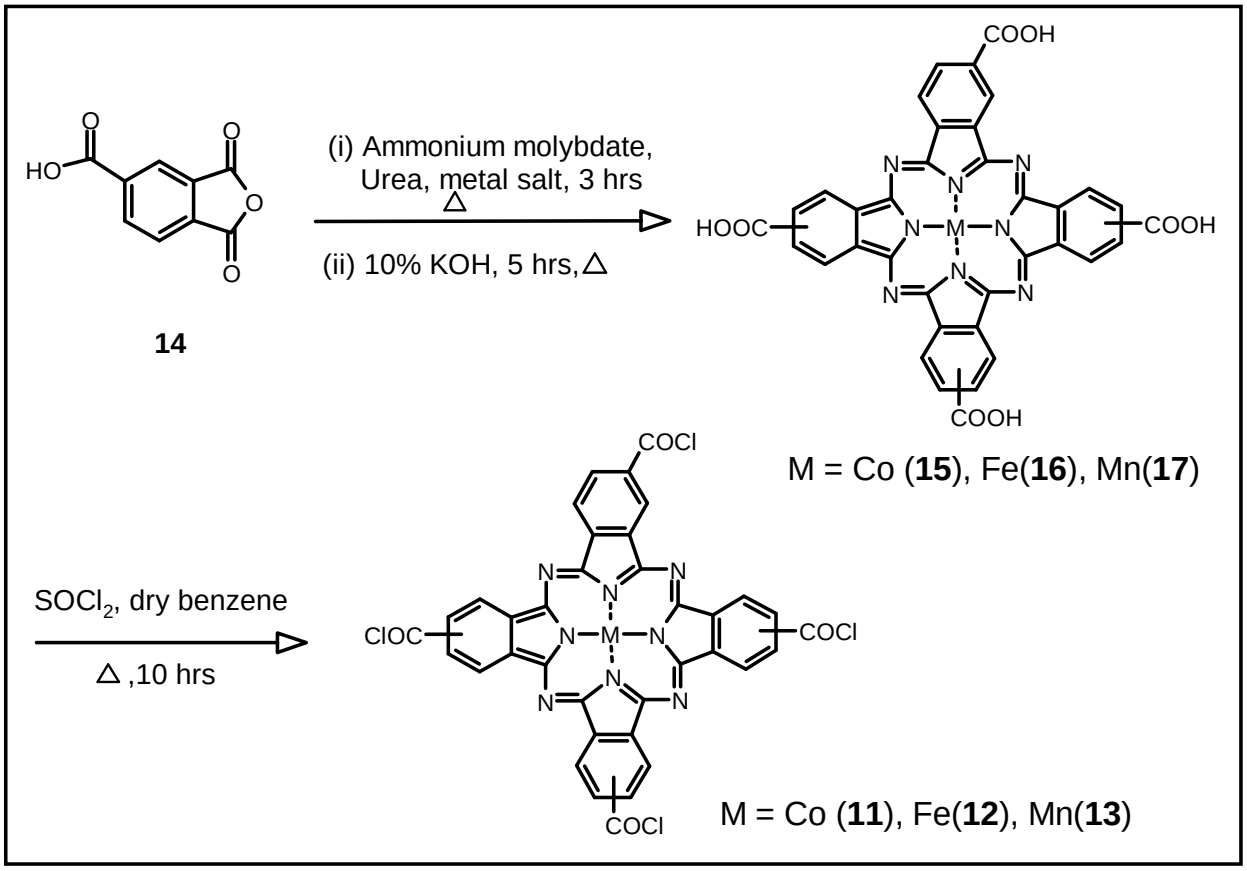

Scheme 3.1: Synthesis of metallo tetra-carboxy acid chloride phthalocyanine (MTCAClPc). M = Co (**11**), Fe (**12**), Mn (**13**).

The first step was the formation of metal tetra-carboxylic acid phthalocyanine (MTCAPc) complexes (**15-17**) in moderate yields which averaged 42%. The MTCAPc complexes were subsequently converted to carboxy acid chloride derivatives (**11-13** in Scheme 3.1) by refluxing

in dry benzene containing thionyl chloride and a few drops of pyridine (used to solubilize the carboxylic acid phthalocyanines). The synthesis of iron and cobalt tetra-carboxy acid chloride phthalocyanine complexes (**11** and **12**) have been reported before [87] and manganese tetra carboxy acid chloride phthalocyanine (**13**) was synthesized following a similar method.

3.1.1 Spectroscopic characterization of MTCAClPc (11-13)

The UV-vis spectra of the synthesized complexes shown in Figure 3.1 exhibited a typical Q band for a monomeric species observed at 678 nm for (**11**), 676 nm for (**12**) and 713 nm for (**13**). All the complexes obeyed Beer's law at low concentration with the extinction coefficients of all the synthesized complexes in the orders of 10^5 $dm^3/(mol.cm)$.

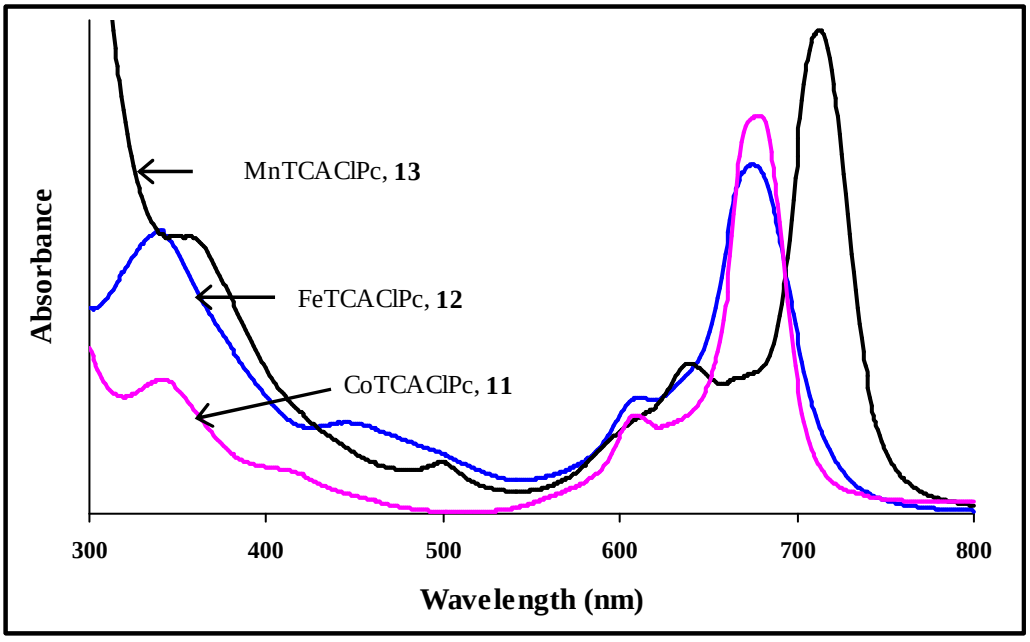

Figure 3.1: UV-vis spectra of 1.0 x 10^{-4} $mol.L^{-1}$ for CoTCAClPc (**11**), FeTCAClPc (**12**) and MnTCAClPc (**13**) in dry DMF.

All synthesized complexes exhibited B or Soret band between 300 – 350 nm which results from the transition of the deeper π orbitals (b_{2u} and a_{2u}) to the π* orbitals (e_g). The UV-vis spectrum of MnTCAClPc (**13**) is typical of $Mn^{III}Pc$ complexes with a red shifted Q band [60,104,178]. The absorption bands near 500 nm for the MnTCAClPc and 450 nm for FeTCAClPc are typical of iron and manganese phthalocyanine complexes, and are associated with charge transfer bands [95,179]. Charge transfer bands normally occur when the central metal ion has d-orbital lying within the HOMO-LUMO gap of the phthalocyanine ring, and the transitions that gives rise to these bands are either metal-to-ligand charge transfer (MLCT) or ligand-to-metal charge transfer (LMCT). The charge transfer bands normally occur as weak absorption bands as was observed in Figure 3.1, in the near infrared (NIR) region or between the Q and B bands (i.e. 400-500 nm) [95]. Using the four orbital model energy diagram (Figure 3.2), the occurrence of charge transfer bands can be understood [95]. The ligand-to-metal charge transfer (LMCT) transitions are the transitions from HOMO levels, i.e. a_{2u} or a_{1u} of the phthalocyanine ligand orbitals to e_g or a_{1g} of the metal orbitals. The metal-to-ligand charge transfer (MLCT) transitions occur from metal orbitals (e_g) to the ligand e_g and b_{1u} as shown in Figure 3.2. For FeTCAClPc, the metal-to-ligand charge transfer band at 450 nm is typical of FePc complexes with an oxidation state of +2 [90,95,180-186].

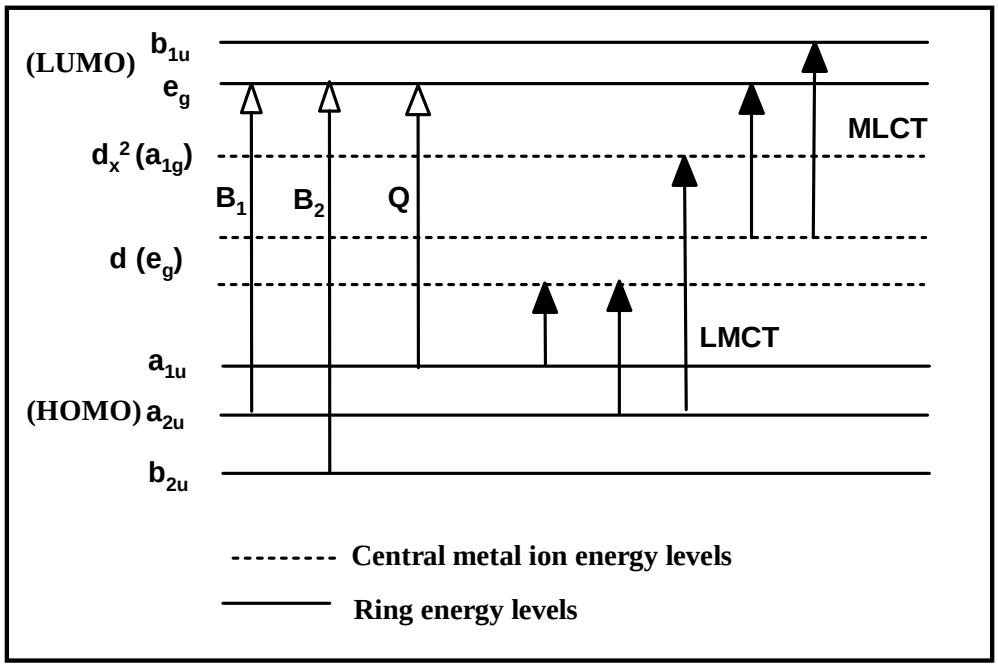

Figure 3.2: Energy diagram showing the charge transfer transition between phthalocyanine ring and the central metal ion [95].

Infrared (IR) spectroscopy was also used for characterization of the synthesized MPc complexes (**11-13**) and they all exhibited the same trend. The IR spectra in Figure 3.3 were useful in monitoring formation of the carboxy acid chloride phthalocyanines. The appearance of the band at 1752 cm^{-1}, 1755 cm^{-1} and 1773 cm^{-1} for CoTCAClPc (**11**), FeTCAClPc (**12**) and MnTCAClPc (**13**), respectively corresponds to the carbonyl (C=O) stretch, thus confirming the conversion of the carboxylic acid (COOH) groups to carboxy acid chloride (COCl) groups. The OH band at 3439 cm^{-1} for CoTCAPc (**15**) in Figure 3.3(a) disappeared upon the formation of CoTCAClPc (**11**) as observed in Figure 3.3(b). Similar results were also observed for other MPc complexes, whereby the OH bands at 3422 cm^{-1} for FeTCAPc (**16**) and 3450 cm^{-1} for MnTCAPc (**17**) disappeared upon the formation of FeTCAClPc (**12**) and MnTCAClPc (**13**), respectively. The disappearance of the OH band was accompanied by the appearance of C-Cl bands at 1050

cm^{-1}, 1027 cm^{-1} and 905 cm^{-1} for CoTCAClPc (**11**), FeTCAClPc (**12**) and MnTCAClPc (**13**), respectively. The spectroscopic characterization using IR confirmed the successful synthesis of the desired complexes and was comparable to the reported IR characterization of these complexes from literature [87].

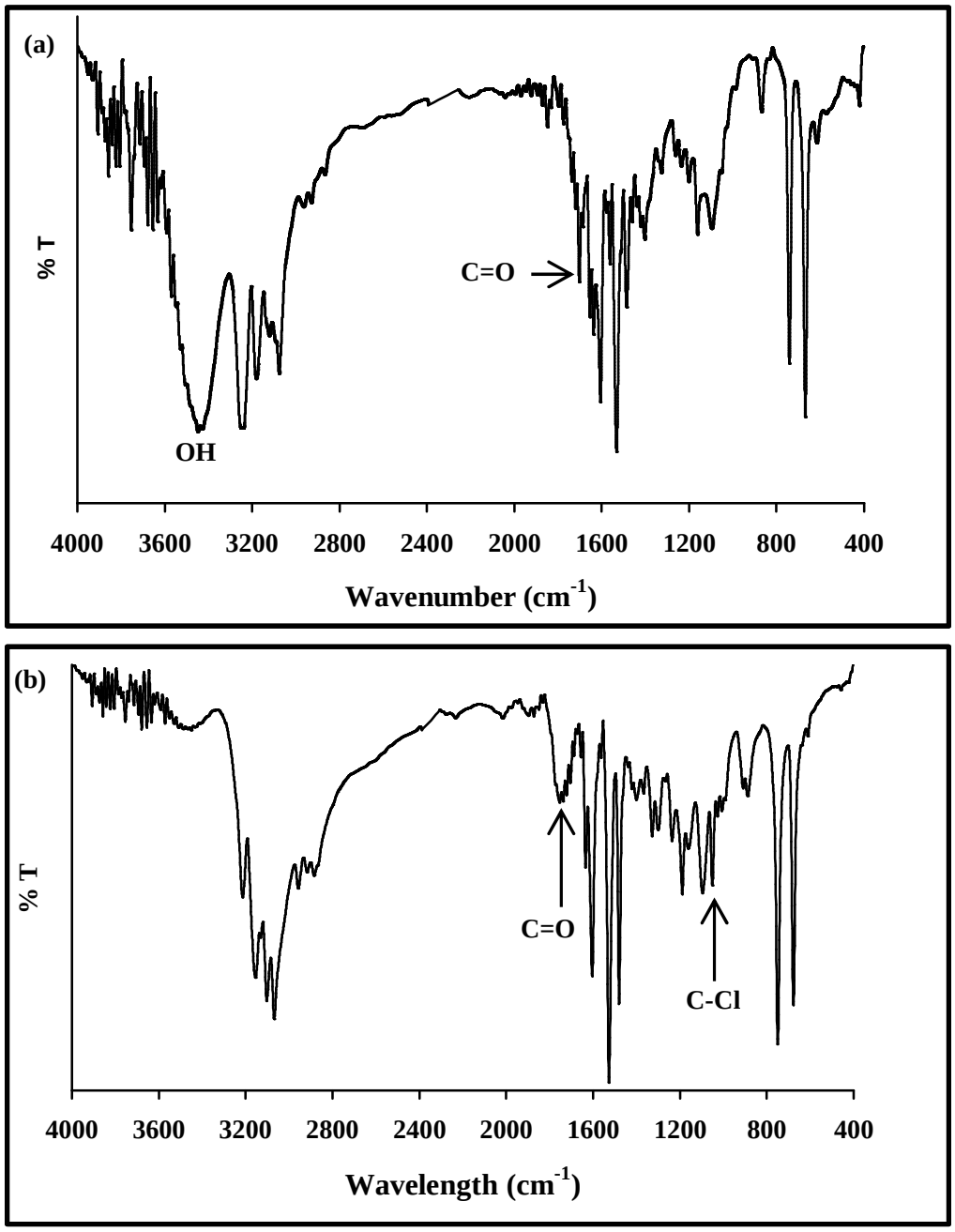

Figure 3.3: FTIR spectra for (a) CoTCAPc, (**15**) and (b) CoTCAClPc, (**11**).

3.1.2 Electrochemical and spectroelectrochemical characterization of MTCAClPc

The electrochemical and spectroelectrochemical characterization of MTCAClPc complexes were performed in dry freshly distilled DMF solution containing (0.10 $mol.L^{-1}$) TEAP as an electrolyte. The cyclic voltammogram (CV), Figure 3.4(b) and square wave voltammogram (SWV), Figure 3.4(a) are shown for MnTCAClPc (**13**) as an example. The redox potentials of Co, Fe and Mn complexes are listed in Table 3.1. The typical cyclic voltammogram in Figure 3.4(b) shows three clear redox peaks labeled **I**, **III** and **IV**. The Osteryoung square wave voltammogram, in Figure 3.4(a) showed an extra weak peak (**II**) which could not be observed in the cyclic voltammogram, Figure 3.4(b). The redox couples for the MnTCAClPc (**13**) were observed at $E_{1/2}$ (vs Ag|AgCl) = 1100 mV (**I**), 400 mV (E_P) (**II**), -200 mV (**III**) and -1000 (**IV**). The redox couples exhibited reversible to quasi-reversible behaviour with the anodic and cathodic peak separation ($\Delta E_p = E_{pa} - E_{pc}$) for redox couples **III** and **IV** found to be 100 mV. Redox peak **I** was not highly reversible, showing a weak cathodic component. In comparison with literature [178], **III** is assigned to $Mn^{III}Pc/Mn^{II}Pc$, **IV** to $Mn^{II}Pc^{-3}/Mn^{II}Pc^{-2}$, **II** to $Mn^{IV}Pc/Mn^{III}Pc$ and **I** to $Mn^{IV}Pc^{-1}/Mn^{IV}Pc^{-2}$. For some of the complexes, the assignments of the redox couples in Table 3.1 have been confirmed below using spectroelectrochemistry. For Co and Fe complexes the redox peaks were as listed in Table 3.1 in comparison with literature [108].

Table 3.1: Summary of redox potentials of MTCAClPc complexes (**11-13**) in DMF containing TEAP. Potentials versus Ag|AgCl. Half-wave potentials ($E_{1/2}$) reported.

Complex	$M^{IV}Pc^{-1}/ M^{IV}Pc^{-2}$	$M^{IV}Pc^{-2} / M^{III}Pc^{-2}$	$M^{III}Pc^{-2} / M^{II}Pc^{-2}$	$M^{II}Pc^{-2} / M^{II}Pc^{-3}$
MnTCAClPc (**13**)	1.1 V (**I**)	0.4 V (E_P) (**II**)	-0.2 V (**III**)	-1.0 V (**IV**)

Complex	$M^{III}Pc^{-1}/M^{III}Pc^{-2}$ (**I**)	$M^{III}Pc^{-2}/M^{II}Pc^{-2}$ (**II**)	$M^{II}Pc^{-2}/M^{I}Pc^{-2}$ (**III**)	$M^{I}Pc^{-3}/M^{I}Pc^{-2}$ (**IV**)
CoTCAClPc (**11**)	0.85	0.46	-0.52	-1.20
FeTCAClPc (**12**)	0.80	0.20	-0.60	-1.20

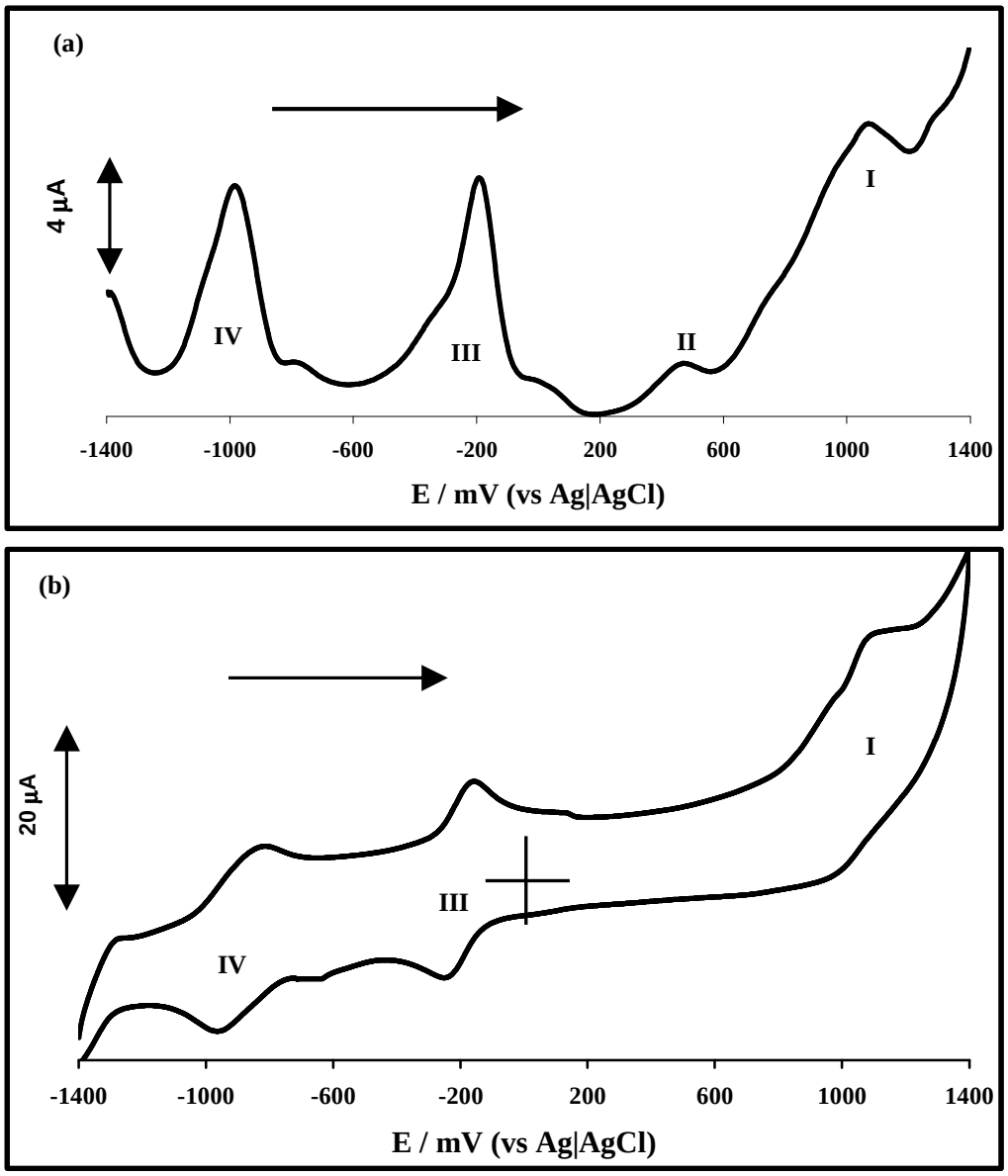

Figure 3.4: (a) Osteryoung square wave voltammogram scanned from -1400 to 1400 mV and the sensitivity of 10 µA/V, recording the net current for the redox processes observed in (b) and (b) cyclic voltammogram (CV) of 1.0 x 10^{-4} mol.L^{-1} MnTCAClPc (**13**) in dry DMF containing 0.1 mol.L^{-1} TEAP. Scan rate = 100 mV/s.

Spectroelectrochemical studies using optically transparent thin layer electrode (OTTLE) were used to assign electrode reactions for the MnTCAClPc (**13**) complex observed from the CV and SWV in Figure 3.4. The spectroelectrochemical studies are very useful as they give insight into the origin of redox couples observed during voltammetric experiments. Figure 3.5(a) shows the UV-vis spectral changes at potentials of process **III** and Figure 3.5(b) for application at potentials of process **IV** from Figure 3.4.

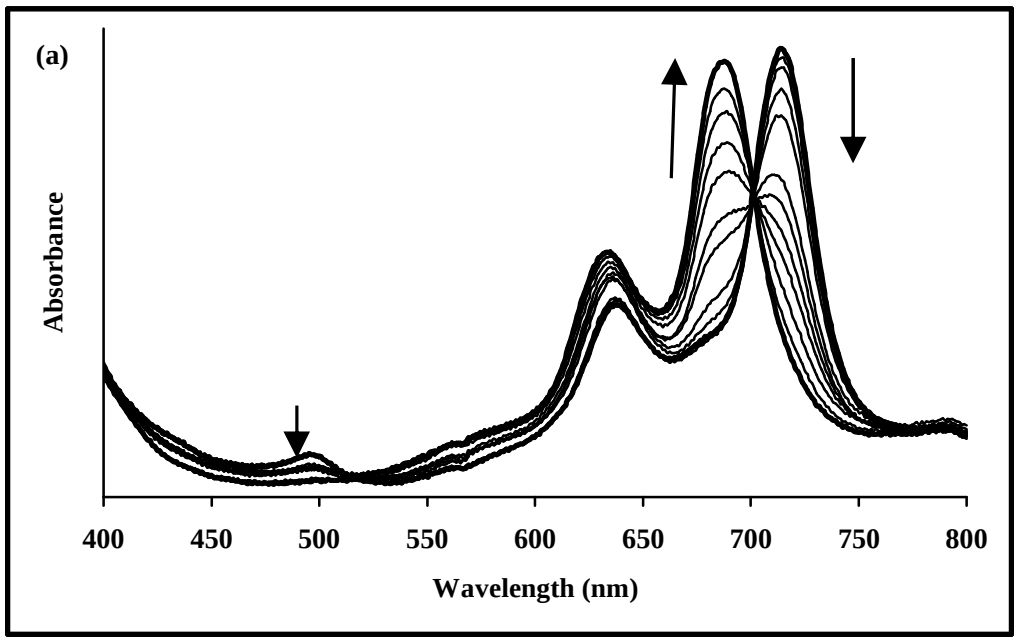

Figure 3.5(a): Changes in spectral features observed for MnTCAClPc (**13**) complex (1.0×10^{-4} mol.L^{-1} in DMF containing 0.10 mol.L^{-1} TEAP) during the controlled reduction potentials –0.6 V vs Ag|AgCl in the OTTLE cell.

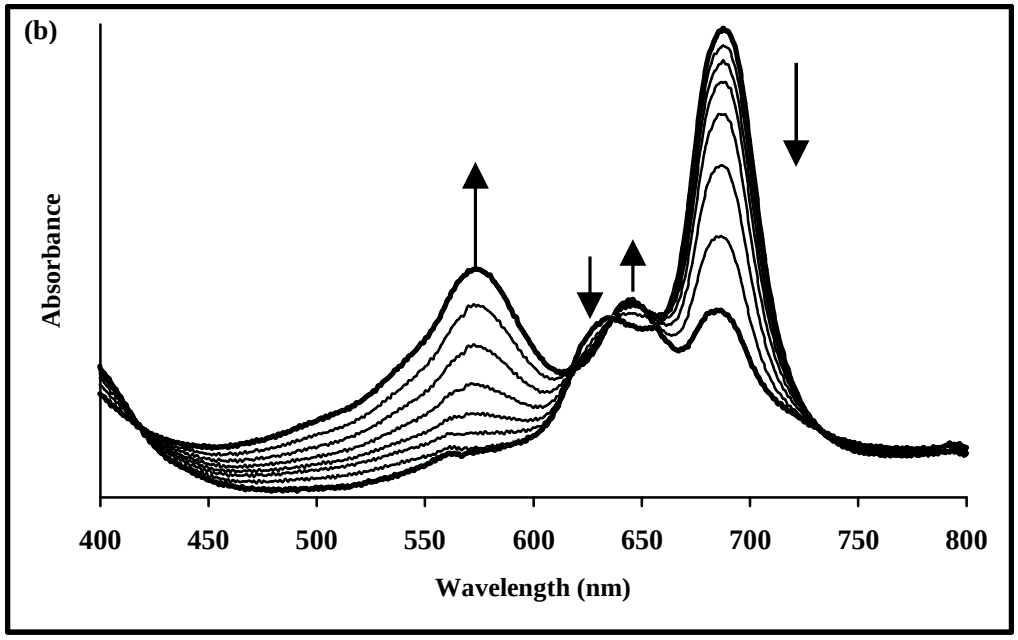

Figure 3.5(b): Changes in spectral features observed for MnTCAClPc (**13**) complex (1.0×10^{-4} mol.L^{-1} in DMF containing 0.10 mol.L^{-1} TEAP) during the controlled reduction potentials -1.2 V vs Ag|AgCl in the OTTLE cell. The first spectrum in (b) is the same as the last one in Figure 3.5(a).

Figure 3.5(a) shows that the Q band at 713 nm decreased in intensity and this was accompanied by the formation of a new band at 688 nm and a disappearance of a charge transfer band at 495 nm. The uncomplicated spectral changes were nicely observed with clear isosbestic points at 701 nm and 510 nm. The observed spectral changes, i.e. decrease in Q band at 713 nm and formation of the new band at 688 nm, are typical of metal-based reduction processes of $Mn^{III}Pc$ [95,178] complexes. These spectral changes resulting in the Q band shift from 713 nm to 688 nm are characteristic [178] of the conversion of $Mn^{III}Pc^{-2}$ to $Mn^{II}Pc^{-2}$. Therefore, the redox couple **III** in Figure 3.4 is assigned to metal reduction process from $Mn^{III}TCAClPc^{-2}$ to $Mn^{II}TCAClPc^{-2}$. Further reduction of the species formed in Figure 3.5(a) at potentials of couple

IV, resulted in spectral changes as observed in Figure 3.5(b). The spectral changes in Figure 3.5(b) showed a decrease in the Q band at 688 nm accompanied by a formation of new bands at 575 nm and 646 nm. These spectral changes were clearly observed with isosbestic points at 734 nm, 654 nm, 635 nm, 618 nm and 414 nm. The decrease in Q band intensity is typical behaviour for the ring-based reduction in MPc complexes [95,178] and the formation of the manganese ring-reduced species ($Mn^{II}TCAClPc^{-3}$). Therefore, the spectral changes in Figure 3.5(b) clearly confirm that the process at redox couple **IV** in Figure 3.4 is a ring-based reduction process ($Mn^{II}TCAClPc^{-2}/Mn^{II}TCAClPc^{-3}$).

CHAPTER FOUR:

MODIFICATION AND CHARACTERISATION OF SAM

MODIFIED GOLD ELECTRODES

4.1 Surface modification

Prior to modifying gold electrode, the surface roughness factor of the unmodified gold electrodes was calculated and these calculations are important for the characterization of an unmodified gold electrode as they give a clear indication of the surface morphology. The surface morphology of gold electrode is known to affect the properties of self-assembled monolayers [187], such as defect densities [187] and molecular packing [28]. An ideally smooth gold electrode surface is known to give the most highly ordered and regularly packed monolayer [28]. The surface roughness factor calculations are also important in the determination of the real surface area of gold surface as by definition the surface roughness factor is the ratio of the real surface area to the geometric area [188,189]. In this work, the real surface area of gold electrode was measured using the conventional methodology [29,190], using $K_3Fe(CN)_6$ solution and Randles-Sevcik equation (4.1) at 25^0C:

$$I_{pa} = (2.69x10^5)n^{3/2}AD^{1/2}C\nu^{1/2} \qquad (4.1)$$

where n is the number of electrons involved (n = 1 in the $Fe(CN)_6^{3-}/Fe(CN)_6^{4-}$ system), A is the geometric surface area of the gold electrode (0.0201 cm^2), C the bulk concentration of $K_3Fe(CN)_6$ (5.0 x 10^{-4} $mol.L^{-1}$), D = 7.6 x 10^{-6} $cm^2.s^{-1}$ is the diffusion coefficient of $K_3Fe(CN)_6$ [191], and ν is the scan rate (0.050 $V.s^{-1}$). Figure 4.1 shows a typical redox couple for $Fe(CN)_6^{3-}$/ $Fe(CN)_6^{4-}$ at bare gold electrode. Therefore, using equation 4.1 and anodic peak current of I_{pa} = 2.78 x 10^{-6} A from Figure 4.1, the real surface area of gold electrode was calculated to be 0.0335 cm^2. The surface roughness factor resulting from the ratio of real to geometric surface area is

1.67. The calculated surface roughness factor was found to be within the reported values for gold electrodes [188-190, 192-194] used for SAM modification.

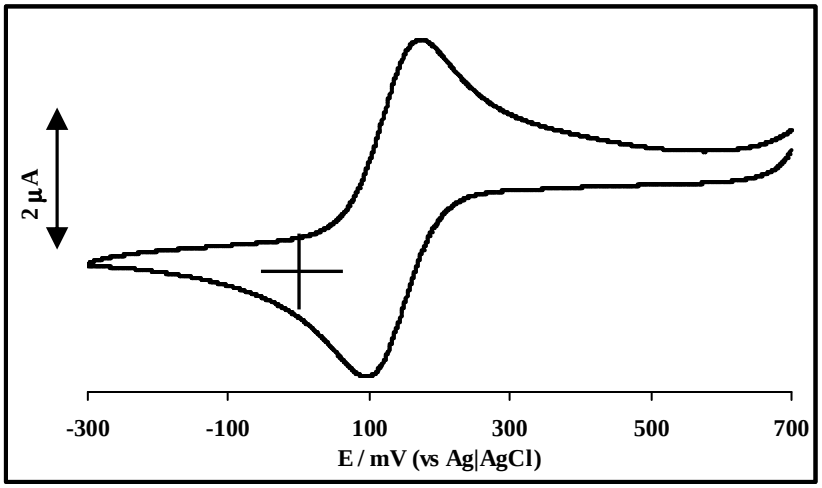

Figure 4.1: Cyclic voltammogram for 5.0 x 10^{-4} mol.L^{-1} $K_3Fe(CN)_6$ in 0.01 mol.L^{-1} KCl solution. Scan rate = 50 mV/s.

4.2 Fabrication of SAMs on gold surface

4.2.1 Immobilization of MTCAClPc onto pre-modified gold electrode

In this work the gold electrode surface after thorough cleaning, was rinsed with absolute ethanol solution and immediately placed into a nitrogen saturated absolute ethanol solution of 2-mercaptoethanol (3 x 10^{-3} mol.L^{-1}) at ambient temperature for 10 – 14 hrs (Scheme 4.1, step 1). The 2-mercaptoethanol (2-ME) modified gold electrode (Au-ME SAM) was thoroughly rinsed with absolute ethanol and dry DMF to remove all the physically adsorbed 2-mercaptoethanol molecules. The coupling reaction between the substituents of MTCAClPc complexes (**11-13**) and Au-ME SAM was performed by immersing the 2-mercaptoethanol modified electrode (Au-ME SAM) into a dry DMF solution of MTCAClPc (2.0 x 10^{-4} mol.L^{-1}) for 24 hours (Scheme 4.1,

step 2). Upon the removal of MTCAClPc modified gold electrode from the deposition solution, it was rinsed with dry DMF and dried in nitrogen prior to electrochemical experiments. Immediately after the covalent attachment of the MTCAClPc onto Au-ME SAM, represented as Au-ME-MTCAClPc SAM, the freshly prepared sensor was exposed to pH 4.0 phosphate buffer solution and the unreacted acid chloride groups hydrolyzed to acid groups. The hydrolyzed carboxy acid chloride groups lead to the carboxylic acid groups modified phthalocyanine SAM (Au-ME-MTCAPc SAM). This is a simple method by which the phthalocyanine can be immobilized onto gold surface and is achieved in two steps: (i) the pre-modification of gold electrode with the simple thiol, followed by (ii) coupling reaction between the phthalocyanine substituents and the exposed functional group on the pre-formed SAM.

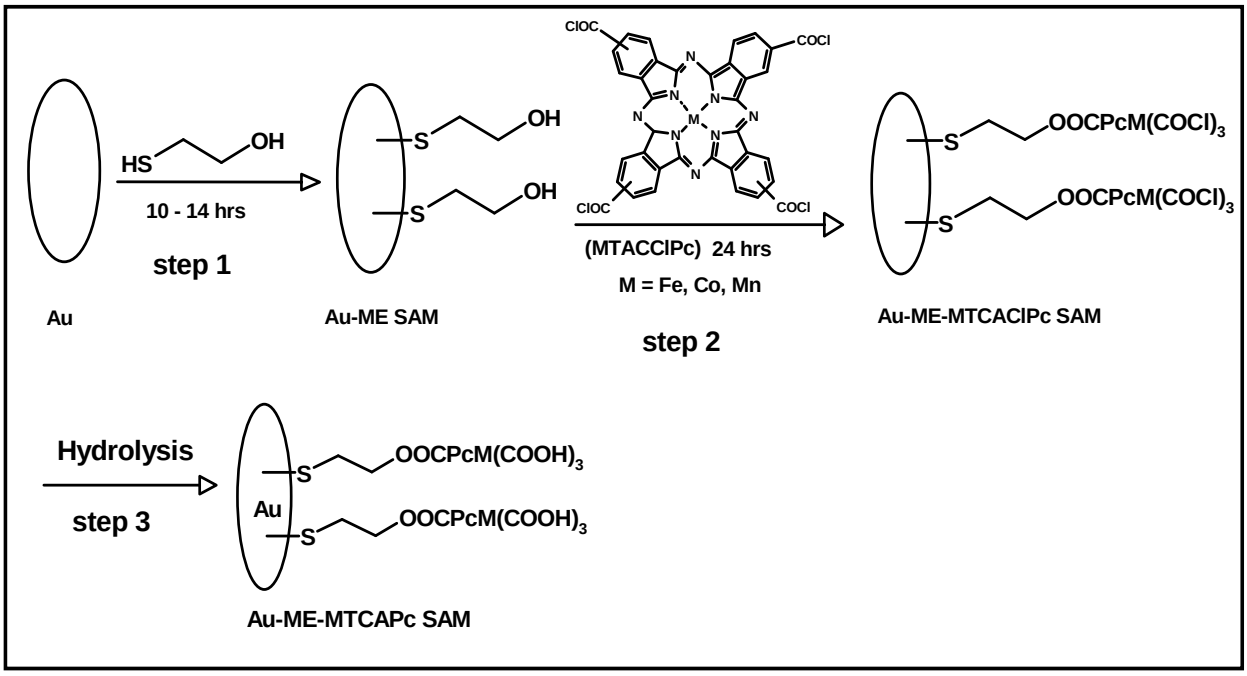

Scheme 4.1: Schematic representation of the immobilization of MTCAClPc (Au-ME-MTCACIPc SAM) onto preformed 2-mercaptoethanol (Au-ME) SAM onto gold electrode. M = Co, Fe and Mn, and subsequent hydrolysis to Au-ME-MTCAPc SAM.

To confirm the coupling reaction between the terminal OH group of the mercaptoethanol SAM and the CoTCAClPc substituents, the reaction between 2-mercaptoethanol and CoTCAClPc (**11**) was carried out in tri-ethylamine solution and the product was filtered, dried and IR spectra recorded. The IR spectra of the product exhibited two interesting absorption bands which are characteristic of the product formed and these bands were observed at 1699 cm^{-1} (C=O stretch) and 1141 cm^{-1} (C-O-C stretch). The formation of the ether linkage (C-O-C) confirmed the successful coupling reaction between 2-mercaptoethanol to CoTCAClPc. The C=O stretch which was at 1752 cm^{-1} shifted to 1699 cm^{-1} and this is due to the removal of Cl ion upon the formation of the ether bond (C-O-C). Similar reactions were observed for the other complexes (FeTCAClPc and MnTCAClPc) and clearly confirm the coupling reaction between 2-mercaptoethanol and MTCAClPc complexes.

The MTCAClPc modified gold electrodes (Au-ME-MTCAClPc SAM) were placed in pH 4.0 solution for conditioning before use. During this conditioning step the acid chloride groups undergo hydrolysis to COOH as shown in Scheme 4.1 (step 3) forming Au-ME-MTCAPc SAM. Therefore, the MTCAClPc modified electrodes has been represented as Au-ME-MTCAPc SAM on the assumption that hydrolysis has occurred during conditioning. The hydrolysis step in Scheme 4.1 (step 3) for the CoTCAClPc was also investigated by exposing CoTCAClPc (with the IR spectrum shown in Figure 3.3(b)) in pH 4 phosphate buffer solution, and the resulting product filtered, dried and the IR spectrum recorded. The IR spectrum of the product CoTCAPc (similar to the IR spectrum in Figure 3.3(a)) exhibited absorption bands at 3422 cm^{-1} (OH) and 1699 cm^{-1} (C=O stretch) confirming the hydrolysis of CoTCAClPc to CoTCAPc. Similar IR absorption bands were also observed for other complexes (FeTCAClPc and MnTCAClPc) confirming hydrolyses of COCl groups to COOH.

4.2.2 Immobilization of amino substituted compounds (enzymes)

MPc complexes are biocompatible with several enzymes, with the most reported being glucose oxidase (GOx). The coupling reaction between the MPc and GOx forms the MPc-GOx based biosensors [117-123]. However, most reports on the modification of electrodes with enzymes and phthalocyanines are mostly based on the physisorption of MPc onto glassy carbon electrode (GCE), poly graphite electrode (PGE), carbon paste matrix (CPM) and screen-printed carbon electrode (SPCE). However, physisorbed MPc complexes are unstable [27] as these complexes are attached using π-π interactions between the surface and the adsorbed molecules. Therefore, the method by which these molecules and enzymes can be chemisorbed by forming a covalent bond thus yielding a stable monolayer is desirable. Gooding et al. [41-44] have reported the immobilization of enzymes onto gold electrode modified with the mercaptopropionic acid (MPA) SAM (Scheme 4.2), where the acid group of the pre-formed MPA SAM will react with the amino group from the enzyme. This method affords a covalent immobilization of the enzyme onto gold surface, by forming an amide bond resulting from the reaction between the acid and amino groups. However, the reaction between the acid and the amino group does not occur readily. Therefore, coupling agents are employed to catalyze the reaction between acid and amino groups by activating the acid group, making it susceptible to attack by amino groups resulting in the formation of an amide bond. The acid groups are first activated using coupling agents: N-ethyl-N(3-dimethylamino-propyl) carbodiimide (EDC) and N-hydroxy succinimide (NHS) as shown in Scheme 4.2.

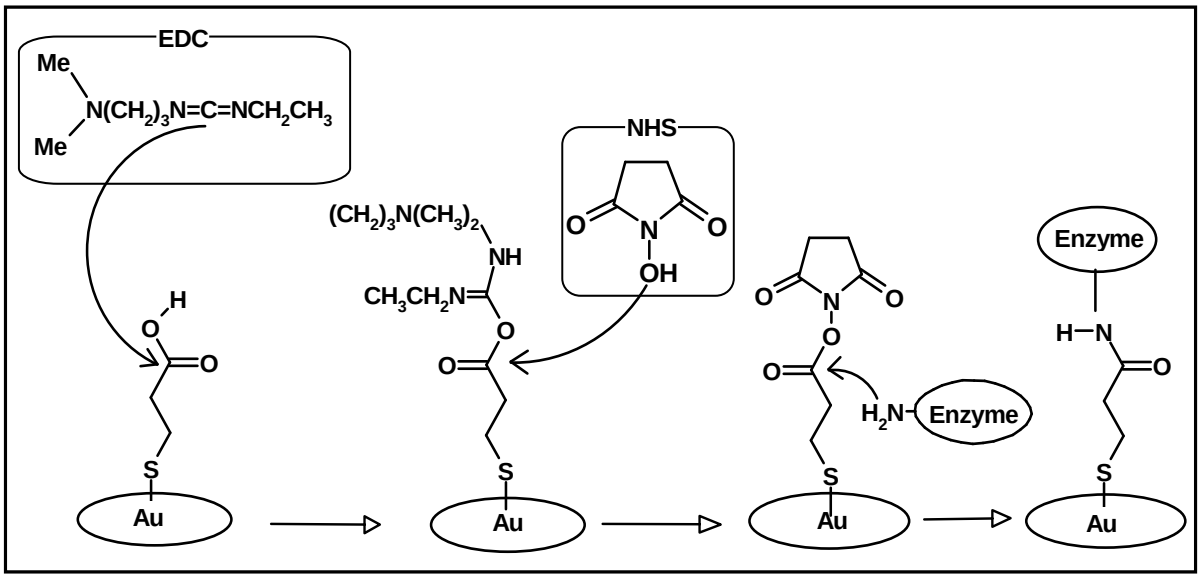

Scheme 4.2: Schematic representation showing the activation of acid group of MPA SAM and the immobilization of enzyme on activated SAM forming an amide bond [41-44].

EDC can activate the acid group on its own and NHS as well, but Jiang et al [176] reported that the combination of EDC and NHS yielded a more highly activated surface, making the immobilization of enzyme easy. The combination of EDC and NHS affords about 60 % of the surface activated by NHS, 30 % by EDC leaving only 10 % of the surface inactive. Scheme 4.3 shows the *activation* (step 1) of the acid groups of the Au-ME-CoTCAPc SAM using EDC/NHS coupling agents. The immobilization of the GOx enzyme, as a monolayer onto an EDC/NHS activated Au-ME-CoTCAPc SAM, was achieved as shown in Scheme 4.3 (step 2) represented as Au-ME-CoTCAPc-GOx SAM.

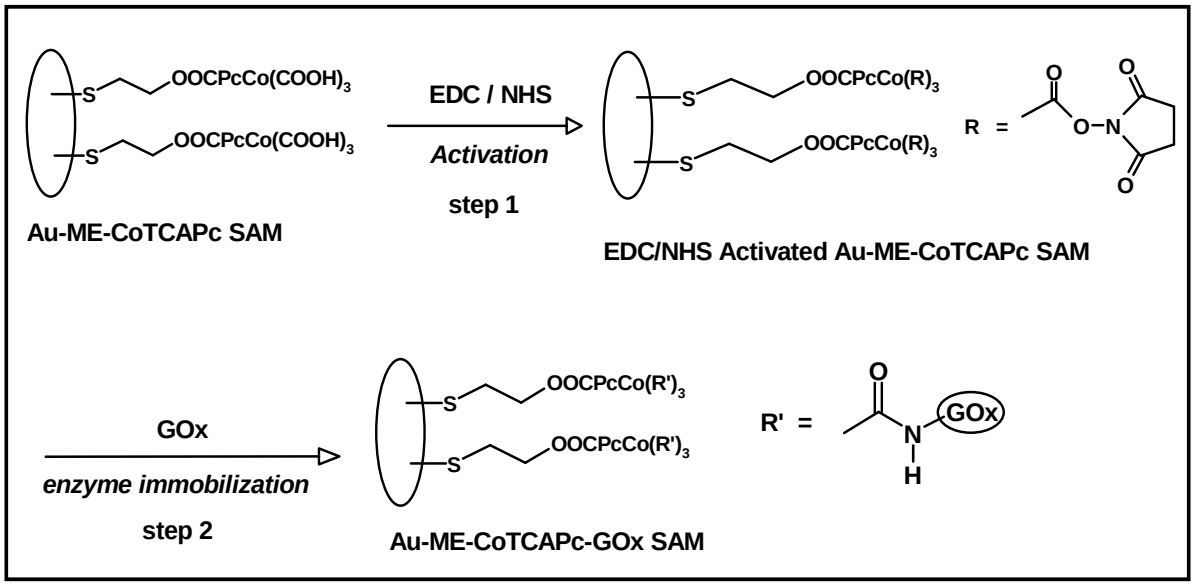

Scheme 4.3: Schematic representation showing the immobilization of glucose oxidase (GOx) enzyme onto gold electrode modified with acid cobalt phthalocyanine monolayer (Au-ME-CoTCAPc-GOx SAM).

In Scheme 4.3, MPc layer will act as an electron mediator thus facilitating electron transfer between the redox center of the enzyme and the gold surface. The mediation role played by the MPc SAM is very important as there have been several reports that involve the use of the mediator for glucose oxidase enzyme reactions [117-123]. Enzyme reactions are known to produce an electroactive hydrogen peroxide (H_2O_2) [136] which can be detected at gold surfaces. However gold surfaces are known for their poor catalytic detection for hydrogen peroxide due to high anodic potentials making them unfavourable for biological measurements. The use of the mediator fulfills two requirements: (i) lower the potential of H_2O_2 detection to more favourable values and (ii) as stated before, improve electron transfer between the enzyme layer and the gold electrode surface.

The immobilization method was followed using different electrochemical and spectroscopic surface characterization methods. Electrochemical methods have gained popularity due to their simplicity and ability to study properties of monolayers formed on gold surface [28,30] and also have been employed in studying the electroactive SAMs of MPc complexes [23,24,54-60]. Whereas, spectroscopic methods are useful in studying the chemical constituents and nature of at which the film interact with the substrate (gold surface).

4.2.3 Electrochemical characterization of MPc-SAMs

The characterization of SAM modified electrode (in Scheme 4.1) was followed using cyclic voltammetry. The SAM properties studied are the ion permeation (electrochemical capacitance), blocking of under-potential deposition (UDP) of copper and of Fe^{3+}/Fe^{2+} [28,30].

Figure 4.2A-C shows the cyclic voltammograms of (i) bare gold electrode, (ii) Au-ME SAM and (iii) Au-ME-MTCAPc SAM (M = Co, Fe and Mn). In general, the SAM modified gold electrode is known for limiting or blocking access of solution molecules to the gold surface. This blocking behaviour occurs because the hydrocarbon layer inserted between the electrode and electrolyte ions form an insulating layer, thus leading to the reduction of charging current [28,30]. However, as can be noticed in Figure 4.2 there was no noticeable reduction in charging current and the opposite, i.e. increase in charging or background current for Au-ME SAM and Au-ME-MTCAPc SAM, was observed. This increase in charging current upon modifying gold electrode with SAMs is known [28,30] to be affected by the terminal functional groups on SAMs following this trend: $-CH_3$ < -OH < -COOH and also different chain lengths are known to affects the properties of SAMs on gold electrode, for example short alkane chain SAMs behave

differently from the long alkane chain SAMs [28]. In this work, the increase in background current is observed for Au-ME-SAM and Au-ME-MTCAPc SAM and this is because of the exposed terminal functional groups, i.e. -OH for Au-ME SAM and -COOH for Au-ME-MTCAPc SAM. Therefore, the increase in background currents in Figure 4.2A-C(ii) and (iii) is due to the fact that Au-ME SAM is a short alkane chain thiol SAM and the fact that –OH (for Au-ME SAM) and –COOH (for Au-ME-MTCAPc SAM) terminal functional groups are by nature quasi-liquids, i.e. hydrophilic groups. From this observation one can conclude that the SAMs terminated with either -OH or -COOH are permeable to solution ions thus leading to surface gold reactions still taking place even at SAM modified gold surfaces. There was no peak observed for Au-ME SAM in Figure 4.2A-C(ii) nor for Au-ME-FeTCAPc SAM in Figure 4.2B(iii). For Au-ME-CoTCAPc SAM in Figure 4.2A(iii) a reduction peak (at 450 mV vs Ag|AgCl) was observed and this peak has been reported for adsorbed CoPc derivatives and it corresponds to the metal oxidation ($Co^{III}Pc/Co^{II}Pc$) [113,195]. Also for Au-ME-MnTCAPc SAM in Figure 4.2C(iii) a broad oxidation peak (at ~0.40 V vs Ag|AgCl) was observed and is at similar potential range as the peak assigned to metal oxidation ($Mn^{IV}Pc/Mn^{III}Pc$) known for MnPc derivatives [178,196], Table 3.1.

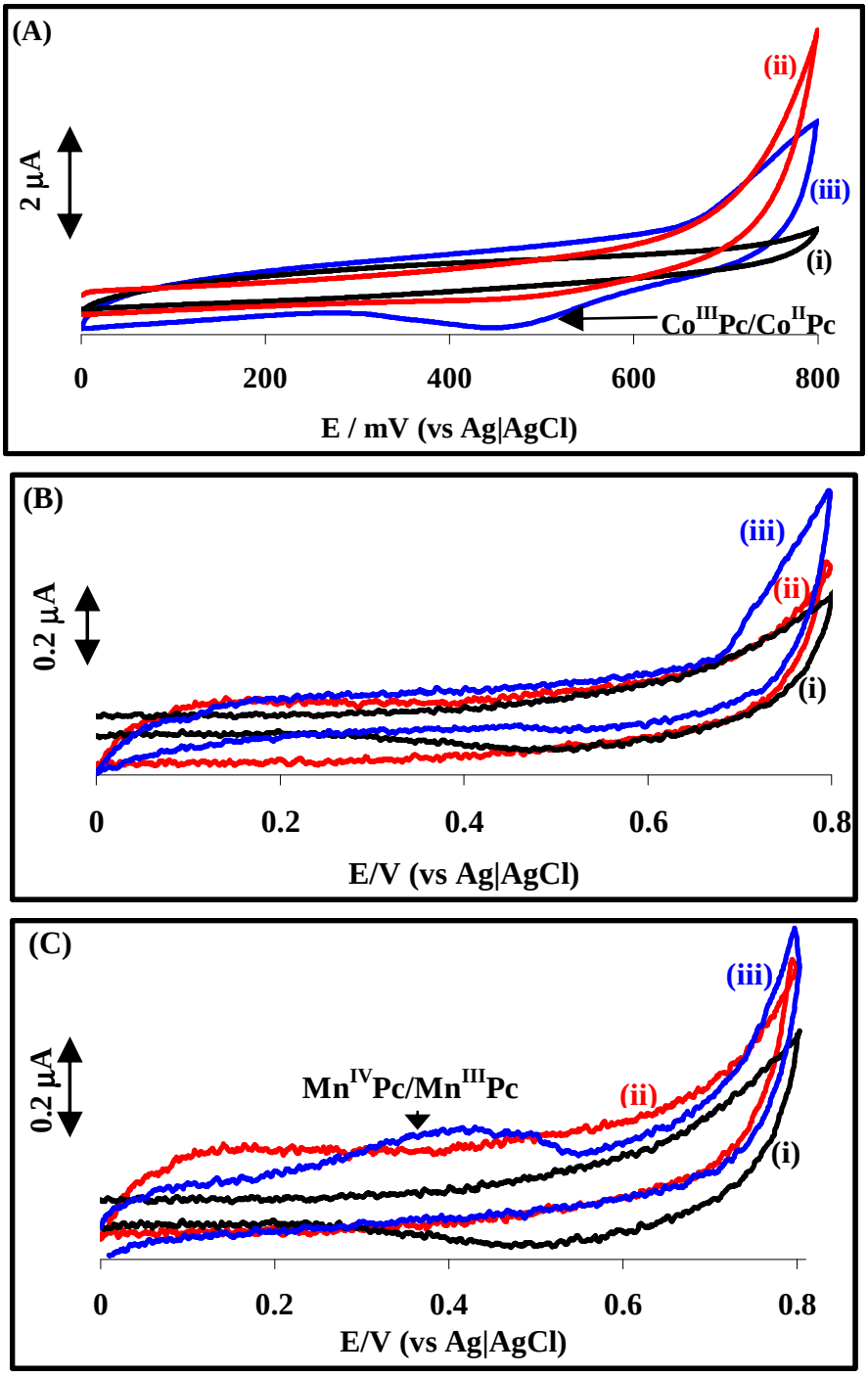

Figure 4.2: Cyclic voltammograms of (A-C)(i) bare, (A-C)(ii) Au-ME SAM and (A)(iii) Au-ME-CoTCAPc SAM, (B)(iii) Au-ME-FeTCAPc SAM and (C)(iii) Au-ME-MnTCAPc SAM in pH 4.0 buffer solution. Scan rate = 50 mV/s.

The influence of solution pH on the electrochemical behavior of the reduction peak for the redox process of Au-ME-CoTCAPc SAM, i.e. $Co^{III}Pc/Co^{II}Pc$ was studied, Figure 4.3. The cyclic voltammogram in Figure 4.3 shows the reduction peak of Au-ME-CoTCAPc SAM in different pH solutions ranging from pH 4 to pH 9. At pH lower than pH 4 the reduction peak was not observed and at concentrated alkaline pH solutions (> 9) were not studied as SAMs desorb in such solution conditions and this desorption of SAMs also depend on the potential window used [23,56]. Hence the use of small potential window for low concentrations (0.01 M KOH) solution discussed later. A peak potential shift to less positive values with an increase in pH was observed in Figure 4.3. A linear plot in Figure 4.3(inset) gave the slope of -0.053 V/pH, and this value is close enough to the theoretical value (-0.059 V/pH) suggesting the participation of approximately one proton in the one electron transfer reaction. Similar values of slopes for the plot of potential versus pH have been reported in literature for different phthalocyanine complexes with cobalt as a metal center [197-199]. The potential shift of the $Co^{III}Pc/Co^{II}Pc$ redox process to the less positive values with the increasing pH may be due to axial coordination of the hydroxyl ion to the $Co^{III}Pc$ as suggested before [200]. Other phthalocyanine SAMs (Au-ME-FeTCAPc SAM and Au-ME-MnTCAPc SAM) were not studied as their metal redox processes were too broad or not observed in pH solutions as shown in Figure 4.2.

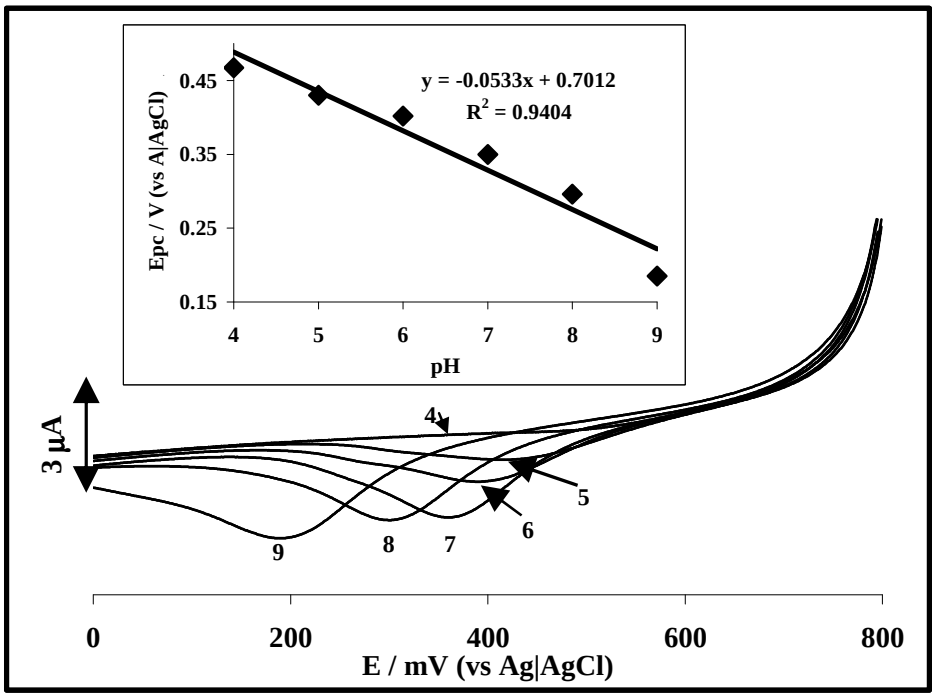

Figure 4.3: Cyclic voltammetric (showing only the reverse scan) response of Au-ME-CoTCAPc SAM with the changes in pH (pH 4, 5, 6, 7, 8 and 9, shown as numbers on the peaks). The inset shows the plot of the changes in peak potential with pH.

Figure 4.4 shows cyclic voltammograms of (i) bare gold electrode and (ii) Au-ME-CoTCAPc SAM in 0.01 mol.L^{-1} KOH electrolyte solution. A well-resolved redox couple was observed at a negative potentials with E_{pc} at -395 mV (vs Ag|AgCl) and E_{pa} = -320 mV (vs Ag|AgCl) and this redox peaks are at the potential ranges known [195,113] for metal reduction of CoPc complexes, therefore this couple corresponds to $Co^{II}Pc/Co^{I}Pc$. The differences observed for different surface modifications as well as the presence (in some cases) of the redox couples of the surface-confined electroactive species confirms that the gold surface properties changes upon modification with SAMs.

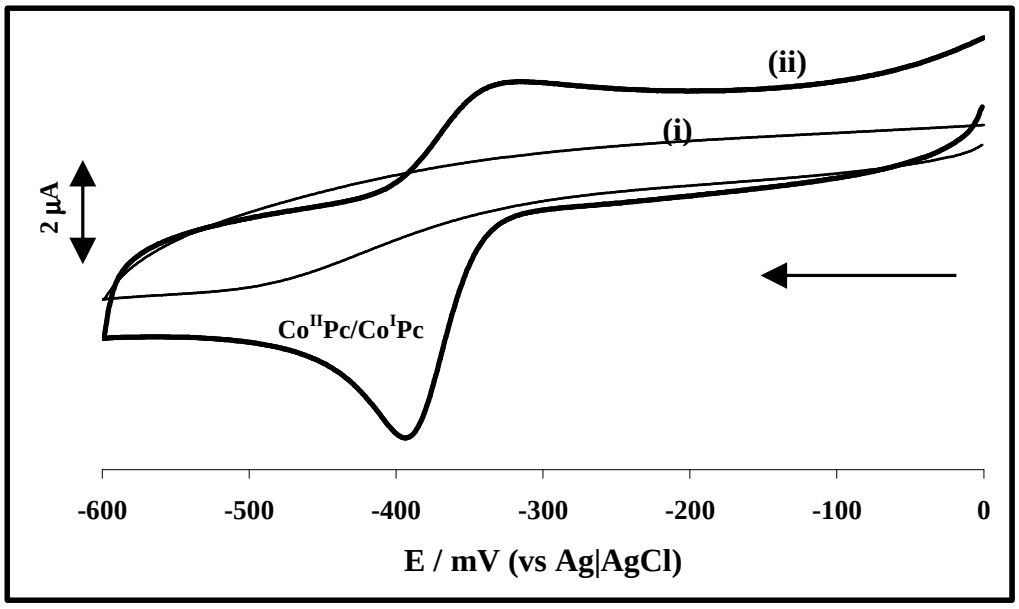

Figure 4.4: Cyclic voltammograms of (i) bare gold electrode and (ii) Au-ME-CoTCAPc SAM modified gold electrode in 0.01 mol.L^{-1} KOH solution showing $Co^{II}Pc/Co^{I}Pc$ redox process. Scan rate = 50 mV/s.

Figure 4.5 shows a CVs of (i) bare, (ii) Au-ME SAM and A(iii) Au-ME-CoTCAPc SAM, B(iii) Au-ME-FeTCAPc SAM and C(iii) Au-ME-MnTCAPc SAM in $[Fe(CN)_6]^{3-}$ solution. An oxidation and reduction peaks at bare gold electrode were observed and these peaks correspond to the reversible behaving of the $[Fe(CN)_6]^{3-}/[Fe(CN)_6]^{4-}$ redox couple. This redox couple was also observed at SAM modified gold electrodes. The MPc SAM modified gold electrodes have carboxylic acid groups which are in acidic form (-COOH) at low pH and basic form ($-COO^-$) at neutral to high pH. At pH 7.5, which is the pH of the $K_3Fe(CN)_6$ in KCl solution, the carboxylic acid terminal groups of MPc modified electrode are in basic form ($-COO^-$). The basic form of carboxylic groups should repel the negatively charged $[Fe(CN)_6]^{3-}/[Fe(CN)_6]^{4-}$ species, hence the redox couple should not be observed. But from the voltammograms in Figure 4(A-C)(iii), this redox couple is still observed even at MPc SAM modified gold electrode and this phenomenon

has been observed for MPc modified electrodes [201] to be due to electronic conducting properties of these modified electrode, thus allowing rapid electron transfer to the solution to take place. The peak-to-peak potential separation (ΔE_p) of the bare and modified gold electrodes increased following this trend: 81 mV < 82 mV < 96 mV for bare gold, Au-ME-FeTCAPc SAM and Au-ME SAM, respectively. From this trend, one can clearly notice that modifying gold electrode with SAMs in particular MPc SAM, resulted in a slight increase in ΔE_p. This increase is due to slight electron transfer barrier by the SAM on gold surface. Also it is worth stating that the ΔE_p at bare gold electrode should ideally be between 60 and 70 mV for $[Fe(CN)_6]^{3-}$/ $[Fe(CN)_6]^{4-}$ highly reversible, one-electron system. The ΔE_p value found in this work is 81 mV, which is slightly higher than the expected value (between 60 and 70 mV), but it is within the allowed range for one-electron reversible $[Fe(CN)_6]^{3-}/[Fe(CN)_6]^{4-}$ system. The presence of the redox couple even after the electrode has been modified with SAMs could be attributed to the catalytic or electronic conducting properties of these SAMs and this was also evidenced by an increase in current densities as observed in Figure 4.5(A-C)(ii) and (iii). These results are not surprising as modified electrodes have been reported [201] not to inhibit the $[Fe(CN)_6]^{3-}$ /$[Fe(CN)_6]^{4-}$ redox couple. Also since the $[Fe(CN)_6]^{3-}/[Fe(CN)_6]^{4-}$ system is a fast electron transfer species, mass transport determines the rate determining step even at small over potential. Similar results were also observed for other complexes investigated in this work, Au-ME-CoTCAPc SAM (Figure 4.5(B), ΔE_p = 96 mV) and Au-ME-MnTCAPc SAM (Figure 4.5(C), ΔE_p = 87 mV). Since the fast electron $Fe(CN)_6$ system gave these results, the slow electron system such as ferric ammonium sulfate solution $\{Fe(NH_4)(SO_4)_2\}$ was also studied instead of $[Fe(CN)_6]^{3-}$.

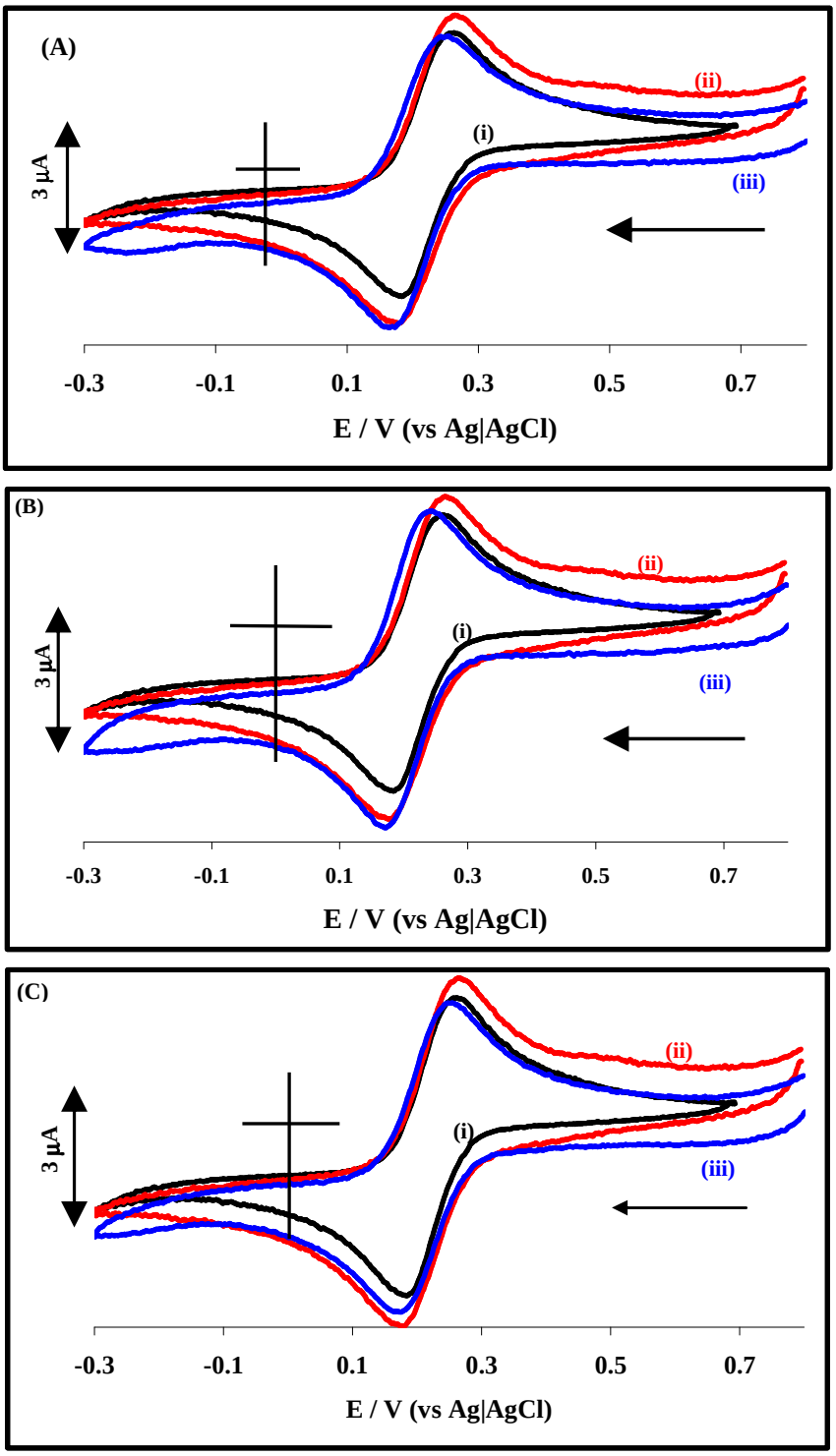

Figure 4.5: Cyclic voltammograms for (i) bare gold, (ii) Au-ME-SAM and A(iii) Au-ME-CoTCAPc SAM, B(iii) Au-ME-FeTCAPc SAM and C(iii) Au-ME-MnTCAPc SAM in 1 x 10^{-3} mol.L^{-1} $K_3Fe(CN)_6$ of 0.1 mol.L^{-1} KCl solution (pH 7.5). Scan rate = 50 mV/s.

Figure 4.6 shows the CVs of (i) bare, (ii) Au-ME SAM, (A)(iii) Au-ME-CoTCAPc SAM, (B)(iii) Au-ME-FeTCAPc SAM and (C)(iii) Au-ME-MnTCAPc SAM modified electrode in $Fe(NH_4)(SO_4)_2$ solution. The redox couple $[Fe(H_2O)_6]^{3+}/[Fe(H_2O)_6]^{2+}$ observed at $E_{1/2}$ = 0.47 V (vs Ag|AgCl) in Figure 4.6(i) is a known [23,57,56,202] reversible behaviour of $Fe(NH_4)(SO_4)_2$ solution at bare gold electrode. At the modified gold electrodes the oxidation peak disappeared and the decrease in current density was observed. The disappearance of the oxidation peak is due to the fact that the modified electrode is (to some extent) exhibiting slow kinetics towards $[Fe(H_2O)_6]^{3+}/[Fe(H_2O)_6]^{2+}$ redox species. These results indicate that electrode kinetics of the Fe^{II} oxidation reaction to Fe^{III} at Au-ME SAM and Au-ME-FeTCAPc SAM exhibits slow kinetic mechanism leading to the irreversible nature of the redox couple $[Fe(H_2O)_6]^{3+}/[Fe(H_2O)_6]^{2+}$ as shown in Figure 4.6(A-B)(ii) and (iii). This irreversible nature at modified electrode confirms the modification of gold electrode with different SAMs. It is also worth stating that the $Fe(NH_4)(SO_4)_2$ has positively charged redox couple, $[Fe(H_2O)_6]^{3+}/[Fe(H_2O)_6]^{2+}$, while the $K_3Fe(CN)_6$ solution has negatively charged redox couple, $[Fe(CN)_6]^{3-}/[Fe(CN)_6]^{4-}$. Therefore, these solutions have different chemistry and redox behaviour hence the difference in charge transfer abilities as observed in Figure 4.5 and Figure 4.6. The slow kinetics at modified gold electrodes contributed to the observed shift in peak potentials of the $[Fe(H_2O)_6]^{3+}/[Fe(H_2O)_6]^{2+}$ redox couple in the voltammograms, Figure 4.6(A-C)(ii) and (iii). The fact that the reduction peaks at E_{pc} (vs Ag|AgCl, 3.0 mol.L^{-1} NaCl) = 0.35 V in Figure 4.6(A-C)(ii) for Au-ME SAM and at ~0.40 V in Figure 4.6(A-C)(iii) for Au-ME-MTCAPc SAM can still be observed at modified gold electrodes could be attributed to the Fe^{III} ion being more permeable than the Fe^{II} ion. This was not expected as the reduced Fe^{II} ions should be more permeable because of the low charge. The observed permeability of the SAMs modified electrode is due to hydrophilic

properties of the SAMs functional groups (–OH for Au-ME SAM and –COOH for Au-ME-MTCAPc SAMs) which allow solution ions to penetrate though the SAM.

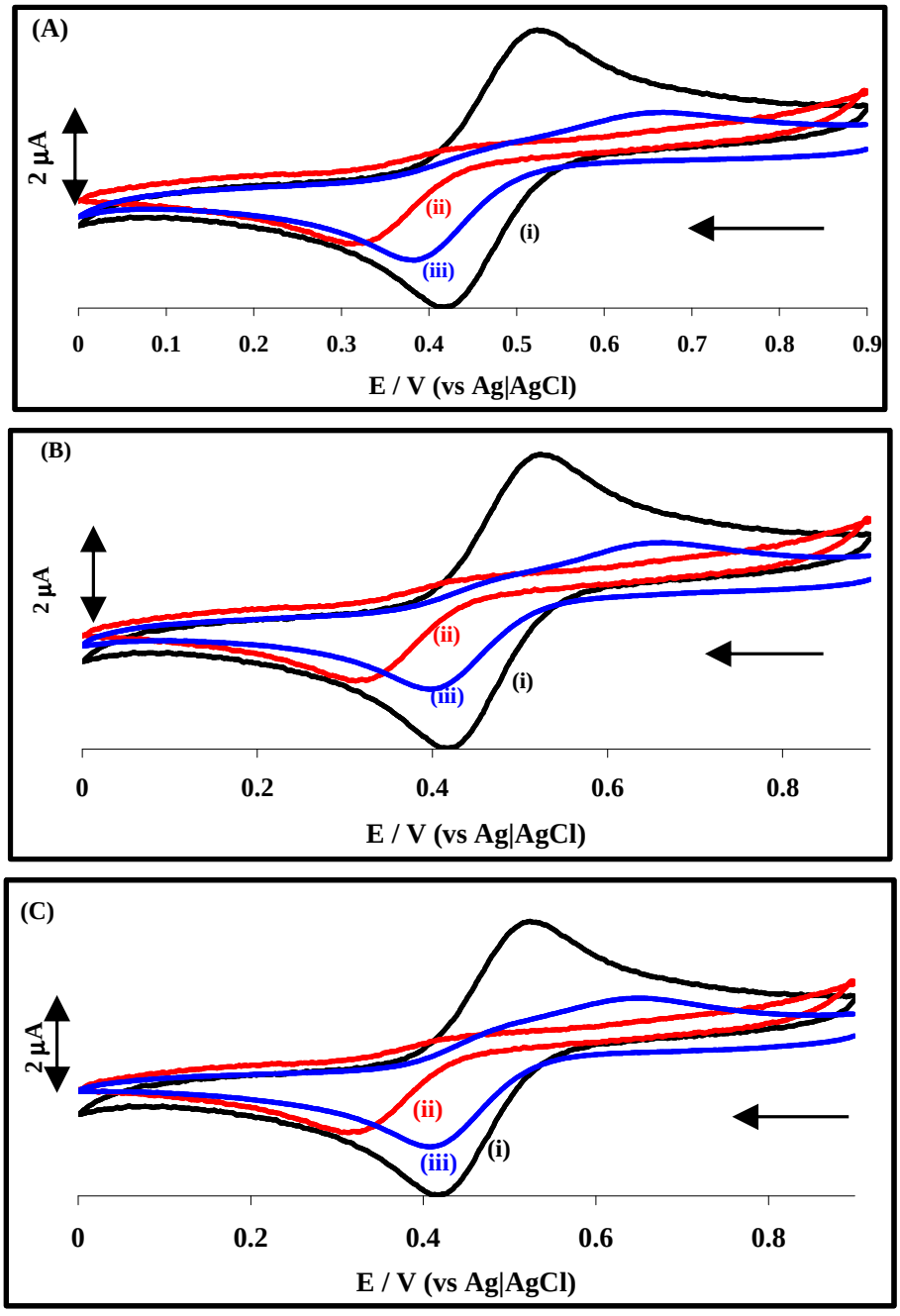

Figure 4.6: Cyclic voltammograms for A-C(i) bare gold, (ii) Au-ME-SAM and A(iii) Au-ME-CoTCAPc SAM, B(iii) Au-ME-FeTCAPc SAM or C(iii) Au-ME-MnTCAPc SAM in 1 x 10^{-3} mol.L^{-1} $Fe(NH_4)(SO_4)_2$ of 1.0 x 10^{-3} mol.L^{-1} $HClO_4$ solution. Scan rate = 50 mV/s.

The deposition of copper metal (Cu) involves the under-potential deposition (UDP) at potentials close or well-positive of the thermodynamic potential [28]. Figure 4.7 shows the cyclic voltammograms of (i) bare gold, (ii) Au-ME SAM and A(iii) Au-ME-CoTCAPc SAM, B(iii) Au-ME-FeTCAPc SAM or C(iii) Au-ME-MnTCAPc SAM. Figure 4.6(i) clearly shows the deposition peak at E_p = -80 mV during the negative going scan and this peak is attributed to Cu^{II}/Cu^0 reduction [28]. The return scan shows a large oxidation peak at E_p = 20 mV and this peak corresponds to the stripping of a copper metallic layer from gold electrode surface. The CV show similarities to the reported work [23,24,28,57] even though the peaks were at different peak potentials and this is due to different reference electrodes used. These peaks disappeared upon modifying the electrode with SAMs as shown in Figure 4.7A-C(ii) and (iii). The broad redox couple in Figure 4.7A-C(ii) was observed for Au-ME SAM and this peak could be attributed to Cu^{II}/Cu^{I} redox behaviour at the hydroxyl functional group. This peak was also observed at bare gold electrode but was enhanced at modified gold electrode, possibly due to the catalytic properties of Au-ME SAM. At Au-ME-MTCAPc SAM in Figure 4.7A-C(iii) the gold reaction peaks, i.e. Cu deposition and stripping peaks, disappeared and also the redox couple on Au-ME SAM disappeared. This experiment then indicates that different SAMs inhibit gold reactions, i.e. the deposition and stripping of metallic Cu, confirming the formation of SAMs on gold electrode.

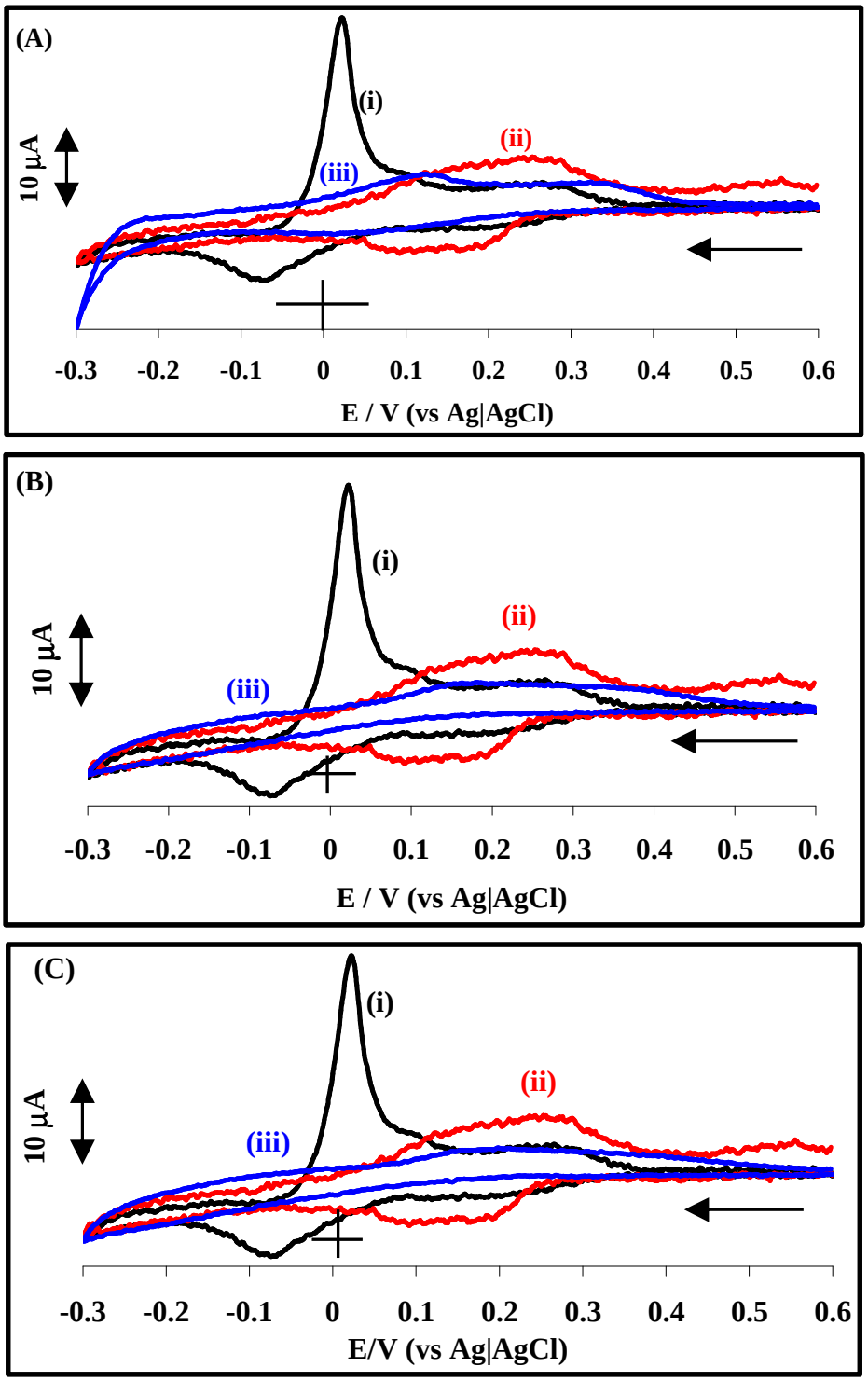

Figure 4.7: Cyclic voltammogram for (i) bare gold, (ii) Au-ME SAM and A(iii) Au-ME-CoTCAPc SAM, B(iii) Au-ME-FeTCAPc SAM or C(iii) Au-ME-MnTCAPc SAM in 1 x 10^{-3} mol.L^{-1} $CuSO_4$ of 0.5 mol.L^{-1} H_2SO_4. Scan rate = 50 mV/s.

The inhibition of gold reactions and surface properties of SAM modified gold electrodes were investigated using aqueous alkaline KOH solution. At bare gold electrode, high positive potentials (+1.5 V vs Ag|AgCl) are normally employed [175,203] to bring about the oxidation of gold at the pinholes even in the presence of SAMs. However, at high positive potentials SAMs can also undergo oxidative desorption [203] and the observed peak may be confused with the oxidation of gold electrode. Therefore, a low positive potential window where gold can undergo oxidation without affecting the SAM would be desirable. Ozoemena *et. al*. [23,56] reported the use of aqueous alkaline solution (0.01 mol.L^{-1} KOH) at a smaller potential window between -0.2 and +0.6 V (vs Ag|AgCl), clearly showing the redox couple corresponding to gold oxide formation and stripping. This aqueous alkaline solution was employed in this work to investigate the integrity of SAMs on gold surface. Figure 4.8 shows cyclic voltammograms of (i) bare gold, (ii) Au-ME SAM and A(iii) Au-ME-CoTCAPc SAM, B(iii) Au-ME-FeTCAPc SAM or C(iii) Au-ME-MnTCAPc SAM in 0.01 mol.L^{-1} KOH solution. Two peaks were observed for bare and SAM modified gold surfaces. However, in comparison to bare gold in Figure 4.8A-C(i), the oxidation and reduction peaks are less pronounced for the Au-ME SAM in Figure 4.8A-C(ii), but in same potential range as for bare gold. For Au-ME-MTCAPc SAM the oxidation peak shifts to more positive potentials. These observations at modified gold electrode suggest a slow electron transfer kinetics in the presence of Au-ME SAM in Figure 4.8A-C(ii) and Au-ME-MTCAPc SAM in Figure 4.8A-C(iii). Also the observed gold reactions even on SAM modified electrodes in aqueous alkaline solution is due to the fact that these SAMs are permeable to solution ions. This observation may be explained by the hydrophilic nature of these SAMs leading to observed gold surface reactions still taking place. These observations were also noticed in literature [24] where the gold reactions were still observed even after the formation of MPc-SAM.

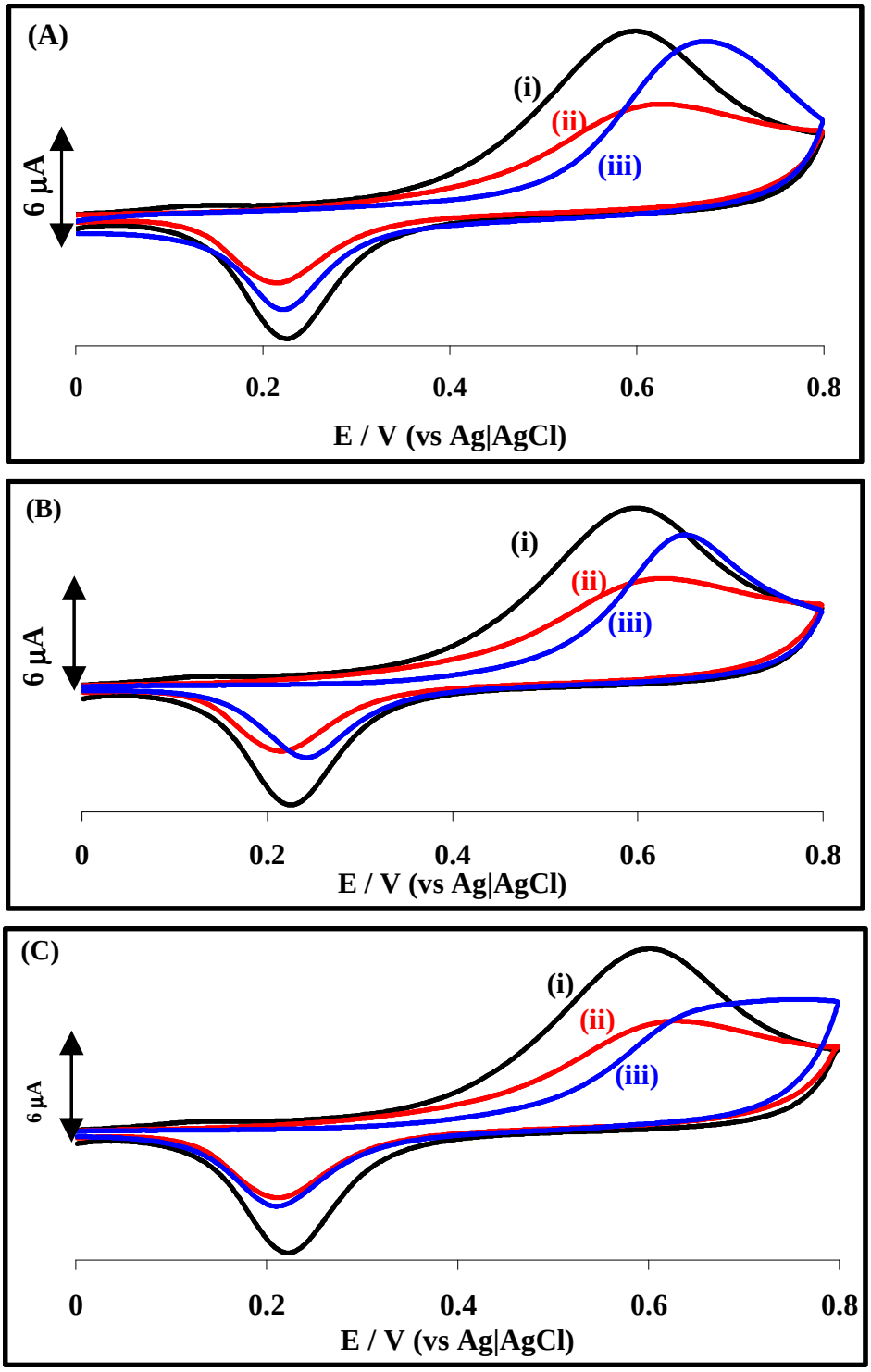

Figure 4.8: Cyclic voltammograms for A-C(i) bare gold, (ii) Au-ME SAM and A(iii) Au-ME-CoTCAPc SAM, B(iii) Au-ME-FeTCAPc SAM and C(iii) Au-ME-MnTCAPc SAM in 0.01 mol.L^{-1} KOH solution. Scan rate = 50 mV/s.

The surface concentrations (Γ_{SAM} / mol.cm^{-2}) of the surface-confined redox-active SAMs on gold electrode can be estimated using either reductive desorption method [28-30,61-63] or the metal (M^{III}/M^{II}) redox couple [28-30]. Since the metal redox couple are weak or sometimes not observed in this work, the reductive desorption method was used for the calculation of SAMs surface coverages. SAMs are known [28-30,61-63] to reductively desorb from gold electrode surface in alkaline solution following the equation 4.2 (introduced in chapter 1):

$$Au\text{-}SR + e^- \longrightarrow Au + RS^- \qquad (4.2)$$

The surface concentration (Γ_{SAM}/ mol.cm^{-2}) was then calculated from the estimated charge (Q) under the reductive desorption peak using the theoretical relationship in accordance to equation 4.3 (also introduced in chapter 1):

$$\Gamma_{SAM} = \frac{Q}{nFA} \qquad (4.3)$$

where n = 1 represents the number of electrons involved in the desorption of thiol, F is the Faraday constant (96485 C mol^{-1}) and A is the surface area of the gold electrode. The geometric surface area (0.0201 cm^2) and the real surface area (0.0335 cm^2) of gold electrodes were used for the calculation of surface concentration. For comparison with surface coverages reported in literature the geometric surface area was used. Reductive desorption experiments for SAMs were performed in 0.2 mol.L^{-1} KOH solution. Figure 4.9 shows typical cyclic voltammograms for reductive desorption obtained for gold electrodes modified with SAMs of (i) Au-ME SAM, (ii) Au-ME-CoTCAPc SAM, (iii) Au-ME-FeTCAPc SAM, (iv) Au-ME-MnTCAPc SAM and (v) bare in 0.2 mol.L^{-1} KOH solution scanning from -0.2 to -1.0 V (vs Ag|AgCl). The CV for the bare gold electrode in Figure 4.9(v) clearly shows no peak as there is nothing on the surface.

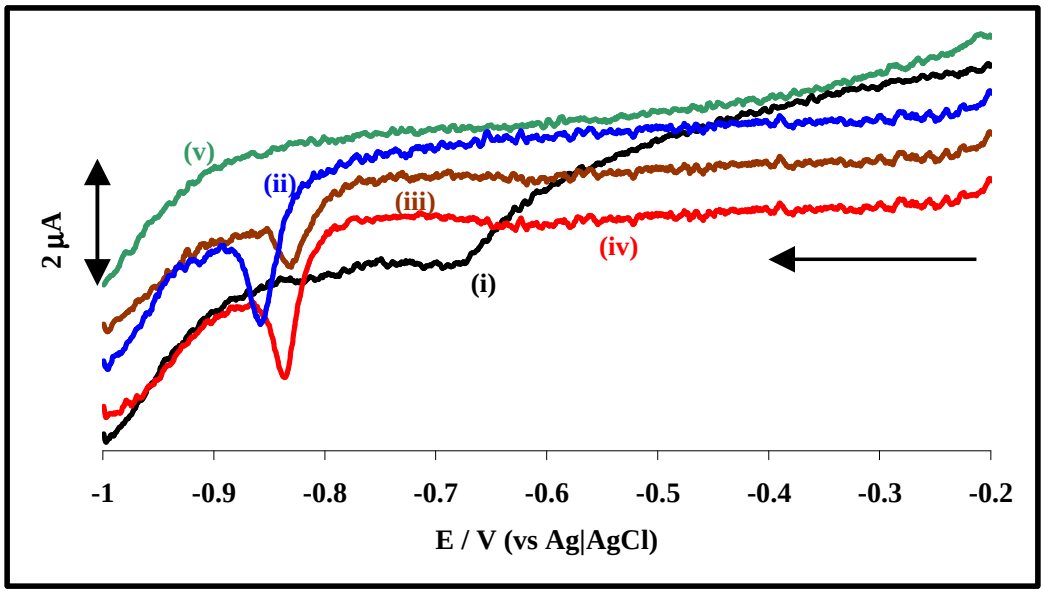

Figure 4.9: Cyclic voltammograms of (i) Au-ME SAM, (ii) Au-ME-CoTCAPc SAM, (iii) Au-ME-FeTCAPc SAM, (iv) Au-ME-MnTCAPc SAM and (v) bare in 0.2 mol.L^{-1} KOH solution. Scan rate = 100 mV/s.

From the CVs in Figure 4.9 it is discernible that the studied SAMs desorb from gold surface. The desorption peaks are observed at different potentials and the peak potentials shift upon the formation of Au-ME-MTCAPc SAM to more negative potentials. The reductive desorption peaks for Au-ME SAM was observed at -0.7 V (vs Ag|AgCl). The potentials for reductive desorption peaks of Au-ME-MTCAPc SAMs were different at each surface, they were -0.83 V, -0.84 V and -0.86 V for Au-ME-FeTCAPc SAM, Au-ME-MnTCAPc SAM and Au-ME-CoTCAPc SAM, respectively. The shift of the desorption peaks, from -0.7 V for Au-ME SAM to more negative potentials for Au-ME-MTCAPc SAM, indicates that the coupling of MTCAPcs on Au-ME SAM stabilizes the SAMs, thus higher negative potentials need to be applied for SAM desorption. From the charge under the desorption peak, the surface coverage (Γ_{SAM}) using the geometric surface area was estimated for the Au-ME SAM (6.45 x 10^{-10} mol.cm^{-2}), Au-ME-MnTCAPc SAM (4.56 x 10^{-10} mol.cm^{-2}), Au-ME-FeTCAPc SAM (2.41 x 10^{-}

^{10} mol.cm^{-2}) and Au-ME-CoTCAPc SAM (4.38 x 10^{-10} mol.cm^{-2}). The surface concentration for Au-ME SAM is similar to reported values for mercaptoethanol or alkanethiol SAM modified gold electrodes [204-206]. The surface concentrations for MTCAClPc SAMs were higher than the reported surface coverage value (1 x 10^{-10} mol.cm^{-2}) for the MPc SAMs lying flat on the gold surface [22,195]. Therefore, the orientation of the studied MTCAPc complexes (Au-ME-MTCAPc SAM) is perpendicular on gold electrode. This is not strange because it is expected that Au-ME SAM and MTCAClPc (before hydrolysis to MTCAPc) connection is obtained via one substituent from the MTCAClPc complex. Since the real surface area (0.0335 cm^2) of the electrode is larger than its geometric (0.0201 cm^2) area, the surface concentration using the geometric surface area sets the upper limits for the surface concentration. The surface concentrations using real surface area for gold were also estimated for Au-ME SAM (3.87 x 10^{-10} mol.cm^{-2}), Au-ME-MnTCAPc SAM (2.74 x 10^{-10} mol.cm^{-2}), Au-ME-FeTCAPc SAM (1.44 x 10^{-10} mol.cm^{-2}) and Au-ME-CoTCAPc SAM (2.63 x 10^{-10} mol.cm^{-2}). Table 4.1 gives the summary of the results for the surface coverage estimation at different surface areas, i.e. geometric and real surface area.

Table 4.1: Comparative peak potentials (E_p), electrical charge (Q) and surface coverages of SAM (Γ_{SAM}) modified gold electrodes using geometric surface area (0.0201 cm^2) and real surface area (0.0335 cm^2).

SAM Electrode	E_p / V (vs Ag|AgCl)	Q (10^{-7} C.mol^{-1})	Γ_{SAM} (x 10^{-10} mol.cm^{-2}) A = 0.0201 cm^{-2}	Γ_{SAM} (x 10^{-10} mol.cm^{-2}) A = 0.0335 cm^{-2}
ME SAM	-0.70	12.5	6.45	3.87
CoTCAPc SAM	-0.86	8.50	4.38	2.63
FeTCAPc SAM	-0.83	4.67	2.41	1.44
MnTCAPc SAM	-0.84	8.85	5.56	2.74

4.2.4 Electrochemical characterization of glucose oxidase enzyme modified electrode

Cobalt phthalocyanine complexes have been reported [117-123] for their efficiency as redox mediators for enzyme based reaction and have also been found to be biocompatible with enzymes, in particular glucose oxidase enzyme [117-123]. This work then further explores the possible use of Au-ME-CoTCAPc SAM for possible fabrication of glucose biosensor by covalently immobilizing glucose oxidase onto cobalt phthalocyanine acid activated SAM as shown in Scheme 4.3, this enzyme modified electrode has been represented as Au-ME-CoTCAPc-GOx SAM electrode. The electrochemical characterization of GOx enzyme electrodes were performed using cyclic voltammetric experiments in the presence of $K_3Fe(CN)_6$ (5.0×10^{-3} $mol.L^{-1}$) in phosphate buffer saline (0.01 $mol.L^{-1}$ PBS, pH 7.4) solution. Figure 4.10A shows typical cyclic voltammograms with redox peaks due to $[Fe(CN)_6^{3-}]/[Fe(CN)_6^{4-}]$ with $E_{1/2}$ values (mV vs Ag|AgCl) for (i) bare gold ($E_{1/2}$ ~=100 mV), (ii) Au-ME SAM ($E_{1/2}$ ~= 112 mV), (iii) Au-ME-CoTCAPc SAM ($E_{1/2}$ = 125 mV) and (iv) Au-ME-CoTCAPc-GOx SAM ($E_{1/2}$ = 145 mV). Figure 4.10B shows a cyclic voltammogram of Au-ME-CoTCAPc SAM during conditioning in 5 mM $K_3Fe(CN)_6$ (0.01 M PBS, pH 7.4) solution, (i) first scan and (ii) sixth scan.

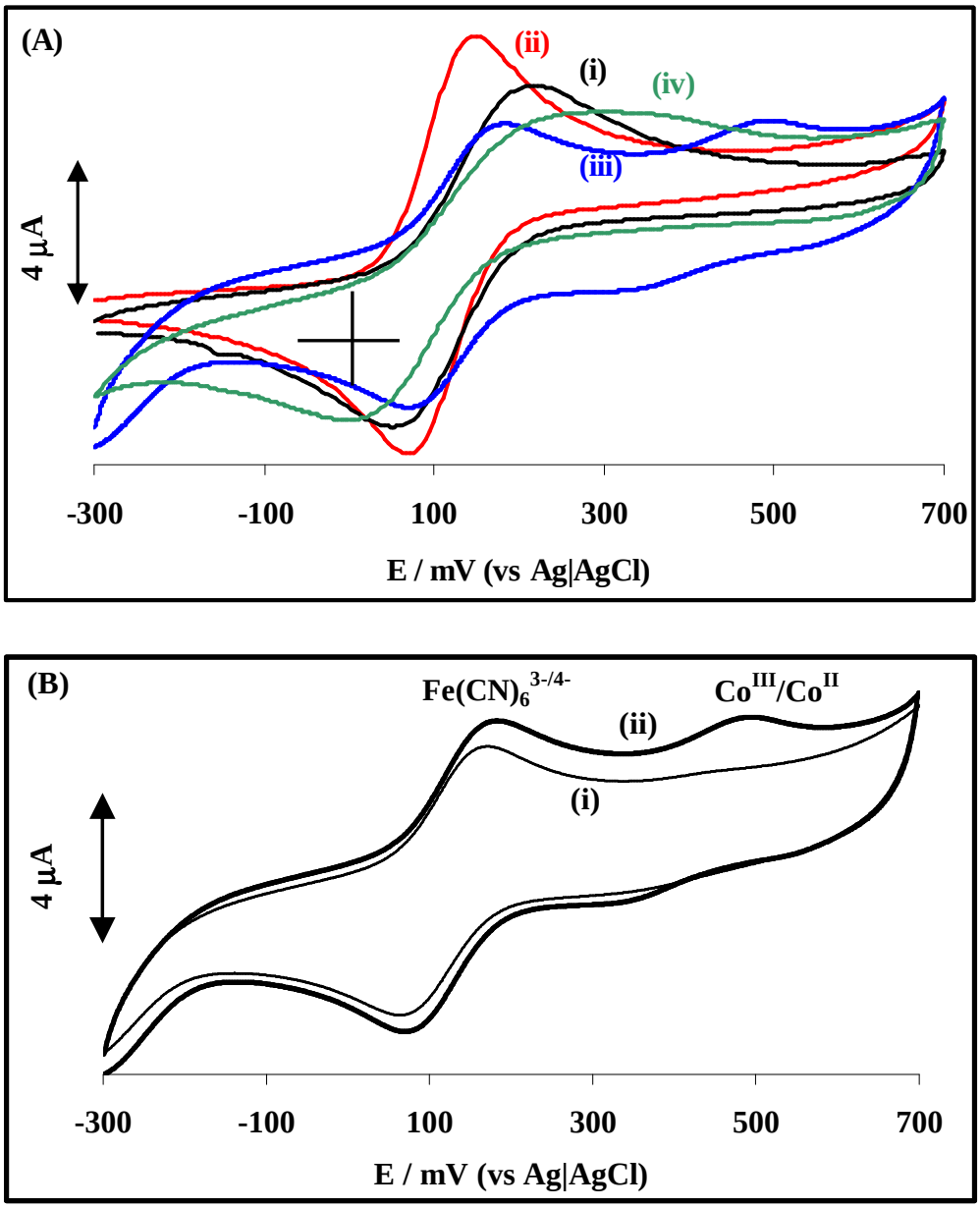

Figure 4.10: Cyclic voltammograms of A: (i) bare gold, (ii) Au-ME SAM, (iii) Au-ME-CoTCAPc SAM and (iv) Au-ME-CoTCAPc-GOx SAM. B: Continuous cycling of Au-ME-CoTCAPc SAM, (i) first cycle and (ii) sixth cycle. $K_3Fe(CN_6)$ (5.0 x 10^{-3} mol.L^{-1}) in 0.01 mol.L^{-1} PBS (pH 7.4) solution at scan rate = 25 mV/s.

The redox couple due to $Co^{III}Pc/Co^{II}Pc$ in Figure 4.10A(iii) and in Figure 4.10B(ii) was observed at $E_{1/2}$ = 400 mV for Au-ME-CoTCAPc SAM and it disappeared after the immobilization of GOx enzyme in Figure 4.10A(iv). The disappearance of the redox couple ($Co^{III}Pc/Co^{II}Pc$) could be attributed to the CoTCAPc SAM embedded under the enzyme layer. The cyclic voltammograms in Figure 4.10A clearly shows the redox peak at ~100 mV due to $[Fe(CN)_6^{3-}]/[Fe(CN)_6^{4-}]$ even after the electrode was coated at with (ii) Au-ME SAM, (iii) Au-ME-CoTCAPc SAM and (iv)Au-ME-CoTCAPc-GOx SAM. A decrease in peak-to-peak potential separation (ΔE_p) upon modifying gold electrode with Au-ME SAM and Au-ME-CoTCAPc SAM was observed compared to the bare electrode. The peak-to-peak potential separation increased upon modifying gold electrode with GOx enzyme following this trend: Au-ME-CoTCAPc-GOx SAM > Au > Au-ME-CoTCAPc SAM> Au-ME SAM, and the ΔE_p values (289 > 166 > 124 > 84) mV, respectively. The fact that $[Fe(CN)_6^{3-}]/[Fe(CN)_6^{4-}]$ peak is observed on modified gold electrode could be attributed to the fact that $[Fe(CN)_6^{3-}]/[Fe(CN)_6^{4-}]$ is a fast electron transfer species, also that the SAM formed is not pinhole free, i.e. solution ion can still penetrate through the SAM to the surface of gold electrode thus allowing the reaction to occur on gold electrode. The decrease in peak potential separation (ΔE_p) on Au-ME-CoTCAPc SAM and Au-ME SAM shows that the surface is catalytic as discussed above. Figure 4.10B shows a cyclic voltammograms for Au-ME-CoTCAPc SAM on conditioning and redox peaks gradually grew with the cycle number and stabilized after the sixth cycle. It was interesting to notice that this behavior was also observed in literature [159] and has been attributed to the conducting film being formed on the surface of the electrode.

4.2.5 Impedance spectroscopic characterization of SAM modified gold electrodes

Electrochemical impedance spectroscopy has received considerable attention as a surface characterization technique [39,207-212] of SAM modified gold electrodes. The impedance measurements in the presence of the redox probes, like $[Fe(CN)_6^{3-}]/[Fe(CN)_6^{4-}]$, may be used to study the conducting and permeability properties of SAMs and also measure the defectiveness associated with the surface coverage behaviour of SAMs. The redox probing species $[Fe(CN)_6^{3-}]$ $/[Fe(CN)_6^{4-}]$ is known to react at the pinholes / defects [39] within the SAM. The form of a Bode plot used in this work is a plot of phase angle versus log frequency, i.e. $-\Theta$ vs log f. The impedance measurements were done in $K_4Fe(CN)_6$ /$K_3Fe(CN)_6$ solution which was used as a redox probe for studying the electron transfer properties of SAMs. Figure 4.11 shows the Nyquist plot of (i) bare gold, (ii) Au-ME SAM and A(iii) Au-ME-CoTCAPc SAM, B(iii) Au-ME-FeTCAPc SAM and C(iii) Au-ME-MnTCAPc SAM in (1:1) mixture of $K_4Fe(CN)_6/K_3Fe(CN)_6$ in 0.1 KCl solution.

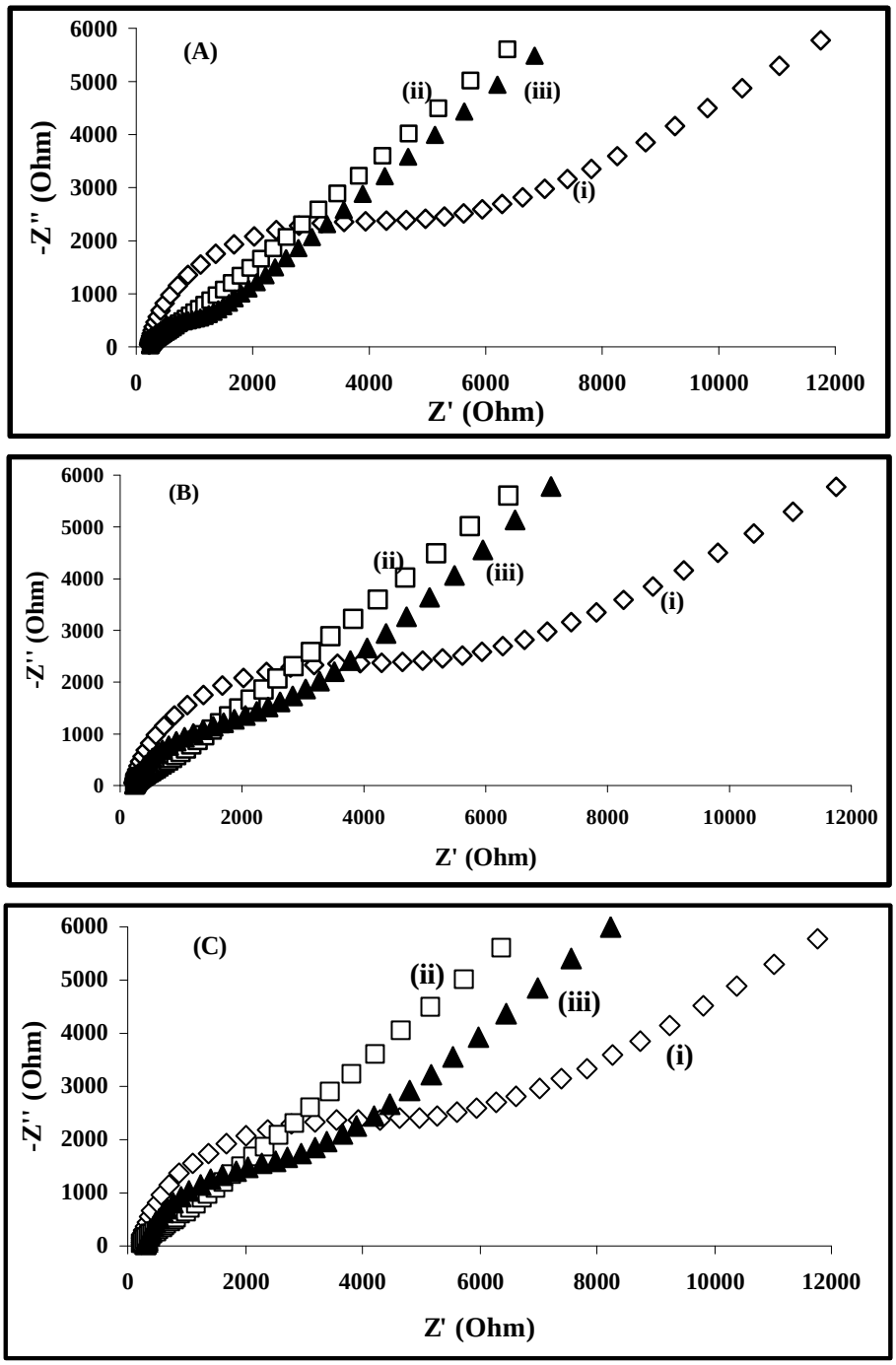

Figure 4.11: Nyquist plot (-Z" vs Z') obtained for impedance measurements in $Fe(CN)_6^{3-/4-}$ (1:1) mixture in 0.1 mol.L^{-1} KCl solution for (i) bare gold, (ii)Au-ME SAM and A(iii) Au-ME-CoTCAPc SAM, B(iii) Au-ME-FeTCAPc SAM and (C)(iii) Au-ME-MnTCAPc SAM. Applied potential = 150 mV.

The Nyquist plot is divided into two frequency regions, the kinetically controlled (high frequency) region where the semi-circle is observed, followed by Warburg line in the low frequency which corresponds to the diffusion step of the overall process. As evidenced in Figure 4.5, the modification of gold electrode did not inhibit the $[Fe(CN)_6^{3-}]/[Fe(CN)_6^{4-}]$ redox couple. Instead it facilitated the electron transfer as can be observed by a decrease in peak potential separation. At high frequency region the charge transfer resistance (R_{CT}) is expected to either increase or decrease due to inhibition or facilitation of charge transfer by the monolayer on the electrode [207,211,212]. In Figure 4.11A-C(i) a big semi-circle was observed for a bare gold electrode and this semi-circle decreased upon modifying the gold electrode with SAMs, Figure 4.11A-C(ii) for Au-ME SAM, Figure 4.11A(iii) for Au-ME-CoTCAPc SAM, Figure 4.11B(iii) for Au-ME-FeTCAPc SAM and Figure 4.11C(iii) for Au-ME-MnTCAPc SAM. The diameter of the semi-circle observed corresponds to the charge transfer resistance (R_{CT}) and the smaller the semi-circle, the faster the charge transfer. The decrease in semi-circle (R_{CT}) followed this trend (Ohm): Au (5991) > Au-ME-MTCAPc {M = (Co, 1284), (Fe, 2957), (Mn, 2572)} > Au-ME SAM (867). The observed trend was due to the fact that the modified electrodes show catalytic behaviour, i.e. facilitate the rate of electron transfer reactions for $[Fe(CN)_6^{3-}]/[Fe(CN)_6^{4-}]$ redox couple. These results are in conformity with the results observed for cyclic voltammetry in Figure 4.5 above. The coupling reaction between MTCAPc and Au-ME SAM resulted in structural changes of the Au-ME SAM, hence different surface properties, resulting in the observed differences in the semi-circle and Warburg line.

The other impedance data representation (Bode plot) was studied where the plot of phase angle (Θ) against log frequency was used. Bode plot data representation will assist in understanding the capacitive behaviour and properties of SAMs as it is known [213] that the

phase angle at low-to-medium frequency region gives important data, whereby the phase angle greater than or equal to 90^0 means that the SAM behaves like an ideal capacitor. This means that there is no current leakage at the defect sites and the SAM forms an insulating film. Whereas, if the phase angle is less than 90^0 the SAM is viewed as a contaminated capacitor meaning the SAM is permeable to solution ions. Figure 4.12 shows the Bode plot (-Θ vs log f) for A-C(i) bare gold, (ii) Au-ME SAM and A(iii) Au-ME-CoTCAPc SAM, B(iii) Au-ME-FeTCAPc SAM and C(iii) Au-ME-MnTCAPc SAM in (1:1) mixture of $K_3Fe(CN)_6/K_4Fe(CN)_6$ in 0.1 KCl solution. The Bode plot in Figure 4.12(i) for bare gold clearly shows that the phase angle is less than 90^0 throughout the frequency range and this was expected as the entire surface is exposed to solution ions. Furthermore, the modified gold surfaces Figure 4.12A-C(ii) and (iii) also exhibited the phase angle less than 90^0 throughout the frequency region. This means that there is a current leakage through the SAM. These results are in agreement with those obtained using the cyclic voltammetry and can be concluded that the electro-active surface of SAMs facilitates electron transfer, i.e. catalytic towards $[Fe(CN)_6^{3-}]/[Fe(CN)_6^{4-}]$.

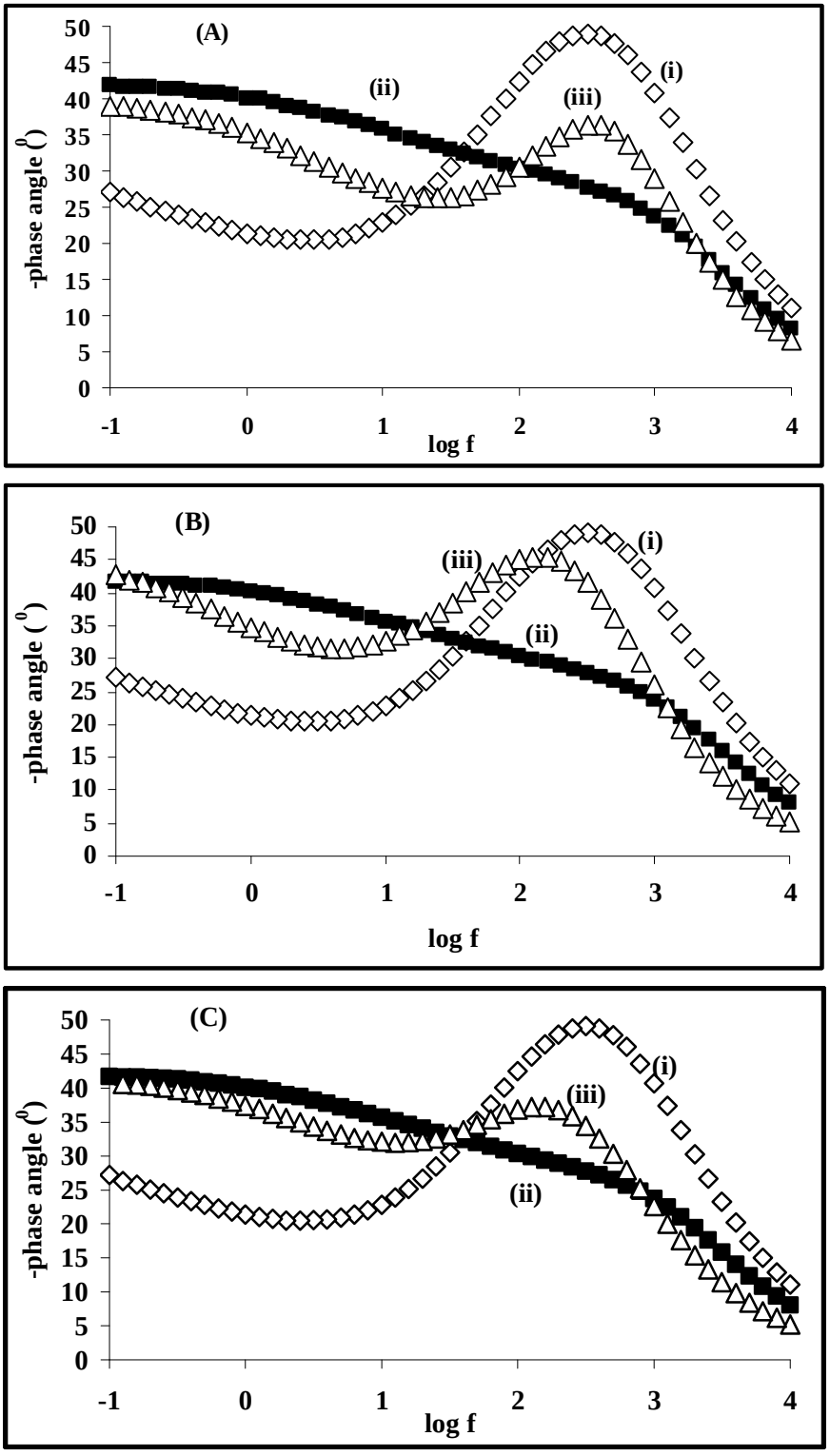

Figure 4.12: Bode plot (-Θ vs log f) for (i) bare gold, (ii) Au-ME SAM and A(iii) Au-ME-CoTCAPc SAM, B(iii) Au-ME-FeTCAPc SAM and (C)(iii) Au-ME-MnTCAPc SAM in (1:1) mixture of 1 x 10^{-3} mol.L^{-1} $K_3/K_4Fe(CN)_6$ in 0.1 mol.L^{-1} KCl solution.

4.2.6 Impedance spectroscopy characterization of glucose oxidase enzyme electrode

The impedance spectroscopy was also used to characterize the CoTCAPc-GOx enzyme SAM modified gold electrode (Au-ME-CoTCAPc-GOx SAM). The impedance measurements were performed in the mixture (1:1) of 1 x 10^{-3} mol.L^{-1} $K_3Fe(CN)_6/K_4Fe(CN)_6$ containing 0.1 KCl in PBS (pH 7.4) solution. Figure 4.13 shows (A) the Nyquist plot (-Z'' vs Z') and (B) the Bode plot of (i) bare gold, (ii) Au-ME SAM, (iii) Au-ME-CoTCAPc SAM and (iv) Au-ME-CoTCAPc-GOx SAM.

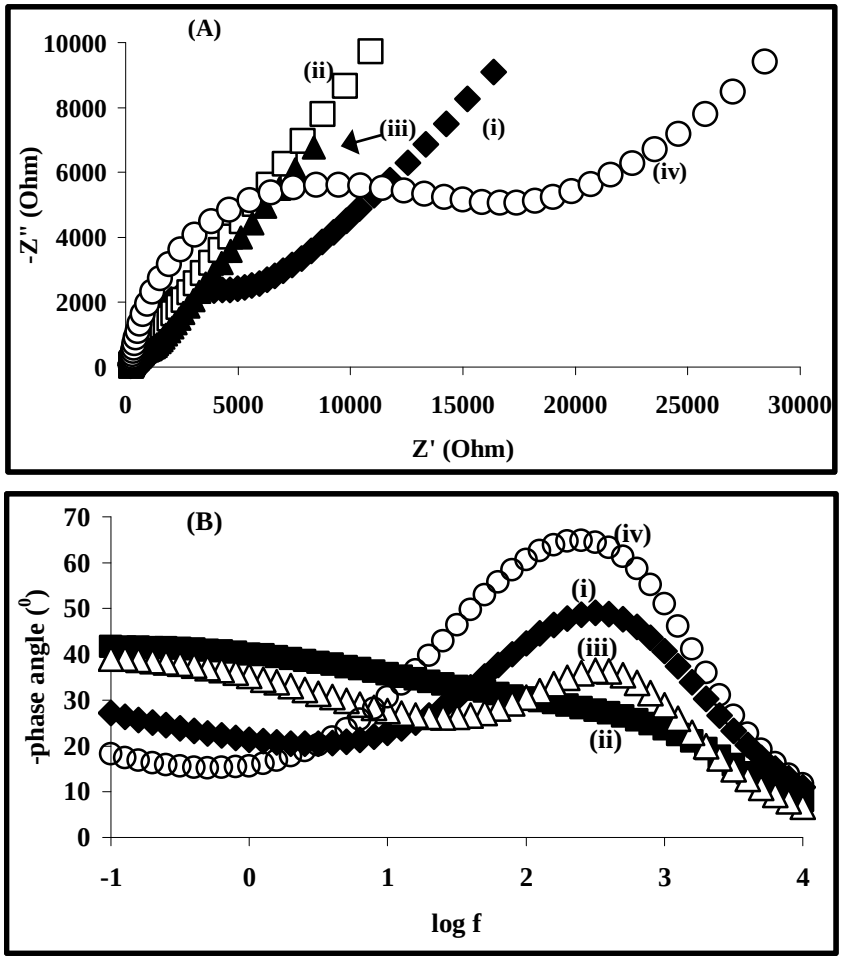

Figure 4.13: (A) the Nyquist plot (-Z'' vs Z') and (B) the Bode plot of (i) bare gold, (ii) Au-ME SAM, (iii) Au-ME-CoTCAPc SAM and (iv) Au-ME-CoTCAPc-GOx SAM in (1:1) mixture of 1 x 10^{-3} mol.L^{-1} $Fe(CN)_6^{3-/4-}$ containing 0.1 mol.L^{-1} KCl in PBS (pH 7.4) solution.

The Nyquist plot in Figure 4.13(A) showed the similar behaviour as observed in Figure 4.11 (above), whereby at high frequency regions a decrease in semi-circle upon modifying the gold electrode with (ii) Au-ME SAM and (iii) Au-ME-CoTCAPc SAM was observed. However, upon modifying the gold electrode with the enzyme (Au-ME-CoTCAPc-GOx SAM) the semi-circle, corresponding to the charge transfer resistance (R_{CT}), increased considerably and this increase followed this trend: Au-ME SAM < Au-ME-CoTCAPc SAM < Au < Au-ME-CoTCAPc-GOx SAM and the R_{CT} (Ohm) values (867 < 1284 < 5991 < 15969), respectively. The increase observed on an enzyme modified gold electrode in Figure 4.13A(iv) is attributed to the surface being covered by an enzyme layer. These impedance measurements for the enzyme are found to be consistent with the cyclic voltammograms obtained in Figure 4.10A. Bode plot (-Θ vs log f) was also used for the analysis of GOx enzyme impedance data. Figure 4.13B shows the Bode plot for (i) Au, (ii) Au-ME SAM, (iii) Au-ME-CoTCAPc SAM and (iv) Au-ME-CoTCAPc-GOx SAM. Figure 4.13B(iv) shows a tremendous increase in phase angle to approximately 70^0 at log f = 2.5 and this increase could be attributed to surface covering ability of enzyme to electrode reaction as observed in cyclic voltammogram in Figure 4.10A. However, the enzyme modified electrode still showed a phase angle less than 90^0 throughout the frequency range investigated and this is the characteristic of a leaking or contaminated capacitor.

Further characterization of SAM modified gold electrode was done by spectroscopic methods, i.e. Raman spectroscopy and X-ray photoelectron spectroscopy. Both these methods Raman spectroscopy and X-ray photoelectron spectroscopy were used in this work to give further experimental evidence of the immobilization and formation of Au-ME SAM and Au-ME-MTCAPc SAM on gold electrode surface.

4.2.7 Raman spectroscopic SAM characterization

Raman spectroscopy is a very useful surface characterization technique and has been used for the characterization of phthalocyanine surface films on metal surfaces, such as silver [214,215] and gold [216]. In this work, Raman spectroscopy was used for the characterization of SAM modified gold electrode. First the Raman spectra for the metallophthalocyanine complexes in powder form was measured and is shown in Figure 4.14(i) for CoTCAClPc (**11**) and (ii) for FeTCAClPc (**12**) and (iii) for MnTCAClPc (**13**). Please note that the data is for MTCAClPc complexes (**11-13**) and not the hydrolyzed MTCAPc (**15-17**). The results are the same for both MTCAPc and MTCAClPc complexes; hence the latter (which was available as powder) was used. The Raman spectra in Figure 4.14 were typical of phthalocyanine complexes in powder form as observed in literature [214-218] which exhibit peaks within the studied range (200 – 1800 cm^{-1}). The Raman bands observed in Figure 4.14 are characteristic bands for phthalocyanine complexes and are briefly summarized in Table 4.2.

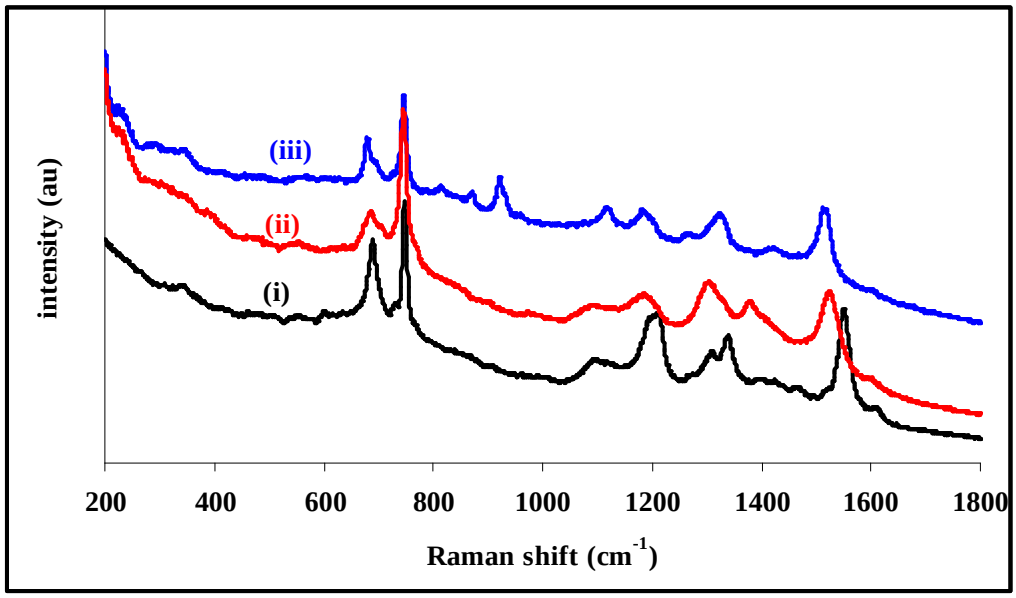

Figure 4.14: Powder Raman spectra of (i) CoTCAClPc (**11**) and (ii) FeTCAClPc (**12**) and (iii) MnTCAClPc (**13**).

Figure 4.15 shows the Raman spectra of the SAM modified gold electrode (A) (i) Au-ME SAM and (ii) Au-ME-CoTCAClPc SAM, (B) Au-ME-FeTCAClPc SAM and (C) Au-ME-MnTCAClPc SAM. Again note, the data is for MTCAClPc complexes (**11-13**) before hydrolysis in order to compare with Figure 4.14 where MTCAClPc complexes were employed. From the Raman spectrum of Au-ME SAM, Figure 4.15A(i), three Raman bands corresponding to Au-S (~230 cm^{-1}), asymmetrical H-C-H (~1300 cm^{-1}) and symmetric H-C-H (~1600 cm^{-1}) were observed, thus confirming the chemisorption of Au-ME SAM on gold surface via Au-S bond. The Au-ME SAM gold electrode was further modified with different metallophthalocyanine complexes (Au-ME-MTCAClPc SAM). The results are shown in Figure 4.15A(ii) for Au-ME-CoTCAClPc SAM, (B) Au-ME-FeTCAClPc SAM and (C) Au-ME-MnTCAClPc SAM. Upon modifying Au-ME SAM with different MTCAClPc complexes extra Raman bands different from Au-ME SAM were observed, and these bands (except the band at 300 cm^{-1}) are characteristic of the studied MTCAClPc complexes on gold surface. The noticeable difference of powder (Figure 4.14) and immobilized complexes was observed, first by the shift in wave numbers of some of the Raman bands as shown by the results summarized in Table 4.2. Also one can notice that the Raman bands for the immobilized MTCAClPc complexes were broad within the range (1000 – 1250 cm^{-1}), especially for Au-ME-CoTCAClPc SAM and Au-ME-FeTCAClPc SAM compared to their powder Raman spectra in Figure 4.14. An additional band at 300 cm^{-1} in Au-ME-MTCAClPc SAM modified gold electrodes was observed and this band corresponds to Au-S vibration as Au-ME-MTCAClPc SAMs are chemisorbed (Au-S) on gold surface. The shift of this band from 230 cm^{-1} for Au-ME SAM to 300 cm^{-1} for Au-ME-MTCAClPc SAMs confirm the coupling reaction of the studied MTCAClPc complexes onto Au-ME SAM pre-modified gold surface. The two peaks observed for Au-ME SAM at 1300 and 1600 cm^{-1} were not observed at

Au-ME-MTCAPc SAM modified electrode, this could be attributed to the Au-ME SAM buried under bulky MTCAPc complexes.

Table 4.2: Molecular vibrations of modified gold electrode with Au-ME SAM and Au-ME-MTCAClPc SAM and the powder of MTCAClPc complexes (**11-13**) observed in the Raman spectra.

ME SAM (cm^{-1})	**CoTCAClPc Powder (cm^{-1})**	**CoTCAClPc SAM (cm^{-1})**	**FeTCAClPc Powder (cm^{-1})**	**FeTCAClPc SAM (cm^{-1})**	**MnTCAClPc Powder (cm^{-1})**	**MnTCAClPc SAM (cm^{-1})**	**Interpretation**
230							Au-S
		300		300		300	Au-S
	690	694	690	695	685	685	Ring deformation
	750	750	750	750	750	750	Ring deformation
					922	840	Out-of-plane bending
	1110	1110	1100	1118	1122	1100	C-H bending
			1188	1198	1190	1190	C-H bending
	1213	1211		1214	1280	1279	C-H bending
1311							CH_2 asymmetric stretch
	1313, 1342	1339	1310	1329	1329	1339	C-N breathing
		1425	1385				Isoindole ring stretch
	1553	1543	1530	1530	1520	1520	C=C pyrrole stretch
1600							CH_2 symmetric stretch

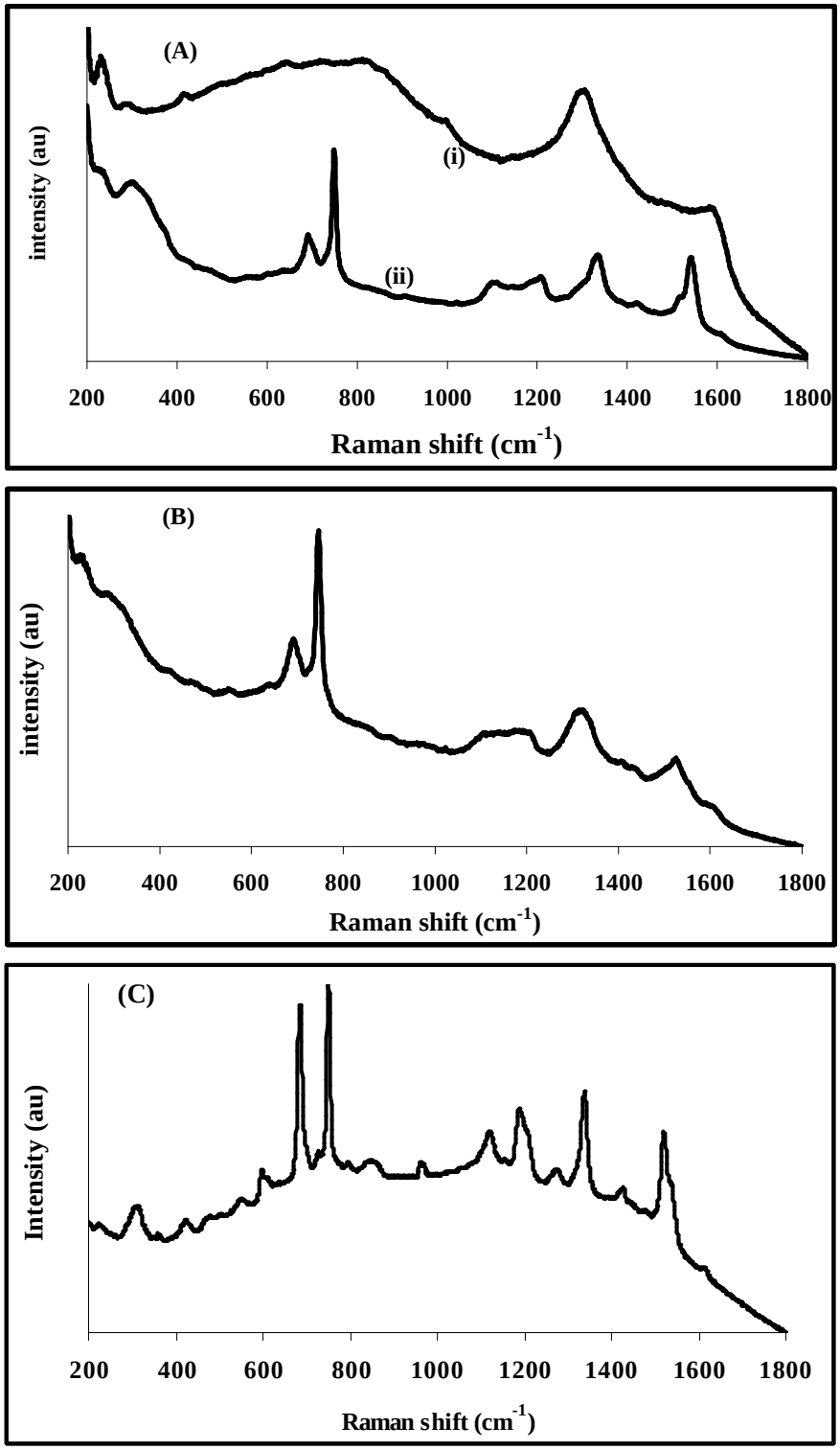

Figure 4.15: Raman spectra of gold modified electrode with (A)(i) Au-ME SAM and A(ii) Au-ME-CoTCAPc SAM, (B) Au-ME-FeTCAPc SAM and (C) Au-ME-MnTCAPc SAM.

4.2.8 X-ray photoelectron spectroscopic SAM characterization

X-ray photoelectron spectroscopy (XPS) measurements were performed in this work to detect the appearance of elements from the SAM modified gold surface with Au-ME SAM and Au-ME-MTCAPc SAMs and also investigate how these SAMs interact with the gold surface. XPS measurements are very useful in studying the surface film composition thus confirming the immobilization and formation of SAMs on gold surface. Figure 4.16 shows the survey XPS spectrum for Au-ME SAM modified gold electrode. The elemental composition (gold, carbon, and oxygen) which arises from the Au-ME SAM modified surface were observed and these elements were expected for Au-ME SAM modified gold surface. The high resolution experiments in the sulfur (S 2p) region of the SAMs have been reported to give clear evidence for the attachment of thiol molecules on gold surface [22,32,35,205,206,219-223]. Therefore, in this work, the sulfur and oxygen were examined using an extended acquisition time or high resolution XPS.

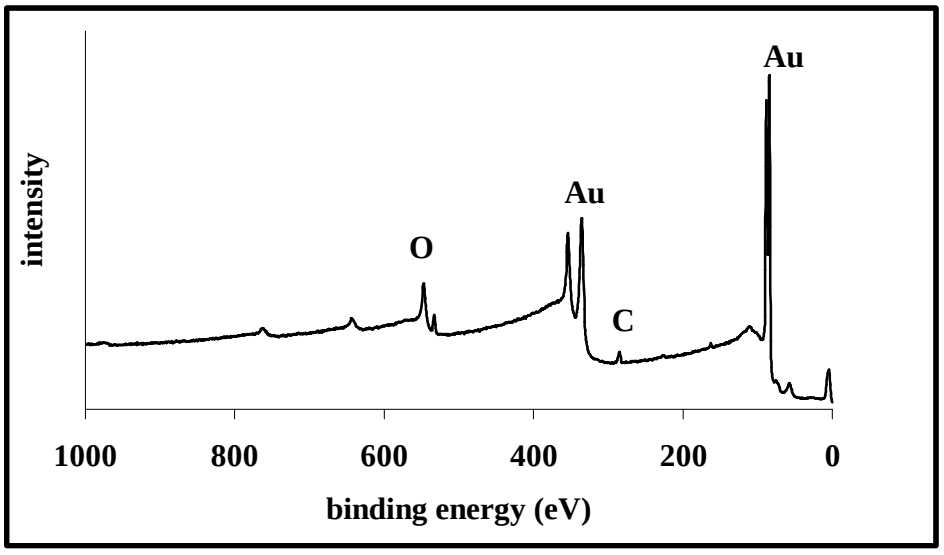

Figure 4.16: XPS low resolution survey spectrum showing the elemental composition for Au-ME SAM modified gold surface.

Figure 4.17 shows the extended high resolution spectra for (A) sulfur (S 2p) and (B) oxygen (O 1s) region of Au-ME SAM modified gold surface.

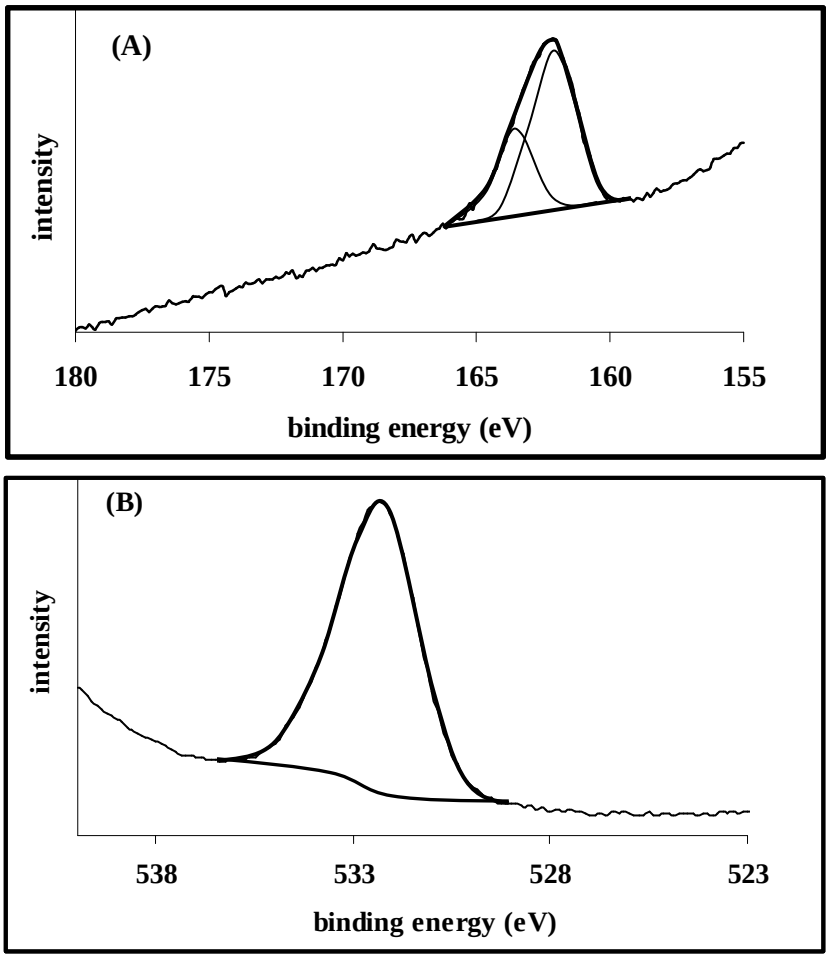

Figure 4.17: XPS spectra showing (A) the S 2p and (B) O 1s core level region of Au-ME SAM monolayer on gold surface.

The high resolution spectrum for sulfur (S 2p) in Figure 4.17 (A) gave two sets of S 2p peaks, one centered at 162.0 eV and another at 163.4 eV. The peak at 162.0 eV is assigned to a sulfur bound to gold surface (Au-S), while the peak at 163.4 eV has been known [22,32,35,205, 206,219-223] to be that of partially bound RSH thiols (2-mercaptoethanol in this work). From these result it is clear that mercaptoethanol forms a thiolate bond (Au-S) on gold surface,

therefore the XPS experiments confirm the chemisorption and formation of mercaptoethanol monolayer (Au-ME SAM) on gold surface. Figure 4.17B shows the high resolution region for oxygen (O 1s) which clearly exhibited one peak centered at 532.4 eV. This peak is be attributed to the oxygen from the terminal hydroxyl (OH) group on Au-ME SAM and these results also confirms that the immobilization of mercaptoethanol is only via the sulfur head, leading to the OH group exposed on the surface of Au-ME SAM modified gold surface.

The Au-ME SAM modified electrode was further modified with MTCAClPc (and not hydrolyzed to MTCAPc for comparative purposes) complexes to give the Au-ME-MTCAClPc SAM modified gold surface and the XPS experiments were also performed for these different MTCAClPc modified gold surfaces. The XPS experiments for the Au-ME-MTCAPc SAM modified electrode exhibited different structural properties compared to that of Au-ME SAM. Figure 4.18 shows low resolution survey spectra of (A) Au-ME-CoTCAClPc SAM, (B) Au-ME-FeTCAClPc SAM and (C) Au-ME-MnTCAClPc SAM. The XPS experiments in Figure 4.18 show an extra nitrogen element which was not seen in the XPS survey spectrum of Au-ME SAM in Figure 4.16, above. The peak intensity for the elements increased from Au-ME SAM to Au-ME-MTCAClPc SAM and this is due to the fact that the Au-ME-MTCAClPc SAM consists of a highly conjugated ring system compared to alkanethiol (Au-ME SAM) on gold surface.

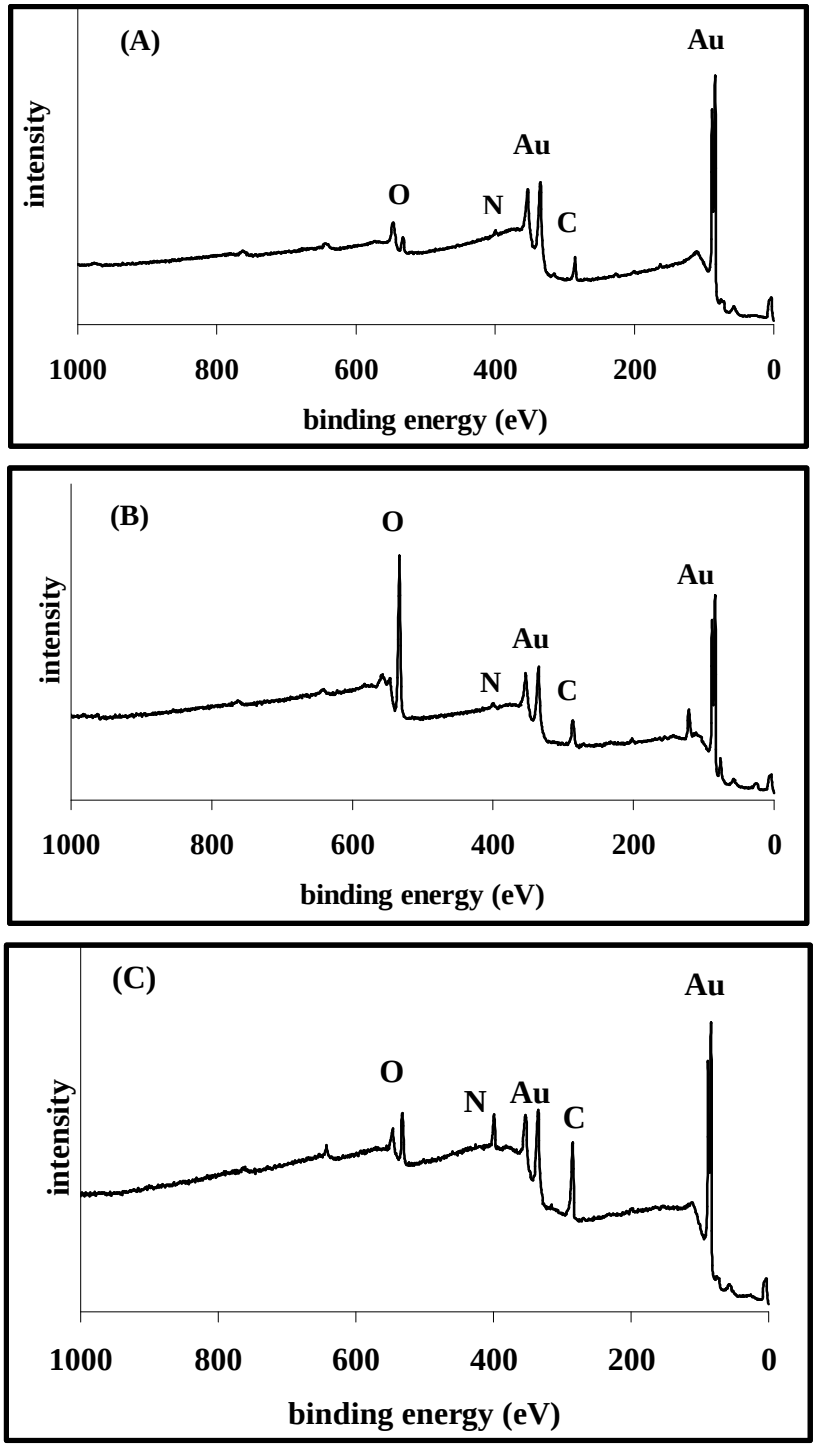

Figure 4.18: XPS low resolution survey spectra of (A) Au-ME-CoTCAClPc SAM, (B) Au-ME-FeTCAClPc SAM and (C) Au-ME-MnTCAClPc SAM.

Figure 4.19 shows the XPS high resolution spectra for the sulfur (S 2p) region of (A) Au-ME-CoTCAClPc SAM, (B) Au-ME-FeTCAClPc SAM and (C) Au-ME-MnTCAClPc SAM modified gold surface. The extended S 2p region for Au-ME-CoTCAClPc SAM in Figure 4.19A gave two peaks at 161.9 and 163.6 eV, these peaks are similar to the peak observed for Au-ME SAM above and are attributed to the strong (161.9 eV) and partial (163.6 eV) chemisorption bonds (Au-S) due to the formation of the thiolate (Au-S) bond. Similar results were observed for Au-ME-MnTCAPc SAM in Figure 4.19C with two peaks at 161.9 and 163.3 eV both corresponding to the strong and partial formation of the thiolate (Au-S) on gold surface. However, Au-ME-FeTCAClPc SAM in Figure 4.19B gave four peaks at 161.8 eV, 163.2 eV, 170.2 eV and 171.9 eV. The first two peaks at 161.8 and 163.2 eV are similar to the observed before for Au-ME-CoTCAClPc SAM and Au-ME-MnTCAClPc SAM which are attributed to strong and partial chemisorption of thiols as thiolate on gold surface. The extra two peaks at 170.2 and 171.9 eV have been reported in literature [220,222,223] to be due to the sulfonate group on gold surface. The sulfonate group in this work is thought to be due to the cleaning method for gold substrates which involves the use of "piranha" solution (i.e. a mixture of H_2SO_4 and H_2O_2). Therefore the presence of the sulfonate group might be from the piranha solution. The other possibility of the formation of sulfonate on gold surface may be due to the oxidation of the sulfur atoms on the thiolate group. This has been reported in literature [220] that the thiolate (Au-S) can undergo oxidation in the atmosphere resulting in an increase in binding energy from thiolate (Au-S) peak at 162 eV to the sulfonate peaks close to 170 eV. Since the XPS measurements for modified gold surfaces were done simultaneously, different surfaces were used for different complexes and the FeTCAClPc modified surface could have been contaminated with sulfonate groups as observed in Figure 4.19B.

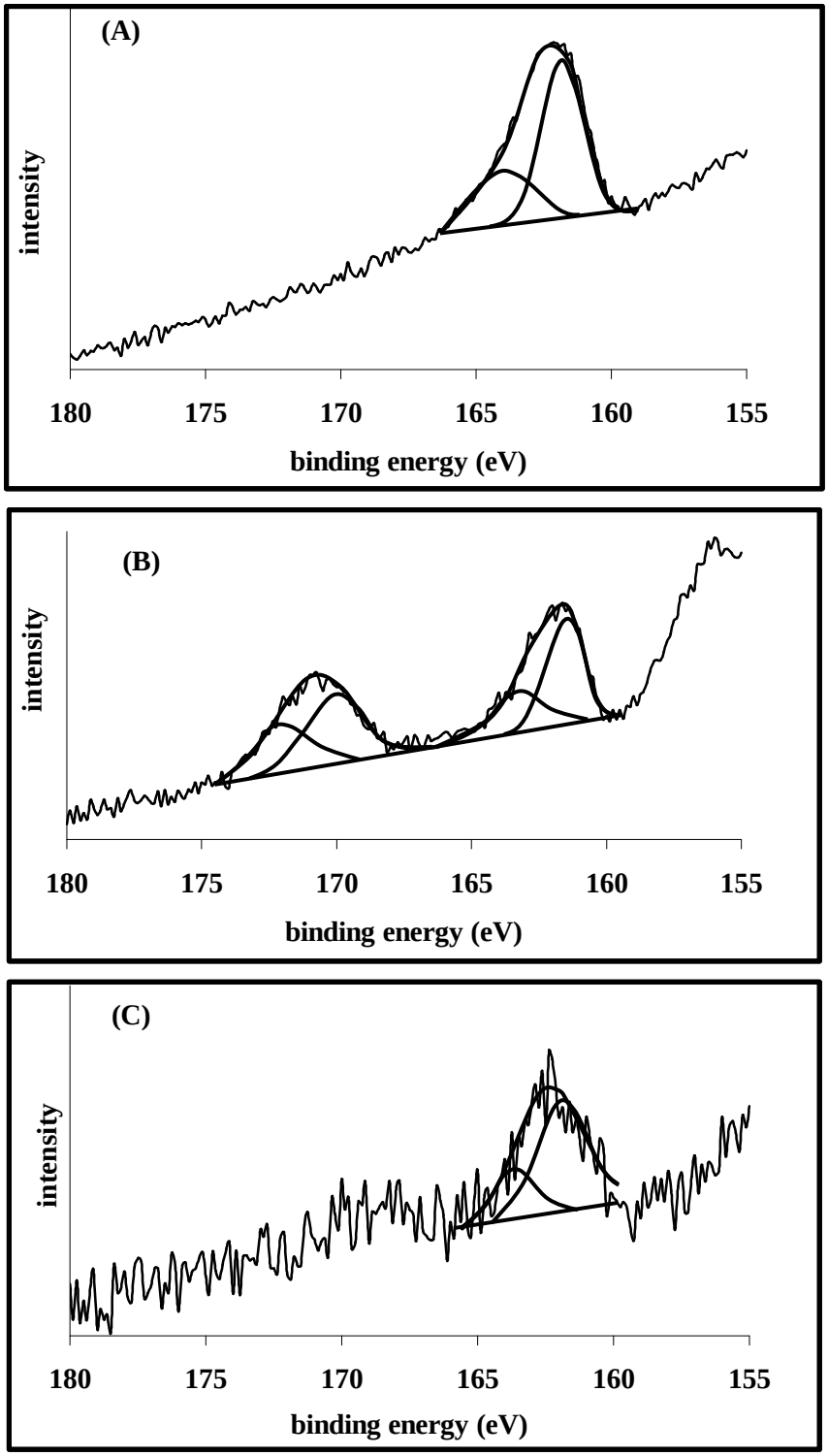

Figure 4.19: XPS spectra showing the S 2p core level region of (A) Au-ME-CoTCAClPc SAM, (B) Au-ME-FeTCAClPc SAM and (C) Au-ME-MnTCAClPc SAM monolayers on gold surface.

The XPS high resolution region for oxygen (O 1s) was also investigated for the Au-ME-MTCAClPc SAM on gold surface. Figure 4.20 shows the XPS high resolution spectra for oxygen (O 1s) region of (A) Au-ME-CoTCAClPc SAM, (B) Au-ME-FeTCAClPc SAM and (C) Au-ME-MnTCAClPc SAM modified gold surface. The observed XPS spectra for Au-ME-MTCAClPc SAM was clearly different from that of Au-ME SAM in Figure 4.17B above which showed only one oxygen atom contribution from the hydroxyl (OH) group. The O 1s region for Au-ME-CoTCAClPc SAM in Figure 4.20A and Au-ME-MnTCAClPc SAM in Figure 4.20C were the same and both exhibited two peaks for oxygen atom (O 1s). These peaks were found at 531.9 and 533.5 eV for Au-ME-CoTCAClPc SAM and can be attributed to the oxygen at the ether linkage (C-O-C) and the carbonyl oxygen (C=O) atoms. Similarly, the oxygen peaks for Au-ME-MnTCAClPc SAM were found at 531.9 and 533.5 eV and could be attributed to the ether linkage oxygen (C-O-C) and carbonyl oxygen (C=O) atoms. However, for Au-ME-FeTCAClPc SAM, the extra oxygen was observed at 535.1 eV which might be from the sulfonate (SO_3^-) group found at the gold surface as was observed at S 2p region in Figure 4.19B, while the other two oxygen atoms were found at 532.2 and 533.6 eV corresponding to the ether (C-O-C) and carbonyl (C=O) oxygen atoms.

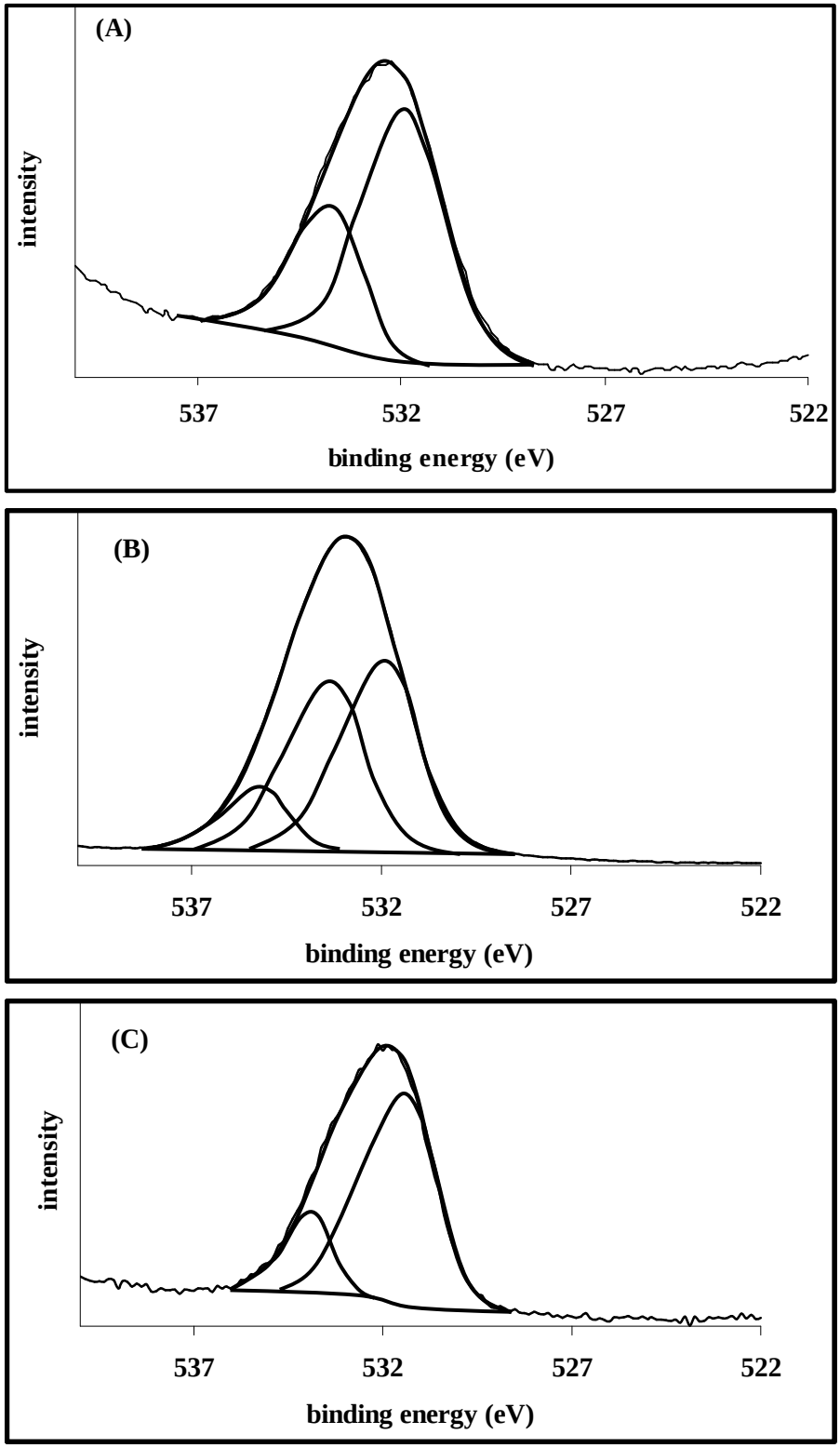

Figure 4.20: XPS spectra showing the O 1s core level region of (A) Au-ME-CoTCAClPc SAM, (B) Au-ME-FeTCAClPc SAM and (C) Au-ME-MnTCAClPc SAM modified gold surface.

Since metallophthalocyanine complexes contain different metal ion centers, for example Co (for Au-ME-CoTCAClPc SAM), Fe (for Au-ME-FeTCAClPc SAM) and Mn (for Au-ME-MnTCAClPc SAM), the metal core level region was investigated using XPS. Figure 4.21 shows the high resolution region for different metal ions (A) Au-ME-CoTCAClPc SAM, (B) Au-ME-FeTCAClPc SAM and (C) Au-ME-MnTCAClPc SAM. For all the metal ion regions (as shown in Figure 4.21) the intensity was very low, therefore no fitting was performed. However, it was interesting to see the peaks corresponding to the presence of the metal ion (though very weak for FeTCAClPc modified surface), thus confirming the presence of the immobilized MTCAClPc complexes (Au-ME-MTCAClPc SAM) on gold surface. The experimental percentage composition of the elements observed in XPS was done and the results are summarized in Table 4.3. It was interesting to note that for Au-ME-CoTCAClPc SAM and Au-MnTCAClPc SAM higher percentages for carbon (C 1s) compared to oxygen (O 1s) atoms were observed, due to the phthalocyanine ring system. For Au-ME-FeTCAClPc SAM the observed result shows that the SAM was highly contaminated with sulfonate ions on gold electrode and this greatly affected the results as noticed with high percentages for O 1s compared to C 1s atoms. The experimental percentage composition also showed the presence of the metal ions even though this was very small for Au-ME-FeTCAClPc SAM due to contamination.

Table 4.3: Experimental percentage composition of elements found on SAM modified gold electrodes.

Au-ME SAM			**Au-ME-CoTCAClPc SAM**			**Au-ME-FeTCAClPc SAM**			**Au-ME-MnTCAClPc SAM**	
O 1s	29.92 %		O 1s	17.73 %		O 1s	68.80 %		O 1s	18.40 %
C 1s	57.81 %		C 1s	75.06 %		C 1s	30.52 %		C 1s	77.75 %
S 2p	12.28 %		S 2p	6.35 %		S 2p	1.63 %		S 2p	1.50 %
			Co 2p	0.86 %		Fe 2p	0.05 %		Mn 2p	2.35 %

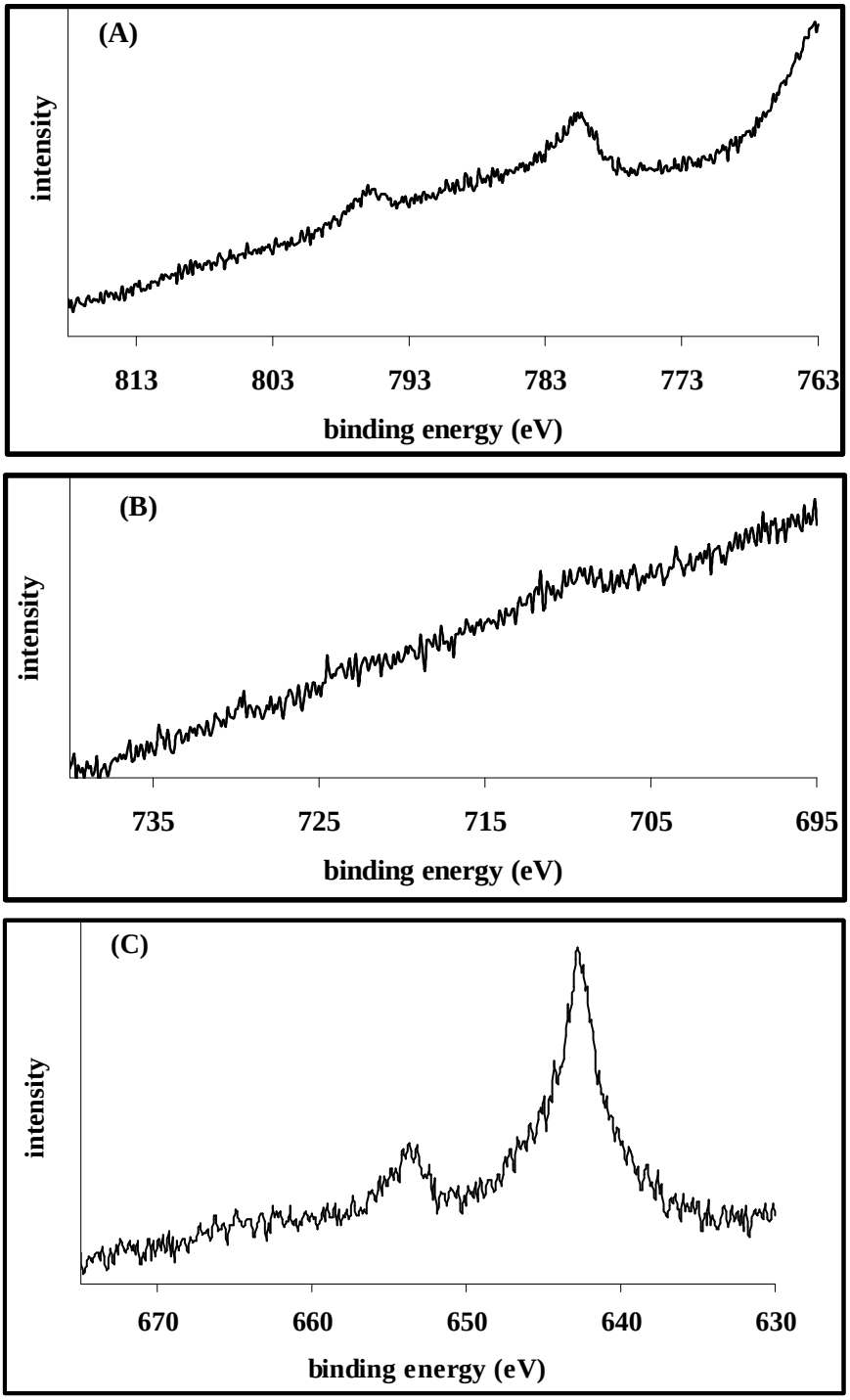

Figure 4.21: XPS spectra showing the metal (M 2p) core level region of (A) Co 2p in Au-ME-CoTCAClPc SAM, (B) Fe 2p in Au-ME-FeTCAClPc SAM and (C) Mn 2p in Au-ME-MnTCAClPc SAM modified gold surface.

4.2.9 Quartz crystal microbalance with dissipation GOx SAM characterization

The poor compatibility of some of the QCM-D flow chamber components with select organic solvents made it difficult to assess the layering of organic-phase biosensor components onto the transducer surface. Therefore, layering of the CoTCAClPc and ME monolayers onto the electrode surface took place using dry DMF (as a CoTCAClPc solubilizing agent) and ethanol solution (deposition solution for ME), which is not compatible with the standard inlet/outlet tubing of the instrument. Then, the quartz crystal microbalance with dissipation (QCM-D) was used in this work to monitor only the covalent immobilization of glucose oxidase enzyme onto Au-ME-CoTCAPc SAM modified gold surface. The gold quartz crystal was first coated with the mercaptoethanol and cobalt tetra-carboxy acid phthalocyanine (Au-ME-CoTCAPc SAM) as shown in Scheme 4.3. The acid groups of Au-ME-CoTCAPc SAM were activated with EDC/NHS solution to afford the EDC/NHS activated Au-ME-CoTCAPc SAM, and the immobilization of the enzyme was monitored using QCM-D. Figure 4.22 shows the plot of changes in frequency (f) and dissipation (D) observed following immobilization and formation of glucose oxidase (GOx) layer onto Au-ME-CoTCAPc NHS SAM.

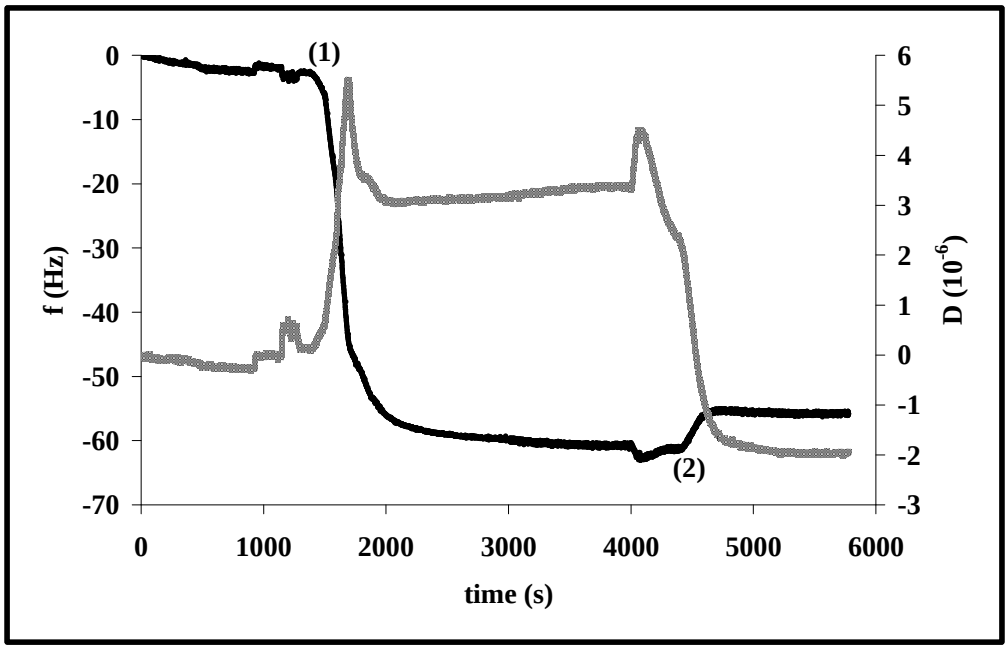

Figure 4.22: Normalized frequency and dissipation shift for 3rd overtone versus time following covalent immobilization of glucose oxidase enzyme onto gold surface pre-modified with acid activate cobalt phthalocyanine SAM. (1) is the start of the immobilization of GOx enzyme and (2) is the start of rinsing step with PBS (pH 7.4) buffer solution.

The immobilization of GOx resulted in a decrease in frequency (f) of approximately -50 Hz and an increase in dissipation (D) of approximately 3.1 x 10^{-6}. The observed frequency change resulted in a mass gain of 1.10μg estimated using a Sauerbrey relationship in the Q-Tools software. The observed frequency changes are due to covalent immobilization of GOx enzyme SAM on gold surface. However, one must note the fact that the measured frequency and dissipation changes leading to the mass of the immobilized GOx enzyme also include water as QCM-D senses the water molecules trapped between the protein molecules.

In conclusion, this chapter convincingly demonstrated the successful covalent immobilization of different metallophthalocyanine complexes onto a pre-modified gold electrode with a simple thiol (Au-ME SAM). Different characterization methods were used successfully for SAM characterization and these methods are cyclic voltammetry (CV), electrochemical impedance spectroscopy (EIS), x-ray photoelectron spectroscopy (XPS), Raman spectroscopy, and quartz crystal microbalance with dissipation (QCM-D). One can conclude that the gold surface was successfully modified with SAMs and that the characterization techniques were in good agreement with each other as they all demonstrated and showed the convincing evidence of the presence of different monolayers on gold electrode. The next chapter (five) investigates the potential electrocatalytic behaviour of the Au-ME-MTCAPc SAM modified gold electrode towards the detection of L-cysteine and hydrogen peroxide. The next chapter (five) will also investigate the potential electrocatalytic behaviour of the glucose oxidase enzyme modified gold electrode (Au-ME-CoTCAPc-GOx SAM) towards the detection of glucose.

CHAPTER FIVE:

ELECTROCATALYTIC BEHAVIOUR OF SAMs

To probe the analytical applications of the SAM modified gold electrodes as potential electrochemical sensors, the electrocatalytic oxidation and analysis of biologically, environmentally and industrially important molecules were performed. The studied important molecules in this work are L-cysteine, hydrogen peroxide and glucose. Therefore, this chapter will investigate electrocatalytic studies, i.e. the detection and analysis of these molecules (analytes) at modified gold electrode.

5.1 Electrocatalytic applications of SAM modified Au-electrode towards L-cysteine

Cysteine oxidation is known to occur at high anodic potentials using the conventional electrodes, in particular at gold electrodes it is known to occur at potentials > 900 mV [130]. Therefore, the use of MPc SAM, with MPc containing transition metals such as Co, Fe and Mn as central metal ions have been shown to reduce the potential and substantially improve electrocatalytic activity of the bare gold electrode towards the detection of cysteine [55,57,58,60] by improving the rate of electron transfer. The initial studies (performed in South Africa) for cysteine detection at Au-ME-CoTCAPc SAM modified gold electrode exhibited two well-defined peaks due to cysteine oxidation. Figure 5.1(A) shows the cyclic voltammograms for Au-ME-CoTCAPc SAM (i) without and (ii) with 1.0 x 10^{-4} mol.L^{-1} L-cysteine and (B) shows the cyclic voltammograms of (i) bare and (ii) Au-ME SAM in the presence of 1.0 x 10^{-4} mol.L^{-1} L-cysteine in phosphate buffer solution (pH 4).

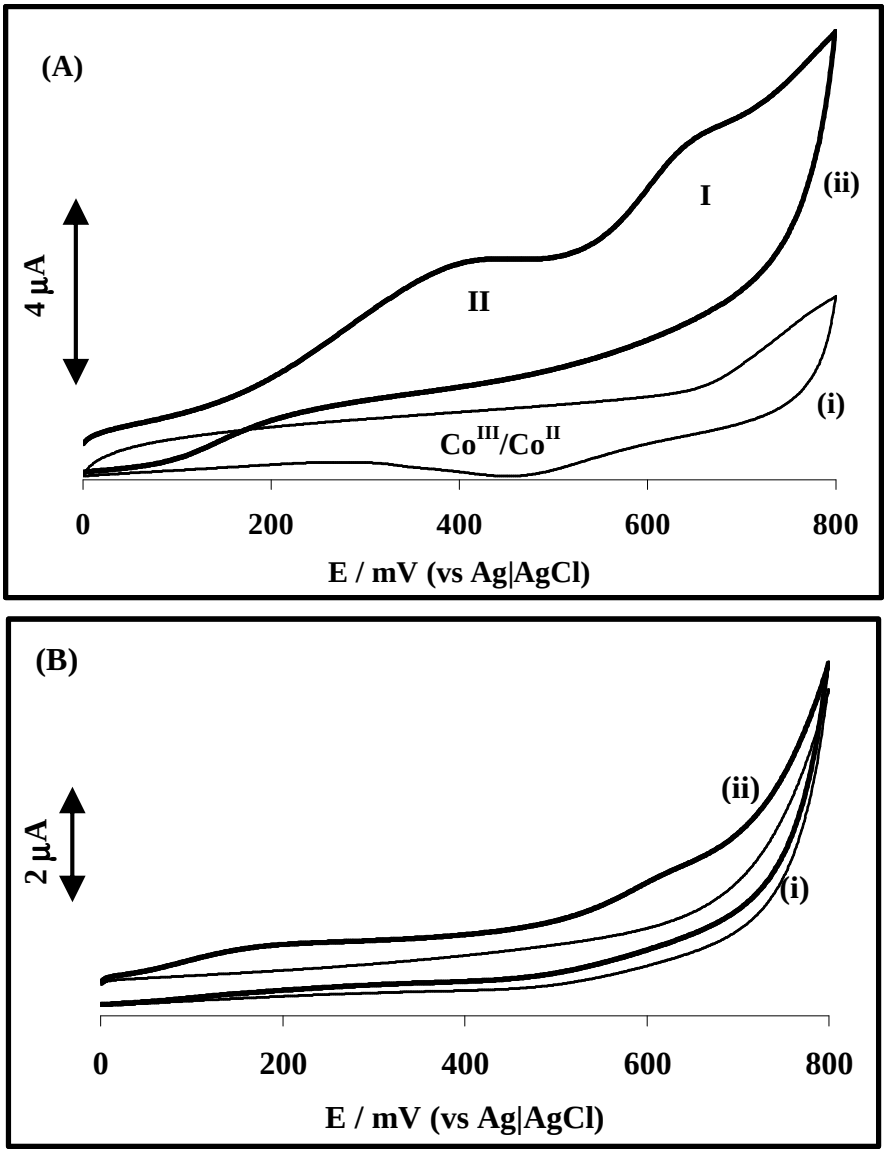

Figure 5.1: Cyclic voltammograms for (A) Au-ME-CoTCAPc SAM (i) without and (ii) with 1.0 x 10^{-4} mol.L^{-1} L-cysteine and (B) cyclic voltammograms of (i) bare and (ii) Au-ME SAM in the presence of 1.0 x 10^{-4} mol.L^{-1} L-cysteine in phosphate buffer solution (pH 4). Scan rate = 25 mV/s.

The two cysteine oxidation peaks in Figure 5.1A were observed at 450 mV (**II**) and 670 mV (**I**) (vs Ag|AgCl) in pH 4 buffer solution, whereas in Figure 5.1B there was no peak observed for bare (i) and an ill-defined peak at ~600 mV (vs Ag|AgCl) was observed at Au-ME SAM in Figure 5.1B(ii). The presence of an ill-defined peak for cysteine oxidation at Au-ME SAM was not surprising as Au-ME SAM is known to catalyze the oxidation of biological important molecules [224,225] and this peak was enhanced in Figure 5.1A(ii) even though the same concentrations for cysteine were employed on both Figure 5.1A(ii) and Figure 5.1B(ii). The enhancement in this peak due to Au-ME SAM could be due to differences in nature of the electrode surface in the presence of CoTCAClPc in Au-ME-CoTCAPc SAM compared Au-ME SAM alone. The first oxidation peak labeled **II** at 450 mV in Figure 5.1A(ii) is typical electrooxidation of cysteine at MPc modified electrodes and has been reported [23,24,55,60] to be mediated by metal oxidation ($M^{III}Pc/M^{II}Pc$). The mechanism involved in cysteine oxidation is shown in equation 5.1 – 5.4 [24,55,56,113,226,227], whereby first the oxidation of the metal (Co) from $Co^{II}Pc$ to $Co^{III}Pc$, occurs followed by chemical oxidation of cysteine and the regeneration of $Co^{II}Pc$. The oxidation peak (**II**) of L-cysteine in Figure 5.1A(ii) is in the range of Co^{III}/Co^{II} oxidation peak in Figure 5.1A(i) and this leads to the conclusion that the oxidized species, $Co^{III}Pc$ is involved in the mechanism for L-cysteine oxidation as shown in equations 5.1 – 5.4:

$$Co^{II}TCAPc \longrightarrow [Co^{III}TCAPc]^{+} + e^{-} \quad (5.1)$$

$$[Co^{III}TCAPc]^{+} + RSH \longrightarrow [RSH\text{-}Co^{III}TCAPc]^{+} \quad (5.2)$$

$$[RSH\text{-}Co^{III}TCAPc]^{+} \longrightarrow Co^{II}TCAPc + RS^{\bullet} + H^{+} \quad (5.3)$$

$$2RS^{\bullet} \longrightarrow RSSR \quad (5.4)$$

where RSH = L-cysteine and RSSR = cystine.

The catalytic activity may be evidenced by lowering of potential and an increase in current. In Figure 5.1A the current in the presence of L-cysteine (Figure 5.1A(ii)) is an order of magnitude larger than the current of the Au-ME-CoTCAPc SAM modified gold electrode in the absence of L-cysteine (Figure 5.1A(i)), hence proving catalytic activity. The second peak labeled **I** at 670 mV in Figure 5.1A(ii) may be a result of the catalytic effect of Au-ME SAM not coordinated to the CoTCAClPc. In order to prove the participation of Au-ME SAM (containing OH terminal functional group), the nature of unreacted Au-ME SAM was changed by reacting the Au-ME-CoTCAPc SAM electrode with acetyl chloride (by simply immersing the Au-ME-CoTCAPc SAM electrode into a solution of acetyl chloride) in order to transform any uncoordinated OH terminal groups to $–OOCCH_3$ terminal groups. Figure 5.2 shows the cyclic voltammograms of (i) Au-ME-CoTCAPc SAM and (ii) Au-ME-CoTCAPc SAM functionalized with acetyl chloride in the presence of cysteine (1×10^{-4} mol.L^{-1}).

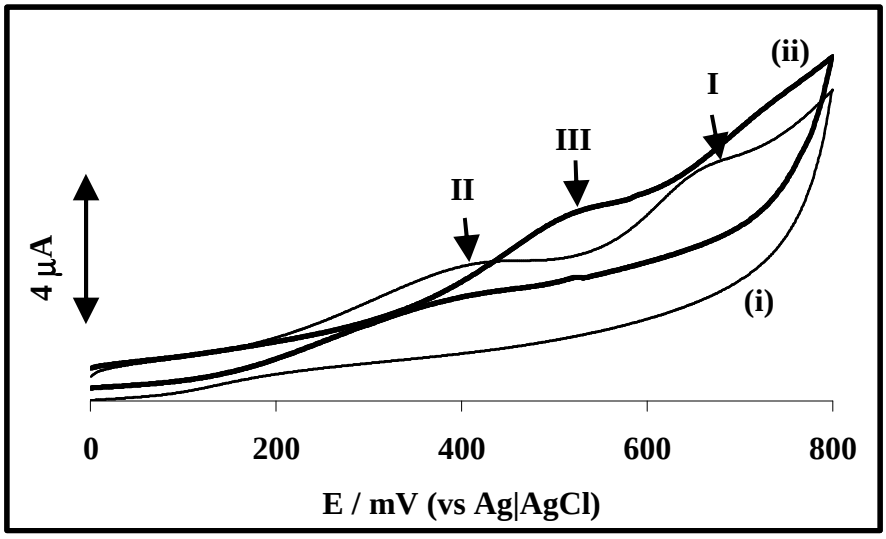

Figure 5.2: Cyclic voltammograms for (i) Au-ME-CoTCAPc SAM and (ii) Au-ME-CoTCAPc SAM functionalized with acetyl chloride in the presence of 1×10^{-4} mol.L^{-1} of L-cysteine in pH 4 buffer solution. Scan rate = 25 mV/s.

The cyclic voltammogram of L-cysteine was recorded on the resulting $–OOCCH_3$ functionalized Au-ME-CoTCAPc SAM electrode in Figure 5.2 (ii) and only one peak **III** was observed at ~540 mV (vs Ag|AgCl). The oxidation of cysteine occurred with a typical [227] dip on the return wave. Thus, the addition of acetyl chloride resulted in an increase in the oxidation potential of cysteine. This increase could reflect the fact that the electrode surface has changed. However the L-cysteine oxidation potential is still low compared to its oxidation on other CoPc modified electrodes [113,227], making the current electrode more favourable. The experiments were also performed whereby the OH of the Au-ME SAM (in the absence of CoTCAPc) was transformed to $–OOCCH_3$, the weak peak seen at 600 mV in Figure 5.1B(ii), was not observed confirming that changes in terminal functional group in Au-ME SAM affect the nature of the Au-ME SAM, rendering it insensitive to L-cysteine, even in the absence of CoTCAPc.

Chronoamperometry experiments were used for the analysis of L-cysteine. Figure 5.3A shows the typical current response (chronoamperomogram) of the Au-ME-CoTCAPc SAM on consecutive additions of cysteine at fixed potential (450 mV vs Ag|AgCl) which is the potential at which L-cysteine oxidation is catalyzed by the cobalt phthalocyanine. A base line was established in 10 mL of 1.0 M PBS (pH 4.0). A well defined increase in current due to L-cysteine oxidation was observed with successive increments of L-cysteine concentration in solution (indicated by arrows, Figure 5.3A). The linear plot in Figure 5.3B shows the current versus concentration of L-cysteine and gave a straight line within the studied concentration range ($2.8 – 20\ \mu mol.L^{-1}$). The limit of detection (LoD), based on signal to noise ratio of 3, was $5.0 \times 10^{-7}\ mol.L^{-1}$ close or equal to the reported values [23,24,55] of detection limit of L-cysteine on

CoPc SAM reported in Table 1.2 in chapter 1. The response time of the modified electrode to L-cysteine additions was found to be 2 seconds.

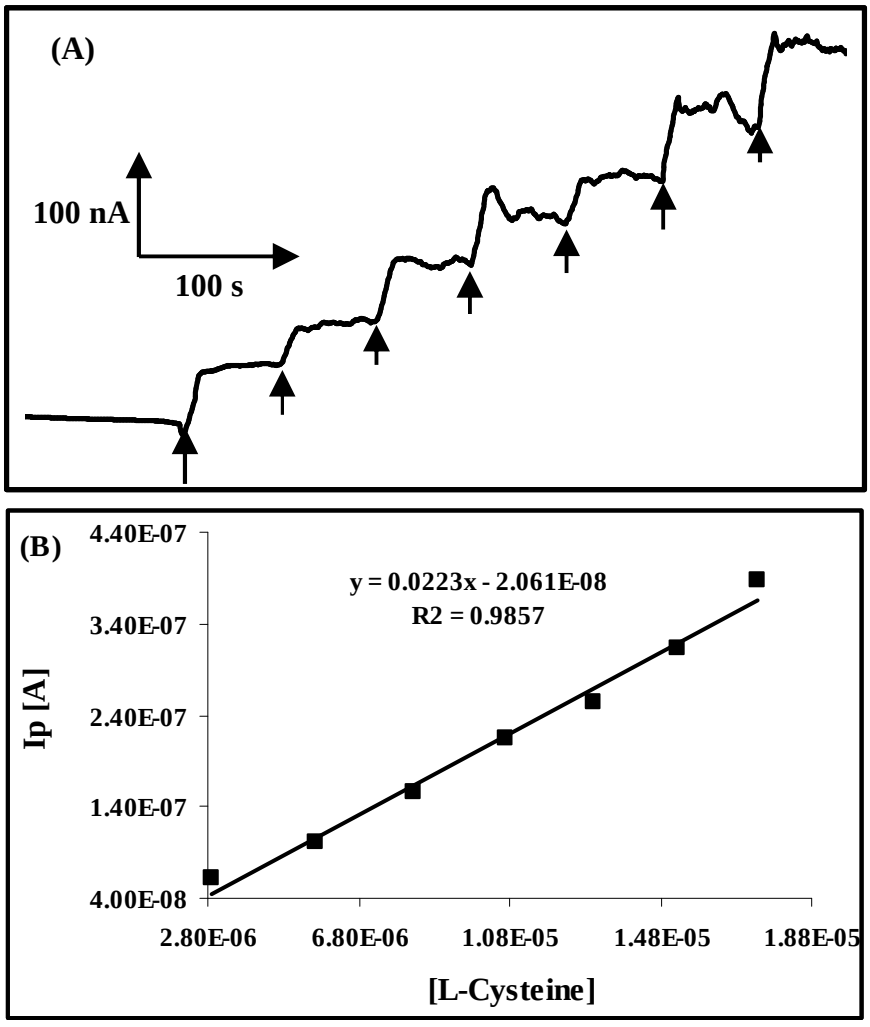

Figure 5.3: (A) Amperometric current responses of Au-ME-CoTCAPc SAM on additions (indicated by arrows) of 1.0 x 10^{-4} mol.L^{-1} L-cysteine in PBS (pH4) at 450 mV applied potential. (B) Plot of current vs concentration of L-cysteine.

L-cysteine was further studied at different MTCAPc modified electrodes and these studies were conducted in Belgium (Ghent University). Figure 5.4 shows the CVs of 1 x 10^{-4} mol.L^{-1} L-cysteine in pH 4 buffer solution on bare gold and SAM modified gold electrode.

Figure 5.4A shows CVs of L-cysteine oxidation at (i) bare gold electrode, (ii) Au-ME SAM and (iii) Au-ME-FeTCAPc SAM. At bare gold electrode there was no peak observed for cysteine detection. On Au-ME SAM the oxidation peak due to cysteine oxidation was observed around 0.60 V (vs Ag|AgCl) as was the case above in Figure 5.1. The cysteine oxidation peak shifted to less positive potential values, i.e. 0.47 V (vs Ag|AgCl) at Au-ME-FeTCAPc SAM compared to 0.60 V (vs Ag|AgCl) at Au-ME SAM. The shape of the peak obtained with Au-ME-FeTCAPc SAM shows clear electrocatalytic behaviour: (1) a peak shift to less positive potential values; (2) enhanced peak currents; (3) higher slope at inclining part of the peak and better defined peak shaped wave are observed. Similar results were also observed at other MTCAPc modified electrodes, i.e. Au-ME-CoTCAPc SAM and Au-ME-MnTCAPc SAM. The other work only gave one oxidation peak for cysteine detection in Figure 5.4B(ii) for Au-ME-CoTCAPc SAM at 0.48 V and this could be attributed to the more effective coverage of the Au-ME SAM as longer reaction times were employed. The cysteine oxidation peak was at 0.48 V for Au-ME-CoTCAPc SAM in Figure 5.4B(ii) and the reduction peak in Figure 5.4B(i) at 0.50 V is due to $Co^{III}Pc/Co^{II}Pc$ oxidation peak. For Au-ME-MnTCAPc SAM in Figure 5.4C(ii) the observed cysteine oxidation peak was at 0.47 V. In comparison to other MPc-SAM modified gold electrode (results summarized in Table 1.2 in chapter 1) the peak potentials for the oxidation of cysteine studied in this work are in the same range as those reported for the thiol derivatized MPc SAM [55,57,58] and axial ligand immobilized MPc SAM [60] on gold electrodes. In comparison to the work discussed above for Au-ME-CoTCAPc SAM, where two oxidation peaks for cysteine at 450 mV (**II**) and 670 mV (**I**) were observed, mediated by Au-ME-CoTCAPc SAM and Au-ME SAM, respectively.

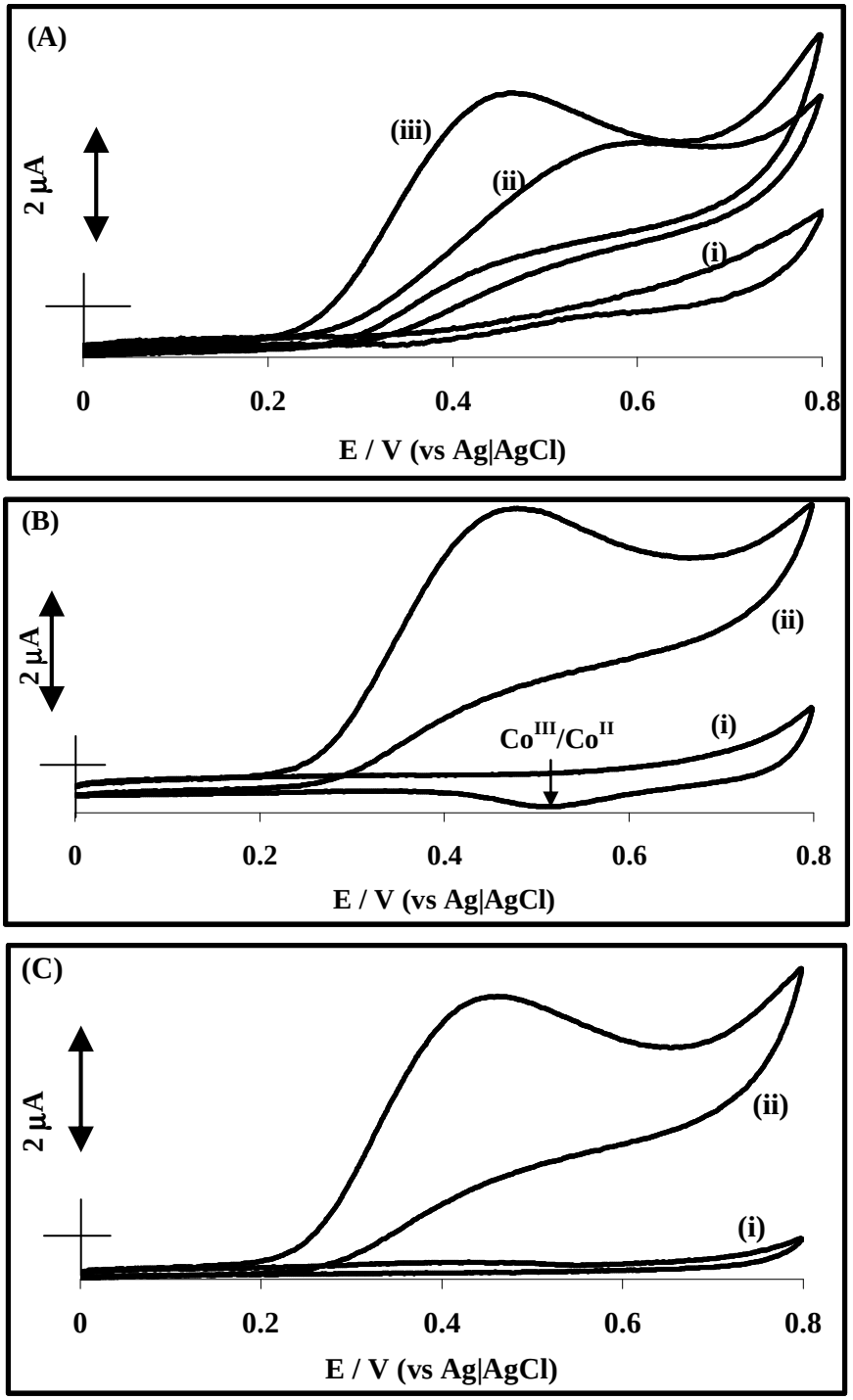

Figure 5.4: Cyclic voltammograms responses of (A) (i) bare gold electrode, (ii) Au-ME SAM and (iii) Au-ME-FeTCAPc SAM in pH 4 solution containing 1 x 10^{-4} mol.L^{-1} cysteine. (B) Au-ME-CoTCAPc SAM and (C) Au-ME-MnTCAPc SAM (i) without and (ii) with 1 x 10^{-4} mol.L^{-1} cysteine in pH 4 solution. Scan rate = 50 mV/s.

The detection of cysteine at 0.47 V for Au-ME-FeTCAPc SAM and 0.48 V for Au-ME-CoTCAPc SAM occurs near the formal potential for the metal oxidation ($M^{III}Pc/M^{II}Pc$), especially that of Au-ME-CoTCAPc SAM, thus suggesting that the metal oxidation-based process is involved in the catalytic oxidation of L-cysteine. The FeTCAClPc complex has been discussed earlier to show metal oxidation process (Fe^{III}/Fe^{II}) at 0.2 V and ring redox process at 0.8 V (Table 3.1). The ring process is too high for it to be involved in the oxidation of L-cysteine, hence the metal redox couple was proposed to participate in the mechanisms below (equation 5.5 – 5.8). The metal oxidation couple is known to catalyze the oxidation of cysteine as shown in equation 5.1 – 5.4 for Au-ME-CoTCAPc SAM and for Au-ME-FeTCAPc SAM the mechanism is shown in equations 5.5 to 5.8:

$$Fe^{II}TCAPc \longrightarrow [Fe^{III}TCAPc]^{+} + e^{-} \quad (5.5)$$

$$[Fe^{III}TCAPc]^{+} + RSH \longrightarrow [RSH\text{-}Fe^{III}TCAPc]^{+} \quad (5.6)$$

$$[RSH\text{-}Fe^{III}TCAPc]^{+} \longrightarrow Fe^{II}TCAPc + RS^{\bullet} + H^{+} \quad (5.7)$$

$$2RS^{\bullet} \longrightarrow RSSR \quad (5.8)$$

where RSH and RSSR are as defined above.

The mechanisms discussed above involve the metal oxidation couple ($M^{III}Pc/M^{II}Pc$) in equations 5.1 and 5.5. However, for $Mn^{III}Pc$ complexes the metal oxidation ($M^{III}Pc/M^{II}Pc$) normally occurs at negative potentials (-0.20 V) as shown in Figure 3.4 (chapter 3) and also reported in literature [228,229]. The $Mn^{III}Pc$ complexes are known to undergo metal oxidation ($Mn^{IV}Pc/Mn^{III}Pc$) at positive potentials as shown in Table 3.1 and reported in literature [178,196,228,229]. The peak due to cysteine oxidation at 0.47 V is in range for the observed broad oxidation peak ($Mn^{IV}TCAPc/Mn^{III}TCAPc$) at approximately 0.4 V in Figure 4.2C(iii).

Therefore, this metal oxidation catalyzes the cysteine oxidation following the mechanism shown in equation 5.9 – 5.12:

$$Mn^{III}TCAPc \longrightarrow [Mn^{IV}TCAPc]^{+} + e^{-} \quad (5.9)$$

$$[Mn^{IV}TCAPc]^{+} + RSH \longrightarrow [RSH\text{-}Mn^{IV}TCAPc]^{+} \quad (5.10)$$

$$[RSH\text{-}Mn^{IV}TCAPc]^{+} \longrightarrow Mn^{III}TCAPc + RS^{\bullet} + H^{+} \quad (5.11)$$

$$2RS^{\bullet} \longrightarrow RSSR \quad (5.12)$$

RSH and RSSR are as defined above.

Cysteine coordination to $Co^{III}Pc$ derivatives (equation 5.2) has been reported before [113]. The coordination of cysteine to the oxidized state of $Fe^{III}TCAClPc$ and $Mn^{IV}TCAClPc$ (as observed in equation 5.6 and 5.10 in mechanisms above) was confirmed by recording spectra with and without cysteine as shown in Figure 5.5, which shows the spectral changes observed upon chemical oxidation with bromine (Br_2) of complexes followed by addition of cysteine to the oxidized complexes. Again unhydrolyzed MTCAClPc complexes were used in this work and these experiments were conducted dry DMF to prevent the hydrolysis in water.

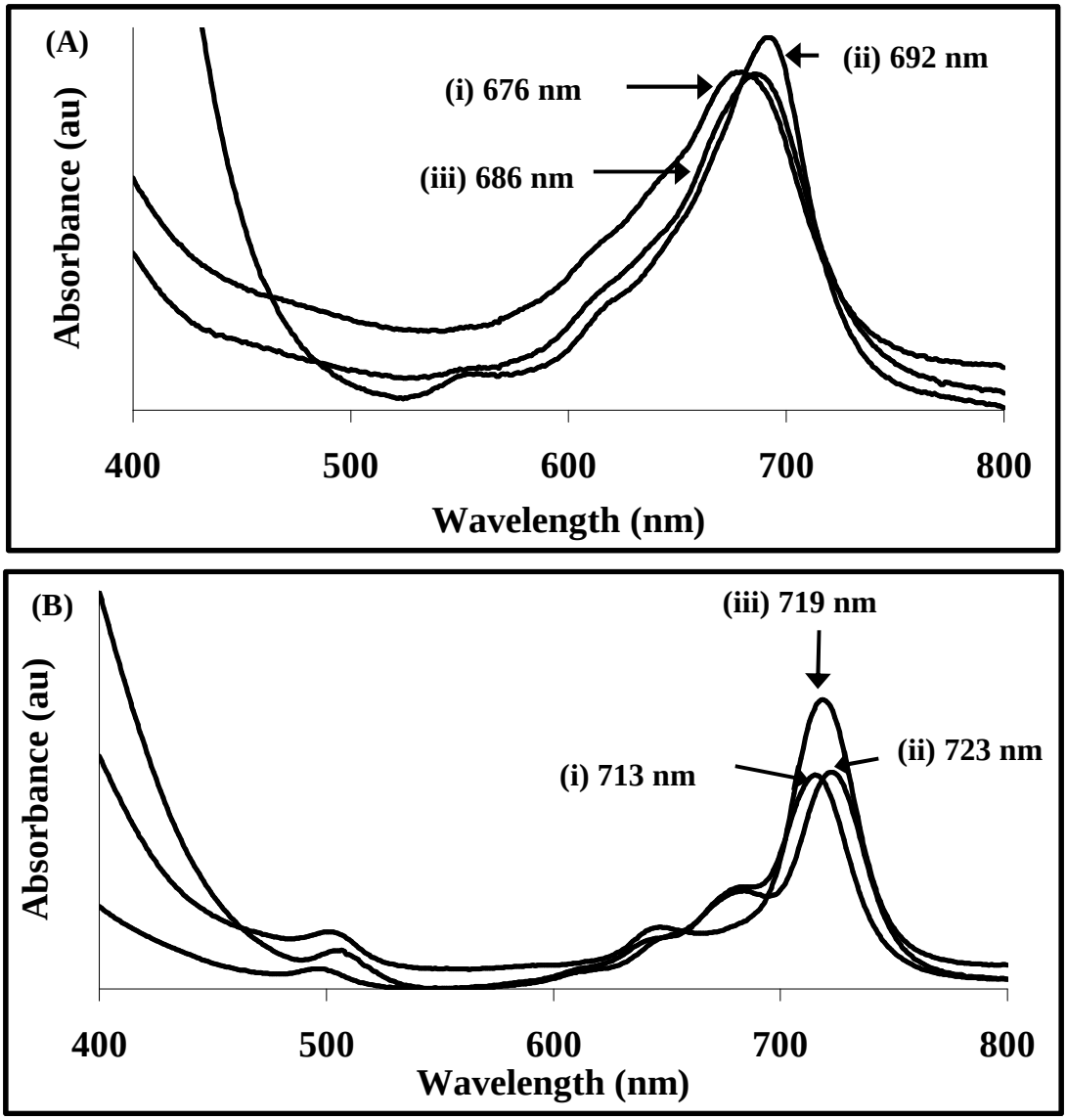

Figure 5.5: Spectroscopic changes observed for oxidation of A(i) Fe^{II}TCAClPc to (ii) Fe^{III}TCAClPc and (iii) coordination of cysteine to Fe^{III}TCAClPc. (B)(i) Mn^{III}TCAClPc to (ii) Mn^{IV}TCAClPc and (iii) coordination of cysteine to Mn^{IV}TCAClPc in dry DMF.

Figure 5.5A shows the oxidation of (i) Fe^{II}TCAClPc with the Q band at 676 nm to form (ii) the oxidized Fe^{III}TCAClPc with the Q band at 692 nm upon exposure to Br_2 fumes and (iii) the addition of cysteine to the oxidized Fe^{III}TCAClPc. The Q band shifts from 676 nm to 692 nm (24 nm) is due to the formation of Fe^{III}TCAClPc [104] typical of metal oxidation. Upon

introduction of cysteine the Q band shift to 686 nm. This shift (6 nm) in Q band after the introduction of cysteine is typical of axial ligation [113], thus confirming the coordination of cysteine (equation 5.6). Also for the manganese complex (MnTCAClPc) the spectral changes in Figure 5.5B shows that the oxidation of (i) Mn^{III}TCAClPc with a Q band at 713 nm results in the generation of (ii) Mn^{IV}TCAClPc with a Q band at 723 nm. The shift (10 nm) in Q band from 713 nm to 723 nm could be attributed to the generation of Mn^{IV}TCAClPc upon exposure to Br_2 fumes which results in the oxidation of the central metal ion [104]. This shift of a Q band which takes place without much change in intensity is known metal oxidation process [104,113]. The Q band of the oxidized Mn^{IV}TCAClPc species shifted from 723 nm to 719 nm (4 nm) when cysteine was added (Figure 5.5B (iii)) and this Q band shift is attributed to the coordination of cysteine to Mn^{IV}TCAPc. These results confirm the mechanism for cysteine oxidation as proposed in equations (5.1-5.4), (5.5-5.8) and (5.9-5.12) for Au-ME-CoTCAPc SAM, Au-ME-FeTCAPc SAM and Au-ME-MnTCAPc SAM, respectively.

Quantitative analysis of cysteine was achieved from the linear variation of peak current as a function of cysteine concentration. Figure 5.6 shows the increase in peak current as cysteine concentration increases at (A) Au-ME-CoTCAPc SAM, (B) Au-ME-FeTCAPc SAM and (C) Au-ME-MnTCAPc SAM and the linear relationship plots of peak current (I_P) versus cysteine concentration.

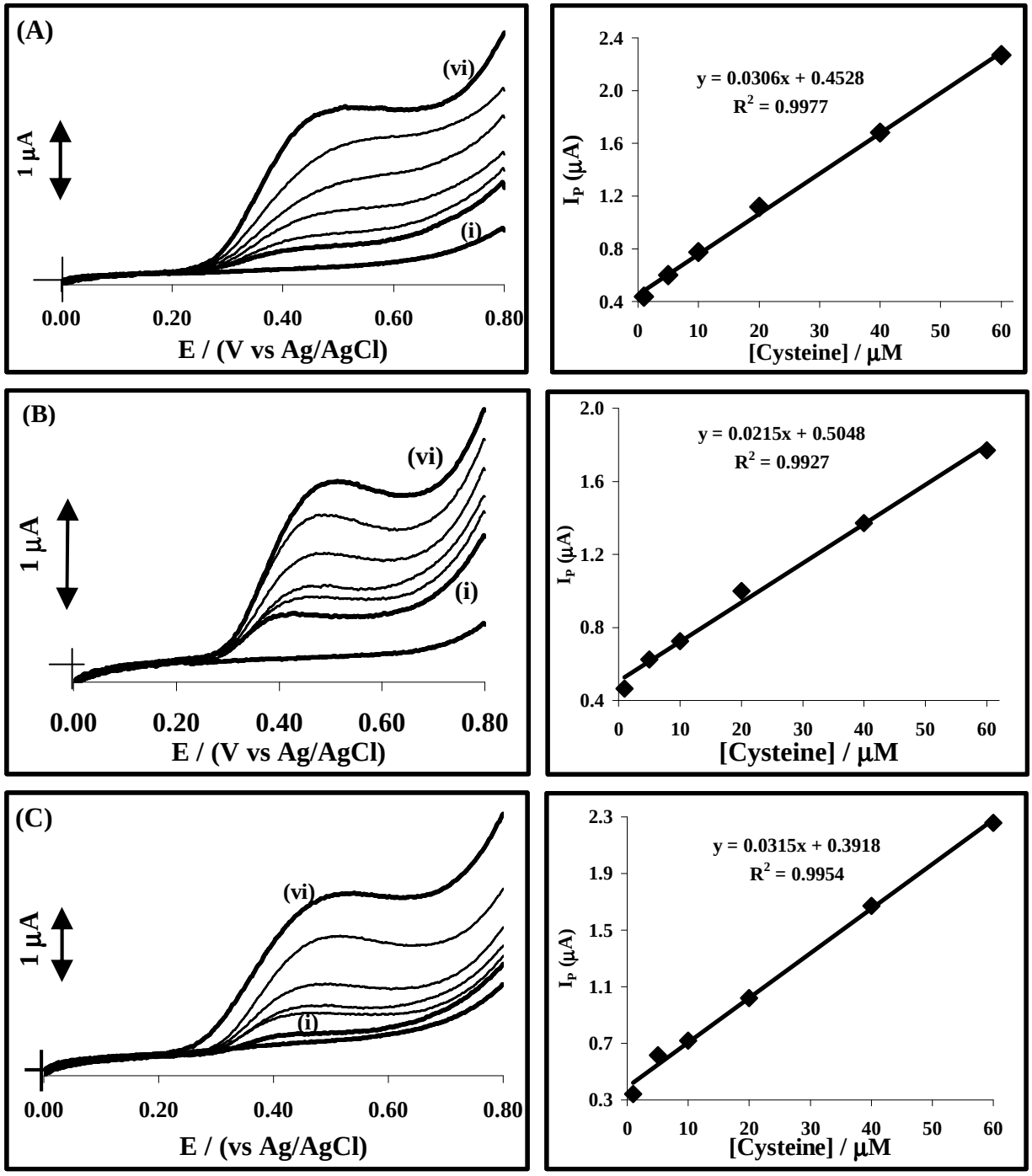

Figure 5.6: Cyclic voltammetric responses of catalytic oxidation of L-cysteine at (A) Au-ME-CoTCAPc SAM, (B) Au-ME-FeTCAPc SAM and (C) Au-ME-MnTCAPc SAM at varying concentrations: (i) 1 µmol.L^{-1}, (ii) 5 µmol.L^{-1}, (iii) 10 µmol.L^{-1}, (iv) 20 µmol.L^{-1}, (v) 40 µmol.L^{-1} and (vi) 60 µmol.L^{-1}. Alongside are linear plots of peak current vs cysteine concentration.

The increase in concentration of cysteine was linear (as observed in Figure 5.6) within the studied concentration range up to 60 μmol.L^{-1}. The limit of detection (LoD, mol.L^{-1}) based on a signal to noise ration of 3, was found to be 5.0 x 10^{-7} mol.L^{-1}, 3.4 x 10^{-7} mol.L^{-1} and 8.9 x 10^{-7} mol.L^{-1} for Au-ME-CoTCAPc SAM, Au-ME-FeTCAPc SAM and Au-ME-MnTCAPc SAM, respectively. These values are within the reported values for SAM modified gold electrodes, results shown in Table 5.1.

Table 5.1: Comparative peak potential (E_P), peak current density (I_P) and limits of detection (LoD) for the electro-oxidation of L-cysteine in pH 4.0 conditions for MPc-SAM modified electrodes.

MPc SAM	**L-cysteine (1.0 x 10^{-4} mol.L^{-1})**			**Ref.**
	E_P (V)	**Ip (μA.cm^{-2})**	**LoD (x 10^{-7} mol.L^{-1})**	
CoTCAPc	0.48 (0.450)[a]	229.4	5.0	This work
FeTCAPc	0.47	219.4	3.4	
MnTCAPc	0.47	216.4	8.9	
CoOBTPc	0.42	_____	3.1	[55]
CoOHETPc	0.50	_____	5.2	[24]
FeOBTPc	0.33	_____	3.0	[23]
FeOHETPc	0.38	_____	5.2	[24]
CoPc	0.20	13.92	_____	[60]
FePc	0.18	16.41	_____	[60]
MnPc	0.20	9.95	_____	[60]

[a] value obtained from studies of cysteine at Au-ME-CoTCAPc SAM which showed two oxidation peaks.

Abbreviations: CoOBTPc (cobalt octabutylthiophthalocyanine), CoOHETPc (cobalt octahydroxyethylthiophthalocyanine), FeOBTPc (iron octabutylthiophthalocyanine), FeOHETPc (iron octahydroxyethylthiophthalocyanine).

The stability of the MTCAPc SAM modified electrodes were investigated by subjecting the modified electrodes to repetitive cycling (10 scans) where the variation of the peak with the scan number at the fixed concentration of cysteine, i.e. 1.0×10^{-4} mol.L^{-1}. Figure 5.7 shows the catalytic peak decrease as the scan number increases for (A) Au-ME-CoTCAPc SAM, (B) Au-ME-FeTCAPc SAM and (C) Au-ME-MnTCAPc SAM in pH 4.0 buffer solution. A decrease of about 59% in peak currents was obtained for all three modified electrodes after the first cycle and stabilized after the fifth cycle. The loss of catalytic current after the first cycle may be attributed to the poisoning of the modified electrode by cystine (oxidation products of L-cysteine). This means that cystine is physically adsorbed onto the electrode and responsible for the electrode fouling. However, the electrode surface can be renewed by rinsing with copious amounts of pH 4 buffer solution and the initial catalytic current was obtained. The modified electrode if stored in pH 4 phosphate buffer solution can be reused for at least a month and this stability is attributed to the phthalocyanine ring-system protecting the sulfur-group.

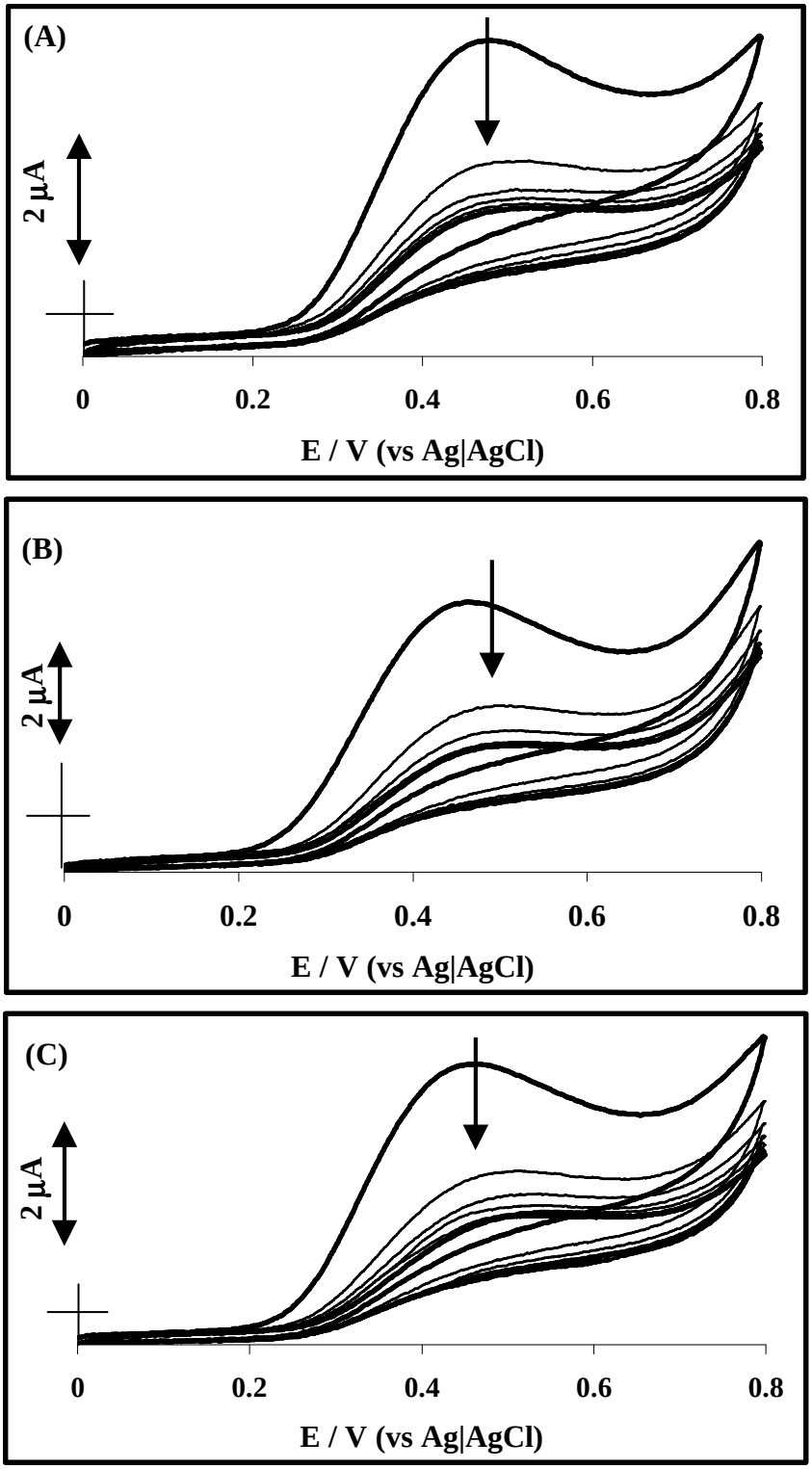

Figure 5.7: Repetitive cyclic voltammogram of 1.0 x 10^{-4} mol.L^{-1} L-cysteine at (A) Au-ME-CoTCAPc SAM, (B) Au-ME-FeTCAPc SAM and (C) Au-ME-MnTCAPc SAM modified gold electrode in pH 4.0 buffer solution: 10 repetitive CV cycles. Scan rate = 50 mVs^{-1}.

5.2 Electrocatalytic applications of SAM modified Au-electrode towards H_2O_2

Hydrogen peroxide (H_2O_2) oxidation was investigated in this work because of its important properties in both biomedical and industrial samples. Figure 5.8 shows the cyclic voltammograms of MTCAPc SAM modified gold electrode with (A) Au-ME-CoTCAPc SAM, (B) Au-ME-FeTCAPc SAM and (C) Au-ME-MnTCAPc SAM in PBS (pH 7.0) (i) without and (ii) with 1.0 x 10^{-4} mol.L^{-1} hydrogen peroxide, in phosphate buffer (pH 7.0). For all the modified electrodes in the absence of H_2O_2, an irreversible peaks were observed at -200 mV on Au-ME-CoTCAPc SAM (Figure 5.8A(i)), -0.35 V on Au-ME-FeTCAPc SAM (Figure 5.8B(i)) and at -0.35 V on Au-ME-MnTCAPc SAM (Figure 5.8C(i)). This peak corresponds to metal reduction ($M^{II}Pc/M^{I}Pc$), i.e. $Co^{II}Pc/Co^{I}Pc$ (also shown in Figure 4.4 by KOH medium) for Au-ME-CoTCAPc SAM and $Fe^{II}Pc/Fe^{I}Pc$ for Au-ME-FeTCAPc SAM. For Au-ME-MnTCAPc SAM this peak could be attributed to metal reduction from $Mn^{III}Pc/Mn^{II}Pc$ as this process is within the potential range known for this metal reduction process. In the presence of H_2O_2, in Figure 5.8A(ii) for Au-ME-CoTCAPc SAM shows the electrocatalytic oxidation and the reduction of H_2O_2 with peaks at 600 mV and -200 mV, respectively. However, at Au-ME-FeTCAPc SAM in Figure 5.8B(ii) and at Au-ME-MnTCAPc SAM in Figure 5.8C(ii) there were no well-defined peaks observed, only increase in currents for both oxidation and reduction. This absence of the oxidation or reduction peak, as compared to Figure 5.8A(ii), can be attributed to the decomposition of H_2O_2 at the Au-ME-FeTCAPc SAM and Au-ME-MnTCAPc SAM. FePc complexes are known to degrade H_2O_2 following the Fenton reaction [125] and also on exposure to FePc complexes [230,231]. Since similar results were obtained for Au-ME-MnTCAPc SAM in Figure 5.8C(ii) similar conclusion can be drawn that the Au-ME-MnTCAPc SAM layer decomposes H_2O_2.

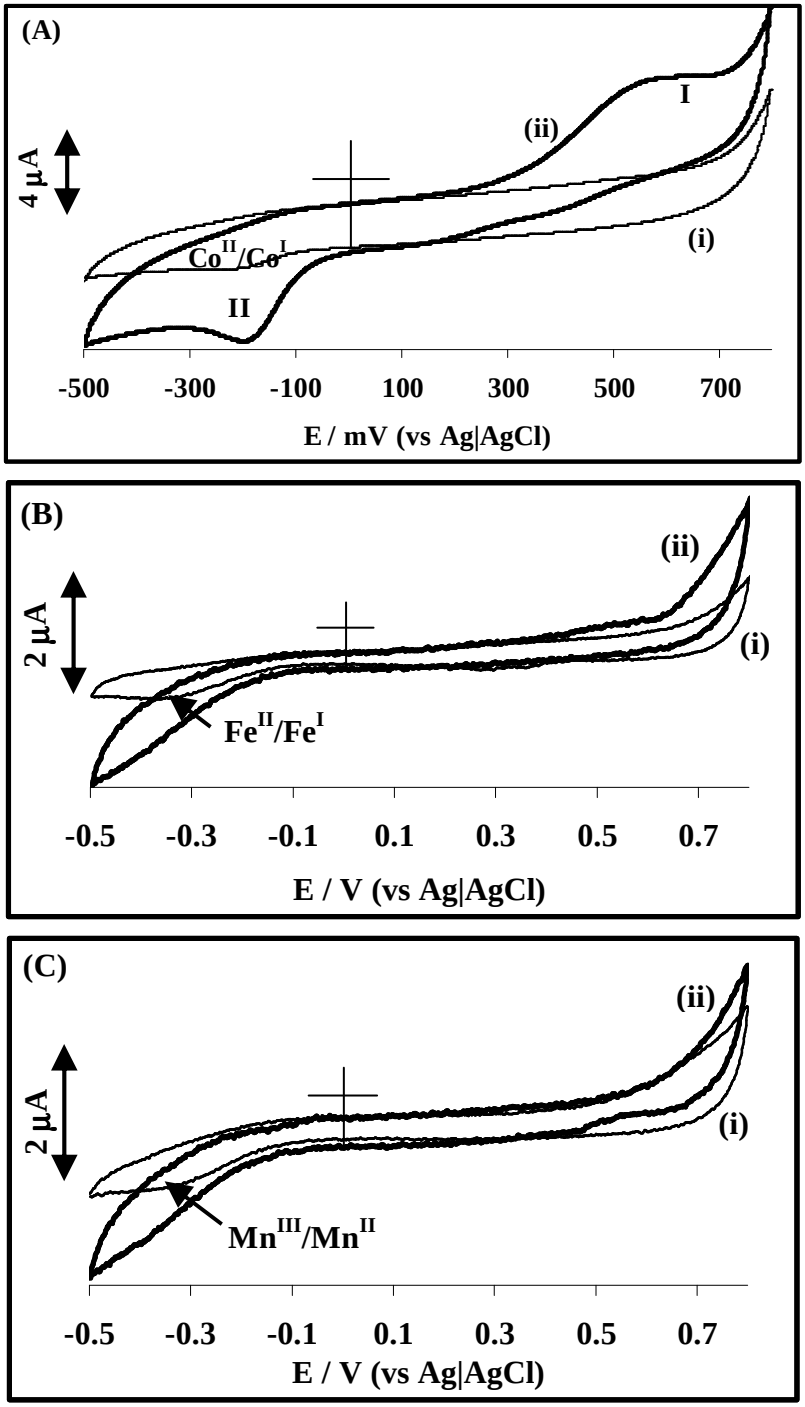

Figure 5.8: Cyclic voltammograms of (A) Au-ME-CoTCAPc SAM, (i) without and (ii) with 1.0 x 10^{-4} mol.L^{-1} H_2O_2 in PBS (pH 7.4) solution, (B) Au-ME-FeTCAPc SAM and (C) Au-ME-MnTCAPc SAM, (i) without and (ii) with 1.0 x 10^{-4} mol.L^{-1} H_2O_2 in PBS (pH 7.0) solution.

The Au-ME-CoTCAPc SAM showed good results as it is discernible from Figure 5.8A(ii) that Au-ME-CoTCAPc SAM mediates the oxidation and reduction of H_2O_2 at peaks labeled **I** and **II**, respectively. From these results then Au-ME-CoTCAPc SAM was further studied for catalytic activity towards H_2O_2 and the possible mechanisms for these observations are summarized in equations (5.13) – (5.16):

$$Co^{II}TCAPc \longrightarrow [Co^{III}TCAPc]^{+} + e^{-} \quad (5.13)$$

$$[Co^{III}TCAPc]^{+} + \tfrac{1}{2}H_2O_2 \longrightarrow \tfrac{1}{2}O_2 + H^{+} + Co^{II}TCAPc \quad (5.14)$$

$$Co^{II}TCAPc + e^{-} \longrightarrow [Co^{I}TCAPc]^{-} \quad (5.15)$$

$$[Co^{I}TCAPc]^{-} + \tfrac{1}{2}H_2O_2 + H^{+} \longrightarrow H_2O + Co^{II}TCAPc \quad (5.16)$$

It is clear from Figure 5.8A(ii) that on addition of H_2O_2, there is an enhancement of currents in the region of $Co^{III}TCAPc/Co^{II}TCAPc$ hence this couple catalyzes the H_2O_2 oxidation, with peak labeled **I**. Furthermore, H_2O_2 catalytic reduction peak was observed at the region where $Co^{II}TCAPc/Co^{I}TCAPc$ occurred in Figure 5.8A(i), therefore this couple catalyzes the H_2O_2 reduction, with a peak labeled **II**. Based on these observations, equation 5.13 and 5.14 corresponds to the H_2O_2 oxidation and equations 5.15 and 5.16 correspond to the H_2O_2 reduction. Equations 5.13 and 5.14 are known mechanistic steps for the oxidation of H_2O_2 at CoPc modified electrodes [120,148]. First the metal oxidation takes place from $Co^{II}TCAPc$ to $Co^{III}TCAPc$ (equation 5.13), followed by oxidation of H_2O_2 to molecular oxygen as the metal is reduced back to $Co^{II}TCAPc$ (equation 5.14). Equation 5.15 and 5.16 are proposed mechanistic steps for the reduction of H_2O_2 at Au-ME-CoTCAPc SAM modified gold electrode. The metal reduction takes place from $Co^{II}TCAPc$ to $Co^{I}TCAPc$ (equation 5.15), followed by the reduction of H_2O_2 to water as the metal is oxidized to from $Co^{I}TCAPc$ to $Co^{II}TCAPc$ (equation 5.16).The oxidation of H_2O_2 at CoPc modified electrode is known [120,148], however the reduction of

H_2O_2 has only been done at enzyme modified electrode [152] and no report of H_2O_2 reduction at CoPc modified electrode. Therefore, the proposed reduction mechanism for H_2O_2 was further investigated using spectroscopic methods whereby first the generation of Co^{I}TCAPc from Co^{II}TCAPc was achieved using a strong reducing agent, $NaBH_4$. Figure 5.9 shows the spectral changes (A) upon reducing the Co^{II}TCAPc to Co^{I}TCAPc and (B) the addition of H_2O_2 at Co^{I}TCAPc generated in (A).

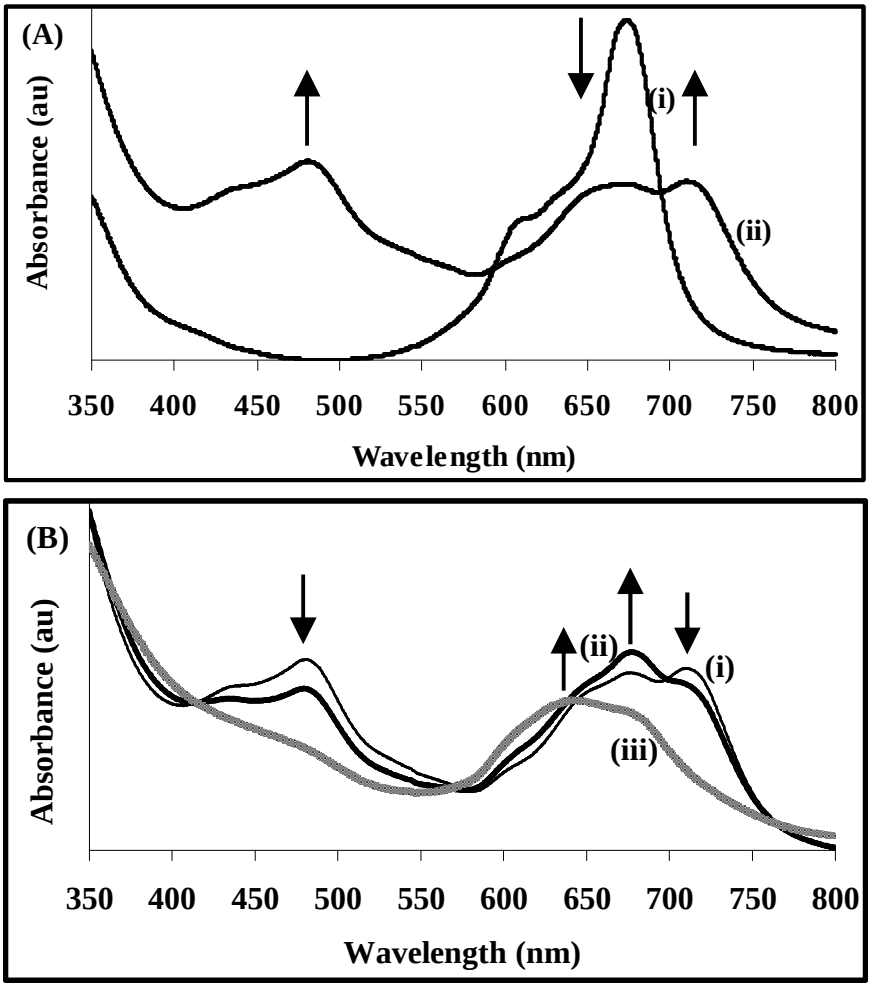

Figure 5.9: (A) UV-vis spectral changes observed during the reduction of Co^{II}TCAPc to Co^{I}TCAPc (i) before and (ii) after adding $NaBH_4$ in DMF. (B) Changes observed (i) before, (ii) after addition of H_2O_2 in DMF and (iii) further oxidation in the presence of H_2O_2 reaction left for a longer period. First trace in (B)(i) is the same as the last trace in (A)(ii).

Figure 5.9A is a typical spectrum showing the generation of Co^{I}TCAPc upon adding $NaBH_4$ in dry DMF (to prevent hydrolysis in water) solution of Co^{II}TCAPc. The Q band at 676 nm decreased in intensity while new bands at 710 and 480 nm appear as the reduction process continues, Figure 5.9A(ii). These changes are known for the reduction of CoPc complexes and the absorption band at 480 nm is typical of Co^{I}TCAPc species [95]. Following the formation of Co^{I}TCAPc species, addition of H_2O_2 resulted in the oxidation of Co^{I}TCAPc back to Co^{II}TCAPc (Figure 5.9B(ii)) as evidenced by the decrease in bands at 710 and 480 nm and a slight increase of a Q band at 676 nm, confirming the regeneration of Co^{II}TCAPc. The spectra of the regenerated Co^{II}TCAPc did not completely go back to the original spectra as observed in Figure 5.9A(i), which consisted of mainly a monomer, but showed aggregation when left to react with H_2O_2 over a long period as shown by a dimer peak at 638 nm, Figure 5.9B(iii).These spectral changes proved the regeneration of Co^{II}TCAPc in the presence of H_2O_2 even though aggregated.

The analysis of H_2O_2 was achieved by chronoamperometric experiments at neutral pH conditions (pH 7.4). Figure 5.10A shows the typical chronoamperomogram of Au-ME-CoTCAPc SAM upon consecutive additions of H_2O_2 at fixed oxidative potential (600 mV). The response of Au-ME-CoTCAPc SAM modified gold electrode was investigated under stirring in PBS (pH 7.4) solution with 0.5 $\mu mol.L^{-1}$ H_2O_2 added in steps. A base line was established in 10 ml of PBS (pH 7.4) solution. A well-defined current response due to H_2O_2 oxidation was observed with successive increments of H_2O_2 concentration in solution (indicated by arrows). However, the successive addition of 0.5 $\mu mol.L^{-1}$ H_2O_2 led to the decrease in current response, signifying saturation in concentration. Figure 5.10B displays the calibration curve (the plot of current response versus the concentration of H_2O_2) for Au-ME-CoTCAPc SAM.

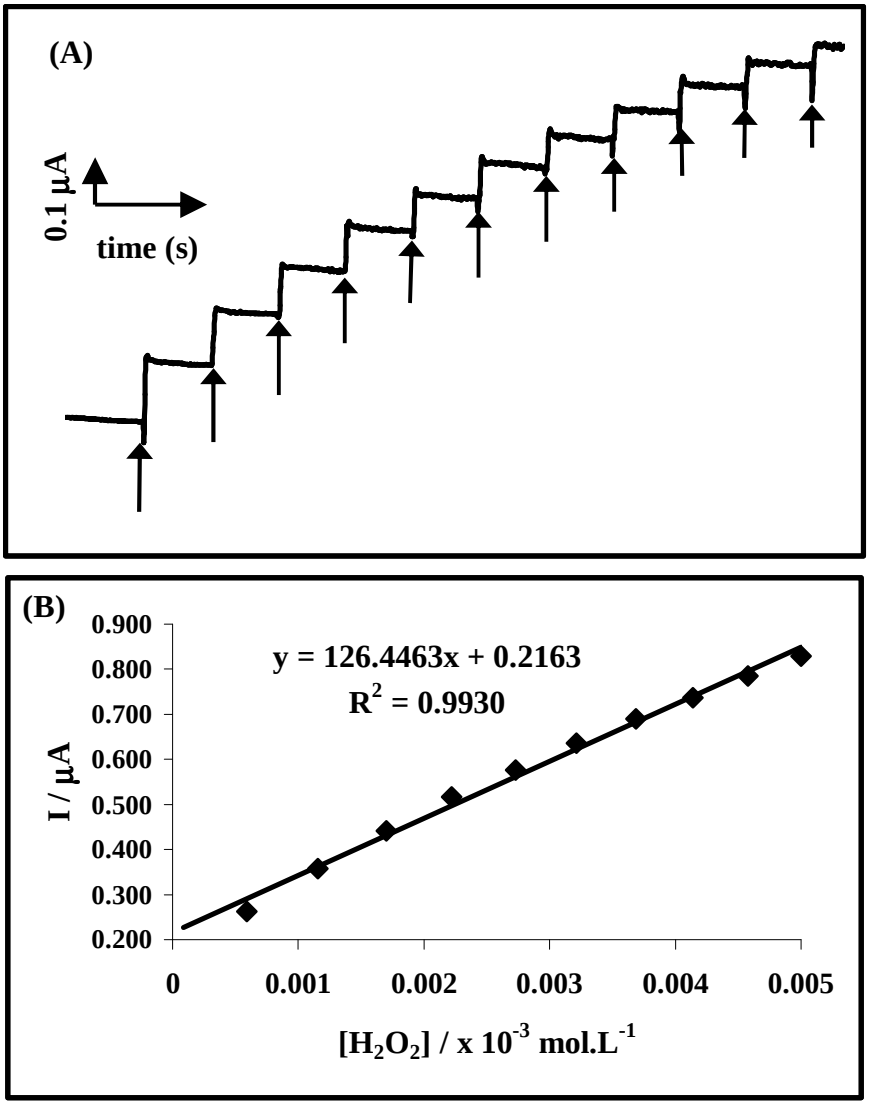

Figure 5.10: (A) Amperometric current response of Au-ME-CoTCAPc SAM on addition (indicated by arrows) of 1.0 x 10^{-4} mol.L^{-1} H_2O_2 in 0.01 mol.L^{-1} PBS solution at 600 mV applied potential. (B) is the linear plot of steady-state current versus concentration of H_2O_2.

The curve of steady-state current versus concentration of H_2O_2 in Figure 5.10B, yielded a straight line within the studied concentration range (0.5 – 5 µmol.L^{-1}) with the correlation coefficient of 0.993. The limit of detection (LoD) was found to be 4.0 x 10^{-7} mol.L^{-1} at 3σ and the electrode gave a best response time of approximately 1 second to the additions of H_2O_2. The

electrode gave the best results towards the electrocatalytic oxidation of H_2O_2 than the recent reports which gave a LoD of 8.0 x 10^{-6} mol.L^{-1} for the detection of H_2O_2 using (i) carbon paste electrodes modified with nanostructured cryptomelane-type manganese oxides [147], (ii) glassy carbon electrode modified with $CoPc(CoTPP)_4$ using drop dry method [151] and (iii) horseradish peroxidase-colloid gold-based sensor [152], but performed less satisfactory compared to when the glassy carbon electrode combined with carbon nanotube and nano-platinum was employed [232] with a LoD of 25 x 10^{-9} mol.L^{-1}.

The analysis of H_2O_2 on the reduction side was also investigated. Figure 5.11A shows a typical chronoamperomogram of Au-ME-CoTCAPc SAM upon successive additions of H_2O_2 at applied reduction potential (-200 mV). The similar procedure applied for the oxidation of H_2O_2 was employed, except that the applied potential was -200 mV. The negative increase in current response due to the reduction of H_2O_2 was observed with the successive increments of 0.5 μmol.L^{-1} H_2O_2 concentration in solution (indicated by arrows). In the same way as the oxidation, the successive increase in concentration of H_2O_2 led to a decrease in current response as a result of saturation in concentration. Figure 5.11B displays the calibration curve of Au-ME-CoTCAPc SAM electrode which gave a linear plot within the studied concentration range 0.5-5 μmol.L^{-1} with the coefficient of 0.986. The LoD was found to be 2.0 x 10^{-7} mol.L^{-1} at 3σ and the electrode gave best response time of approximately 1 second to the additions of H_2O_2. Compared to most electrodes in Table 1.3 in chapter 1, this electrode gave best response time (1 s) and best LoD (2.0 x 10^{-7} mol.L^{-1}), but performed less satisfactory for reduction of H_2O_2 compared to gold-horseradish peroxidase-based sensor [143,144] which gave a limit of detection in the orders of 10^{-8} and 10^{-9} mol.L^{-1} as shown in Table 1.3 in chapter 1.

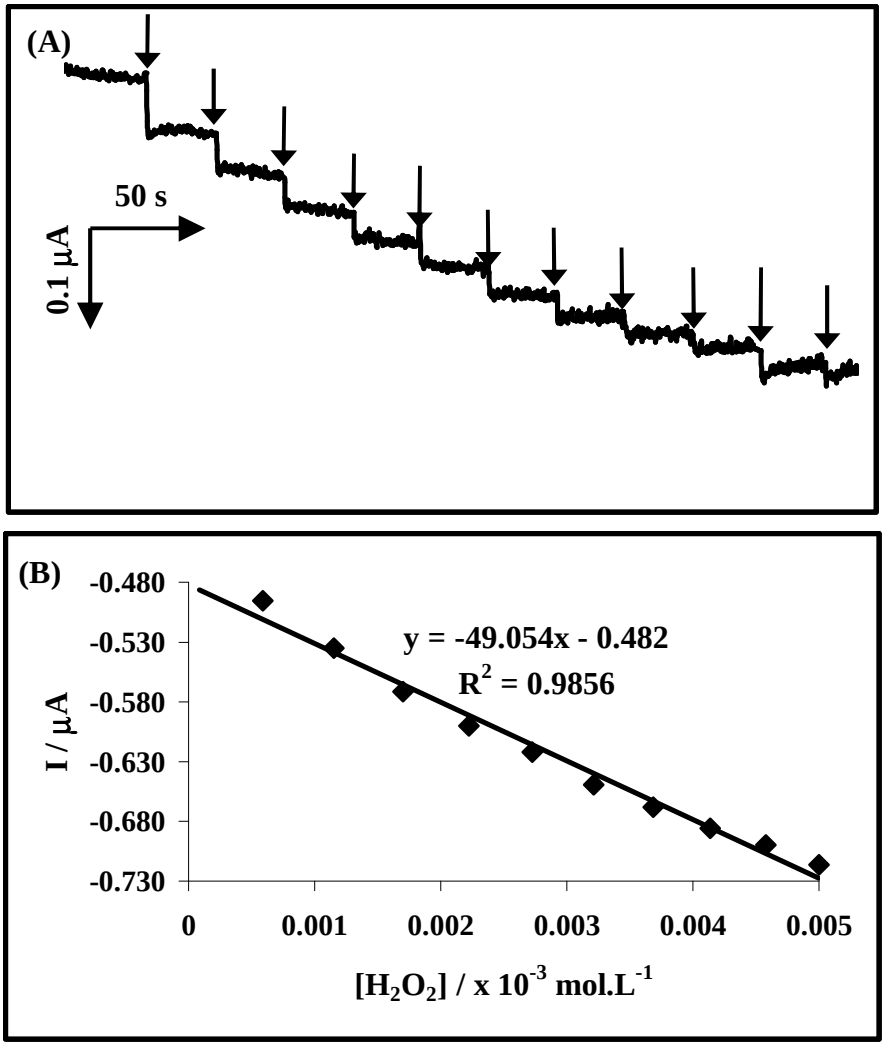

Figure 5.11: (A) Amperometric current response of Au-ME-CoTCAPc SAM on addition (indicated by arrows) of 1.0 x 10^{-4} mol.L^{-1} H_2O_2 in 0.01 mol.L^{-1} PBS solution at -200 mV applied potential. (B) is the linear plot of steady-state current versus concentration of H_2O_2.

Since the general mechanism for glucose oxidase (GOx) enzyme-based amperometric sensing involves a mediator (CoTCAPc in this work) as an electron mediator (Scheme 4.3) and Au-ME-CoTCAPc SAM showed good results for the detection of H_2O_2, the immobilized enzyme following Scheme 4.3 was then studied for glucose analysis.

5.3 Electrocatalytic applications of GOx-SAM modified electrode towards glucose

The oxidation potential of 600 mV (also used for H_2O_2 above) was chosen as the working potential for the detection of glucose on Au-ME-CoTCAPc-GOx SAM. Figure 5.12 shows the plot of current response of Au-ME-CoTCAPc-GOx SAM electrode as a function of glucose concentration, i.e. the plot of steady-state current (I_{SS}) versus concentration of glucose ($C_{glucose}$). Figure 5.12 (inset) shows a typical chronoamperomogram of Au-ME-CoTCAPc-GOx SAM upon successive additions of 0.3 mM glucose (indicated by arrows).

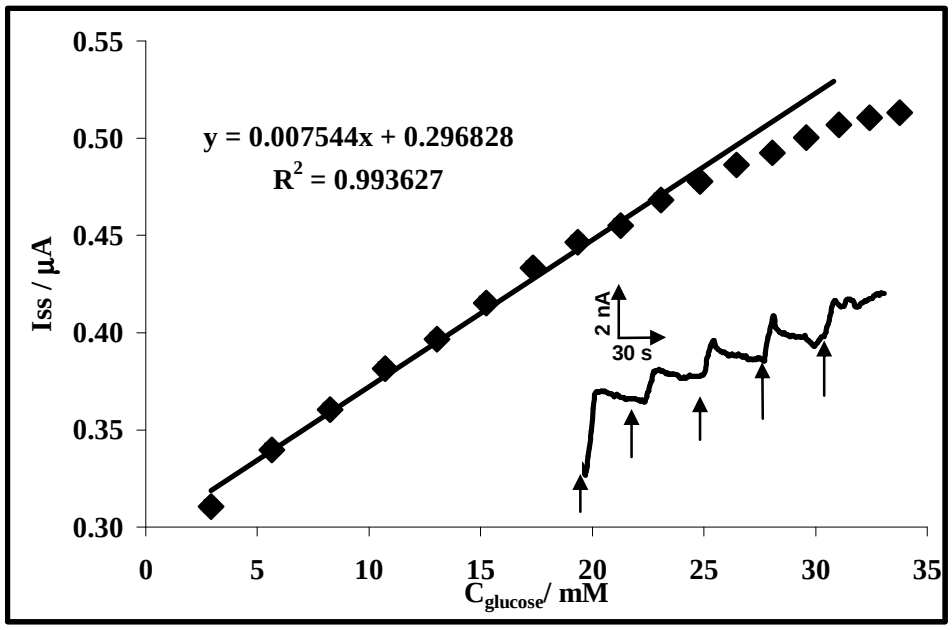

Figure 5.12: Calibration curve of current response of Au-ME-CoTCAPc-GOx SAM versus glucose concentration ($C_{glucose}$) in PBS (pH 7.4) solution. Inset: is the amperometric current response of Au-ME-CoTCAPc-GOx SAM on additions (indicated by arrows) of 0.1 mol.L^{-1} glucose in 0.01 mol.L^{-1} buffer pH 7.4 solution at 600 mV applied potential.

The calibration curve (Figure 5.12) is linear for the concentration range between 0.3 – 25 mM and a curvature at high concentration was observed. This linear concentration range of 0.3 – 25 mM is of advantage as is almost within the likely glucose level in normal and diabetic person which is 0.2 – 20 mM [131]. In comparison with the values of CoPc modified electrodes [117-123] as shown in Table 1.4 (chapter 1), this enzyme electrode gave a wide concentration range of up to 25 mM. The enzyme electrode (Au-ME-CoTCAPc-GOx SAM) exhibited a rapid response of 1 second to the changes of glucose concentrations indicating excellent electrocatalytic behaviour of this biosensor electrode. The LoD at 3σ was found to be 8.4 μM and this value was found to be similar to the value (LoD = 8.2 μM) obtained using a nano-gold particle by Zhang et al [172] and was slightly higher than other CoPc modified electrodes [117-123] in Table 1.4 (chapter 1) with LoD ranging from 0.2 to 5 μM. The sensitivity of the biosensor which is 7.5 nA/mM was obtained from the slope of the linear part of the calibration curve in Figure 5.12. At high glucose concentrations (above 25 mM) a current plateau was observed in Figure 5.12. The curvature from the initial straight line shows characteristics of Michaelis-Menten kinetics. The apparent Michaelis-Menten constant (K_m^{app}), which gives an indication of the enzyme-substrate kinetics for the biosensor (Au-ME-CoTCAPc-GOx SAM) electrode, can be calculated from an electrochemical version of Lineweaver-Burk [136,233] and Hanes [234] equations. Many reports on enzyme kinetics are based on Lineweaver-Burk, hence both are discussed in this thesis. The Lineweaver-Burk equation (5.17) follows:

$$\frac{1}{I_{SS}} = \frac{K_m^{app}}{i_{max}} \cdot \frac{1}{C_{glucose}} + \frac{1}{i_{max}} \qquad (5.17)$$

where I_{SS} is the steady-state current after the addition of the substrate, i_{max} is the maximum current measured under saturation of the substrate and $C_{glucose}$ is the concentration of the

substrate. The K_m^{app} value was calculated from the slope (K_m^{app}/i_{max}) and the intercept ($1/i_{max}$) from the plot of reciprocal steady-state current ($1/I_{SS}$) versus the reciprocal of glucose concentration ($1/C_{glucose}$) shown in Figure 5.13A. The K_m^{app} value for the Au-ME-CoTCAPc-GOx SAM was found to be 7.9 mM, which is smaller than the recently reported values for nano-CoPc (12.4 mM) [121] and CoPc-$(CoTPP)_4$ (14.91 mM) [123]. The smaller K_m^{app} value means that the immobilized enzyme (GOx) possesses a higher binding affinity for glucose. The data was also analyzed using the Hanes plot (Figure 5.13B), i.e. the plot of ($C_{glucose}/I_{SS}$) versus $C_{glucose}$ from the equation (5.18):

$$\frac{C_{glucose}}{I_{SS}} = \frac{C_{glucose}}{i_{max}} + \frac{K_m^{app}}{i_{max}} \qquad (5.18)$$

the symbols are the same as defined in Lineweaver-Burk equation (5.17). The K_m^{app} value was determined by the analysis of the slope ($1/i_{max}$) and the intercept (K_m^{app}/i_{max}) from Figure 5.13B. The K_m^{app} value was found to be 4.8 mM, noticeably smaller than 7.9 mM calculated using Lineweaver-Burk plot equation. According to Cornish-Bowden [234] the Lineweaver-Burk plot gives a grossly misleading impression of experimental errors hence over estimated K_m^{app} values, compared to Hanes plot which gives a fair range of experimental errors leading to more realistic K_m^{app} values. The results imply that the biosensor (Au-ME-CoTCAPc-GOx SAM) electrode with CoTCAPc as a mediator on gold electrode is actually valuable and sensitive.

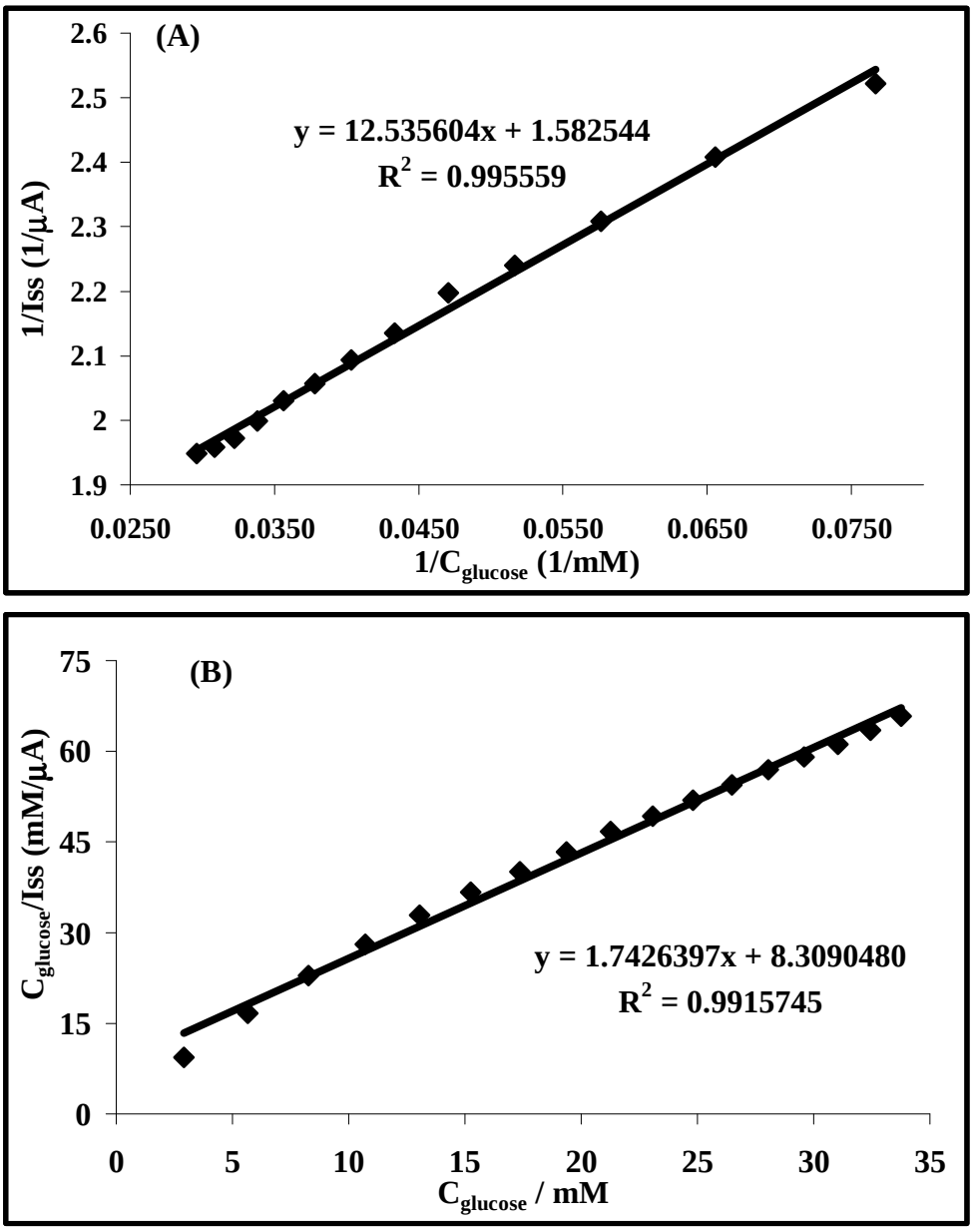

Figure 5.13: (A) Lineweaver-Burk ($1/I_{SS}$ versus $1/C_{glucose}$) plot and (B) Hanes ($C_{glucose}/I_{SS}$ versus $C_{glucose}$) plot, according to data in Figure 5.12.

5.3.1 Real sample analysis and interference studies at GOx SAM modified electrode

The applicability of the developed biosensor electrode (Au-ME-CoTCAPc-GOx SAM) towards real sample detection was assessed using a commercially available clinical ALPHA® glucose powder, chronoamperometrically. From standard addition method, the glucose content was 99.97 ± 0.06% (n = 7). The result is in conformity with the expected clinical glucose content and manufacturers' values. The results indicate that this sensor could successfully be applied for glucose detection and monitoring and also indicate the suitability of the developed biosensor (Au-ME-CoTCAPc-GOx SAM) towards a quick clinical analysis of glucose solution.

Another important analytical parameter for a biosensor is its ability to discriminate between the interfering species commonly present in similar physiological environment and the target analyte. The effect of the common electroactive interferents such as cysteine, ascorbic acid, oxalic acid and uric acid to the response of glucose with Au-ME-CoTCAPc-GOx SAM was investigated using the mixed solution method [235]. These interferent species were selected as they are likely to appear in biological and food samples. The concentration of these interfering species was chosen as the concentration close to their relevant clinical levels [170], i.e. in the orders of 10^{-4} M while that of the glucose was maintained at 10^{-3} M. The values of K_{amp} (where K_{amp} is the amperometric selectivity coefficient) were determined from equation (5.19) reported in literature [234] for the analysis in the presence of the interference species:

$$K_{amp} = \left(\frac{\Delta I_{mixture}}{\Delta I_{glucose}} - 1 \right) x \frac{[glucose]}{[Interference - species]} \qquad (5.19)$$

where $\Delta I_{mixture}$ and $\Delta I_{glucose}$ are respectively, the changes in current for the mixture containing glucose and interfering ions, and glucose alone.

Figure 5.14 shows the typical chronoamperomograms for Au-ME-CoTCAPc-GOx SAM modified gold electrode in (i) buffer (pH 7.4) solution, (ii) 5 mM glucose buffer solution and (iii) mixture of 5 mM glucose + 0.5 mM interfering species (L-cysteine) in pH 7.4 buffer solution. The chronoamperomograms are stopped once they have stabilized and the change in current (ΔI) values recorded.

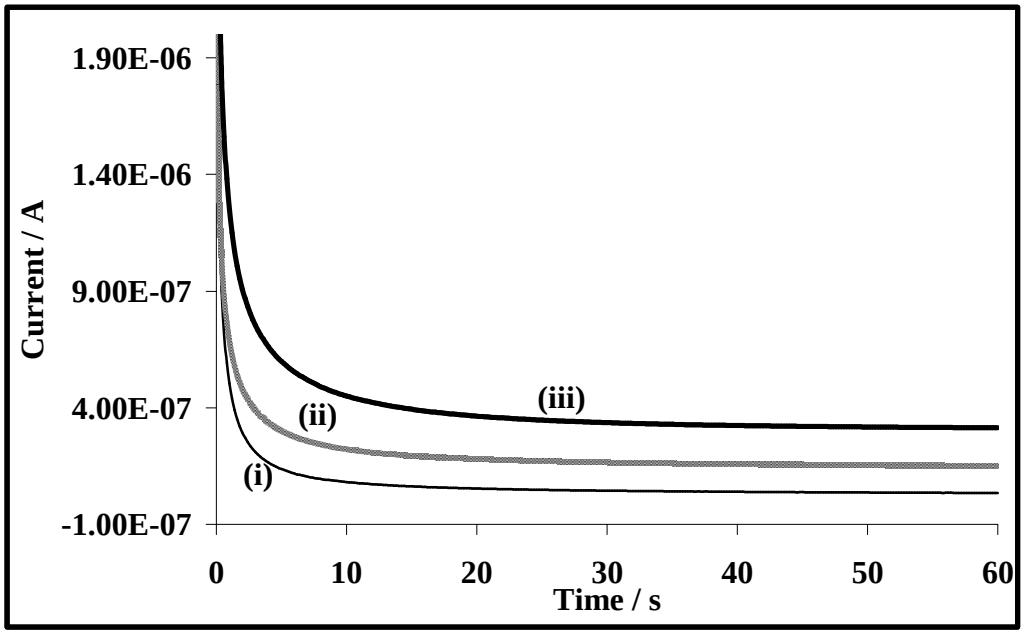

Figure 5.14: Chronoamperomograms of enzyme modified gold electrode (Au-ME-CoTCAPc-GOx SAM) in (i) buffer solution, (ii) 5 mM glucose buffer solution and (iii) 5 mM glucose + 0.5 mM L-cysteine in pH 7.4 buffer solution.

The estimated K_{amp} values (shown in Table 5.2) for the interfering species are: L-cysteine (8.25×10^{-3}), ascorbic acid (1.86×10^{-2}), oxalic acid (6.36×10^{-5}) and uric acid (8.97×10^{-3}). The K_{amp} value less than 10^{-3} (as for oxalic acid) indicates a non-interfering species and the K_{amp} value greater than 10^{-3} (as for ascorbic acid) indicates an interfering species [235]. However, if the K_{amp} values fall within orders of 10^{-3} (as for L-cysteine and uric acid), they indicate that the

species is an interferent but not a strong one. These K_{amp} values thus suggest that ascorbic acid is a strong interferent while the other species (uric acid, L-cysteine and oxalic acid) are relatively not interfering with glucose detection. Therefore the biosensor electrode (Au-ME-CoTCAPc-GOx SAM) can be successfully used for the detection of glucose in the presence of cysteine, oxalic acid and uric acid under the conditions employed in this thesis.

Table 5.2: Summary and conclusion of the results obtained for the interference studies.

Interference (concentration)	**L-Cysteine (0.5 mM)**	**Uric Acid (0.5 mM)**	**Oxalic Acid (0.5 mM)**	**Ascorbic Acid (0.5 mM)**
K_{amp}	8.25×10^{-3}	8.97×10^{-3}	6.36×10^{-5}	1.86×10^{-2}
Conclusion	Not a strong interferent	Not a strong interferent	Not an interferent	Strong interferent

5.3.2 Stability studies of the GOx-enzyme electrode

The long-term stability of the GOx-enzyme electrode (Au-ME-CoTCAPc-GOx SAM) was studied by recording the current response of the enzyme upon addition of glucose under stirring conditions. A steady decrease in current generated during successive days of measurements was observed and on the fourth day only 76% of the current response was retained. This current response dropped drastically on the fifth day to about 36% and this decrease in current response can be attributed to the continuous use of the electrode and also the loss of enzyme activity.

In conclusion, this chapter has demonstrated the potential electrocatalytic applications of the covalently immobilized metallophthalocyanines SAMs on gold electrode (Au-ME-MTCAPc SAM) towards the detection and analysis of biologically, industrially and biomedically important molecules, i.e. L-cysteine in acidic solution (pH 4) and hydrogen peroxide in neutral or physiological conditions (pH 7.4). Furthermore, this chapter has demonstrated the electrocatalytic applications of the covalently immobilized glucose oxidase enzyme-based biosensor towards the detection of glucose and the practical applications of this biosensor electrode in real sample analysis. The applications of the biosensor also demonstrated the efficiency of the metallophthalocyanine to be used as mediator, i.e. relay electrons between enzyme (GOx) and the gold electrode surface.

CONCLUSIONS

The metal tetra-carboxy acid chloride phthalocyanine complexes containing transition metals such as Co (**11**), Fe (**12**) and Mn (**13**) have been synthesized and characterized using spectroscopic methods such as infrared and UV-vis spectroscopy. The observed spectroscopic characterization of these complexes was comparable to similar complexes in literature. The MnPc complex (**13**) was further characterized using electrochemical methods which showed four redox couples and spectroelectrochemistry was employed to assign these redox processes.

The synthesized MPc complexes (**11-13**) were, for the first time, immobilized covalently onto a pre-modified gold electrode with 2-mercaptoethanol using self-assembling technique to yield a monolayer thin film of these MPc complexes. Electrochemical characterization, using cyclic voltammetry in $[Fe(CN)_6]^{3-}$ solution, of the modified gold electrodes showed that the SAMs show catalytic behaviour as evidenced by decrease in peak potential separation and are also permeable to solution ions. These results were also confirmed by the impedance spectroscopy, whereby the decrease in charge transfer resistance was observed upon modifying the gold electrode with 2-mercaptoethanol SAM and different MPc SAMs. The integrity of the SAM modified gold electrodes was investigated using electrochemical experiments in different aqueous solution. The results showed that SAMs partially blocks the gold oxide reactions (observed decrease in peak current), but the permeability of these SAMs still allow the solution ions to penetrate through the monolayer. Similar results were also observed for ferric ammonium sulphate solution in perchloric acid. However, the under-potential deposition (UDP) studies showed an excellent blocking behaviour as the deposition and stripping of copper metallic layer was completely blocked at modified gold electrode. The reductive desorption experiments gave the surface concentration in the orders of 10^{-10} mol.cm^{-2}, and this value is more than the reported surface concentration of flat lying MPc complexes suggesting that the MPc complexes

investigated in this thesis assume a perpendicular orientation. This orientation was expected as the coupling reaction occurs on one substituent of an MPc complex. The stability of the SAM modified electrode is dependent on the solution and the potential window used and the studies in this thesis were conducted in neutral to acidic pH conditions (pH <8). The potential window used was between -0.5 to +0.8 V (vs Ag|AgCl, 3.0 mol.L^{-1} NaCl) and this window was chosen so as to avoid oxidative or reductive desorption of SAMs.

The electrochemical characterization of the enzyme modified gold was conducted in neutral pH solutions (pH 7.4). In $Fe(CN)_6^{3-}$ solution, using cyclic voltammetry the increase in peak potential separation was observed showing blocking behaviour of the enzyme monolayer. Also the increase in charge transfer resistance using impedance spectroscopy was observed and this further confirmed the blocking behaviour of enzyme monolayer modified gold electrode. Quartz crystal microbalance experiments also showed the immobilization of the enzyme onto activated carboxylic acid CoPc SAM with the change in frequency of about -50 Hz, leading to a mass of about 1.10 μg of the covalently immobilized glucose oxidase enzyme monolayer.

Spectroscopic characterization (using x-ray photoelectron spectroscopy and Raman spectroscopy) confirmed the chemisorption of the 2-mercaptoethanol and MPc complexes on gold electrode by forming a thiolate (Au-S) bond. Furthermore, XPS showed that the coupling of MPc complexes formed an ether link (C-O-C) observed from the high resolution oxygen (O 1s) spectrum. The spectroscopic and electrochemical experiments were in agreement with each other, thus confirming the formation of SAMs on gold electrode.

The potential applications of these electrochemical sensors were studied towards the detection and analysis of L-cysteine and hydrogen peroxide. Acidic pH 4 conditions were used for electrocatalytic detection of L-cysteine on SAM modified gold electrodes and these

electrodes gave detection limits of the orders of 10^{-7} mol.L^{-1}. The electrocatalytic detection of hydrogen peroxide was studied in physiological pH conditions (pH 7.4) and only CoPc complex gave good results with both electrocatalytic oxidation and reduction peaks observed. The analysis of hydrogen peroxide at CoPc SAM modified gold electrode was studied and the results gave good limits of detections of the orders of 10^{-7} mol.L^{-1} both oxidatively and reductively. At FePc and MnPc complexes the hydrogen peroxide degraded and this was comparable to the studies reported in literature for FePc complexes.

CoPc SAM modified gold electrode was further studied as an electrode mediator between the enzyme (glucose oxidase) and gold electrode. Glucose oxidase enzyme was covalently immobilized onto CoPc SAM, thus forming an electrochemical biosensor. The applications and electrocatalytic behaviour of the biosensor was investigated towards the detection of glucose. The biosensor gave good results for the analysis of glucose with the detection limit of the orders of 10^{-6} mol.L^{-1} and wide concentration range (0.3 – 25 mM) which is within the concentration range for normal and diabetic person. The real sample analysis for a commercially available glucose gave good results comparable to the manufacture's value. The kinetic studies using Lineweaver-Burk equation gave a small Michaelis-Menten constant (7.9 mM) compared to other CoPc modified electrode reported in literature. An even smaller and more realistic Michaelis-Menten constant (4.8 mM) was obtained using Hanes equation. The smaller the Michaelis-Menten constant means better and more complete the enzyme-substrate reaction. The interferent studies for the investigated interfering species (L-cysteine, oxalic acid, ascorbic acid and uric acid) showed that only ascorbic acid interfere strongly with the detection signal of glucose. These results then showed that the enzyme modified electrode is valuable and can be used for glucose detection.

REFERENCES

[1] P. Gregory, *J. Porphyrins Phthalocyanines*, 2000 (**4**) 432.

[2] N. B. McKeown, *Chem. Ind.*, 1999, 92.

[3] D. Worhle, D. Meissener, *Adv. Mater.*, 1991 (**3**) 129.

[4] A. B. P. Lever, M. R. Hempstead, C. C. Leznoff, W. Liu, M. Melnic, W. A. Nevin, P. Seymour, *Pure Appl. Chem.*, 1986 (**58**) 1467.

[5] C. C. Leznoff, A. B. P. Lever (eds), *Phthalocyanine: Properties and Applications*, VCH Publishers, New York, 1989 – 1996, Vol. **1-4**.

[6] N. B. McKeown in *Phthalocyanine Materials: Synthesis, Structure and Function*, Cambrodge University Press, New York, 1998.

[7] A. W. Snow, W. R. Barger in *Phthalocyanine: Properties and Applications*, (Eds): C. C. Leznoff and A. B. P. Lever, VCH Publishers, New York, 1989, Vol. **1**.

[8] S. Vilakazi, T. Nyokong, *Polyhedron*, 2000 (**19**) 229.

[9] J. Oni, T. Nyokong, *Anal. Chim. Acta*, 2001 (**434**) 9.

[10] H. Hanabusa, H. Shirai in *Phthalocyanine: Properties and Applications*, (Eds): C. C. Leznoff and A. B. P. Lever, VCH Publishers, New York, 1993, Vol. **2**.

[11] H. Kasuga in *Phthalocyanine: Properties and Applications*, ((Eds): C. C. Leznoff and A. B. P. Lever, VCH Publishers, New York, 1996, Vol. **4**.

[12] M. Thamae, T. Nyokong, *J. Electroanal. Chem.*, 1999 (**470**) 126.

[13] E. A. Luckyanets, *J. Porphyrins Phthalocyanines*, 1999 (**3**) 424.

[14] J. D. Spikes, *J. Photochem. Photobiol.*, 1986 (**43**) 691.

[15] I. Rosenthal, E. Ben-Hur in *Phthalocyanine: Properties and Applications*, (Eds): C. C. Leznoff and A. B. P. Lever, VCH Publishers, New York, 1989, Vol. **1**.

[16] A. Arrieta, M.L. Rodriguez-Mendez, J.A. de Saja, *Sens. Actuators B*, 2003 (**95**) 357.

[17] S. Palacin, *Adv. Colloid Interface Sci*., 2000 (**87**)165.

[18] Q. Zhang, D. Huang, Y. Liu, *Synth. Met.*, 2003 (**137**) 989.

[19] M. J. Cook, D. A. Russell, *J. Mater. Chem.*, 2000 (**11**) 31.

[20] M.J. Cook, *Pure Appl. Chem.*, 1999 (**71**) 2145.

[21] M. J. Cook, *J. Mater. Chem.*, 1996 (**6**) 677.

[22] Z. Li, M. Lieberman, W. Hill, *Langmuir*, 2001 (**17**) 4887.

[23] K. Ozoemena, T. Nyokong, *Electrochim. Acta*, 2002 (**47**) 4035.

[24] K.I. Ozoemena, T. Nyokong, P. Westbroek, *Electroanal.*, 2003 (**14**) 1762.

[25] D. J. Revell, I Chambrier, M. J. Cook, D. A. Russell, *J. Mater. Chem.*, 2000 (**10)** 31.

[26] J. J. Gooding, F. Mearns, W. Yang, J. Liu, *Electroanal.*, 2003 (**15**) 81.

[27] R. K. Smith, P. A. Lewis, P. S. Weiss, *Prog. Surf. Sci.*, 2004 (**75**) 1.

[28] H. O. Finklea in *Electroanalytical Chemistry*, (Eds): A. J. Bard and I. Rubunstein, Marcel Dekker, New York, 1996, Vol. **19**.

[29] A.E. Kaifer, M. Gomez-Kaifer, *Supramolecular Electrochemistry*, Wiley-VCH, Germany, 1999.

[30] H. O. Finklea in *Encyclopaedia of Analytical Chemistry: Applications, Theory and Instrumentations*, (Eds): R. A. Meyer, Wiley & Sons, Chichester, 2000, Vol. **11**.

[31] R.G. Nuzzo, D.L. Allara, *J. Am. Chem. Soc*., 1983 (**105**) 4481.

[32] R. G. Nuzzo, F. A. Fusco, D. L. Allara, *J. Am. Chem. Soc*., 1987 (**109**) 2358.

[33] M. D. Porter, T. B. Bright, D. Allara, C. E. D. Chidsey, *J. Am. Chem. Soc.*, 1987 (**109**) 3559.

[34] H. O. Finklea, S. Avery, M. Lynch, T. Furtsch, *Langmuir*, 1987 (**3**) 409.

[35] E. B. Troughton, C. D. Bain, G. M. Whitesides, R. G. Nuzzo, D. L. Allara, M. D. Porter, *Langmuir*, 1988 (**4**) 365.

[36] L. Strong, G. M. Whitesides, *Langmuir*, 1988 (**4**) 546.

[37] (a) C. D. Bain, G. M. Whitesides, *J. Am. Chem. Soc.*, 1988 (**110**) 3665.

(b) C. D. Bain, G. M. Whitesides, *J. Am. Chem. Soc.*, 1988 (**110**) 5897.

(c) C. D. Bain, G. M. Whitesides, *J. Am. Chem. Soc.*, 1988 (**110**) 6560.

(d) C. D. Bain, G. M. Whitesides, *Science*, 1988 (**240**) 62.

[38] C. D. E. Chidsey, D. N. Loiacono, *Langmuir*, 1990 (**6**) 682.

[39] M. J. Cook, I. Chambrier, *Porphyrin Handbook*, (Eds) K. M. Kadish, K. M. Smith, R. Guilard, Academic Press, San Diego, California, 2003, Vol. **17**.

[40] G. Che, Z. Li, H. Zhang and C.R. Cabrera, *J. Electroanal. Chem.*, 1998 (**453**) 9.

[41] J .J. Gooding, V. Praig and E.A.H. Hall, *Anal. Chim Acta*, 1998 (**70)** 2396.

[42] J. J. Gooding, D. B. Hibbert, *TrAC*, 1999 (**18**) 525.

[43] J.J. Gooding, P. Erokhin, D. B. Hibbert, *Biosens. Bioelectron.*, 2000 (**15**) 229.

[44] J. J. Gooding, L. Pugliano, D. B. Hibbert, P. Erokhin, *Electrochem. Comm.*, 2000 (**2**) 217.

[45] D.L. Pilloud, X. Chen, P.L. Dutton and C.C. Moser, *J. Phys. Chem. B*, 2000 (**104**) 2868.

[46] C.D. Bain, E.B. Troughton, Y-T. Tao, J. Eval, G.M. Whitesides and R.G. Nuzzo, *J. Am. Chem. Soc.*, 1989 (**111**) 321.

[47] R. G. Pearson, *J. Am. Chem. Soc.*, 1963 (**85**) 3533.

[48] R. G. Pearson, *Science*, 1966 (**151**) 172.

[49] I. Chambrier, M. J. Cook, D. A. Russell, *Synthesis*, 1995 (**10**) 1283.

[50] M. J. Cook, R. Hersans, J. McMurdo, D. A. Russell, *J. Mater. Chem.*, 1996 (**6**) 149.

[51] T. R. E. Simpson, D. J. Revell, M. J. Cook, D. A. Russell, *Langmuir*, 1997 (**13**) 460.

[52] T. R. E. Simpson, D. A. Russell, I. Chambrier, M. J. Cook, A. B. Horn, S.C. Thorpe, *Sens. Actuators B*, 1995 (**29**) 353.

[53] Z. Li, M. Lieberman, *Supramol. Sci.*, 1998 (**5**) 485.

[54] K. I. Ozoemena, T. Nyokong, *Talanta*, 2005 (**67**) 162.

[55] K. Ozoemena, P. Westbroek, T. Nyokong, *Electrochem. Comm.*, 2001 (**3**) 529.

[56] K. Ozoemena, P. Westbroek, T. Nyokong, *J. Porphyrins Phthalocyanines*, 2002 (**6**) 98.

[57] N. Sehlotho, T. Nyokong, *Electrochim. Acta*, 2006 (**51**) 4463.

[58] K.I. Ozoemena, T. Nyokong, *Microchem. J.*, 2003 (**75**) 241.

[59] K. I. Ozoemena, T. Nyokong, *J. Electroanal. Chem.*, 2005 (**579**) 283.

[60] K. I. Ozoemena, T. Nyokong, *Electrochim. Acta*, 2006 (**51**) 2669.

[61] N. Kanayama, T. Kanbara, H. Kitomi, *J. Phys. Chem. B*, 2000 (**104**) 271.

[62] J. R. de Sousa, A. A. Batista, I. C. N. Diogenes, G. F. S. Andrade, M. L. A. Temperini, L. F. Lopes, I. S. Moreira, *J. Electroanal. Chem.*, 2003 (**543**) 93.

[63] B. D. Lamp, D. Horaba, M. D. Porter, K. Niki, T. M. Cotton, *Langmuir*, 1997 (**13**) 736.

[64] S. Krause, *Instrumentation and Electroanalytical Chemistry*, (Eds) A. J. Bard, M. Stratmann, P. R. Inwin, Wiley-VCH GmbH & Co. KGaA, 2003, Vol. **3**.

[65] A. J. Bard, L. R. Faulkner, *Electrochemical Methods: Fundamentals and Applications*, John Wiley & Sons, New York, 1980.

[66] M. A. C. Brett, A. M. O. Brett, *Electrochemistry Principles, Methods and Applications*, Oxford University Press: New York, 1993.

[67] P. Westbroek, G. Priniotakis, P. Kiekens, *Analytical Electrochemistry in Textiles*, Woodhead Publishing Limited and CRC Press LLC, Cambridge England, 2005.

[68] P. Curie, J. C. Curie, *Comput. Rend. Acad. Sci. Paris.*, 1880 (**91**) 294.

[69] A. R. Hillman, *Instrumentation and Electroanalytical Chemistry*, (Eds) A. J. Bard, M. Stratmann, P. R. Ulwin, Wiley-VCH GmbH & Co. KGaA, 2003, Vol. **3**.

[70] (a) M. Rodahl, F. Hook, A. Krozer, P. Brzezinski, B. Kasemo, *Rev. Sci. Instrum.*, 1995 (**66**) 3294.

(b) M. Rodahl, B. Kasemo, *Rev. Sci. Instrum.*, 1996 (**67**) 3238.

(c) M. Rodahl, *On the frequency and Q factor response of the quartz crystal microbalance to liquid overlayers*, Ph.D. Thesis, Chalmers (1995).

[71] G. Sauerbrey, *Z. Phys.*, 1959 (**155**) 206.

[72] F. Höök, B. Kasemo, T. Nylander, C. Fant, K. Sott, and H. Elwing, *Anal. Chem.*, 2001 (**73**) 5796.

[73] R. Saber, S. Mutlu, E. Piskin, *Biosens. Bioelectron.*, 2002 (**17**) 727.

[74] C. A. Keller, B. Kasemo, *Biophys. J.*, 1998 (**75**) 1397.

[75] M. Liebau, A. Hilderbrand, R.H. H. Neubert, *Eur. Biophys. J.*, 2001 (**30**) 42.

[76] L. Tedeschi, L. Citti, C. Domenici, *Biosens. Bioelectron.*, 2005 (**20**) 2376.

[77] F. Hook, M. Rodahl, P. Brzezinski, B. Kasemo, *Langmuir*, 1998 (**14**) 729.

[78] E. J. Calvo, R. Etchenique, L. Pietrasanta, A. Wolosiuk, *Anal. Chem.*, 2001 (**73**) 1161.

[79] J. B. Hudson, *Surface Science: An Introduction*, John Wiley & Sons, New York, 1998.

[80] M. H. Kibel, *Surface Analysis Methods in Material Science*, (Eds) D. J. O'Connor, B. A. Sexton, R. St. C. Smart, Springer-Verlag, Berlin Heidelberg, Germany, 1993.

[81] A.-S. Duwez, *J. Electron. Spectrosc. Relat. Phenom.*, 2004 (**134**) 97.

[82] M. J. Pelletier, *Analytical Applications of Raman Spectroscopy*, Michigan, USA, 1999.

[83] J. Popp, W. Kiefer, *Encyclopedia of Analytical Chemistry: Applications, Theory and Instrumentation*, (Eds) R. A. Meyer, John Wiley & Sons, New York, 2000, Vol. **15**.

[84] D. Dini, M. Hanack in *Phthalocyanine: Properties and Materials*, (Eds) K. M. Hadish, K. M. Smith, R. Guilard, Academic Press, San Diego, California, 2003, Vol. **17**.

[85] D. Worhle, L. Kreienhoop, D. Schlettwein in *Phthalocyanine: Properties and Applications*, (Eds) A. B. P. Lever, C. C. Leznoff, VCH Publishers, New York, 1996, Vol. **4**.

[86] B. Simic-Glavaski in *Phthalocyanine: Properties and Applications*, Eds) A. B. P. Lever, C. C. Leznoff, VCH Publishers, New York, 1993, Vol. **3**.

[87] H. Shirai, A. Maruyama, K. Kobayashi, N. Hojo, *Makromol. Chem.*, 1980 (**181**) 575.

[88] K. Kasuga, M. Tsutsui, *Coord. Chem. Rev.*, 1980 (**32**) 67.

[89] D. Worhle, M. Eskes, K. Shigehara, A. Yamada, *Synthesis*, 1993, 194.

[90] J. Metz, O. Schneidre, M. Hanack, *Inorg. Chem.*, 1984 (**23**) 1065.

[91] M. Hanack, P. Haisch, L. Lehmann, L. R. Subramanian, *Synthesis*, 1993, 397.

[92] S. Foley, J. Gurnos, R. Luizzi, D.J. McGarvey, M. Perry and T.G. Truscott, *J. Chem. Soc., Perk. Trans.*, 1997 (**2**) 1725.

[93] G. Torre and A.T. Torres, *J. Porphyrins Phthalocyanines*, 1997 (**1**) 221.

[94] M. Suzuki, Y. Ohta, H. Nagae, T. Ichinohe, M. Kimura, K. Hanabusa, H. Shirai, D. Worhle, *Chem. Comm.*, 2000, 213.

[95] M. J. Stillman, T. Nyokong in *Phthalocyanine: Properties and Applications*, (Eds) A. B. P. Lever, C. C. Leznoff, VCH Publishers, New York, 1989, Vol. **1**.

[96] A. B. P. Lever, *Adv. Inorg. Radiochem.*, 1965 (**7**) 28.

[97] M. Gouterman, *J. Mol. Spectrosc.* 1961 (**6**) 138.

[98] P. J. Spellane, M. Gouterman, A. Antipas, S. Kim, Y. C. Liu, *Inorg. Chem.*, 1980 (**19**), 386.

[99] D. B. Hibbert, *Introduction of Electrochemistry*, Macmillan, London, 1993.

[100] F. M. Hawkridge, *Laboratory Techniques in Electroanalytical Chemistry*, 2nd edition, (Eds) P. T. Kissinger and W. R. Heineman, Marcel Dekker, New York, 1996.

[101] J. G. Osteryoung, R. A. Osteryoung, *Anal. Chem.*, 1985 (**57**) 101A.

[102] J. Wang, *Analytical Electrochemistry*, VCH Publishers, New York, 1994.

[103] A. J. Bard, L. R. Faulkner, *Electrochemical Methods: Fundamentals and Applications*, John Wiley & Sons, New York, 1996.

[104] M. J. Stillman in *Phthalocyanines: Properties and Applications*, (Eds) C. C. Leznoff, A. B. P. Lever, VCH Publishers, New York, 1993, Vol. **3**.

[105] K. Ban, K. Nishizawa, K. Ohta, H. Shirai, *J. Mater. Chem.*, 2000 (**10**) 1083.

[106] T. Nyokong, *S. Afr. J. Chem.*, 1995 (**48**) 23.

[107] J. F. Myers, R. G. W. Canham, A. B. P. Lever, *Inorg. Chem.*, 1975 (**14**) 461.

[108] A. B. P. Lever, E. R. Milaeva, G. Spier in *Phthalocyanines: Properties and Applications*, (Eds) C. C. Leznoff, A. B. P. Lever, VCH Publishers, New York, 1993, Vol. **3**.

[109] N. Chabotareva, T. Nyokong, *Electrochim. Acta*, 1997 (**42**) 3519.

[110] J. H. Zagal, *Coord. Chem. Rev.*, 1992 (**119**) 89.

[111] S. Griveau, J. Pavez, J. Zagal, F. Bedioui, *J. Electroanal. Chem.*, 2001 (**497**) 75.

[112] J. H. Zagal, M. A. Galppi, G. Cardenas-Jiron, *Polyhedron*, 2000 (**19**) 2255.

[113] S. Maree, T. Nyokong, *J. Electroanal. Chem.*, 2000 (**492**) 120.

[114] M. Sekota and T, Nyokong, *Polyhedron* 1997 (**16**) 3279.

[115] S. Vilakazi and T. Nyokong, *Polyhedron*, 2000 (**19**) 229.

[116] H. O. Finklea, D. D. Hansheu, *J. Am. Chem. Soc.*, 1992 (**114**) 3137.

[117] I. Rosen-Margalit, A. Bettelheim, J. Rishpon, *Anal. Chim. Acta*, 1993 (**281**) 327.

[118] F. Mizutani, S. Yakubi, S. Iijima, *Anal. Chim. Acta*, 1995 (**300**) 59.

[119] J. P. Hart, S. A. Wright, *TrAC*, 1997 (**16**) 89.

[120] G. Shi, J. Liu, F. Xu, H. Zhou, L. Jin, J. Jin, *Anal. Chim. Acta*, 2000 (**314**) 131.

[121] K. Wang, J-J. Xu, H-Y. Chen, *Biosens. Bioelectron.*, 2005 (**20**) 1388.

[122] E. Crouch, D. C. Cowell, S. Hoskins, R. W. Pittson, J. P. Hart, *Anal. Biochem.*, 2005 (**347**) 17.

[123] K. I. Ozoemena, T. Nyokong, *Electrochim. Acta*, 2006 (**51**) 5131.

[124] W.A. Kleinman, J.P. Richie, *Biochem. Pharmacol.*, 2000 (**60**) 19.

[125] M. Ebadi, S. K. Srinivasan, M. D. Baxi, *Prog. Neurobiol*., 1996 (**48**) 1.

[126] M. T. Heafield, S. Fearn, G. B. Steventon, R. H. Waring, A. C. Williams, S. G. Sturman, *Neurosc. Lett.*, 1990 (**110**) 216.

[127] M. Cengiz, A. Yuksel, M. Seven, *Pharmacol. Res.*, 2000 (**41**) 423.

[128] E. Bald, E. Kaniowska, G. Chwatko and R. Glowacki, *Talanta*, 2000 (**50**) 1233.

[129] I. Chatti, A. Ghorbel, P. Grange, J. M. Colin, *Catal. Today*, 2002 (**75**) 113.

[130] J. A. Reynaud, B. Malfoy, P. Canesson, *J. Electroanal. Chem*., 1980 (**114**) 195.

[131] B.R. Eggins, *Chemical Sensors and Biosensors*, John Wiley & Sons, Chichester, 2003.

[132] P. Westbroek, B. van Hayte, E. Temmerman, *Fres. J. Anal. Chem.*, 1996 (**354**) 405.

[133] P. A. Tanner, A. Y. S. Wong, *Anal. Chim. Acta*, 1998 (**370**) 279.

[134] W. Sun, H. Jiang, K. Jiao, *J. Chem. Sci*., 2005 (**117**) 317.

[135] P. Westbroek, E. Temmerman, *J. Electroanal. Chem*., 2000 (**482**) 40.

[136] G. G. Guildibault, *Enzymatic Methods of Analyst*, Pergamon, Oxford, 1970.

[137] P. Westbroek, E. Temmerman, F. Govaert, B. Van Houte, *Bull. Soc. Chim. B*, 1997 (**106**) 755.

[138] C. Matsubara, N. Kawamoto, K. Takamura, *Analyst*, 1992 (**117**) 1781.

[139] U. Pinkernell, S. Effkemann, U. Karst, *Anal. Chem*., 1997 (**69**) 3623.

[140] M. J. Navas, A. M. Jimenez, G. Galan, *Atmos. Environ*., 1999 (**33**) 2279.

[141] N. Kiba, T. Tokizawa, S. Kato, M. Tachibana, K. Tani, H. Koizuma, M. Edo, E. Yonezawa, *Anal. Sci.*, 2003 (**19**) 823.

[142] E. C. Hurdis, H. Romeyn Jr., *Anal. Chem.*, 1954 (**26**) 320.

[143] E. Ferapontova, L. Gorton, *Bioelectrochem*., 2002 (**55**) 83.

[144] E. E. Ferapontova, V. G. Grigorenko, A. M. Egorov, T. Bőrchers, T. Ruzgas, L. Gorton, *Biosens. Bioelectron*., 2001 (**16**) 147.

[145] E. Ferapontova, K. Schmengler, T. Bőrchers, T. Ruzgas, L. Gorton, *Biosens. Bioelectron.*, 2002 (**17**) 953.

[146] A. Morales, F. Céspedes, J. Muňoz, A. Martinez-Fasbregas, S. Alegret, *Anal. Chim. Acta*, 1996 (**332**) 131.

[147] Y. Lin, X. Ciu, L. Li, *Electrochem. Comm*., 2005 (**7**) 166.

[148] M. A. Gilmartin, R. J. Ewen, J. P. Hart, *J. Electroanal. Chem*., 1996 (**401**) 127.

[149] M. S. M. Quintino, H. Wimischofer, K. Araki, H. E. Toma, L. Angnes, *Analyst*, 2005 (**130**) 221.

[150] M. Somasundrum, K. Kirtikara, M. Tanticharoen, *Anal. Chim. Acta*, 1996 (**319**) 59.

[151] K. I. Ozoemena, Z. Zhao, T. Nyokong, *Electrochem. Comm*., 2005 (**7**) 679.

[152] L. Wang, E. Wang, *Electrochem. Comm*., 2004 (**6**) 225.

[153] M. A. Gilmartin, R. J. Ewen, J. P. Hart, C. L. Honeybourne, *Electroanal.*, 1995 (**7**) 547.

[154] X. Ji, J. Huang-Xian, C. Hong-Yuan, *Anal. Biochem*., 2000 (**278**) 22.

[155] K. I. Ozoemena, Z. Zhao, T. Nyokong, *Inorg. Chem. Comm*., 2006 (**9**) 223.

[156] D. R. Shankaran, K.-I. Iimura, T. Kato, *Sens. Actuators B*, 2003 (**96**) 523.

[157] G. Leegsma-Vogt, M. M. Rhemrev-Boom, R. G. Tiessen, K. Venema, J. Korf, *Bio-Med. Mater. Eng.*, 2004 (**14**) 455.

[158] S. Warren, T. McCormac, E. Dempsey, *Bioelectrochem.*, 2003 (**67**) 23.

[159] D. Pan, J. Chen, L. Nie, W. Tao, S. Yao, *Electrochim. Acta*, 2004 (**49**) 795.

[160] J. Fei, Y. Wu, X. Ji, J. Wang, S. Hu, Z. Gao, *Anal. Sci.*, 2003 (**19**) 1259.

[161] S-F. Hou, K-S. Yang, H-Q. Fang, H-Y. Chen, *Talanta*, 1998 (**47**) 561.

[162] M. E. Ghica, C. A. Brett, *Anal. Chim. Acta*, 2005 (**532**) 145.

[163] X. Zhong, R. Yuan, Y. Chai, Y. Liu, J. Dai, D. Tang, *Sens. Actuators B*, 2005 (**104**) 191.

[164] A. S. N. Murthy, J. Sharma, *Anal. Chim. Acta*, 1998 (**363**) 215.

[165] X. Jing-Juan, C. Hong-Yuan, *Anal. Biochem.*, 2000 (**280**) 221.

[166] S. E. Creager, L. A. Hockett, G. K. Rowe, *Langmuir*, 1992 (**8**) 854.

[167] C. Zhang, Q. Gao, M. Aizawa, *Anal. Chim. Acta*, 2001 (**426**) 33.

[168] S. Liu, H. Ju, *Biosens. Bioelectron.*, 2003 (**19**) 177.

[169] H. Tang, J. Chen, S. Yao, L. Nie, G. Deng, Y. Kuang, *Anal. Biochem.*, 2004 (**331**) 89.

[170] H. Zhou, H. Chen, S. Lou, W. Wei, Y. Kuang, *Sens. Actuators B*, 2004 (**101**) 224.

[171] D. Pan, J. Chen, S. Yao, L. Nie, J. Xia, W. Tao, *Sens. Actuators B*, 2004 (**104**) 68.

[172] S. Zhang, N. Wang, H. Yu, Y. Niu, C. Sun, *Bioelectrochem.*, 2005 (**67**) 15.

[173] D. Pan, J. Chen, S. Yao, W. Tao, L. Nie, *Anal. Sci.*, 2005 (**21**) 367.

[174] D. Song, Y. Mu, X. Liu, L. Zhao, H. Zhang and Q. Jin, *Microchem. J.*, 2003 (**74**) 93.

[175] D. Losic, J. G. Shapter, J. J. Gooding, *Langmuir*, 2001 (**17**) 3307.

[176] L. Jiang, A. Glidle, A. Griffith, C. J. McNeil, J. M. Cooper, *Bioelectrochem. Bioenerg.*, 1997 (**42**) 15.

[177] J. Limson, O. O. Odununga, H. Green, F. Hook, G. L. Blatch, *SA J. Science 100*, 2004, 678.

[178] J. Obirai, T. Nyokong, *Electrochim. Acta*, 2005 (**50**) 5427.

[179] A. B. P. Lever, S. R. Pickens, P. C. Minor, L. Liccoccia, B. S. Ramaswamy, K. Magnel, *J. Am. Chem. Soc.*, 1981 (**103**) 6800.

[180] B.W. Dale, *Trans. Faraday Soc.*, 1969 (**65**) 331

[181] M.J. Stillmann and A.J. Thomson, *J. Chem. Soc., Faraday Trans. 2*, 1974 (**70**) 790.

[182] A.B.P lever and J.P. Wilshire, *Inorg. Chem.*, 1978 (**17**) 1145.

[183] N. Kobayashi, M. Koshiyama, K. Funayama, T. Osa, H. Shirai, K. Hanabusa, *J. Chem. Soc., Chem. Comm.*, 1983, 913.

[184] N. Kobayashi, H. Shirai, N. Hojo, *J. Chem. Soc., Dalton Trans.*, 1984, 2107.

[185] N. Kobayashi, Y. Nishiyama, *J. Phys. Chem.*, 1985 (**89**) 1167.

[186] A. B. P. Lever, *Adv. Inorg. Chem. Radiochem.*, 1965 (**7**) 28.

[187] S. E. Creager, L. A. Hockett, G. K. Rowe, *Langmuir*, 1992 (**8**) 854.

[188] U. Oesch, J. Janata, *Electrochim. Acta*, 1983 (**28**) 1237.

[189] K. V. Gobi, T. Okajima, K. Tokuda, T. Ohsaka, *Langmuir*, 1998 (**14**) 1108.

[190] Z. Wang, A.-M. Nygard, M. J. Cook, D. A. Russell, *Langmuir*, 2004 (**20**) 5850.

[191] J.-S. Ye, Y. Wen, W. D. Zhang, H. F. Cui, G. Q. Xu, F.-S. Shen, *Electroanal.*, 2005 (**17**) 89.

[192] P. Ocon, P. Herrasti, L. Vazquez, R. C. Salvarezza, J. M. Vara, A. J. Arvia, *J. Electroanal. Chem.*, 1991 (**319**) 101.

[193] S.-S. Wong, M.D. Porter, *J. Electroanal. Chem.*, 2000 (**485**) 153.

[194] A.G. Brolo, D. E. Irish, G. Szymanski, J. Lipkowski, *Langmuir*, 1998 (**14**) 517.

[195] Y.-H. Tse, P. Janda, H. Lam, J. Zhang, W. J. Pietro, A. B. P. Lever, *J. Porphyrins Phthalocyanines*, 1997 (**1**) 3.

[196] C. C. Leznoff, L. S. Black, A. Hiebert, P. W. Causey, D. Christendat, A. B. P. Lever, *Inorg. Chim. Acta*, 1992 (**31**) 5172.

[197] M. Isaacs, M. J. Aguirre, A. Toro-Labbe, J. Costamagma, M. Paez, J. H. Zagal, *Electrochim. Acta*, 1998 (**43**) 182.

[198] D. Schlettwein, T. Yoshida, *J. Electroanal. Chem.*, 1998 (**441**) 139.

[199] N. Kobayashi, P. Janda, A. B. P. Lever, *Inorg. Chem.*, 1992 (**31**) 5172.

[200] W. A. Nevin, M.R. Hempstead, W. Liu, C. C. Leznoff, A. B. P. Lever, *Inorg. Chem.*, 1987 (**26**) 570.

[201] S. Griveau, G. Pavez, J.H. Zagal, F. Bedioui, *J. Electroanal. Chem.*, 2001 (**497**) 75.

[202] M.D. Porter, T.B. Bright, D. Allara, C.E.D. Chidsey, *J. Am. Chem. Soc.*, 1987 (**109**) 3559.

[203] E. Sabatani, I. Rubinstein, *J. Phys. Chem.*, 1987 (**91**) 6663.

[204] D. E. Weisshaar, B. D. Lamp, M. D. Porter, *J. Am. Chem. Soc.*, 1992 (**114**) 5860.

[205] M. M. Walczak, C. A. Alves, B. D. Lamp, M. D. Porter, *J. Electroanal. Chem.*, 1995 (**396**) 103.

[206] C. J. Zhong, J. Zak, M. D. Porter, *J. Electroanal. Chem.*, 1997 (**421**) 9.

[207] M. P. Somashekarappa, J. Keshavayya, S. Sampath, *Pure Appl. Chem.*, 2002 (**74**) 1609.

[208] L. V. Protsailo, W. R. Fawcett, D. A. Russell, R. L. Meyer, *Langmuir*, 2002 (**18**) 9342.

[209] R. P. Janek, W. R. Fawcett, A. Ulman, *Langmuir*, 1998 (**14**) 3011.

[210] R. K. Mendes, R. S. Freire, C. P. Fonseca, S. Neves, L. T. Kubota, *J. Braz. Chem. Soc.*, 2001 (**15**) 849.

[211] A. Lasia, A. Rami, *J. Electroanal. Chem.*, 1990 (**294**) 123.

[212] C. Amotore, J. M. Saveant, D. Tessier, *J. Electroanal. Chem.*, 1983 (**147**) 39.

[213] V. Lakshminarayanan, U. K. Sur, *J. Phys.*, 2003 (**61**) 361.

[214] B. Simic-Glavaski, S. Zecevic, E. Yeager, *J. Am. Chem. Soc.*, 1985 (**107**) 5625.

[215] B. Simic-Glavaski, S. Zecevic, E. Yeager, *J. Electroanal. Chem.*, 1983 (**150**) 469.

[216] K. De Wael, P. Westbroek, P. Bultinck, D. Depla, P. Vandenabeele, A. Andriens, E. Temmerman, *Electrochem. Comm.*, 2005 (**7**) 87.

[217] D.R. Tackley, G. Dent, W.E. Smith, *Phys. Chem. Chem. Phys.*, 2000 (**2**) 3949.

[218] D. R. Tackley, G. Dent, W.E. Smith, *Phys. Chem. Chem. Phys.*, 2001 (**3**) 1419.

[219] P.E. Laibinis, G. M. Whitesides, D. L. Allara, Y.-T. Tao, A. N. Parikh, R. G. Nuzzo, *J. Am. Chem. Soc.*, 1991 (**113**) 7152.

[220] C. Pale-Grosdemange, E. S. Simon, K. L. Prime, G. M. Whitesides, *J. Am. Chem. Soc.*, 1991 (**113**) 12.

[221] J. E. Hutchison, T. A. Postlethmaite, R. W. Murray, *Langmuir*, 1993 (**9**) 3277.

[222] A. Dalmia, C. C. Liu, R. F. Savinell, *J. Electroanal. Chem.*, 1997 (**430**) 205.

[223] W. Zhou, T. Baunach, V. Ivanova, D. M. Kolb, *Langmuir*, 2004 (**20**) 4590.

[224] C. R. Raj, T. Ohsaka, *Bioelectrochem*., 2001 (**53**) 251.

[225] X.-H. Zhang, S.-F. Wang, *Sensors*, 2003 (**3**) 61.

[226] A. Napier, J. P. Hart, *Electroanal*., 1996 (**8**) 1006.

[227] M. K. Halbert, R. P. Baldwin, *Anal. Chem.*, 1985 (**57**) 591.

[228] J. Obirai, T. Nyokong, *Electrochim. Acta*, 2004 (**49**) 1417.

[229] C. C. Leznoff, L. S. Black, A. Hiebert, P. W. Causey, D. Christendat, A. B. P. Lever, *Inorg. Chim. Acta*, 2006 (**359**) 2690.

[230] H. Shirai, S. Higaki, K. Hanabusa, N. Hojo, *J. Polym. Sci.;Polym. Letters Edu.*, 1983 (**21**) 157.

[231] H. Shirai, S. Higaki, K. Hanabusa, N. Hojo, *J. Chem. Soc. Chem. Comm.*, 1983, 751.

[232] S. Hrapovic, Y. Liu, K. B. Male, J. H. T. Luong, *Anal. Chem.*, 2004 (**76**) 1083.

[233] R. A. Kamin, G. S. Wilson, *Anal. Chem.*, 1980 (**52**) 1189.

[234] A. Cornish-Bowden, *Fundamentals of Enzyme Kinetics*, Butterworths, London, 1979.

[235] R. I. Stefan, J. F. van Staden, H. Y. Aboul-Enien, *Electrochemical Sensors in Bioanalysis*, Marcel Dekker, New York, 2001.